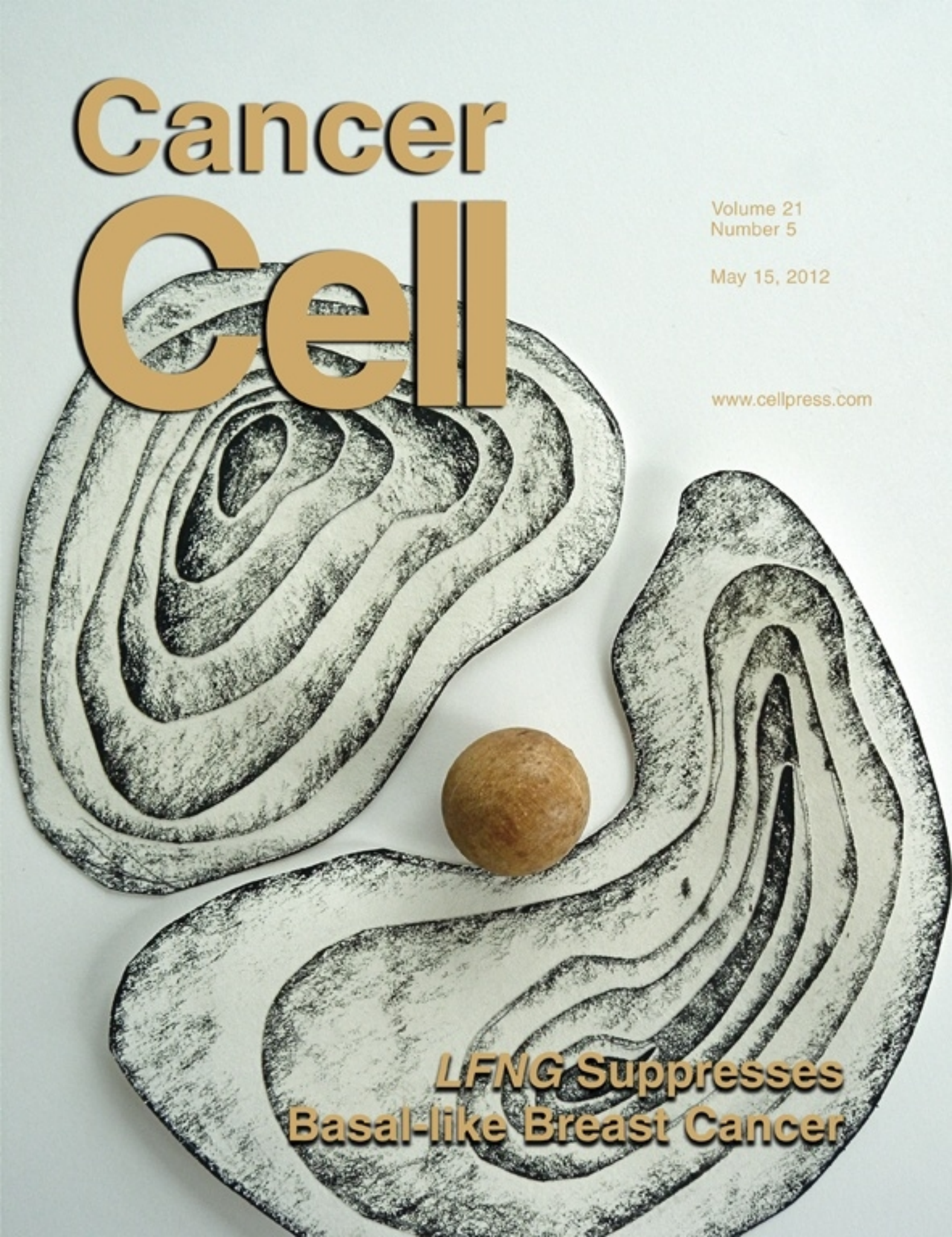


Cancer Cell



Volume 21
Number 5

May 15, 2012

www.cellpress.com

**LFNG Suppresses
Basal-like Breast Cancer**

There's a Time and a Place for *MYCN*

Timothy N. Phoenix¹ and Richard J. Gilbertson^{1,*}

¹Departments of Developmental Neurobiology and Oncology, St. Jude Children's Research Hospital, 262 Danny Thomas Place, Memphis, TN 38105, USA

*Correspondence: richard.gilbertson@stjude.org

DOI 10.1016/j.ccr.2012.05.001

Brain tumors display extensive diversity. In this issue of *Cancer Cell*, Swartling et al. provide evidence that the temporal and spatial transcriptional programs in neural stem cells underlie a diverse response to the *MYCN* oncogene, potentially contributing to cancer diversity.

The billions of neurons and glia that form the central nervous system (CNS) arise from neural stem cells (NSCs) derived from the neural tube (Kriegstein and Alvarez-Buylla, 2009). Throughout development, the daughters of NSCs follow topographically and temporally discrete cellular programs; spinal neurons are distinct from those that form in the cortex, and neurogenesis precedes gliogenesis in the forebrain. These programs are controlled by a combination of cell intrinsic and extrinsic factors e.g., chromatin marks and morphogens (Gräff et al., 2011; Ihrie and Alvarez-Buylla, 2011). Recent evidence suggests that highly specific developmental programs might render cells peculiarly susceptible to particular oncogenic events, resulting in the formation of discrete subgroups of cancer (Gilbertson, 2011). For example, robust subgroups of the brain tumors ependymoma and medulloblastoma contain global gene expression profiles that reflect their developmental and molecular origins in the CNS (Gibson et al., 2010; Johnson et al., 2010; Kawachi et al., 2012; Pei et al., 2012).

In this issue of *Cancer Cell*, Swartling et al. (2012) investigate how different mouse NSC populations respond to aberrant expression of *MYCN*—an oncogene commonly deregulated in various human brain tumors. Through a series of elegant in vitro and in vivo studies, the authors challenged cells from different regions of the developing CNS with wild-type or mutant *MYCN*. They show that distinct populations of NSCs display different cellular response to this oncogene, including transformation capacity, and ultimately the type of tumor produced (Figure 1).

First, using their previously reported GTML mouse model of *MYCN*-driven

medulloblastoma (Swartling et al., 2010), the authors show that *MYCN* drives Sonic Hedgehog (SHH) independent proliferation of GTML cells and that tumor growth likely correlates with *MYCN* expression in these tumors. Switching to the developing CNS, the authors then surveyed potential susceptibility to N-myc driven transformation by assessing the response of NSCs from different neurogenic regions to wild-type (N-Myc^{WT}) or stabilized mutant N-Myc^{T58A}. N-Myc^{T58A}, but not N-Myc^{WT}, significantly increased the proliferation of cerebellar and forebrain NSCs isolated from either embryonic day 16 (E16) or postnatal day 0 (P0) mice. In contrast, E14 rather than E16 lower rhombic lip progenitors (LRLPs), proliferated in response to N-Myc^{T58A}, confirming previous reports that these cells are susceptible to transformation early in development (Gibson et al., 2010) and revealing temporal differences in susceptibility to N-Myc.

In addition to inducing proliferation, N-Myc^{T58A} also appeared to subvert intrinsic cell signals in certain NSCs. Once again, this effect varied with the time and the place from which NSCs were isolated. Prompted by changes in Sox9 expression that acts downstream of SHH signaling in NSCs (Scott et al., 2010), the authors noted that while N-Myc^{T58A} promoted SHH-independence in E16 cerebellar and P0 forebrain cells, this did not appear to occur in P0 cerebellar and E16 forebrain cells.

Armed with these data, the authors asked whether cell context might dictate the capacity of N-Myc^{WT} or N-Myc^{T58A} to drive tumorigenesis in the CNS. In keeping with their observations in vitro, N-Myc^{WT}-transduced NSCs failed to form tumors when orthotopically implanted in mice. But N-Myc^{T58A} drove transformation of

E16 and P0 cerebellar and forebrain NSCs as well as E14, but not E16 or P0, LRLPs. Interestingly, N-Myc^{T58A}-transduced P0 cerebellar NSCs formed tumors in the cerebellum that resembled human and mouse GTML medulloblastoma, while N-Myc^{T58A}-transduced P0 forebrain NSCs generated gliomas in the cerebrum. To clarify the influence of intrinsic versus extrinsic factors on the type of brain tumor formed in these models, the authors transplanted P0 forebrain and cerebellar NSCs, each transduced with N-Myc^{T58A}, into the cerebellum and forebrain, respectively. Their results suggest that the cell of origin plays a dominant role in determining tumor phenotype, as forebrain cells still made gliomas in the cerebellum, and cerebellar cells made primitive neuroectodermal tumors in the forebrain. The only difference noted was a modest reciprocal change in Sox9 and Olig2 within “misplaced” tumor implants. So while programs intrinsic to particular NSCs may primarily determine the course of tumorigenesis, a role for environmental influence in tumor specification remains a possibility.

Together, these data support a growing body of evidence that the cellular origin of cancers heavily dictates disease phenotype and biology and that this lineage relationship is often revealed by a cancer's transcriptome (Gilbertson, 2011). Indeed, using Affymetrix exon arrays, Swartling et al. (2012) identified a close alignment between the gene expression patterns of N-Myc^{T58A} tumors and the corresponding, originating, cerebellar or forebrain NSC. In an additional twist on this theme, the authors showed that NSCs derived from different developmental stages of the cerebellum generate distinct forms of medulloblastoma. Medulloblastomas derived from

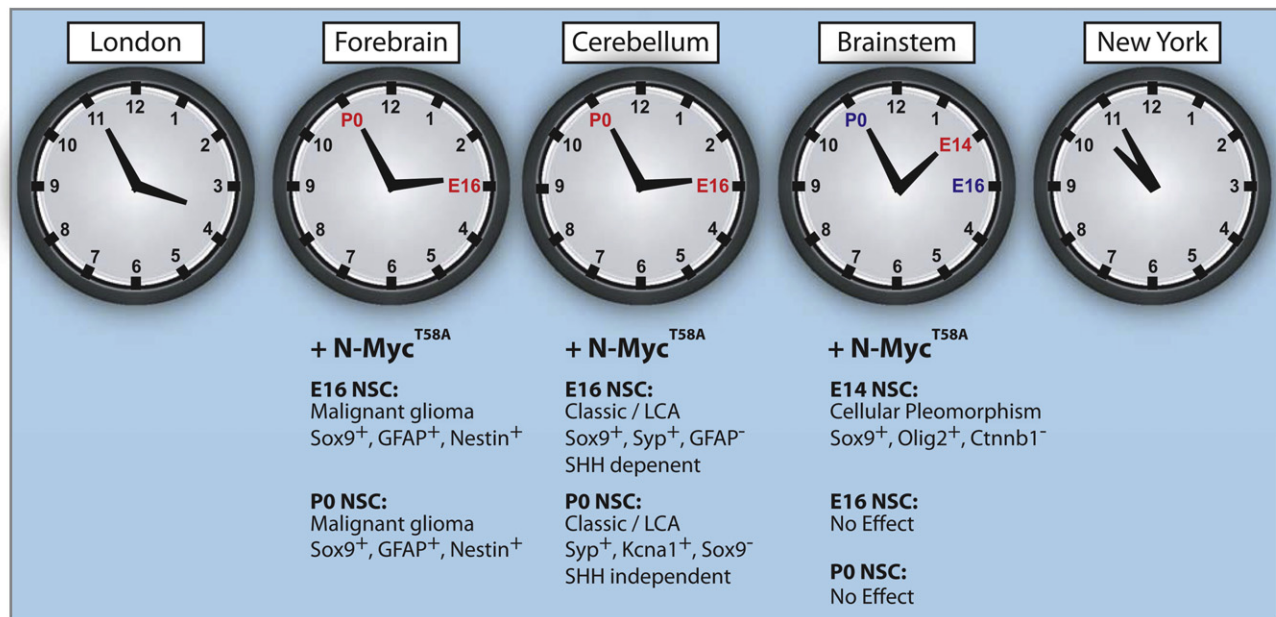


Figure 1. There Is a Time and a Place for N-Myc-Driven Tumorigenesis in the CNS

Swartling et al. (2012) show that different NSCs in the mouse CNS are differentially susceptible to transformation by N-Myc, driving time and location-specific tumors.

E16 cerebellar cells expressed high levels of *Sox9*, *Mycn*, and the granule neuron precursor marker *Math1*, suggesting a Shh-dependent form of the disease. In contrast, medulloblastomas derived from P0 cells displayed lower expression of *Sox9*, *Mycn*, and *Math1* compatible with a SHH-independent origin. Forebrain N-Myc^{T58A} P0 tumors (P0 glioma) also showed high levels of *Sox9* and *Mycn* with no *Math1*, consistent with transformation of a forebrain cell type that shows Shh-dependence independently of *Math1*.

Finally, the authors used their model systems to begin to unravel some of the cell signals that drive tumorigenesis in concert with N-Myc. Focusing on *Sox9*, the authors investigated whether this putative effector of SHH signaling plays a functional role in transforming P0 cerebellar NSCs. Overexpression of *Sox9* with N-Myc^{T58A} in P0 cerebellar NSCs suppressed proliferation but enhanced self-renewal, ultimately causing tumors to arise with shorter latencies and higher penetrance. Tumors driven by *Sox9* with N-Myc^{T58A} also showed elevated levels of *Gli2*, and focal expression of GFAP, not seen in those driven by N-Myc^{T58A} alone. These studies reveal potential

cooperative interactions between N-Myc and *Sox9* in the development of brain tumor subtypes.

This work by Swartling et al. (2012) represents an important step forward in understanding the mechanisms that contribute to tumor diversity in the CNS. Using a single oncogene, *MYCN*, the authors were able to generate different types of CNS tumor by varying the age and location of the originating NSC. These data not only confirm a role for *MYCN* in forebrain and hindbrain tumorigenesis but also underscore the emerging importance of the originating cell type in dictating the cancer phenotype. The observation that N-Myc^{T58A} drives anaplastic medulloblastomas from E14 LRLPs independent of WNT signaling is noteworthy, because these same cells were shown to generate WNT-subgroup medulloblastomas (Gibson et al., 2010). Thus, LRLPs that reside outside the cerebellum might be a source of multiple forms of medulloblastoma. Comparison of Swartling's *MYCN*-driven model with recently reported tumors driven by *MYC* should also help unravel the different roles of these "sister" oncogenes in medulloblastoma (Kawauchi et al., 2012; Pei et al., 2012). The authors note appro-

priately that the originating cell types in their models are yet to be defined formally as NSCs, but this does not detract from the importance of their work that demonstrates time and location specific tumorigenesis in the CNS. The data and models generated by Swartling et al. (2012) should provide an extremely useful resource to the brain tumor research community as we seek to unravel the diversity of these diseases and develop curative therapies for all patients.

REFERENCES

- Gibson, P., Tong, Y., Robinson, G., Thompson, M.C., Currie, D.S., Eden, C., Kranenburg, T.A., Hogg, T., Poppleton, H., Martin, J., et al. (2010). *Nature* 468, 1095–1099.
- Gilbertson, R.J. (2011). *Cell* 145, 25–29.
- Gräff, J., Kim, D., Dobbin, M.M., and Tsai, L.-H. (2011). *Physiol. Rev.* 91, 603–649.
- Ihrle, R.A., and Alvarez-Buylla, A. (2011). *Neuron* 70, 674–686.
- Johnson, R.A., Wright, K.D., Poppleton, H., Mohankumar, K.M., Finkelstein, D., Pounds, S.B., Rand, V., Leary, S.E., White, E., Eden, C., et al. (2010). *Nature* 466, 632–636.
- Kawauchi, D., Robinson, G., Uziel, T., Gibson, P., Reh, J., Gao, C., Finkelstein, D., Qu, C., Pounds, S., Ellison, D.W., et al. (2012). *Cancer Cell* 21, 168–180.

Kriegstein, A., and Alvarez-Buylla, A. (2009). *Annu. Rev. Neurosci.* 32, 149–184.

Pei, Y., Moore, C.E., Wang, J., Tewari, A.K., Eroshkin, A., Cho, Y.J., Witt, H., Korshunov, A., Read, T.A., Sun, J.L., et al. (2012). *Cancer Cell* 21, 155–167.

Scott, C.E., Wynn, S.L., Sesay, A., Cruz, C., Cheung, M., Gomez Gavro, M.V., Booth, S., Gao, B., Cheah, K.S.E., Lovell-Badge, R., and Briscoe, J. (2010). *Nat. Neurosci.* 13, 1181–1189.

Swartling, F.J., Grimmer, M.R., Hackett, C.S., Northcott, P.A., Fan, Q.-W., Goldenberg, D.D.,

Lau, J., Masic, S., Nguyen, K., Yakovenko, S., et al. (2010). *Genes Dev.* 24, 1059–1072.

Swartling, F.J., Savov, V., Persson, A.I., Chen, J., Hackett, C.S., Northcott, P.A., Grimmer, M.R., Lau, J., Chesler, L., Perry, A., et al. (2012). *Cancer Cell* 21, this issue, 601–613.

What a Difference a Phosphate Makes: Life or Death Decided by a Single Amino Acid in MDM2

Yao-Cheng Li¹ and Geoffrey M. Wahl^{1,*}

¹Gene Expression Laboratory, Salk Institute for Biological Studies, La Jolla, CA 92130, USA

*Correspondence: wahl@salk.edu

DOI 10.1016/j.ccr.2012.04.033

In this issue of *Cancer Cell*, Gannon and colleagues create genetically engineered mice to test the role phosphorylation plays in the modification of one serine long thought to play a critical role in controlling the activity of MDM2, one of p53's main negative regulators.

The tumor suppressor p53 is activated by numerous stressors and results in expression or repression of hundreds of genes that elicit a broad range of biological responses culminating in effective tumor suppression. However, p53 activation must be controlled with exquisite care because as little as a 2-fold reduction in its activity can cause radio resistance and increased tumorigenicity (Bond et al., 2004; Wang et al., 2009). Conversely, a 2-fold increase in p53 activity such as in *p53^{7KR/7KR}* mice (a knock-in model in which seven conserved C-terminal lysine residues were replaced by arginine) can lead to myeloblastosis and death by heart failure (Wang et al., 2011).

Ubiquitin-mediated proteolysis is central to controlling p53's protein level and activity. In unstressed cells, the E3 ubiquitin-ligase MDM2 recruits E2 ubiquitin-conjugating enzymes to transfer ubiquitins onto p53 and MDM2 itself, resulting in proteasomal degradation of both proteins. MDM4 (also known as MDMX), a protein related to MDM2 but lacking intrinsic E3 ubiquitin-ligase activity, hetero-oligomerizes with MDM2 to modulate MDM2's E3 ligase activity (Wade et al., 2010). MDM2 and MDM4 play non-overlapping and tissue-specific roles to precisely control p53 levels and activity (Wade et al., 2010). Deleting

Mdm2 typically elicits a more extreme phenotype than deleting *Mdm4*, but eliminating p53 rescues both. This demonstrates that both MDM2 and MDM4 are critical nodes in p53 regulation. *MDM2* is a p53-induced gene, and in vitro studies show that increasing MDM2 abundance can attenuate p53 activation, leading p53 to return to low basal levels upon resolution of the inducing stress. The importance of this negative feedback loop for p53 regulation in vivo in different tissues remains unclear.

Correct temporal control of p53 responses is critical, but how this is achieved in vivo remains to be resolved. Posttranslational modifications play critical roles in p53 regulation, so the residues of p53, MDM2, and MDM4 that are modified by damage-activated kinases, phosphatases, and other modifying enzymes are prime candidates for temporal regulators. The acceptable thresholds for p53 regulation have been dramatically revealed by studies showing that mice heterozygous for *Mdm2* or *Mdm4*, with reduced expression of *Mdm2* or *Mdm4*, or with blocked posttranslational modification at damage-modifiable residues have profoundly altered radiation responses (Bondar and Medzhitov, 2010; Wang et al., 2009). Ionizing radiation activates DNA

damage-activated kinases such as ATM and CHK2, resulting in phosphorylation of multiple residues on MDM2, MDM4, and p53 (Wade et al., 2010). Studies in human cancer cell lines first suggested that preventing MDM2 Ser395 (mouse Ser394) phosphorylation could impair its damage-dependent degradation and consequently attenuate p53 activation (Maya et al., 2001). DNA damage also induces MDM4 phosphorylation at serine 341, 367, and 402, resulting in its MDM2-dependent degradation. Mice expressing *Mdm4* 3SA, an MDM4 mutant with alanine substitutions at these three positions, are remarkably resistant to ionizing radiation due to attenuated radiation-induced p53 responses in the hematopoietic system but are very sensitive to c-Myc induced lymphomagenesis (Wang et al., 2009). Both phenotypes result from a modest 2-fold reduction in p53 basal and induced activity. These data suggest the importance of regulating MDM4 stability in vivo for controlling p53 activity.

In this issue of *Cancer Cell*, Gannon et al. (2012) demonstrate the importance of MDM2 Ser394 phosphorylation in regulating the responses of mice to irradiation by making S394A (non-phosphorylatable) and S394D (phosphomimetic) mutations. They show that this amino acid can swing the pendulum

from exquisite radio-sensitivity to extraordinary radio resistance. Thus, just as shown for *Mdm4*^{3SA/3SA} and *p53*^{7KR/7KR} mice, it is not DNA damage caused by irradiation that induces lethality; rather, it is the p53 response that is critical. Importantly, and in contrast to *Mdm4*^{3SA/3SA} mice that do not display increased lymphomagenesis following irradiation, 65% of *Mdm2*^{S394A/S394A} mice developed spontaneous lymphomas in 24 months, a rate similar to that in *p53*^{+/-} animals. These data indicate that proper MDM2 Ser394 phosphorylation contributes to effective p53-mediated tumor suppression. The mechanistic differences underlying the variance in lymphomagenesis remain unclear, though it appears that p53 levels are reduced significantly more in *Mdm2*^{S394A/S394A} mice than in *Mdm4*^{3SA/3SA} mice. Interestingly, the phenotype observed by Gannon et al. (2012) were not associated with differences in MDM2 stability, suggesting that another mechanism may be at play.

Given the attenuated p53 responses in *Mdm2*^{S394A/S394A} mutants, would constitutive phosphorylation of this residue cause persistent p53 activation and consequent embryonic lethality similar to *Mdm2* and *Mdm4* null mice? Gannon et al. (2012) address this question by substituting Ser394 with aspartic acid (S394D) to create a phosphomimetic mutation. Surprisingly, *Mdm2*^{S394D/S394D} mice were born at Mendelian ratios, and p53 baseline level and activity were similar to those in wild-type mice. The only difference appeared to be that the duration of irradiation-induced p53 activation was extended in *Mdm2*^{S394D/S394D} cells. The authors posit that removal of damage-induced Ser394 phosphorylation may be critical for correct temporal regulation of p53 responses to radiation. Interestingly, the p53-induced phosphatase WIP1 can dephosphorylate MDM2 Ser395 and is overexpressed in breast and other cancers with wild-type p53, so WIP1 may play a role in the attenuation response (Lu et al., 2007). Further studies are needed to investigate this intriguing idea.

The surprisingly modest phenotype of *Mdm2*^{S394D/S394D} mice could be explained in several ways. First, p53 activation may require modification of more MDM2 residues than just Ser394 as suggested by a recent study in human cancer cells (Cheng et al., 2011). A second possibility is that replacing Ser by Asp does not provide a faithful mimic of phosphorylation. The side-chain carboxyl groups in Asp and glutamic acid (Glu) exhibit a -1 charge at physiologic pH, while a phosphate group carries -1.5 charges. Furthermore, the atomic radius of a phosphate group is about three times that of the carboxyl side-chain of Asp or Glu. These differences may be critical when considering the mechanisms by which MDM2 Ser394 may actually impact MDM2 E3 ubiquitin-ligase activity.

How could substitutions of the single C-terminal residue Ser394 cause such dramatic phenotypes? Recent biochemical studies in human cancer cell lines suggest that mutations in six MDM2 C-terminal phosphorylation sites (S386, S395, S407, T419, S425, and S429; MDM2 6A) may impact MDM2 oligomerization and affect E3 ligase function (Cheng et al., 2011). Consistent with the *Mdm2*^{S394A/S394A} results, the MDM2 6A mutant also exhibited increased E3 ubiquitin-ligase activity toward p53. These observations may be reconciled by a phosphorylation-induced structural alteration model, as observed recently for the E3 ubiquitin-ligase CBL (Dou et al., 2012). CBL regulates the stability of growth factor-activated receptor tyrosine kinases. In the absence of growth factor, CBL adopts an auto-inhibited conformation. However, upon growth factor signaling, CBL undergoes a conformational change that is initiated by phosphorylation of a single tyrosine residue (Y371). This enables CBL to better bind and position an E2 so that it can ubiquitylate its receptor tyrosine kinase substrate, resulting in a 1,400-fold increase in ubiquitylation activity (Dou et al., 2012). However, for MDM2, perhaps lack of phosphorylation enables

E2 recruitment for the purpose of p53 degradation whereas phosphorylation may create a conformational change that prevents this. Alternatively, MDM2 S395 phosphorylation by ATM may activate p53 by increasing MDM2 binding of p53 mRNA which reportedly increases p53 mRNA translation (Gajjar et al., 2012). The importance of good hypotheses is that they suggest experiments to test them, and we suspect these will constitute the next phase of deciphering mechanisms of p53 regulation.

ACKNOWLEDGMENTS

Due to space limitation, we apologize to many scientists whose important studies could not be cited.

REFERENCES

- Bond, G.L., Hu, W., Bond, E.E., Robins, H., Lutzker, S.G., Arva, N.C., Bargonetti, J., Bartel, F., Taubert, H., Wuerl, P., et al. (2004). *Cell* 119, 591–602.
- Bondar, T., and Medzhitov, R. (2010). *Cell Stem Cell* 6, 309–322.
- Cheng, Q., Cross, B., Li, B., Chen, L., Li, Z., and Chen, J. (2011). *Mol. Cell. Biol.* 31, 4951–4963.
- Dou, H., Buetow, L., Hock, A., Sibbet, G.J., Vouden, K.H., and Huang, D.T. (2012). *Nat. Struct. Mol. Biol.* 19, 184–192.
- Gajjar, M., Candeias, M.M., Malbert-Colas, L., Mazars, A., Fujita, J., Olivares-Illana, V., and Fähræus, R. (2012). *Cancer Cell* 21, 25–35.
- Gannon, H.S., Woda, B.A., and Jones, S.N. (2012). *Cancer Cell* 21, this issue, 668–679.
- Lu, X., Ma, O., Nguyen, T.A., Jones, S.N., Oren, M., and Donehower, L.A. (2007). *Cancer Cell* 12, 342–354.
- Maya, R., Balass, M., Kim, S.T., Shkedy, D., Leal, J.F., Shifman, O., Moas, M., Buschmann, T., Ronai, Z., Shiloh, Y., et al. (2001). *Genes Dev.* 15, 1067–1077.
- Wade, M., Wang, Y.V., and Wahl, G.M. (2010). *Trends Cell Biol.* 20, 299–309.
- Wang, Y.V., Leblanc, M., Wade, M., Jochemsen, A.G., and Wahl, G.M. (2009). *Cancer Cell* 16, 33–43.
- Wang, Y.V., Leblanc, M., Fox, N., Mao, J.H., Tinkum, K.L., Krummel, K., Engle, D., Piwnicka-Worms, D., Piwnicka-Worms, H., Balmain, A., et al. (2011). *Genes Dev.* 25, 1426–1438.

SMIP-016 in Action: CD37 as a Death Receptor

Lei Jin¹ and John C. Cambier^{1,*}¹Department of Immunology, University of Colorado School of Medicine and National Jewish Health Denver, Denver, CO 80206, USA*Correspondence: cambierj@njhealth.org

DOI 10.1016/j.ccr.2012.04.034

CD37 is a tetraspannin that triggers cell death and is a potential therapeutic target in cancers. In this issue of *Cancer Cell*, Lapalombella et al. show that CD37 is tyrosine phosphorylated following engagement by a bivalent engineered antibody fragment that binds CD37 and activates both SHP-1-dependent apoptotic signaling and PI3K-AKT-mediated survival signaling.

Small modular immuno-pharmaceuticals (SMIP) are disulfide-linked dimers of single-chain proteins comprised of one antigen binding VH/VL, a connecting hinge region, and an Fc (fragment, crystallizable) region (CH2-CH3) (Figure 1). Because of their smaller size, these candidate therapeutics may have better tissue penetration than monoclonal antibodies (mAbs). SMIP-016 is a dimeric recombinant single-chain polypeptide engineered to exhibit the full binding activity of an anti-CD37 mAb but at one-third less of the size (Zhao et al., 2007). Previous studies have shown that SMIP-016 is a potent inducer of apoptosis and antibody-dependent cellular cytotoxicity in B-cell leukemia/lymphoma cell lines and primary chronic lymphocytic leukemia (CLL) cells and is superior to the therapeutic antibodies used in these diseases (Zhao et al., 2007). TRU-016 is a humanized variant of SMIP-016 and is currently undergoing clinical trials for patients with CLL (<http://www.clinicaltrials.gov>).

CLL is the most common type of leukemia. To date, the anti-CD20 mAb Rituximab remains the most widely used mAb in the treatment of CLL. A high response rates of 51% with 4% complete response (CR) were achieved when Rituximab was used in previously untreated patients with CLL (Hainsworth et al., 2003). SMIP-016 acts by a mechanism distinct from Rituximab, inducing caspase independent and tyrosine phosphorylation-dependent apoptosis (Zhao et al., 2007). Thus, it was not surprising that TRU-016 and Rituximab showed complementary activity (Robak et al., 2009).

CD37 is a four transmembrane glycoprotein expressed at high

levels on B cells and to a lesser extent on T cells and myeloid cells (Barrena et al., 2005). The physiological ligand for CD37 is unknown, though it is shown that CD37 interacts with the C-type lectin dectin-1. Dectin-1 recognizes β -glucans found in cell walls of fungi. It is possible that together with dectin-1, CD37 forms a pattern-recognition-receptor for pathogen-associated molecule pattern. Indeed, CD37^{-/-} mice are better protected from *Candida albicans* infection than WT mice (van Spruiel et al., 2009).

CD37 belongs to the tetraspannin protein family and associates with other tetraspanins, such as CD53, CD81, and CD82 to form multiprotein complexes, the so-called tetraspanin web, on cell surfaces (Tarrant et al., 2003). Like other tetraspanins, CD37 has short cytoplasmic tails (8–14 aa) that lack typical signaling domains. CD37^{-/-} mice display impaired T cell-dependent antibody responses

(Knobeloch et al., 2000) and increased dendritic cell antigen-presenting capacity (Sheng et al., 2009).

In this issue of *Cancer Cell*, Lapalombella et al. (2012) show that CD37 has intrinsic tyrosine-based signaling capacity that is important for SMIP-016 induced apoptosis in primary CLL cells. SMIP-016-induced apoptosis in CLL patients' samples depends upon tyrosine phosphorylation (Zhao et al., 2007). The authors started their investigation by identifying tyrosine phosphorylated proteins associated with CD37 upon SMIP-016 stimulation. One of the targets they identified is the SH-2-containing tyrosine phosphatase SHP-1. They showed that reducing SHP-1 expression dramatically decreases SMIP-016 induced apoptosis in CLL samples. SHP-1 downregulates signaling pathways that promote proliferation, and it is considered a tumor suppressor (Wu et al., 2003). The authors

then explored how SHP-1 is recruited to CD37. They noticed that the N-terminal cytoplasmic tail of CD37 contains a weak S/I/V/LxYxxI/V/L immuno-tyrosine inhibitory motif (ITIM) that is known to bind the SH2 domains of SHP-1. Using biochemistry, mass spectrometry, and mutagenesis approaches, the authors convincingly demonstrate that CD37 itself is tyrosine phosphorylated upon SMIP-016 stimulation. Furthermore, most of this phosphorylation occurs on the N-terminal ITIM motif. A Y¹³ to F¹³ CD37 ITIM mutant does not bind SHP-1, and SMIP-016 is less effective in killing cells expressing this mutant.

Exploring other functional consorts, the authors found that the C-terminal cytoplasmic tail of

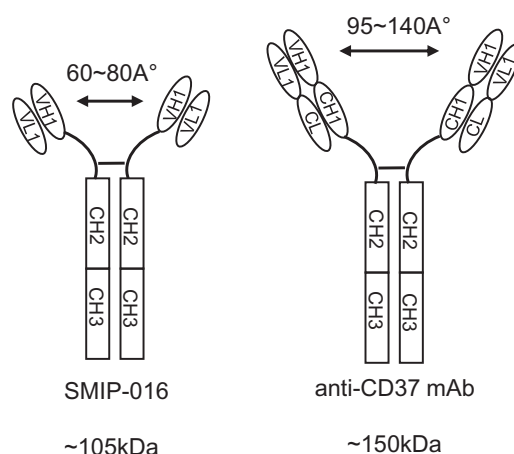


Figure 1. SMIP-016 Is an Anti-CD37 Polypeptide

Comparison of SMIP-016 and an anti-CD37 mAb. VH, variable heavy chain; VL, variable light chain; CH, constant heavy chain.

CD37, which contains two additional tyrosines Y²⁷⁴ and Y²⁸⁰, somehow inhibits CD37 phosphorylation and the cytotoxic effects of SMIP-016. This led to the finding that SMIP-016 also activates the PI3K-AKT proliferative signaling pathway. Treatment of cells with the PI3K inhibitor LY294002 or deleting the C-terminal tail of CD37 increases SMIP-016-induced killing. In summary, SMIP-016 simultaneously activates both SHP-1 mediated death signaling and PI3K-AKT mediated survival signaling.

The study of Lapalombella et al. (2012) not only provides deeper insight into the molecular mechanisms of SMIP-016 action but may also help guide current and future clinical trials using TRU-016. For example, the current study reveals an opposing role for PI3K and an absolute requirement for SHP-1 expression for efficacy of SMIP-016. Consistent with its tumor suppressor role, expression of

SHP-1 is diminished or absent in many leukemias and lymphomas (Wu et al., 2003). Thus, it can be expected that cancers with low or no SHP-1 expression may not respond to TRU-016 treatment. The results from current TRU-016 clinical trials on CLL are expected in the first half of 2013, and in interpreting the outcome, it may be useful to stratify subjects based on the SHP-1 expression level and the PI3K pathway activity in their tumors.

REFERENCES

- Barrena, S., Almeida, J., Yunta, M., Lopez, A., Fernandez-Mosteirin, N., Giral, M., Romero, M., Perdiguier, L., Delgado, M., Orfao, A., and Lazo, P.A. (2005). *Leukemia* 19, 1376–1383.
- Hainsworth, J.D., Litchy, S., Barton, J.H., Houston, G.A., Hermann, R.C., Bradof, J.E., and Greco, F.A. (2003). *J. Clin. Oncol.* 21, 1746–1751.
- Knobeloch, K.P., Wright, M.D., Ochsenbein, A.F., Liesenfeld, O., Lohler, J., Zinkernagel, R.M., Horak,

I., and Orinska, Z. (2000). *Mol. Cell. Biol.* 20, 5363–5369.

Lapalombella, R., Yeh, Y., Wang, L., Ramanunni, A., Rafiq, S., Jha, S., Staubli, J., Lucas, D.M., Mani, R., Herman, S.E.M., et al. (2012). *Cancer Cell* 21, this issue, 694–708.

Robak, T., Robak, P., and Smolewski, P. (2009). *Curr. Opin. Investig. Drugs* 10, 1383–1390.

Sheng, K.C., van Spriell, A.B., Gartlan, K.H., Sofi, M., Apostolopoulos, V., Ashman, L., and Wright, M.D. (2009). *Eur. J. Immunol.* 39, 50–55.

Tarrant, J.M., Robb, L., van Spriell, A.B., and Wright, M.D. (2003). *Trends Immunol.* 24, 610–617.

van Spriell, A.B., Sofi, M., Gartlan, K.H., van der Schaaf, A., Verschueren, I., Torensma, R., Raymakers, R.A., Loveland, B.E., Netea, M.G., Adema, G.J., et al. (2009). *PLoS Pathog.* 5, e1000338.

Wu, C., Sun, M., Liu, L., and Zhou, G.W. (2003). *Gene* 306, 1–12.

Zhao, X., Lapalombella, R., Joshi, T., Cheney, C., Gowda, A., Hayden-Ledbetter, M.S., Baum, P.R., Lin, T.S., Jarjoura, D., Lehman, A., et al. (2007). *Blood* 110, 2569–2577.

Opening a New GATaWay for Treating KRAS-Driven Lung Tumors

Mariano Barbacid^{1,*}

¹Molecular Oncology Programme, Centro Nacional de Investigaciones Oncológicas (CNIO), E-28029 Madrid, Spain

*Correspondence: mbarbacid@cnio.es

DOI 10.1016/j.ccr.2012.04.032

In a recent issue of *Cell*, Kumar and colleagues uncovered a synthetic lethal interaction between oncogenic KRAS and the transcription factor GATA2 in non-small cell lung carcinoma. Pharmacological inhibition of GATA2-mediated pathways with bortezomib and fasudil results in dramatic tumor inhibition. These observations unveil new armamentaria to fight this deadly disease.

Non-small cell lung carcinoma (NSCLC) has one of the highest incidence and lowest survival rates, a combination that makes this tumor type one of the deadliest human cancers. At least a quarter of NSCLC express a mutant KRAS allele that encodes a constitutively active small G protein known to signal through a series of kinases. While these kinases are in principle amenable to pharmacological intervention, a selective treatment for KRAS mutant NSCLC is not yet available in the clinic.

During the last decade, there have been significant efforts directed to reproduce

the natural history of NSCLC in genetically engineered mouse (GEM) models (Heyer et al., 2010). Recently, these models have been utilized to evaluate potential therapeutic targets. Some of the validated targets include well-known downstream elements of KRAS signaling such as components of the mitogenic RAF/MEK/ERK cascade and the PI3K/AKT survival pathway, most of which are druggable kinases (Gupta et al., 2007; Engelman et al., 2008; Blasco et al., 2011) (Figure 1A). However, these studies cannot be directly extrapolated to the clinic because target

ablation occurred during tumor initiation rather than during tumor progression. Moreover, these Kras oncogene-driven GEM models retained the full component of tumor suppressors and, hence, do not develop metastatic tumors.

Other studies have attempted to validate pathways less directly linked to KRAS signaling. In one study, elimination of CDK4, but not the other interphase CDKs, elicited a rapid senescence response that resulted in partial tumor regression, an observation validated with clinically available CDK4 inhibitors (Puyol

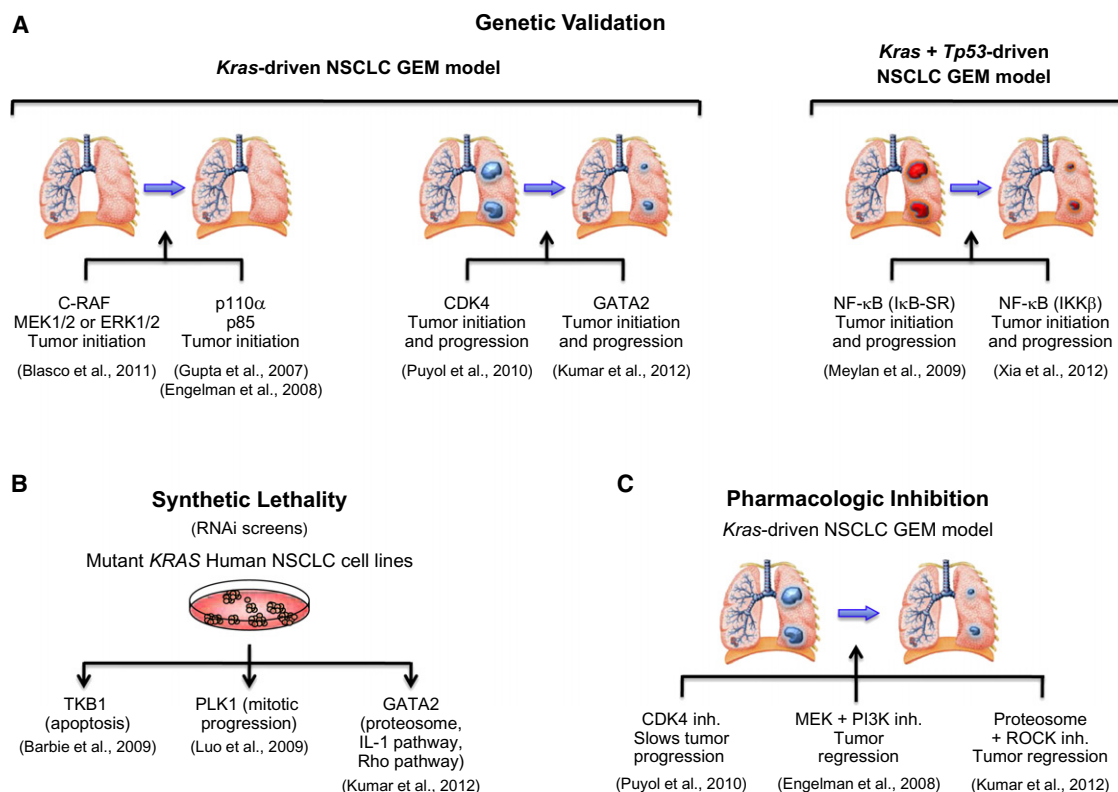


Figure 1. Preclinical Studies to Validate Therapeutic Targets in *KRAS*-Driven NSCLC

(A) Schematic diagram of putative therapeutic targets validated by genetic approaches in GEM models of NSCLCs driven by resident *Kras* oncogenes. (Left) GEM models driven by conditional mutant *Kras* alleles develop adenomas and non-metastatic adenocarcinomas (in blue). (Right) GEM models that also carry mutated or null *Tp53* or have *Tp53* knockdown develop more aggressive adenocarcinomas (in red) that frequently metastasize to distant organs.

(B) RNAi screens aimed at identifying human genes capable of inducing synthetic lethality in combination with *KRAS* oncogenes.

(C) Pharmacologic approaches using selective targeted inhibitors in the above *Kras*-driven GEM models. Original references for these GEM models have been omitted due to space limitations.

et al., 2010) (Figure 1A). Other studies have examined the therapeutic consequences of inhibiting the NF- κ B pathway in GEM models carrying *Tp53* null alleles or expressing reduced levels of p53 (Meylan et al., 2009; Xia et al., 2012). When challenged with an I κ B super-repressor or when IKK β expression was knocked down, tumors regressed, although they were not completely eliminated (Figure 1). These observations suggest that blocking NF- κ B-driven survival pathways might serve as a therapeutic strategy to thwart *KRAS*-driven tumor progression.

Other investigators have expanded the repertoire of *KRAS* targets by searching for synthetic lethal genes using RNA interference (RNAi) libraries. Screens of human NSCLC cell lines carrying either wild-type or mutant *KRAS* have identified targets linked to the cell cycle such as PLK1, a kinase involved in mitotic pro-

gression and to the NF- κ B pathway such as TKB1, a non-canonical I κ B kinase (Barbie et al., 2009; Luo et al., 2009) (Figure 1B). In vivo validation of these synthetic lethal genes will establish their therapeutic value in *KRAS*-driven lung tumors.

In a recent issue of *Cell*, the Downward laboratory (Kumar et al., 2012) went all the way from identifying GATA2 as a novel synthetic lethal gene to validating it using *Kras*-driven GEM models and, finally, to demonstrating its therapeutic potential by using surrogate drugs already approved for clinical use (Figure 1). Kumar et al. (2012) screened human NSCLC cell lines carrying either wild-type or mutant *KRAS* with an RNAi library against 7,000 human genes. Using cell viability as the biological read-out, they identified the transcription factor GATA2 essential for the proliferation of cell lines carrying oncogenic *KRAS*. GATA2 knockdown

also reduced the viability of cell lines carrying mutated loci functionally related to *KRAS* such as *NRAS*, *NF1*, *EML4-ALK*, and *EGFR*. Interestingly, GATA2 is an unlikely actor in lung cancer because its function has, so far, only been linked to the hematopoietic system.

Gene set enrichment analysis revealed that reduction of GATA2-mediated transcription in lung tumor cells affected several pathways, suggesting that a pleiotropic effect is required for the observed synthetic lethality. Knockdown of GATA2 affected proteosomal activity in lung tumor cells, an observation reminiscent of that obtained in previous screens (Barbie et al., 2009; Luo et al., 2009). This effect appears to be independent of the presence of oncogenic *KRAS* and is not sufficient to induce loss of cell viability. GATA2 depletion also led to transcriptional repression of IL-1 and NF- κ B signaling pathways. In this case,

some of the observed effects, mainly expression of TRAF6, were specific for *KRAS* mutant cells. Yet, direct inhibition of either IL-1 signaling by its antagonist IL-1ra or of NF- κ B signaling by TRAF6 knockdown did not result in loss of cell viability, suggesting that inhibition of either pathway alone is not sufficient to phenocopy loss of GATA2 expression. Finally, Kumar et al. (2012) identified that some genes involved in RHO-related signaling pathways were occupied by GATA2 in *KRAS* mutant but not wild-type tumor cells. Not surprisingly, GATA2 knockdown in *KRAS* mutant cells resulted in a striking reduction of active GTP-bound RHO proteins, including the downstream ROCK kinase. Restoration of RHO activity by expression of constitutively active RHO proteins or by a ROCK-ER fusion kinase did not rescue cell viability in the absence of GATA2, again suggesting that blocking RHO signaling is not sufficient to mimic loss of GATA2 activity. Intriguingly, *KRAS* oncogene knockdown, while affecting cell viability of *KRAS* mutant cells to a similar extent as GATA2 knockdown, had no effect on the proteasome pathway, NF- κ B activity, or RHO signaling. These observations suggest that GATA2 is not a downstream component of the *KRAS* oncogenic signaling pathway.

Conditional ablation of *Gata2* alleles in a *Kras*-driven GEM model of NSCLC prevented tumor initiation. More importantly, systemic elimination of *Gata2* in mice already presenting *Kras*-driven lung tumors resulted in substantial tumor regression without major side effects suggesting that blocking GATA2 activity

could have therapeutic value and might be well tolerated in patients. Whether inhibition of GATA2 results in defects in the immune system (a phenotype that might not be obvious in the protected environment of an animal facility) remains to be determined.

Finally, Kumar et al. (2012) combined available inhibitors selective for two of the pathways regulated by GATA2 to treat mice with *Kras*-driven NSCLCs. The chosen inhibitors bortezomib (a proteasome inhibitor) and fasudil (a RHO/ROCK inhibitor) have already been approved for use in human patients. When combined, these inhibitors induced almost complete regression of well-established lung tumors in the *Kras*-driven GEM model (Figure 1C). These observations are reminiscent of a previous report in which similar tumors also regressed upon treatment with a combination of MEK and PI3K inhibitors (Engelman et al., 2008). However, MEK inhibitors have not been approved by the FDA due to undesired toxicities, and PI3K inhibitors have thus far shown rather limited anti-tumor activity.

Are we on the verge of a major breakthrough in the treatment of *KRAS*-induced NSCLC? Possibly; however, we should consider the data of Kumar et al. (2012) as an exciting but early step in the long process of drug discovery. The GEM model used in this study retains wild-type *Tp53*, suggesting that the tumors successfully treated with bortezomib and fasudil might not be as aggressive as those in most NSCLC patients. Moreover, the in vivo data is still preliminary and other potential roadblocks such as

drug resistance have not been examined. In spite of these caveats, the results of Kumar et al. (2012) represent a very important advance in the long-standing fight to conquer lung cancer. Undoubtedly, they have opened an important “GATAway” toward this challenging goal.

REFERENCES

- Barbie, D.A., Tamayo, P., Boehm, J.S., Kim, S.Y., Moody, S.E., Dunn, I.F., Schinzel, A.C., Sandy, P., Meylan, E., Scholl, C., et al. (2009). Nature 462, 108–112.
- Blasco, R.B., Francoz, S., Santamaría, D., Cañamero, M., Dubus, P., Charron, J., Baccarini, M., and Barbacid, M. (2011). Cancer Cell 19, 652–663.
- Engelman, J.A., Chen, L., Tan, X., Crosby, K., Guimaraes, A.R., Upadhyay, R., Maira, M., McNamara, K., Perera, S.A., Song, Y., et al. (2008). Nat. Med. 14, 1351–1356.
- Gupta, S., Ramjaun, A.R., Haiko, P., Wang, Y., Warne, P.H., Nicke, B., Nye, E., Stamp, G., Alitalo, K., and Downward, J. (2007). Cell 129, 957–968.
- Heyer, J., Kwong, L.N., Lowe, S.W., and Chin, L. (2010). Nat. Rev. Cancer 10, 470–480.
- Kumar, M.S., Hancock, D.C., Molina-Arcas, M., Steckel, M., East, P., Diefenbacher, M., Armenteros-Monterroso, E., Lassailly, F., Matthews, N., Nye, E., Stamp, G., Behrens, A., and Downward, J. (2012). Cell 149, 642–655.
- Luo, J., Emanuele, M.J., Li, D., Creighton, C.J., Schlabach, M.R., Westbrook, T.F., Wong, K.K., and Elledge, S.J. (2009). Cell 137, 835–848.
- Meylan, E., Dooley, A.L., Feldser, D.M., Shen, L., Turk, E., Ouyang, C., and Jacks, T. (2009). Nature 462, 104–107.
- Puyol, M., Martín, A., Dubus, P., Mulero, F., Pizcueta, P., Khan, G., Guerra, C., Santamaría, D., and Barbacid, M. (2010). Cancer Cell 18, 63–73.
- Xia, Y., Yeddula, N., Leblanc, M., Ke, E., Zhang, Y., Oldfield, E., Shaw, R.J., and Verma, I.M. (2012). Nat. Cell Biol. 14, 257–265.

Distinct Neural Stem Cell Populations Give Rise to Disparate Brain Tumors in Response to N-MYC

Fredrik J. Swartling,^{1,2,*} Vasil Savov,^{2,5} Anders I. Persson,^{1,5} Justin Chen,¹ Christopher S. Hackett,¹ Paul A. Northcott,³ Matthew R. Grimmer,¹ Jasmine Lau,¹ Louis Chesler,⁴ Arie Perry,¹ Joanna J. Phillips,¹ Michael D. Taylor,³ and William A. Weiss^{1,*}

¹University of California, Departments of Neurology, Pathology, Pediatrics, Neurosurgery, Brain Tumor Research Center and Helen Diller Family Comprehensive Cancer Center, San Francisco, CA 94158, USA

²Department of Immunology, Genetics and Pathology, Rudbeck Laboratory, Uppsala University, SE-75185 Uppsala, Sweden

³The Hospital for Sick Children, Toronto, ON M5G 1X8, Canada

⁴The Institute of Cancer Research, Sutton, Surrey SM2 5NG, UK

⁵These authors contributed equally to this work

*Correspondence: fredrik.swartling@igp.uu.se (F.J.S.), waweiss@gmail.com (W.A.W.)

DOI 10.1016/j.ccr.2012.04.012

SUMMARY

The proto-oncogene *MYCN* is mis-expressed in various types of human brain tumors. To clarify how developmental and regional differences influence transformation, we transduced wild-type or mutationally stabilized murine *N-myc*^{T58A} into neural stem cells (NSCs) from perinatal murine cerebellum, brain stem, and forebrain. Transplantation of *N-myc*^{WT} NSCs was insufficient for tumor formation. *N-myc*^{T58A} cerebellar and brain stem NSCs generated medulloblastoma/primitive neuroectodermal tumors, whereas forebrain NSCs developed diffuse glioma. Expression analyses distinguished tumors generated from these different regions, with tumors from embryonic versus postnatal cerebellar NSCs demonstrating Sonic Hedgehog (SHH) dependence and SHH independence, respectively. These differences were regulated in part by the transcription factor SOX9, activated in the SHH subclass of human medulloblastoma. Our results demonstrate context-dependent transformation of NSCs in response to a common oncogenic signal.

INTRODUCTION

Medulloblastoma (MB), the most common malignant primary brain tumor of childhood, arises in the cerebellum. Classic, desmoplastic (nodular), and large cell/anaplastic (LC/A) pathologies are described (Eberhart et al., 2004) and transcriptional profiling has identified distinct subgroups characterized by signaling through WNT, Sonic Hedgehog (SHH), or other signaling pathways that include MYC and MYCN (Taylor et al., 2011). Activation of SHH signaling occurs in ~25% of tumors (Browd et al., 2006; Kessler et al., 2009; Polkinghorn and Tarbell, 2007). Patients with WNT-driven tumors show a favorable outcome when compared with SHH-driven tumors, while tumors of transcriptomal groups 3

and 4 have the worst outcomes (Eberhart et al., 2004; Ellison et al., 2011; Pfister et al., 2009; Polkinghorn and Tarbell, 2007).

Amplification of MYC and MYCN occurs in ~10% of MB, associated with aggressive LC/A tumors and poor survival. Expression of MYCN is high in SHH-driven human tumors, and murine N-MYC can potentiate preclinical models of MB driven by activated SHH signaling. In contrast, MYCN-amplified tumors are predominantly of non-SHH MB subtypes (Korshunov et al., 2011); and mis-expression of MYCN occurs in the majority of MB in all histopathologies (Northcott et al., 2009; Pomeroy et al., 2002; Swartling et al., 2010). Neither gain nor mis-expression of MYCN is exclusive to MB, as MYCN is also amplified and/or mis-expressed in malignant glioma, the most common

Significance

Medulloblastoma (MB)/primitive neuroectodermal tumors (PNETs) and glioma represent the most common primary malignant brain tumors in children and adults. These tumors presumably arise from a population of cells that share with normal NSCs, a requirement for self-renewal and multilineage differentiation. *N-myc*, a proto-oncogene implicated in both normal brain development and brain tumors, induced a Sonic Hedgehog (SHH)-dependent program in normal NSCs derived from prenatal, and a SHH-independent program in NSCs derived from postnatal hindbrain. Orthotopic transplantation of *N-myc*-transduced NSCs generated MB/PNETs from hindbrain NSCs, and glioma from forebrain NSCs. Thus, the diversity of brain tumors in patients may be controlled by a limited set of transcription factors, reflecting both regional and temporal developmental restrictions among normal NSCs.

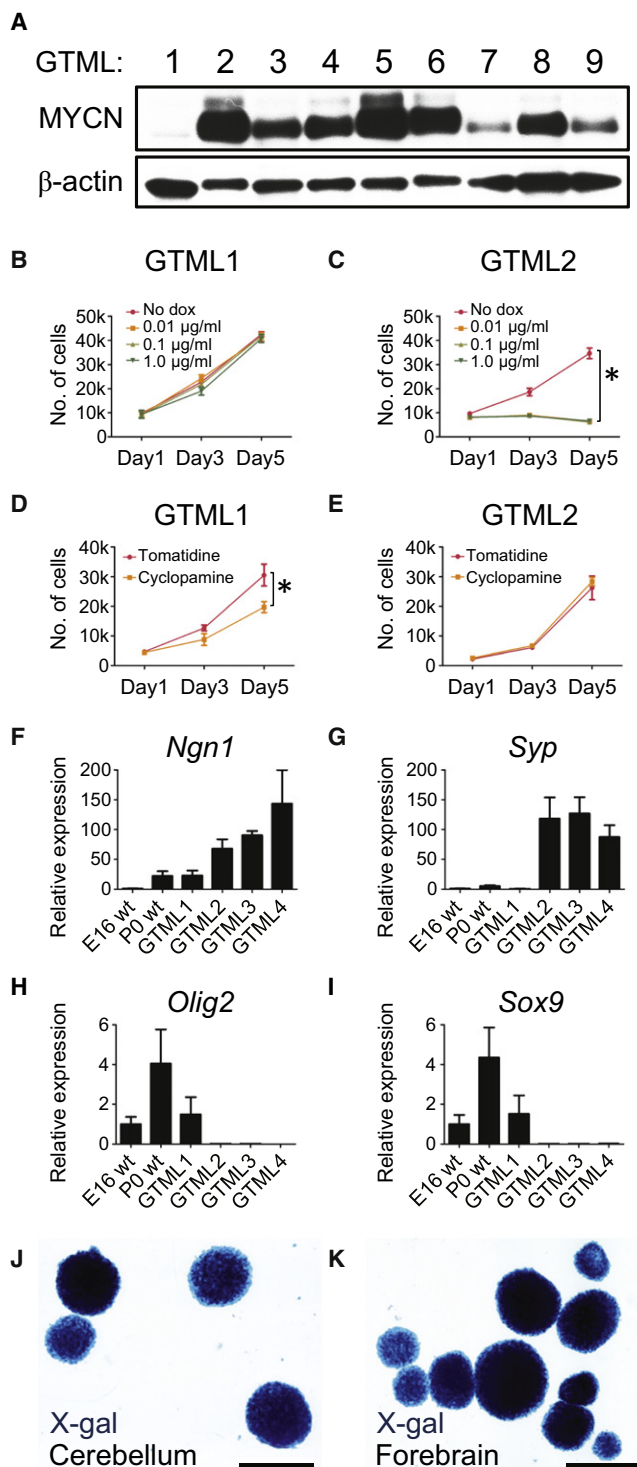


Figure 1. GLT1 Drives MYCN-Dependent, Predominantly SHH-Negative Medulloblastoma and Is a Fate Determinant for NSCs

(A) Immunoblot of MYCN in GTML MB spheres (passages 6–10). (B and C) Proliferation of MYCN-low (GTML1) and MYCN-high (GTML2) spheres as indicated. (D and E) All GTML sphere lines except GTML1 were insensitive to the SMO inhibitor cyclopamine (5 μM). Tomatidine, 5 μM, was used as control.

primary brain tumor of adults, and typically localized to forebrain (cerebrum) rather than hindbrain (cerebellum) (Brennan et al., 2009; Hui et al., 2001; Perry et al., 2009).

The cell of origin for both MB and glioma is debated. One candidate is the neural stem cell (NSC) with self-renewal capacity and potential to generate progenitors and differentiated cells of all neural lineages. NSCs can be derived from either cerebellum or cerebrum both during development and in adulthood (Lee et al., 2005; Reynolds and Weiss, 1992). During both normal cerebellar development and MB tumorigenesis, N-MYC drives proliferation of granule neuron precursors (GNPs). GNPs are marked by transcription factors including MATH1 and PAX6, and are derived from radial glia or NSCs of the developing cerebellum (Hatton et al., 2006; Knoepfler et al., 2002; Lin et al., 2001; Schüller et al., 2008; Yang et al., 2008). Constitutive deletion of *N-myc* is embryonic lethal (Charron et al., 1992; Stanton et al., 1992) while inactivation in NSCs leads to thinning of the NSC-rich ventricular zone (VZ), a markedly reduced cortex, and a diminutive cerebellum (Knoepfler et al., 2002). These results indicate a role for N-MYC in regulating normal forebrain and hindbrain development.

To understand whether changes in normal developmental programs could influence transformation, we transduced *N-myc* into forebrain, cerebellar, or brain stem tissues isolated at distinct developmental time points. We studied mechanisms for tumor development and compared expression profiles among the disparate brain tumors generated by this common oncogene. In the analysis we included our recently described murine MYCN-driven MB model in which the Glutamate Transporter 1 (GLT1) promoter drove a bidirectional Tetracycline-Response Element (TRE), directing expression of MYCN and Luciferase (GTML) (Swartling et al., 2010).

RESULTS

MB Spheres Are MYCN-Dependent and Express Neuronal Markers

We isolated brain tumors from nine mice from the transgenic GTML model, and derived tumor spheres in neurobasal (NB) media supplemented with epidermal growth factor (EGF) and fibroblast growth factor (FGF). Eight representative sphere lines, GTML2-9, arose independently of SHH (Swartling et al., 2010), and showed elevated expression of MYCN protein and Luciferase (LUC) (Figure 1A and Figure S1A available online). SHH-dependent GTML tumors arise at <5% frequency. A single line (GTML1) was isolated from a SHH-dependent GTML tumor and showed low levels of MYCN mRNA (described previously as GTML-T7 [Swartling et al., 2010]). While MYCN-low GTML1 cells showed no response to doxycycline (dox), proliferation of MYCN-high GTML spheres was blocked after 3–5 days of dox treatment, reflecting MYCN dependence (Figures 1B and 1C,

(F–I) Relative expression of neuronal markers Ngn1 and Syp; and Olig2 and Sox9 that are expressed in glial cells in embryonic (E16 WT), and postnatal (P0 WT) normal neurospheres and tumor spheres GTML1-4.

(J and K) GLT1-positive origin shown by X-gal fate mapping in NSCs isolated from postnatal (P0) cerebellum and postnatal (P0) forebrain from a *Glt1-tTA*; TRE-Cre-Rosa26-LSL-LacZ mouse.

Error bars: ±SD. Scale: 100 μm. See also Figure S1.

Figures S1B–S1D). This proliferation block, associated with loss of Cyclin D2, did not recover after dox washout, as compared to controls (Figure S1D and data not shown). These observations are consistent with our earlier *in vivo* observations in GTML mice that withdrawal of MYCN in tumors led to senescence (Swartling et al., 2010).

To confirm SHH independence of MYCN-positive GTML2-9 tumor spheres, we cultured spheres with the SMO inhibitor cyclopamine (Taipale et al., 2000), which blocks signaling downstream from SHH. GTML1 SHH-dependent spheres responded to SMO inhibition. However, no significant differences in proliferation were observed after treating GTML2-9 spheres with cyclopamine (Figures 1D and 1E and data not shown), or with SHH-N or SMO agonists that activate SHH signaling (data not shown). These data are consistent with tumors arising through a SHH-independent pathway. However, it remains possible that signaling downstream of SMO could contribute to tumor formation.

Compared to WT cerebellar spheres and SHH-dependent GTML1 spheres, GTML2-4 tumor spheres with high levels of MYCN protein showed elevated levels of mRNA for *Ngn1* and *Syp* (Figures 1F and 1G). NGN1, an inducer of neurogenesis and a marker of immature GABAergic cells originating from the roof of the fourth ventricle, is typically expressed in MATH1-negative, classic MB (Farah et al., 2000; Salsano et al., 2007). Spheres from GTML 2-4 showed low levels of glial-lineage transcription factors *Olig2* and *Sox9* (Figures 1H and 1I), both of which are also typically low in human MB, and high in cultured normal human cerebellar NSCs (Alcock and Sottile, 2009; de Bont et al., 2008; Ligon et al., 2004). These marker data collectively verify that GTML2-4 spheres resemble SHH-negative human MB.

Freshly isolated GTML tumor cells can be transplanted orthotopically into the brains of immunocompromised mice to regenerate MB (Swartling et al., 2010). While SHH-dependent GTML1 tumor spheres did not grow orthotopically, spheres from SHH-independent tumors (GTML2 and GTML3) generated lethal tumors (Figure S1E). Transplanted GTML2 tumor spheres grew significantly more rapidly than transplanted GTML3 tumor spheres consistent with higher levels of MYCN protein in GTML2 cells (Figures S1D and S1E).

To determine whether NSCs isolated from normal cerebellum could represent cells of origin for GTML MB, we crossed Glt1-tTA mice to TRE-Cre:Rosa26-lsl-LacZ reporter animals, enabling us to visualize LacZ as a marker of cell fate. Indeed, NSCs cultured as spheres from these triply transgenic mice at postnatal ages were β -galactosidase positive, suggesting that the GLT1 promoter is active and that GTML tumors could originate from normal NSCs (Figures 1J and 1K).

Transduction of *N-myc*^{T58A} into the GFAP-Positive NSCs Boosts Proliferation

GFAP is a stem cell and astroglial marker (Doetsch et al., 1999) and shows tight coexpression with GLT1 both in cerebellar and cerebral cells *in vivo* (Schmitt et al., 1996) as well as in our NSC cultures (Figure S1F). We therefore investigated how GFAP-positive populations of NSCs would respond to *N-myc*, using mice transgenic for the avian *tv-a* retroviral receptor driven by the GFAP promoter (*Gtv-a*) (Holland et al., 2000). We

dissected cells at embryonic day 16 (E16) and postnatal day 0 (P0) from three different brain regions of *Gtv-a* mice (Figure 2A): luminal parts of forebrain ventricular zone (<0.1 mm), total cerebellum, and the top layer (<0.1 mm) isolated from the ventricular zone region of the dorsal brain stem. This isolated region encompassed both VZ brain stem cells and the lower rhombic lip (LRL) structure that contains candidate cells of origin for MB (Gibson et al., 2010).

Dissected cells were cultured in neurobasal media for 1 week and subsequently transduced with harvested RCAS viruses containing either a green fluorescent protein (GFP) reporter, Flag-tagged wild-type *N-myc*^{WT}, or mutationally stabilized Flag-tagged *N-myc*^{T58A} (Figures S2A–S2E). After differentiation for 72 hr without growth factors, most GFP-transduced NSCs from both E16 and P0 cerebellar and forebrain NSCs remained positive for the NSC marker GFAP, but were negative for the neuronal marker, TUJ1, confirming selective transduction of GFAP-positive NSCs (Figure 2B and Figure S2F).

To further characterize the types of cells transduced, we sorted GFP-positive and -negative NSC fractions from E16 cerebellum, and P0 cerebellum and forebrain, 72 hr after transduction with RCAS-GFP. The percentage of GFP-positive cells ranged from 2.5% up to 8% of the entire cell population (Figure 2B and Figure S2F). Interestingly, GFP-sorted single NSCs from these conditions produced significantly more secondary spheres than GFP-negative NSCs after 2 weeks in culture (Figure S2G). These data are consistent with selective transduction of GFAP-positive cells within these primary cultures, showing increased self-renewal as compared with more differentiated populations of cells.

We next analyzed cells transduced with RCAS-*N-myc* constructs. *N-myc*^{T58A}-transduced cerebellar NSCs stained intensely for Flag on western blot as compared to *N-myc*^{WT}-transduced cells (Figure 2C), likely reflecting stabilization of N-MYC protein due to decreased proteasomal degradation (Salghetti et al., 1999). As compared to cerebellar NSCs transduced with GFP or *N-myc*^{WT}, NSCs transduced with *N-myc*^{T58A} and GTML2 tumor spheres were both resistant to blockade of new protein synthesis by cycloheximide (CHX, Figures S2H–S2K) consistent with stabilization of N-MYC^{T58A} or overexpression of MYCN in these cells.

While GFP- and *N-myc*^{WT}-transduced NSCs showed moderate proliferation when cultured on coated plates, transduction of *N-myc*^{T58A} into NSCs from P0 cerebellum promoted increased proliferation, associated with high levels of the fourth ventricular zone marker NGN1 (Figures 2C and 2D). Similarly, transduction of *N-myc*^{T58A} into P0 forebrain NSCs, as well as E16 NSCs from both cerebellum and forebrain, promoted proliferation, as compared to both vector GFP control and *N-myc*^{WT}-transduced NSCs (Figure 2E and data not shown).

Because NSCs in the brain stem may also generate brain tumors (Gibson et al., 2010), we next tested VZ-derived NSCs from dorsal brain stem. *N-myc*^{T58A} did not clearly drive increased proliferation in E16 and P0 brain stem cultures in this system (data not shown), prompting us to test VZ-derived NSCs from E14 dorsal brain stem/LRL (henceforth called E14 LRL). Transduction of E14 LRL NSCs cells with *N-myc*^{T58A} led to increased proliferation as compared to GFP- and *N-myc*^{WT}-transduced NSCs (Figure 2F).

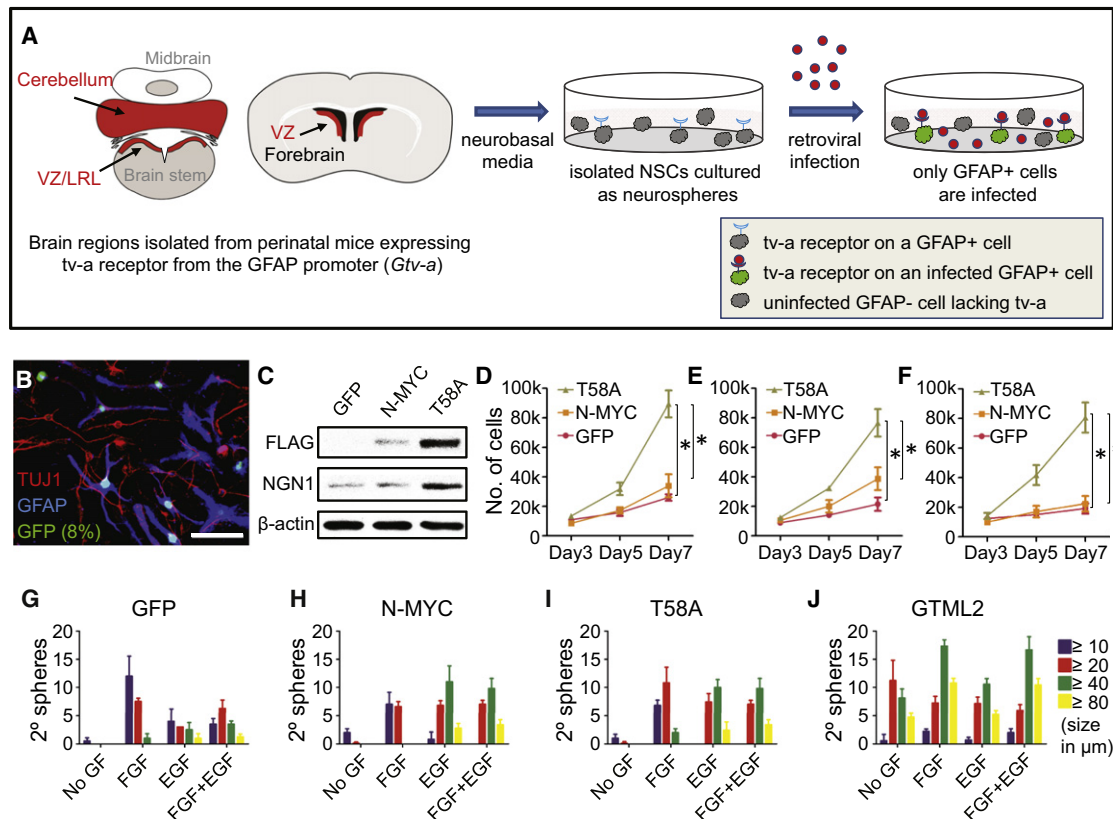


Figure 2. NSC-Selective Infection with *N-myc*^{T58A} Alters Proliferation and Differentiation

(A) NSCs isolated from E16 and P0 forebrain (ventricular zone), E16 and P0 hindbrain (total cerebellum), and E14, E16, and P0 brain stem (ventricular zone/lower rhombic lip) from mice transgenic for *Gtv-a* were cultured for 7 days in NB media on low-affinity plates with one or two passages. RCAS viruses containing GFP, *N-myc*^{WT} (N-MYC), or *N-myc*^{T58A} (T58A) came from supernatants of DF-1 virus-producing cells (see Figure S2). NSCs were transduced with RCAS viruses mixed 1:1 with fresh NB media. Cells were infected (72 hr), dissociated, and cultured in fresh NB media. Cells were orthotopically transplanted in nude mice 7 days after RCAS infection.

(B) Selective infection of GFAP-positive P0 cerebellar NSCs, evidenced by coexpression of RCAS-GFP (green) with GFAP (blue) 72 hr after growth factor depletion. TUJ1 (red). Scale: 25 μ m.

(C) Immunoblot of FLAG-tagged *N-myc*^{WT} or *N-myc*^{T58A} in P0 cerebellar NSCs. NGN1 and β -actin control are also shown.

(D–F) Proliferation at 3, 5, and 7 days after transduction with GFP, *N-myc*^{WT}, or *N-myc*^{T58A} of P0 NSCs isolated from cerebellum (D), forebrain (E), and dorsal brain stem/lower rhombic lip (F), respectively.

(G–J) Growth factor independence assay showing sphere diameter (as indicated) and number of secondary spheres in P0 cerebellar NSCs transduced with GFP, *N-myc*^{WT}, or *N-myc*^{T58A} and in GTML2 spheres. Although not indicated, there are significantly more spheres irrespective of size in “GF conditions” (FGF, EGF, or FGF+EGF) as compared to “no GF conditions” when analyzing GFP-, N-MYC-, and T58A-transduced NSCs, respectively, when using Student’s *t* test ($p < 0.05$). Error bars: \pm SD. See also Figure S2.

Culturing cerebellar NSC for a week in neurobasal media typically removes any residual GNPs (Klein et al., 2005; Sutter et al., 2010). Transduction of *N-myc*^{WT} or *N-myc*^{T58A} retroviruses into purified P0 GNPs did not drive proliferation, presumably because very few PAX6-positive GNPs also expressed GFAP and tv-a, thus evading viral transduction (Figures S2L–S2M).

To clarify whether *N-myc* could drive self-renewal and substitute for growth factors, we cultured NSCs and tumor spheres in limiting dilution for 1 week with or without EGF and FGF (ten cells/well). To distinguish effects on NSCs from effects on neural progenitors, 100 cells/well were replated in a secondary sphere formation assay for a second week. *N-myc*^{WT}-, *N-myc*^{T58A}-, and GFP-transduced control secondary spheres retained strict growth factor dependence and showed no significant differences in sphere number (Figures 2G–2I, Figures S2N–S2P). By

contrast, GTML tumor spheres generated secondary spheres even when cultured without growth factors (Figure 2J). MYCN blocked differentiation in GTML tumor spheres, as spheres with high MYCN protein levels neither differentiated nor extended processes upon growth factor starvation or doxycycline treatments (data not shown). In contrast and as expected, SHH-dependent GTML1 cells and control cerebellar NSCs transduced with GFP virus showed multipotent differentiation into both GFAP-positive astrocytes and TUJ1-positive neurons (Figure 2B, Figure S2F and data not shown).

An N-MYC Neuronal Program Depends on Both Developmental Age and Regional Origin

To characterize the potential for *N-myc* to induce distinct differentiation programs as a function of both NSC age and

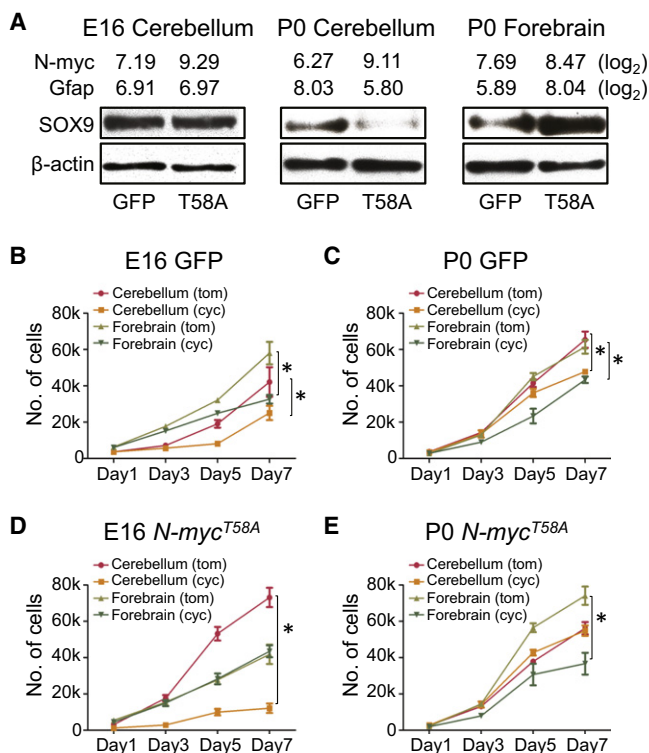


Figure 3. The *N-myc*^{T58A}-Driven Neuronal Program Depends on Regional Origin and NSC Age

(A) Levels of *N-myc* and *Gfap* from Affymetrix exon arrays (log₂ values) and immunoblots of *SOX9* and β -actin in E16 and P0 cerebellar and P0 forebrain NSCs transduced with GFP or *N-myc*^{T58A}, respectively.

(B–E) Proliferation (7 days) of cerebellar and forebrain NSCs transduced with GFP (B and C) or *N-myc*^{T58A} (D and E) and treated with cyclopamine (cyc) or tomatidine (tom) in 5 μ M final concentrations for E16 and P0 ages, respectively.

Error bars: \pm SD. **p* < 0.05 from Student's *t* test. See also Figure S3.

regional origin, we analyzed the glial markers *SOX9* (Stolt et al., 2003) and *GFAP*, 72 hr after transduction of *N-myc*^{T58A} into cerebellar NSCs at E16 and P0 and forebrain NSCs at P0. *N-myc*^{T58A}-transduced NSCs all showed increased *N-myc* mRNA levels as by Affymetrix exon array analysis of distinct NSC populations. P0 cerebellar NSCs transduced with *N-myc*^{T58A} showed reduced mRNA expression of *Gfap* and protein levels of *SOX9* as compared to E16 cerebellar NSCs, whereas P0 forebrain NSCs showed elevated levels of *Gfap* and *SOX9* (Figure 3A).

As *SOX9* has been reported to also act downstream of the SHH/SMO to induce and maintain NSCs (Scott et al., 2010), we next asked whether *N-myc*^{T58A} affected SHH signaling. GFP-transduced control NSCs from E16 and P0 cerebellum and forebrain all responded to SMO inhibition through cyclopamine treatment (Figures 3B and 3C), consistent with reports that forebrain NSCs, cerebellar radial glia, and cerebellar NSCs are sensitive to SHH signals in vivo (Ahn and Joyner, 2005; Huang et al., 2010). While *N-myc*^{T58A}-transduced E16 cerebellar cells and *N-myc*^{T58A}-transduced P0 forebrain cells retained sensitivity to cyclopamine, *N-myc*^{T58A}-transduced P0 cerebellar

and E16 forebrain cells, like GTML tumor spheres, were resistant (Figures 3D and 3E).

In comparing cyclopamine-sensitive and -resistant *N-myc*^{T58A}-transduced cerebellar cultures, we again used Affymetrix exon arrays to analyze expression of *Smo*, a coreceptor for the SHH signal; *Sfrp1*, a marker of SHH-driven MB; *Gli1*, a marker of SHH activation, and *Gli3*, a marker of SHH repression. Expression of *Smo* was unchanged in comparing P0 and E16 cultures (Figures S3A and S3B). Cyclopamine-resistant P0 cultures showed repression of SHH signaling. Both *Sfrp1* and *Gli1* were decreased, while *Gli3* was upregulated in P0 *N-myc*^{T58A} cultures, as compared to E16 cerebellar NSCs. Collectively, these studies demonstrate that *N-myc*^{T58A} promotes SHH independence (downstream of SMO) in postnatal cerebellar cells, in embryonic forebrain cells, and in GTML tumors.

N-myc^{T58A} Initiates Brain Tumors from NSCs

To clarify whether *N-MYC* could induce brain tumors from NSCs, and whether the differentiative programs shown in Figure 3 would persist in vivo, we transduced embryonic and postnatal NSCs with *N-myc*^{WT} or *N-myc*^{T58A} and transplanted cells orthotopically into the brains of nude mice. In contrast to *N-myc*^{WT} NSCs, *N-myc*^{T58A} NSCs from E16 and P0 cerebellum or E16 and P0 forebrain all formed brain tumors (Figures 4A and 4B). *N-myc*^{T58A} cerebellar NSCs generated tumors at higher incidence and penetrance than the *N-myc*^{T58A} forebrain NSCs (Figures 4A and 4B). We also analyzed LRL-derived NSC. Consistent with our in vitro data, *N-myc*^{T58A} E16 and P0 LRL NSCs failed to generate brain tumors, while *N-myc*^{T58A}-transduced E14 LRL NSCs generated brain tumors in 40% of mice when transplanted orthotopically (Figure 4C).

Orthotopic transplantation of *N-myc*^{T58A} P0 cerebellar NSCs into cerebellum resulted in massive tumors with morphology of human MB, including Homer Wright (neuroblastic) rosettes, and prominent cell wrapping characteristic of LC/A tumors (Figures 4D and 4E and Figure S4A). The histology of *N-myc*^{T58A} P0 cerebellar tumors also resembled GTML tumors (Swartling et al., 2010), sometimes showing LC/A histopathology (Figures S4B and S4C). Similarly, orthotopic transplantation of *N-myc*^{T58A} P0 forebrain NSCs into cerebellum induced aggressive forebrain tumors (Figure 4F) that were more invasive than the cerebellar tumors (Figure 4G). The P0 forebrain tumors resembled diffuse gliomas in terms of distant spread of individual tumor cells along white matter tracts (Figure 4G and Figure S4D). E14 LRL tumors were typically characterized by marked cellular and nuclear pleomorphism (Figures 4H and 4I).

While no differences in proliferation (Ki67) and vascularity (CD34) were found among the P0 forebrain and P0 cerebellar tumors, P0 cerebellar tumors were significantly more apoptotic than P0 forebrain tumors (Figures S4E–S4J). P0 cerebellar tumors were generally negative or showed only scattered cells positive for the astrocytic markers GFAP, OLIG2, and *SOX9* (Figures 4J–4L) and moderate immunoreactivity for the neuronal marker SYP (Figure 4M). In contrast, P0 forebrain tumor cells were strongly positive for GFAP, OLIG2, and *SOX9* (Figures 4N–4P) and negative for SYP (Figure 4Q). LRL tumors showed an intermediate phenotype with few scattered cells positive for the astrocytic markers GFAP, moderate positivity for OLIG2

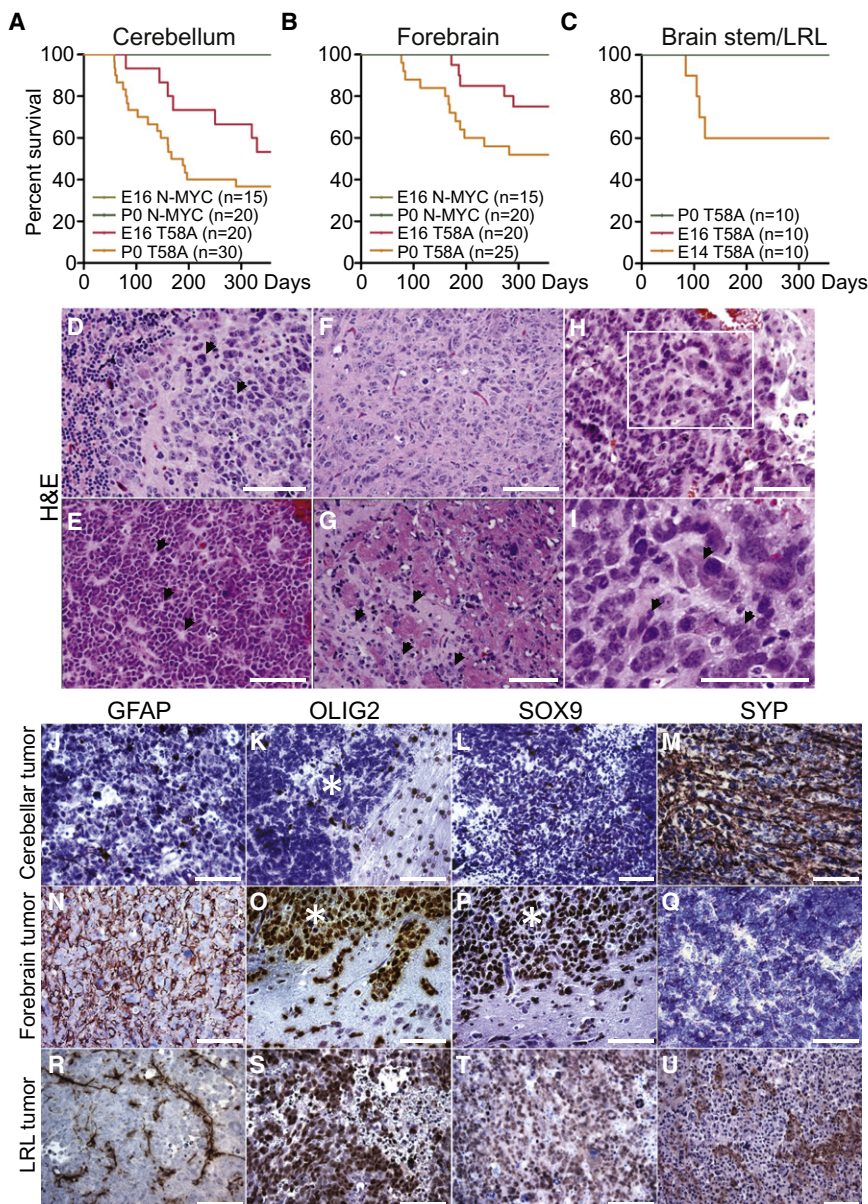


Figure 4. *N-myc*^{T58A} Induces Brain Tumors from Both Cerebellum and Forebrain

(A–C) Survival of mice orthotopically transplanted with 100,000 NSCs isolated from forebrain, cerebellum, and brain stem/LRL, transduced with *N-myc*^{WT} or *N-myc*^{T58A} viruses. n = number of mice per group. Mice injected with *N-myc*^{WT} NSCs (green colors) or *N-myc*^{T58A} E16 and P0 brain stem/LRL (red and green, respectively) generated no tumors.

(D–I) Histopathology of representative P0 cerebellar (D and E), P0 forebrain (F and G), and E14 brain stem/LRL (H–I) *N-myc*^{T58A} tumors (H&E staining). Cerebellar tumors displayed MB features, including cell wrapping in a tumor with prominent LC/A features (D, arrowhead) and Homer Wright rosettes (E, arrowhead). Forebrain tumors displayed diffuse invasion of tumor cells along white matter tracts (arrowhead) (G). LRL tumors displayed marked cellular and nuclear pleomorphism (I, arrowhead). Box in H (200×) denotes region shown at higher magnification in I (400×).

(J–U) Immunostaining, of representative *N-myc*^{T58A}-induced cerebellar, forebrain, and LRL tumors demonstrating greater neuronal differentiation in cerebellar tumors, greater glial differentiation in forebrain tumors, and intermediate differentiation in LRL tumors. *Tumor region in pictures where an adjacent normal brain is present. Scale: 100 μm. See also Figure S4 and Table S1.

affects the ability of GSK3β to phosphorylate and destabilize β-catenin.

Regional Origin Exerts a Dominant Effect on Brain Tumor Type

Transplantation of normal cerebellar NSCs into forebrain VZ generates mostly GFAP-positive astroglial cells (Klein et al., 2005). To determine if the regional brain niche was responsible for the generated tumor phenotypes, we injected *N-myc*^{T58A}-transduced P0 cerebellar NSCs into the forebrain and *N-myc*^{T58A}-transduced P0 forebrain NSCs into the hindbrain. We studied the same markers as in Figure 4 and quantified positive cells (Table S1).

We included three controls each of site-matched tumors for E16 and P0 cerebellum, tumors from E16 forebrain, P0 forebrain, and E14 brain stem, and three GTML tumors.

For all tumors, we also examined protein expression of KCNA1, a Kv1.1 voltage-gated potassium channel-encoding gene associated with Group 4 MB (Taylor et al., 2011) as well as the LRL and WNT markers OLIG3 and β-catenin, respectively (Gibson et al., 2010). The profiles of GFAP, Nestin, and SYP in tumors correlated generally with region from which NSCs were isolated, rather than region of the brain into which we injected transduced cells. Like the LRL tumors (Figure S4O), all tumors examined were negative for nuclear β-catenin (Table S1). Intriguingly, SOX9 and OLIG2 showed a modest and differential

and SOX9 (Figures 4R–4T) and scattered islands of SYP-positive cells (Figure 4U).

The histology of *N-myc*^{T58A} tumors induced from E16 cerebellar, E16 forebrain NSCs generally resembled *N-myc*^{T58A} tumors induced from P0 cerebellar and P0 forebrain NSCs, respectively (Figures S4K and S4L). The majority of tumors derived from E16 cerebellar NSCs were SOX9 positive (Figure S4M). Most embryonic forebrain tumors showed distinct areas of glial differentiation (Figure S4N). Lack of nuclear β-catenin expression in LRL tumors (Figure S4O) suggests a WNT-independent tumor subtype, as compared to a recently reported model for MB also derived from LRL cells originating from brainstem (Gibson et al., 2010). These and tumors from E16 or P0 cerebellum were similarly insensitive to the GSK3β inhibitor TWS119 at 1 μM (data not shown) demonstrating WNT independence, although it remains possible that *N-myc*^{T58A}

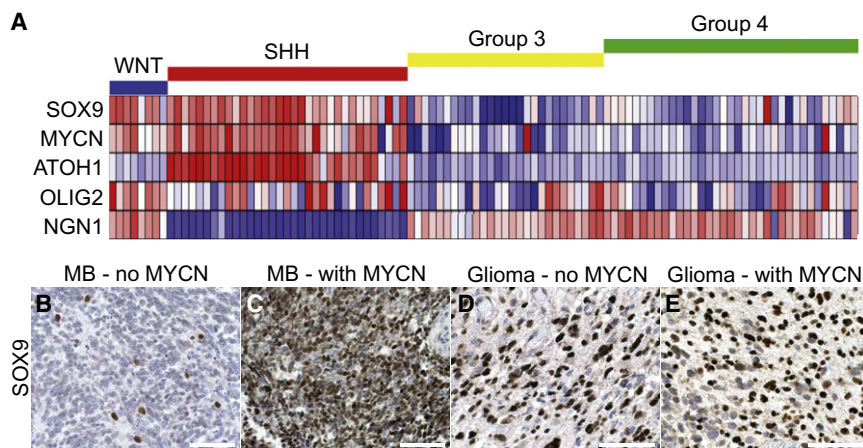


Figure 5. SOX9 Marks a SHH-Dependent Brain Tumor Profile

(A) Expression analysis of SOX9, MYCN, ATOH1 (human MATH1 ortholog), OLIG2, and NGN1 in 103 primary MB samples clustered in four MB subgroups, WNT, SHH, Group 3, and Group 4 with levels normalized to normal adult cerebella ($n = 5$) as described previously (Northcott et al., 2011). Dark blue represents the lowest and dark red the highest expression.

(B–E) SOX9 immunostaining in representative human MB (B and C) and glioma (D and E) sections, without and with MYCN amplification, as determined by fluorescent in situ hybridization (Perry et al., 2009).

Scale: 100 μ m. See also Figure S5 and Table S2.

expression pattern in “misplaced” tumors, with higher levels of protein expression in misplaced hindbrain tumors and lower expression levels in misplaced forebrain tumors (Table S1). Our data still suggest that region of origin exerts a dominant effect on tumor type.

SOX9 Marks SHH-Dependent MB and Malignant Glioma

Transduction of *N-myc*^{T58A} into murine NSCs led to regional and age-dependent changes in levels of SOX9 protein (Figure 3A). To further clarify the expression of SOX9 in MB, we analyzed array data from 103 human MBs segregated into WNT, SHH, Group 3, or Group 4 tumors (Northcott et al., 2011; Taylor et al., 2011). Clustering and expression patterns were consistent with both SOX9 and MYCN as markers for WNT- and SHH-driven human tumors (Figure 5A). NGN1 expression was increased in all subtypes except for the SHH group, marked by the human MATH1 ortholog, ATOH1, and supported by previous data discriminating these subclasses (Cho et al., 2011; Kool et al., 2008; Northcott et al., 2011; Thompson et al., 2006). Consistent with the findings of SOX9 as a marker of SHH-driven tumors, levels of SOX9 levels were highest in infant and adult MB patients (Figure S5), which are typically SHH-dependent (Northcott et al., 2011). Furthermore, SOX9 was only observed in a few scattered cells in a representative human classic MB (Perry et al., 2009) previously reported to lack MYCN amplification (Figure 5B), while a human MYCN-amplified MB showed high levels of SOX9 (Figure 5C).

The pathology and marker expression in P0 forebrain tumors is characteristic of aggressive human malignant glioma with components of primitive neuroectodermal tumors (MG-PNET). We recently described 53 cases of human MG-PNET, detailing both poor survival (essentially identical to human high-grade glioma) and common amplification of MYC and MYCN (43%) in PNET-like foci (Perry et al., 2009). Since MG-PNET may arise in the setting of relapsed glioblastoma (GBM), we next analyzed data from Cancer Genome Atlas Research (TCGA) Network (2008). While OLIG2 and SOX9 were overexpressed in half or more than half of the GBM samples, expression of neuronal markers like NGN1 and SYP were downregulated in most samples (Table S2). Among 424 human GBMs, 20% overexpressed MYCN, consistent with a role for MYCN in the

pathogenesis of some GBMs (Table S2). Irrespective of MYCN amplification, human MG-PNET samples showed high level and distinct nuclear expression of SOX9 (Figures 5D and 5E), consistent with results from glioma cell lines (Swartling et al., 2009) and TCGA data (Table S2).

Alignment of Murine Tumors and Classification Using Human MB Subgroup Identifiers

Having demonstrated that SOX9 can mark SHH-driven human MB, we next applied these observations to murine *N-myc*^{T58A} MB and GTML tumors, using Affymetrix exon arrays. Unsupervised clustering revealed that *N-myc*^{T58A} tumors from E16 cerebellum, P0 cerebellum, and P0 forebrain NSCs were closely aligned to the NSCs from which they were derived (Figure 6). *N-myc*^{T58A} tumors and their corresponding NSCs were more similar to GTML tumors than to normal cerebellum (Figure 6). Within the *N-myc*^{T58A} tumor group, the region of origin (cerebellum versus forebrain) was a larger separator than the age of isolation of the initiating cells. Originating NSCs, *N-myc*^{T58A} tumors, and GTML tumors were all more similar to each other than to normal cerebellum. The signature of NSCs versus tumor was greater than the difference between NSC types, precluding the use of gene expression signatures to identify the most similar potential originating cell.

Using identifiers for subtypes of human MB (Northcott et al., 2011), E16 MB (generated from *N-myc*^{T58A}-transduced E16 cerebellar NSCs) showed a distinct SHH-pathway profile (Figure S6A) while both P0 MB (generated from *N-myc*^{T58A}-transduced P0 cerebellar NSCs) and GTML tumors presented significantly higher expression of the Group 4 identifier KCNA1, as compared to E16 MB. By contrast, the other subgroup identifiers, DKK1 (WNT), SFRP1 (SHH), and NPR3 (Group 3), did not significantly delineate these groups (Figure S6B).

E16 *N-myc*^{T58A} Cerebellar Tumors Model SHH-Dependent MB, while P0 Tumors Model SHH-Independent Disease

Expression levels of Sox9, N-myc, and Math1 further distinguished the various *N-myc*^{T58A} tumors using both Affymetrix arrays as well as quantitative real-time PCR, as compared to expression levels in adult cerebellum (Figures 7A–7C and

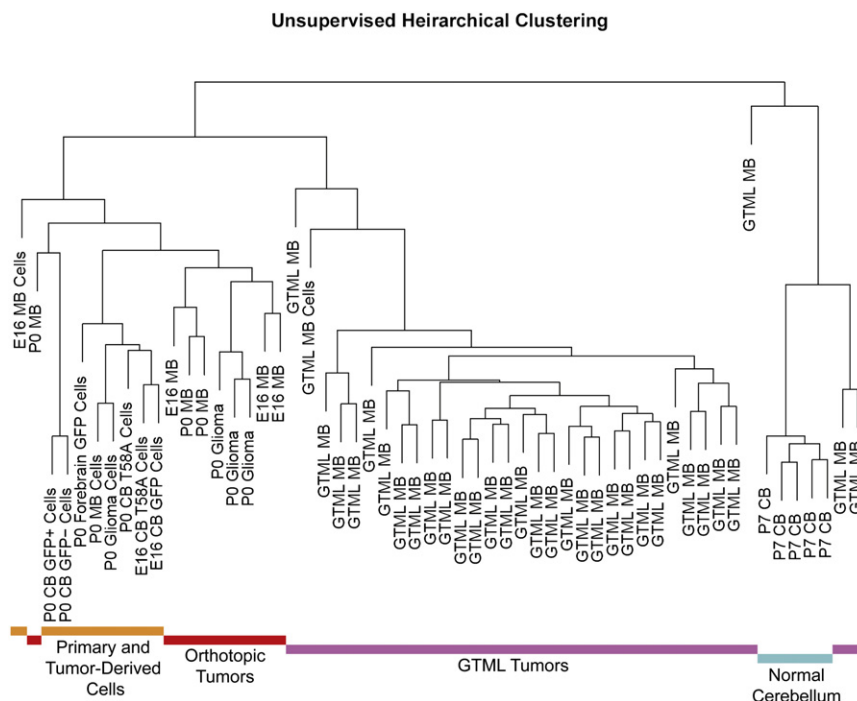


Figure 6. *N-myc*^{T58A} Tumors, GTML Tumors, and Normal Murine Tissues Show Discrete Expression Signatures

Dendrogram showing unsupervised hierarchical clustering from Affymetrix exon array data obtained from: (1) primary and tumor-derived cells (yellow): four individual GFP-transduced E16 and P0 cerebellar (sorted or unsorted for GFP-infection using cell sorting) NSCs, P0 forebrain NSCs, two *N-myc*^{T58A}-transduced E16 and P0 cerebellar NSCs (in low passages), and three cell lines (in low passages) derived from orthotopic E16 and P0 cerebellar and P0 forebrain tumors. (2) Orthotopic tumors (red): nine freshly isolated orthotopic E16 and P0 cerebellar and P0 forebrain *N-myc*^{T58A}-tumors. (3) GTML tumors (purple): 32 isolated GTML tumors and one cultured GTML tumor cell line (GTML2). (4) Normal cerebellum (blue): five samples from P7 GTML double heterozygous total cerebella. The distance in the clustering determines how well samples are related to each other. See also Figure S6.

Figures S7A and S7B). E16 MB showed high levels of Sox9 mRNA, N-myc, and of the EGL marker Math1, suggesting a SHH- rather than a WNT-dependent subtype (Figures 7A–7C). In contrast, P0 MB displayed lower expression of Sox9, N-myc and Math1. Similar to P0 MB, E14 LRL tumors (generated from *N-myc*^{T58A}-transduced prenatal LRL NSCs) showed low N-myc and Math1 levels consistent with a SHH-independent origin (Figures 7A–7C).

Interestingly, forebrain *N-myc*^{T58A} P0 tumors (P0 glioma) showed high levels of Sox9 and N-myc and absent Math1 (Figures 7A–7C), consistent with transformation of a forebrain cell type that shows SHH dependence independently of Math1 (Akazawa et al., 1995). Expression analysis substantiated the glioma phenotype observed in the forebrain tumors, in which levels of Gfap were significantly elevated as compared to hind-brain tumors (Figure S7B). Moreover, Nestin (Nes) was among the top 30 genes overexpressed in P0 glioma as compared to P0 MB (Table S3). P0 MB showed a low immunoreactivity of Nestin, while P0 glioma showed elevated Nestin expression (Figures S7C and S7D and Table S1). As Nestin is a strong marker for glioma and upregulated in 99% of human GBM samples in the TCGA database (Table S2), increased Nestin expression suggests a glioma-like differentiation pattern in forebrain tumors compared to the MB-like pattern seen in cerebellar tumors.

In agreement with SOX9 as a marker for SHH dependence, cultured P0 MB spheres with low levels of SOX9 were resistant to cyclopamine (Figure 7D). Conversely, both E16 MB and P0 glioma with high SOX9 levels were cyclopamine sensitive (Figure 7D). Similar dependence on SHH was also observed in *N-myc*^{T58A} NSCs prior to orthotopic implantation and tumor formation (Figures 3B–3E). These results suggest that *N-myc*^{T58A} initiates SHH-dependent transformation in both E16 cerebellar

NSCs and P0 forebrain NSCs, while transformation of E16 forebrain NSCs and P0 cerebellar NSCs (and possibly in brain stem NSCs) occurs through a SHH-independent pathway.

SOX9 Promotes Self-Renewal and Generates GLI2-Expressing Tumors at Shorter Latency

Our data demonstrate that P0 MBs arise through a SOX9- and SHH-independent program. To establish whether SOX9 plays a functional role in transforming P0 cerebellar NSCs, we generated SOX9 RCAS viruses (Figure S8A) and selectively transduced Gtv-a-positive P0 *N-myc*^{T58A} cerebellar NSCs or P0 MB spheres (isolated from individual P0 MBs). Forced expression of SOX9 suppressed proliferation in P0 *N-myc*^{T58A} cerebellar cells and in P0 MB spheres (Figure S8B), which have low levels of SOX9 (Figures 3A, 4I, and 7A). In contrast, similar forced expression of SOX9 did not affect E16 MB and P0 glioma, which have high SOX9 levels at baseline (Figures S8C and S8D).

Although forced expression of SOX9 suppressed proliferation in *N-myc*^{T58A} cerebellar cells and in P0 MB spheres, SOX9 actually drove increased self-renewal when culturing these at a limited dilution. Single cell clones from normal P0 cerebellar NSCs and P0 cerebellar NSCs transduced with *N-myc*^{T58A} were transduced with SOX9, and clones with high levels of SOX9 were selected (Figure 8A). SOX9 increased self-renewal in both normal and *N-myc*^{T58A}-transduced P0 cerebellar NSC clones, as compared to normal and *N-myc*^{T58A}-transduced P0 cerebellar NSC clones without forced expression of SOX9 (Figure 8B). Single cell spheres and spheres generated from an isolated P0 MB (P0C-T3, also cultured and propagated from a single cell clone) were dependent on growth factors EGF and FGF as compared to single cell clones subcloned out from the GTML2 sphere line (Figure 1A) that generated secondary spheres essentially independently of growth factors. Forced

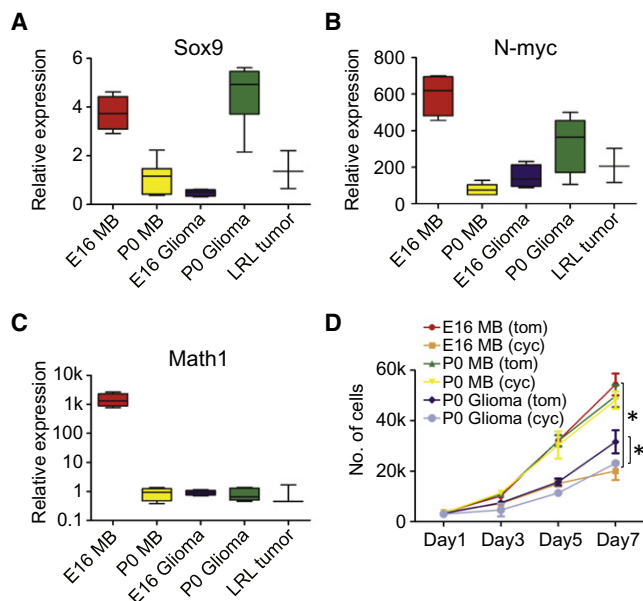


Figure 7. N-MYC Drives Both SHH-Dependent and SHH-Independent MB

(A–C) Relative expression of Sox9, N-myc, and Math1 in five disparate N-MYC-driven murine tumors, E16 MB (n = 4), P0 MB (n = 6), E16 glioma (n = 4), P0 glioma (n = 6), and E14 LRL tumor (n = 3). n = number of individual tumors. Boxes are the first to third quartile with the median indicated. No boxes are shown for LRL tumors because of few samples (n = 3). Whiskers go from minimum to maximum values.

(D) Proliferation of cultures of E16 MB, P0 MB, and P0 glioma isolated from individual tumors and treated with cyclopamine (cyc) or tomatidine (tom) used at final concentrations of 5 μ M. *Statistical significance (p < 0.05) from Student's t test. Error bars: \pm SD.

See also Figure S7 and Table S3.

expression of SOX9 was also associated with higher levels of Gli2 (Figures 8C–8E), suggesting that SOX9 can drive SHH-signaling in these cells.

Since forced expression of SOX9 drove self-renewal while blocking proliferation of cells in vitro, we next asked how these potentially opposing activities would impact tumor formation in vivo. Forced expression of SOX9 and *N-myc*^{T58A} in P0 cerebellar NSCs generated orthotopic tumors at shorter latency and with increased tumor penetrance, as compared with NSCs expressing *N-myc*^{T58A} alone (Figure 8F). The SOX9-expressing tumor cells demonstrated marked cellular and nuclear pleomorphism, numerous mitoses, and numerous apoptotic bodies, consistent with a primitive neuroectodermal phenotype (Figure S8E). Focally tumor cells contained abundant cytoplasm and GFAP immunostaining demonstrated a population of GFAP-positive tumor cells. (Figures S8E and S8F). These observations suggest that SOX9 can cooperate with N-MYC to promote malignant progression acting upstream of Gli2.

Forced expression of *N-myc*^{T58A} repressed SOX9 in P0 cerebellar NSCs. Is SOX9 similarly repressed in GTML tumors? In response to dox-mediated withdrawal of MYCN, some cells within GTML tumors undergo senescence (Swartling et al., 2010). Consistent with this result, dox treatment of GTML3 tumor spheres led to death of most cells, while a few cells remained

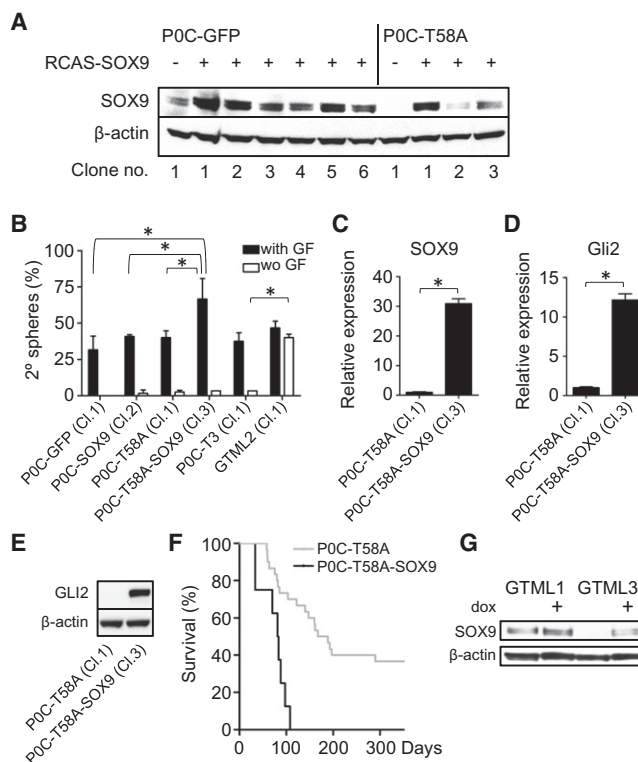


Figure 8. SOX9 Promotes Self-Renewal and N-MYC-Driven Brain Tumor Incidence

(A) Immunoblot of NSCs generated from single cells of GFP- and SOX9-transduced P0 cerebellar NSCs from normal (six individual clones) and *N-myc*^{T58A} transduced NSCs (three individual clones).

(B) Limiting dilution assay showing secondary (2°) spheres cultured starting from one single cell per well (with or without (wo) EGF and FGF). Numbers indicates mean values (from two experiments) of spheres per well from a total of 60 wells counted (shown as %). Clone numbers used (from A) are indicated. Assay results from single clones from a P0 MB tumor (P0C-T3 (Cl.1)) and from a GTML tumor [GTML2 (Cl.1)] are also included. *Statistical significance (p < 0.05) from Student's t test.

(C and D) Relative expression of SOX9 and Gli2 in *N-myc*^{T58A}-transduced P0 cerebellar NSCs and *N-myc*^{T58A}-transduced P0 cerebellar NSCs further transduced with SOX9 (P0C-T58A-SOX9 Cl.3), respectively. For SOX9 expression and clone numbers, see (A). *Statistical significance (p < 0.05) from Student's t test.

(E) Immunoblot showing Gli2 protein expression in *N-myc*^{T58A}-transduced P0 cerebellar normal (P0C-T58A Cl.1) or SOX9-transduced (P0C-T58A-SOX9 Cl.3) clones.

(F) Survival after orthotopic transplantation of 100,000 cells from *N-myc*^{T58A} P0 cerebellar NSCs (P0C-T58A, as used in Figure 4A; n = 30) and *N-myc*^{T58A} P0 cerebellar NSCs further transduced with SOX9 (P0C-T58A-SOX9, n = 10), respectively. Same clone (Cl.3) was used as in (C)–(E).

(G) Re-expression of SOX9 in representative GTML spheres (GTML1 and GTML3) treated with dox (1 μ g/ml) after 72 hr as shown in an immunoblot, with GTML1 cells as controls. *Statistical significance (p < 0.05) from Student's t test.

Error bars: \pm SD.

See also Figure S8.

viable without proliferating (Figures S8G and S8H and data not shown). In response to withdrawal of MYCN, these viable cells showed elevated levels of SOX9 at levels similar to SHH-dependent GTML1 control cells (Figure 8G). This suggests SOX9 is repressed by forced expression of MYCN also in

SHH-independent GTML tumors. Collectively, data in Figure 8 demonstrate that interactions between N-MYC and SOX9 regulate proliferation, differentiation, and self-renewal in P0 *N-myc*^{T58A} MB, and that similar interactions are relevant to *MYCN*-driven GTML MB.

DISCUSSION

Deletion of *N-myc* in neural stem and progenitor cells in the mouse causes reduced cellularity of both forebrain and hindbrain, suggesting an essential role in the growth and development of these structures (Knoepfler et al., 2002). Here, by orthotopic transplantation of *N-myc*^{T58A} NSCs, we validate a reciprocal role for mis-expression of *N-myc* in the pathogenesis of both forebrain and hindbrain tumors. Our data, and the finding that *MYCN* is commonly overexpressed in both forebrain and in hindbrain tumors in humans (Brennan et al., 2009; Eberhart et al., 2004; Hui et al., 2001; Perry et al., 2009; Pfister et al., 2009; Pomeroy et al., 2002), suggest a role for *MYCN* in the development of brain tumors.

Our experiments are consistent with recent results suggesting a relationship between normal NSCs and tumor initiating cells (Holland et al., 2000; Johnson et al., 2010; Schüller et al., 2008; Sutter et al., 2010; Yang et al., 2008). Orthotopic injection of *N-myc*^{T58A} DF-1 virus-producing cells failed to generate brain tumors (Browd et al., 2006 and our unpublished data), perhaps in part because few, if any, NSCs are successfully transduced through this approach. We instead generated five different tumors from distinct NSCs transduced with *N-myc*^{T58A} after a brief propagation in culture. *N-myc*^{T58A} NSCs derived from embryonic cerebellum led to SHH-dependent MB, consistent with transduction of a GFAP-positive NSC with a propensity to become a MATH1-positive granule neuron precursor (Marino et al., 2000; Schüller et al., 2008; Yang et al., 2008). In contrast, *N-myc*^{T58A} NSCs derived from postnatal forebrain led to tumors with characteristics of malignant glioma, consistent with transduction of a GFAP-positive NSC with a propensity to become a MATH1-negative, SHH-dependent forebrain cell (Palma et al., 2005).

N-myc^{T58A} NSCs derived from embryonic forebrain generated brain tumors at low penetrance. Analysis of a limited number of these tumors suggests transduction of a GFAP-positive NSC with a propensity to become a SHH-independent forebrain glioma. *N-myc*^{T58A} NSCs derived from postnatal cerebellum led to SHH-independent MB with low levels of Math1 and Sox9. Tumors were also generated from the lower rhombic lip or the dorsal regions of the VZ of the developing brain stem. Interestingly, only E14 LRL NSCs could induce brain tumors, whereas no tumors were observed from E16 or PO LRL/brain stem NSCs.

That our LRL tumors were only seen at E14 ages correlate with previous findings of WNT-subtype MB in the murine LRL/dorsal brainstem generated between E11.5 and E15.5 (Gibson et al., 2010). Our LRL tumors resembled human anaplastic MB/PNETs and arose independently of WNT signaling, with negative immunoreactivity for nuclear β -catenin and the LRL marker OLIG3. These tumors might thus arise from a brain stem VZ cell type distinct from an OLIG3-positive LRL progenitor (Storm et al., 2009). LRL tumors lacked Math1 expression, and showed moderate levels of Sox9. The low levels of Math1 are also

characteristic of GTML MB arising in transgenic mice, and are consistent with transduction of a GFAP/GLT1 double-positive NSC with potential to become a MATH1-negative, SHH-independent progenitor.

Expression analysis of E16 MB revealed elevated levels of many genes upregulated in the SHH subclass of human MB, while both P0 MB and GTML MB were at least somewhat aligned with human Group 4 MB (Taylor et al., 2011). Collectively, our experiments argue that GFAP-positive NSCs from forebrain and hindbrain can give rise to both malignant glioma and to at least two distinct subtypes of MB, a SHH subgroup and a SHH-independent Group 4 MB subgroup, together representing 38% and 62% of *MYCN*-amplified human MB, respectively (Korshunov et al., 2011). We have not demonstrated that the cells of origin for our tumors truly represent self-renewing tripotent NSCs. Therefore, it remains possible that the cells we refer to as NSCs, actually represent progenitors with a more limited potential for differentiation. In either case, our observations raise questions as to the nature of cells transformed in human tumors. Perhaps mutations that initiate transformation occur at embryonic or postnatal ages, generating partially transformed cells that persist into childhood or adulthood, later giving rise to tumors.

SOX9 acts downstream of SHH signaling, at least in part because GLI1, a marker of SHH activation, binds directly to a regulatory element in the SOX9 promoter region, driving expression (Bagheri-Fam et al., 2006; Vidal et al., 2005). SOX9 is essential for formation and maintenance of multipotent NSCs and is an effector of SHH signaling (Scott et al., 2010). SOX9 levels were high in SHH-driven human MB, a finding aligned with our murine data that E16 cerebellar NSCs retain SOX9 expression upon transformation, and respond to SHH inhibition. Forced expression of SOX9 in P0 *N-myc*^{T58A} cerebellar NSCs showed that SOX9 antagonized proliferation driven by *N-myc*^{T58A} in P0 tumors. However, SOX9 also promoted self-renewal, associated with increased expression of Gli2 in P0 *N-myc*^{T58A} cerebellar NSCs, leading to increased penetrance of a Gli2-expressing tumor. These data demonstrate that SOX9 expression can promote SHH-activation in *N-myc*^{T58A} MB, and suggest SOX9 as an important regulator of SHH MB. Further, our observations are consistent with a model in which N-MYC promotes a neuronal fate in P0 cerebellar NSCs, associated with repression of SOX9 and expression of neuronal markers like NGN1, resulting in a profile similar to the majority of human MB.

N-myc^{T58A} forebrain tumors showed significant glial differentiation without microvascular proliferation, pseudopalisading cells and necrosis. These features are reminiscent of human MG-PNET, a tumor type that we recently detailed, and which shows frequent amplification of *MYCN* (Perry et al., 2009). The association of *MYCN* amplification with MG-PNET and our ability to model these tumors in the mouse collectively support a role for *MYCN* in the pathogenesis of malignant glioma. Since MG-PNET may arise in the setting of pre-existing or recurrent GBM (Perry et al., 2009), our studies also provide a mouse model both for the study of tumor biology and for development of therapies against this highly lethal neoplasm.

Although GBM and MB comprise common malignant brain tumors, the catalog of human brain tumors is extensive, and the richness of cell varieties in the CNS is reflected in the many

varieties of brain tumors observed in the human population. Previous reports demonstrate that NSCs in the forebrain and hindbrain show developmental restrictions based on the brain regions from which they were derived (Klein et al., 2005; Merkle et al., 2007). The murine tumors described here showed striking similarities with specific subtypes of human brain tumors, suggesting a pathogenic role for MYCN in a heterogeneous group of human brain tumors. Together with the recently published models of MYC-driven MB (Kawauchi et al., 2012; Pei et al., 2012), we have recapitulated the most aggressive MYC/MYCN-driven human childhood brain tumors.

EXPERIMENTAL PROCEDURES

Animals and Bioluminescent Imaging

Generation of GTML mice of the FVB/NJ strain has been previously described (Swartling et al., 2010). Tumor progression of doubly *Gl1-tTA/MYCN-TRE* transgenic mice was continuously followed by luciferase signaling using the IVIS Lumina (Caliper Life Sciences, Mountain View, CA) using Living Image 2.5 software (Caliper Life Sciences, Mountain View, CA). Mice were injected with 75 mg/kg of sodium luciferin (LUCNA, Gold Biotechnology, St. Louis, MO) in saline prior to imaging. The mice selected for tumor removal and neurobasal cell culture all had high scores ($>5.0 \times 10^{10}$ photons/cm² sec) from bioluminescence imaging suggesting a functional bidirectional transgene expressing luciferase as previously reported (Swartling et al., 2010). For cell fate experiments, *Gl1-tTA* mice were crossed with *TRE-Cre:R26R-LSL-LacZ* mice obtained from Dr. Robert Blelloch, UCSF. The *G-tva* mice have been described before (Holland and Varmus, 1998) and were generously provided by Dr. Eric Holland and backcrossed at least five generations into FVB/NJ strain before experimental use. Athymic Nude-Foxn1nu mice were obtained by Simonsen Laboratories (Gilroy, CA) or Harlan Laboratories (Venray, The Netherlands) and used in experimental procedures as described below. Mice were maintained in the Animal Facilities at University of California, San Francisco and at Uppsala University, Uppsala. All animal procedures were performed in accordance with national guidelines and regulations and approved by the Institutional Animal Care and Use Committee of the University of California in San Francisco and Uppsala Ethical Committee on Animal Experiments in Uppsala.

Neural Stem/Progenitor Cell and Tumor Cell Culturing

Normal tissue or part of tumor was removed and mechanically dissolved in cold Hank's buffer without calcium and magnesium (Cell Culture Facility, UCSF, Mission Bay, San Francisco). After one more wash in cold Hank's buffer, the sample was incubated for 20 min in activated papain (Worthington, Lakewood, NJ). Tumor cells were gently dissociated and cultured in neurobasal media (GIBCO) without vitamin A, supplemented with antibiotics (Cell Culture Facility, UCSF), B27 without vitamin A (Invitrogen), L-glutamine and 20 ng/ml EGF (Sigma), and 20 ng/ml FGF-2 (Peprotech, Rocky Hill, NJ). Cells were cultured and propagated on low adhesion plates (Corning) for 1 week, further passaged, and used in experiments. SVZ neurospheres were established from FVB/N WT mice and similarly cultured as described above. Forebrains of E16.5 (described as E16) and P0.5 (described as P0) were coronally sectioned (100 μ m thick sections) and sections 2.5–3.5 mm posterior of the base of olfactory bulb and the dorsal regions closest to the ventricles were isolated and dissociated as above. Total cerebellum was carefully removed excluding any parts of meninges, brain stem, or midbrain, dissociated and similarly cultured as above. Cell layers (~0.05–0.1 mm) of dorsal brain stem and lower rhombic lip were isolated from carefully removed brain stems, dissociated and similarly cultured as above. GNPs were enriched and cultured as previously described in 10 ng/ml SHH-N (SHH N-terminal peptide, R&D Systems) containing serum-free media (Swartling et al., 2010).

Array Experiments

Expression analysis (as presented in Figure 5 and Figure S5) was performed on 103 primary human medulloblastoma using Affymetrix exon arrays as previously described (Northcott et al., 2009; Swartling et al., 2010). All tumor

specimens were obtained in accordance with the Research Ethics Board at the Hospital for Sick Children (Toronto, Canada) and deidentified prior to analyses (Northcott et al., 2009). We studied the expression levels of SOX9, MYCN, MATH1, OLIG2, and NGN1 in four distinct molecular variants described as WNT, SHH, group C, and group D tumors as previously identified by multiple unsupervised analyses of these medulloblastoma samples (Northcott et al., 2010). RNA from tumors was isolated using Trizol (Invitrogen, Carlsbad, CA) and purified using the RNeasy Mini Kit (QIAGEN, Valencia, CA). For the GTML tumors, 1 μ g of RNA was used as a starting template for the RiboMinus rRNA subtraction protocol (Invitrogen) followed by the ST labeling protocol (Affymetrix, Santa Clara, CA). For the transplanted tumors, 100 ng of RNA was used as a starting template for the Ambion WT Expression protocol (Applied Biosystems, Carlsbad, CA) followed by the WT Terminal Labeling protocol (Affymetrix). Labeled samples were hybridized to Affymetrix Mouse Exon 1.0 arrays. All arrays were normalized together with expression values calculated using RMA in the XPS package in R. Boxplots were generated in R using the standard graphics package. Two-way comparisons between groups were performed using Significance of Microarrays (SAM) (Tusher et al., 2001).

ACCESSION NUMBERS

Microarray data have been deposited in the GEO public database (<http://www.ncbi.nlm.nih.gov/geo/>), with accession number GSE36594.

SUPPLEMENTAL INFORMATION

Supplemental Information includes eight figures, three tables, Supplemental Experimental Procedures and can be found with this article online at doi:10.1016/j.ccr.2012.04.012.

ACKNOWLEDGMENTS

The authors would like to acknowledge Eric Holland, Anna-Marie Kenney, and Daniel Fuhs for RCAS constructs, Monica Venere and Robert Blelloch for the *TRE-Cre:R26R-LSL-LacZ* transgene, Cynthia Cowdrey and the UCSF Brain Tumor Research Center Tissue Core for tumor samples, and Kim Nguyen and Slava Yakovenko for skillful technical assistance. We thank Jan Grawé and BioVis, SciLifeLab at Uppsala University, for help with cell sorting. We thank David Rowitch and Richard Gilbertson for helpful discussions and Justin Meyerowitz for critical reading of the manuscript. We acknowledge support from the Pediatric Brain Tumor Foundation, the Swedish Research Council, the Swedish Cancer Society, the Swedish Childhood Cancer Foundation, Ake Wibergs Stiftelse, Lions Cancerforskningsfond, Stiftelsen Lars Hiertas Minne, Children's Brain Tumor Foundation, NIH R01 CA133091, CA148699, and CA159859. This work was also supported by funds from NIH K08 NS063456 to J.J.P. and Hellmann Fellowship Award and the American Brain Tumor Association Translational Award to A.I.P.

Received: November 10, 2010

Revised: January 26, 2012

Accepted: April 4, 2012

Published: May 14, 2012

REFERENCES

- Ahn, S., and Joyner, A.L. (2005). In vivo analysis of quiescent adult neural stem cells responding to Sonic hedgehog. *Nature* 437, 894–897.
- Akazawa, C., Ishibashi, M., Shimizu, C., Nakanishi, S., and Kageyama, R. (1995). A mammalian helix-loop-helix factor structurally related to the product of *Drosophila* proneural gene *atonal* is a positive transcriptional regulator expressed in the developing nervous system. *J. Biol. Chem.* 270, 8730–8738.
- Alcock, J., and Sottile, V. (2009). Dynamic distribution and stem cell characteristics of Sox1-expressing cells in the cerebellar cortex. *Cell Res.* 19, 1324–1333.
- Bagheri-Fam, S., Barrionuevo, F., Dohrmann, U., Günther, T., Schüle, R., Kemler, R., Mallo, M., Kanzler, B., and Scherer, G. (2006). Long-range

upstream and downstream enhancers control distinct subsets of the complex spatiotemporal Sox9 expression pattern. *Dev. Biol.* 291, 382–397.

Brennan, C., Momota, H., Hambardzumyan, D., Ozawa, T., Tandon, A., Pedraza, A., and Holland, E. (2009). Glioblastoma subclasses can be defined by activity among signal transduction pathways and associated genomic alterations. *PLoS ONE* 4, e7752.

Browd, S.R., Kenney, A.M., Gottfried, O.N., Yoon, J.W., Walterhouse, D., Pedone, C.A., and Fuhs, D.W. (2006). N-myc can substitute for insulin-like growth factor signaling in a mouse model of sonic hedgehog-induced medulloblastoma. *Cancer Res.* 66, 2666–2672.

Charron, J., Malynn, B.A., Fisher, P., Stewart, V., Jeannotte, L., Goff, S.P., Robertson, E.J., and Alt, F.W. (1992). Embryonic lethality in mice homozygous for a targeted disruption of the N-myc gene. *Genes Dev.* 6 (12A), 2248–2257.

Cancer Genome Atlas Research Network. (2008). Comprehensive genomic characterization defines human glioblastoma genes and core pathways. *Nature* 455, 1061–1068.

Cho, Y.J., Tsherniak, A., Tamayo, P., Santagata, S., Ligon, A., Greulich, H., Berhoukim, R., Amani, V., Goumnerova, L., Eberhart, C.G., et al. (2011). Integrative genomic analysis of medulloblastoma identifies a molecular subgroup that drives poor clinical outcome. *J. Clin. Oncol.* 29, 1424–1430.

de Bont, J.M., Kros, J.M., Passier, M.M., Reddingius, R.E., Sillevis Smitt, P.A., Luidert, T.M., den Boer, M.L., and Pieters, R. (2008). Differential expression and prognostic significance of SOX genes in pediatric medulloblastoma and ependymoma identified by microarray analysis. *Neuro-oncol.* 10, 648–660.

Doetsch, F., Caillé, I., Lim, D.A., García-Verdugo, J.M., and Alvarez-Buylla, A. (1999). Subventricular zone astrocytes are neural stem cells in the adult mammalian brain. *Cell* 97, 703–716.

Eberhart, C.G., Kratz, J., Wang, Y., Summers, K., Stearns, D., Cohen, K., Dang, C.V., and Burger, P.C. (2004). Histopathological and molecular prognostic markers in medulloblastoma: c-myc, N-myc, TrkC, and anaplasia. *J. Neuropathol. Exp. Neurol.* 63, 441–449.

Ellison, D.W., Dalton, J., Kocak, M., Nicholson, S.L., Fraga, C., Neale, G., Kenney, A.M., Brat, D.J., Perry, A., Yong, W.H., et al. (2011). Medulloblastoma: clinicopathological correlates of SHH, WNT, and non-SHH/WNT molecular subgroups. *Acta Neuropathol.* 121, 381–396.

Farah, M.H., Olson, J.M., Sucic, H.B., Hume, R.I., Tapscott, S.J., and Turner, D.L. (2000). Generation of neurons by transient expression of neural bHLH proteins in mammalian cells. *Development* 127, 693–702.

Gibson, P., Tong, Y., Robinson, G., Thompson, M.C., Currie, D.S., Eden, C., Kranenburg, T.A., Hogg, T., Poppleton, H., Martin, J., et al. (2010). Subtypes of medulloblastoma have distinct developmental origins. *Nature* 468, 1095–1099.

Hatton, B.A., Knoepfler, P.S., Kenney, A.M., Rowitch, D.H., de Alborán, I.M., Olson, J.M., and Eisenman, R.N. (2006). N-myc is an essential downstream effector of Shh signaling during both normal and neoplastic cerebellar growth. *Cancer Res.* 66, 8655–8661.

Holland, E.C., and Varmus, H.E. (1998). Basic fibroblast growth factor induces cell migration and proliferation after glia-specific gene transfer in mice. *Proc. Natl. Acad. Sci. USA* 95, 1218–1223.

Holland, E.C., Celestino, J., Dai, C., Schaefer, L., Sawaya, R.E., and Fuller, G.N. (2000). Combined activation of Ras and Akt in neural progenitors induces glioblastoma formation in mice. *Nat. Genet.* 25, 55–57.

Huang, X., Liu, J., Ketova, T., Fleming, J.T., Grover, V.K., Cooper, M.K., Litington, Y., and Chiang, C. (2010). Transventricular delivery of Sonic hedgehog is essential to cerebellar ventricular zone development. *Proc. Natl. Acad. Sci. USA* 107, 8422–8427.

Hui, A.B., Lo, K.W., Yin, X.L., Poon, W.S., and Ng, H.K. (2001). Detection of multiple gene amplifications in glioblastoma multiforme using array-based comparative genomic hybridization. *Lab. Invest.* 81, 717–723.

Johnson, R.A., Wright, K.D., Poppleton, H., Mohankumar, K.M., Finkelstein, D., Pounds, S.B., Rand, V., Leary, S.E., White, E., Eden, C., et al. (2010). Cross-species genomics matches driver mutations and cell compartments to model ependymoma. *Nature* 466, 632–636.

Kawauchi, D., Robinson, G., Uziel, T., Gibson, P., Rehg, J., Gao, C., Finkelstein, D., Qu, C., Pounds, S., Ellison, D.W., et al. (2012). A mouse model of the most aggressive subgroup of human medulloblastoma. *Cancer Cell* 21, 168–180.

Kessler, J.D., Hasegawa, H., Brun, S.N., Emmenegger, B.A., Yang, Z.J., Dutton, J.W., Wang, F., and Wechsler-Reya, R.J. (2009). N-myc alters the fate of preneoplastic cells in a mouse model of medulloblastoma. *Genes Dev.* 23, 157–170.

Klein, C., Butt, S.J., Machold, R.P., Johnson, J.E., and Fishell, G. (2005). Cerebellum- and forebrain-derived stem cells possess intrinsic regional character. *Development* 132, 4497–4508.

Knoepfler, P.S., Cheng, P.F., and Eisenman, R.N. (2002). N-myc is essential during neurogenesis for the rapid expansion of progenitor cell populations and the inhibition of neuronal differentiation. *Genes Dev.* 16, 2699–2712.

Kool, M., Koster, J., Bunt, J., Hasselt, N.E., Lakeman, A., van Sluis, P., Troost, D., Meeteren, N.S., Caron, H.N., Cloos, J., et al. (2008). Integrated genomics identifies five medulloblastoma subtypes with distinct genetic profiles, pathway signatures and clinicopathological features. *PLoS ONE* 3, e3088.

Korshunov, A., Remke, M., Kool, M., Hielscher, T., Northcott, P.A., Williamson, D., Pfaff, E., Witt, H., Jones, D.T., Ryzhova, M., et al. (2011). Biological and clinical heterogeneity of MYCN-amplified medulloblastoma. *Acta Neuropathol.* 123, 515–527.

Lee, A., Kessler, J.D., Read, T.A., Kaiser, C., Corbeil, D., Huttner, W.B., Johnson, J.E., and Wechsler-Reya, R.J. (2005). Isolation of neural stem cells from the postnatal cerebellum. *Nat. Neurosci.* 8, 723–729.

Ligon, K.L., Alberta, J.A., Kho, A.T., Weiss, J., Kwaan, M.R., Nutt, C.L., Louis, D.N., Stiles, C.D., and Rowitch, D.H. (2004). The oligodendroglial lineage marker OLIG2 is universally expressed in diffuse gliomas. *J. Neuropathol. Exp. Neurol.* 63, 499–509.

Lin, J.C., Cai, L., and Cepko, C.L. (2001). The external granule layer of the developing chick cerebellum generates granule cells and cells of the isthmus and rostral hindbrain. *J. Neurosci.* 21, 159–168.

Marino, S., Vooijs, M., van Der Gulden, H., Jonkers, J., and Berns, A. (2000). Induction of medulloblastomas in p53-null mutant mice by somatic inactivation of Rb in the external granular layer cells of the cerebellum. *Genes Dev.* 14, 994–1004.

Merkle, F.T., Mirzadeh, Z., and Alvarez-Buylla, A. (2007). Mosaic organization of neural stem cells in the adult brain. *Science* 317, 381–384.

Northcott, P.A., Fernandez-L, A., Hagan, J.P., Ellison, D.W., Grajkowska, W., Gillespie, Y., Grundy, R., Van Meter, T., Rutka, J.T., Croce, C.M., et al. (2009). The miR-17/92 polycistron is up-regulated in sonic hedgehog-driven medulloblastomas and induced by N-myc in sonic hedgehog-treated cerebellar neural precursors. *Cancer Res.* 69, 3249–3255.

Northcott, P.A., Korshunov, A., Witt, H., Hielscher, T., Eberhart, C.G., Mack, S., Bouffet, E., Clifford, S.C., Hawkins, C.E., French, P., et al. (2011). Medulloblastoma comprises four distinct molecular variants. *J. Clin. Oncol.* 29, 1408–1414.

Palma, V., Lim, D.A., Dahmane, N., Sánchez, P., Brionne, T.C., Herzberg, C.D., Gitton, Y., Carleton, A., Alvarez-Buylla, A., and Ruiz i Altaba, A. (2005). Sonic hedgehog controls stem cell behavior in the postnatal and adult brain. *Development* 132, 335–344.

Pei, Y., Moore, C.E., Wang, J., Tewari, A.K., Eroshkin, A., Cho, Y.J., Witt, H., Korshunov, A., Read, T.A., Sun, J.L., et al. (2012). An animal model of MYC-driven medulloblastoma. *Cancer Cell* 21, 155–167.

Perry, A., Miller, C.R., Gujrati, M., Scheithauer, B.W., Zambrano, S.C., Jost, S.C., Raghavan, R., Qian, J., Cochran, E.J., Huse, J.T., et al. (2009). Malignant gliomas with primitive neuroectodermal tumor-like components: a clinicopathologic and genetic study of 53 cases. *Brain Pathol.* 19, 81–90.

Pfister, S., Remke, M., Benner, A., Mendrzyk, F., Toedt, G., Felsberg, J., Wittmann, A., Devens, F., Gerber, N.U., Joos, S., et al. (2009). Outcome prediction in pediatric medulloblastoma based on DNA copy-number aberrations of chromosomes 6q and 17q and the MYC and MYCN loci. *J. Clin. Oncol.* 27, 1627–1636.

- Polkinghorn, W.R., and Tarbell, N.J. (2007). Medulloblastoma: tumorigenesis, current clinical paradigm, and efforts to improve risk stratification. *Nat. Clin. Pract. Oncol.* **4**, 295–304.
- Pomeroy, S.L., Tamayo, P., Gaasenbeek, M., Sturla, L.M., Angelo, M., McLaughlin, M.E., Kim, J.Y., Goumnerova, L.C., Black, P.M., Lau, C., et al. (2002). Prediction of central nervous system embryonal tumour outcome based on gene expression. *Nature* **415**, 436–442.
- Reynolds, B.A., and Weiss, S. (1992). Generation of neurons and astrocytes from isolated cells of the adult mammalian central nervous system. *Science* **255**, 1707–1710.
- Salghetti, S.E., Kim, S.Y., and Tansey, W.P. (1999). Destruction of Myc by ubiquitin-mediated proteolysis: cancer-associated and transforming mutations stabilize Myc. *EMBO J.* **18**, 717–726.
- Salsano, E., Croci, L., Maderna, E., Lupo, L., Pollo, B., Giordana, M.T., Consalez, G.G., and Finocchiaro, G. (2007). Expression of the neurogenic basic helix-loop-helix transcription factor NEUROG1 identifies a subgroup of medulloblastomas not expressing ATOH1. *Neuro-oncol.* **9**, 298–307.
- Schmitt, A., Asan, E., Püschel, B., Jöns, T., and Kugler, P. (1996). Expression of the glutamate transporter GLT1 in neural cells of the rat central nervous system: non-radioactive in situ hybridization and comparative immunocytochemistry. *Neuroscience* **71**, 989–1004.
- Schüller, U., Heine, V.M., Mao, J., Kho, A.T., Dillon, A.K., Han, Y.G., Huillard, E., Sun, T., Ligon, A.H., Qian, Y., et al. (2008). Acquisition of granule neuron precursor identity is a critical determinant of progenitor cell competence to form Shh-induced medulloblastoma. *Cancer Cell* **14**, 123–134.
- Scott, C.E., Wynn, S.L., Sesay, A., Cruz, C., Cheung, M., Gomez Gavero, M.V., Booth, S., Gao, B., Cheah, K.S., Lovell-Badge, R., and Briscoe, J. (2010). SOX9 induces and maintains neural stem cells. *Nat. Neurosci.* **13**, 1181–1189.
- Stanton, B.R., Perkins, A.S., Tessarollo, L., Sassoon, D.A., and Parada, L.F. (1992). Loss of N-myc function results in embryonic lethality and failure of the epithelial component of the embryo to develop. *Genes Dev.* **6** (12A), 2235–2247.
- Stolt, C.C., Lommes, P., Sock, E., Chaboissier, M.C., Schedl, A., and Wegner, M. (2003). The Sox9 transcription factor determines glial fate choice in the developing spinal cord. *Genes Dev.* **17**, 1677–1689.
- Storm, R., Cholewa-Waclaw, J., Reuter, K., Bröhl, D., Sieber, M., Treier, M., Müller, T., and Birchmeier, C. (2009). The bHLH transcription factor Olig3 marks the dorsal neuroepithelium of the hindbrain and is essential for the development of brainstem nuclei. *Development* **136**, 295–305.
- Sutter, R., Shakhova, O., Bhagat, H., Behesti, H., Sutter, C., Penkar, S., Santucci, A., Bernays, R., Heppner, F.L., Schüller, U., et al. (2010). Cerebellar stem cells act as medulloblastoma-initiating cells in a mouse model and a neural stem cell signature characterizes a subset of human medulloblastomas. *Oncogene* **29**, 1845–1856.
- Swartling, F.J., Ferletta, M., Kastemar, M., Weiss, W.A., and Westermarck, B. (2009). Cyclic GMP-dependent protein kinase II inhibits cell proliferation, Sox9 expression and Akt phosphorylation in human glioma cell lines. *Oncogene* **28**, 3121–3131.
- Swartling, F.J., Grimmer, M.R., Hackett, C.S., Northcott, P.A., Fan, Q.W., Goldenberg, D.D., Lau, J., Masic, S., Nguyen, K., Yakovenko, S., et al. (2010). Pleiotropic role for MYCN in medulloblastoma. *Genes Dev.* **24**, 1059–1072.
- Taipale, J., Chen, J.K., Cooper, M.K., Wang, B., Mann, R.K., Milenkovic, L., Scott, M.P., and Beachy, P.A. (2000). Effects of oncogenic mutations in Smoothened and Patched can be reversed by cyclopamine. *Nature* **406**, 1005–1009.
- Taylor, M.D., Northcott, P.A., Korshunov, A., Remke, M., Cho, Y.J., Clifford, S.C., Eberhart, C.G., Parsons, D.W., Rutkowski, S., Gajjar, A., et al. (2011). Molecular subgroups of medulloblastoma: the current consensus. *Acta Neuropathol.* **123**, 465–472.
- Thompson, M.C., Fuller, C., Hogg, T.L., Dalton, J., Finkelstein, D., Lau, C.C., Chintagumpala, M., Adesina, A., Ashley, D.M., Kellie, S.J., et al. (2006). Genomics identifies medulloblastoma subgroups that are enriched for specific genetic alterations. *J. Clin. Oncol.* **24**, 1924–1931.
- Tusher, V.G., Tibshirani, R., and Chu, G. (2001). Significance analysis of microarrays applied to the ionizing radiation response. *Proc. Natl. Acad. Sci. USA* **98**, 5116–5121.
- Vidal, V.P., Chaboissier, M.C., Lützkendorf, S., Cotsarelis, G., Mill, P., Hui, C.C., Ortonne, N., Ortonne, J.P., and Schedl, A. (2005). Sox9 is essential for outer root sheath differentiation and the formation of the hair stem cell compartment. *Curr. Biol.* **15**, 1340–1351.
- Yang, Z.J., Ellis, T., Markant, S.L., Read, T.A., Kessler, J.D., Bourboulas, M., Schüller, U., Machold, R., Fishell, G., Rowitch, D.H., et al. (2008). Medulloblastoma can be initiated by deletion of Patched in lineage-restricted progenitors or stem cells. *Cancer Cell* **14**, 135–145.

Allele-Specific p53 Mutant Reactivation

Xin Yu,^{1,4,6} Alexei Vazquez,^{1,2,3,6} Arnold J. Levine,^{1,2,5} and Darren R. Carpizo^{1,4,*}

¹The Cancer Institute of New Jersey, New Brunswick, NJ 08903, USA

²Institute for Advanced Study, Princeton, NJ 08540, USA

³Department of Radiation Oncology and Center for Systems Biology

⁴Division of Surgical Oncology, Department of Surgery

⁵Department of Pediatrics

University of Medicine and Dentistry of New Jersey, New Brunswick, NJ 08903, USA

⁶These authors contributed equally to this work

*Correspondence: carpizdr@umdnj.edu

DOI 10.1016/j.ccr.2012.03.042

SUMMARY

Rescuing the function of mutant p53 protein is an attractive cancer therapeutic strategy. Using the National Cancer Institute's anticancer drug screen data, we identified two compounds from the thiosemicarbazone family that manifest increased growth inhibitory activity in mutant p53 cells, particularly for the p53^{R175} mutant. Mechanistic studies reveal that NSC319726 restores WT structure and function to the p53^{R175} mutant. This compound kills p53^{R172H} knockin mice with extensive apoptosis and inhibits xenograft tumor growth in a 175-allele-specific mutant p53-dependent manner. This activity depends upon the zinc ion chelating properties of the compound as well as redox changes. These data identify NSC319726 as a p53^{R175} mutant reactivator and as a lead compound for p53-targeted drug development.

INTRODUCTION

TP53 is the most frequently mutated gene in human cancer with mutation frequencies ranging from 38%–50% in some reports to as high as 75% and 96% in pancreatic adenocarcinoma and high-grade serous ovarian carcinomas, respectively (Hingorani et al., 2005; Cancer Genome Atlas Research Network, 2011; Petitjean et al., 2007). The majority of mutations are mis-sense mutations that occur most frequently in six “hotspot” codons within the DNA binding domain (Olivier et al., 2010). These mutant proteins are classified as either DNA contact mutants (e.g., p53^{R273H}) when the mutation occurs in a DNA binding residue or conformational mutants (e.g., p53^{R175H}) when a conformational change causes a loss of WT p53 DNA binding.

Mutant p53 proteins are found at high concentrations in tumor cells relative to WT p53, mostly because of a loss of WT p53 transcription of the *MDM2* gene that negatively regulates p53, as well as other tumor-specific alterations, such as loss of *p16^{INK4a}* (Haupt et al., 1997; Midgley and Lane, 1997; Terzian et al., 2008). The concept that these mutant proteins are functional

and regulate important processes relevant to tumor biology is referred to as the mutant p53 gain-of-function (GOF) phenotype (Sigal and Rotter, 2000). Properties attributed to mutant p53 GOF include enhanced tumorigenesis, invasion, and metastasis (Adorno et al., 2009; Dittmer et al., 1993; Liu et al., 2000; Muller et al., 2009). Taken together, these properties make mutant p53 an attractive target for drug development.

The National Cancer Institute's (NCI) anticancer drug screen has reported growth inhibition half maximal inhibitory concentration (IC₅₀) on 48,129 compounds tested on a panel of sixty human tumor cell lines (NCI60 screen). Given that the p53 status (WT, null, or mutant) of these cell lines is known (Ikediobi et al., 2006; Shoemaker, 2006), we hypothesized that this screen could be used to uncover drugs targeting p53 mutant tumors. Thus, we developed a methodology to identify compounds with increased activity in a panel of tumor cell lines with p53 mutations, relative to p53 WT controls. In this study, we attempted to validate this methodology using two compounds that belong to the thiosemicarbazone family of metal ion chelators. We further investigated one of the compounds with particular toxicity to cell lines

Significance

The next generation of anticancer drugs will be defined by compounds that selectively kill cancer cells while leaving normal cells undisturbed. We developed an in silico screening methodology that identified such a compound that selectively kills cancer cells with a p53^{R175} mutation. The mechanism of action restores WT structure and function to the p53^{R175} protein using its zinc-chelating and redox properties. This unique mechanism may allow medicinal chemistry to design other compounds that renature other p53 mutants that fail to coordinate zinc. *TP53* is the most commonly mutated gene in human cancer, and the p53^{R175} mutant is the third most frequently found mis-sense mutant. The potential pool of patients in the United States for this drug would approximate 32,000 annually.

containing a p53^{R175} mis-sense mutation, identifying the mechanism of this toxicity and the properties of the compound that are relevant to this mechanism.

RESULTS

Identification of Thiosemicarbazones with Activity in Cell Lines Expressing Mutant p53

Our methodology deals with the intrinsic heterogeneities of the NCI60 screen (Figure 1A; Supplemental Experimental Procedures available online). This takes as input IC₅₀ data, applies data normalization to obtain a working definition of a good response, and then ranks compounds manifesting a good response using a scoring function. This score function identifies those compounds with an enrichment of good responders in the case group (mutant p53), while simultaneously having a depletion of good responders in the control group (wild-type p53). To reduce the heterogeneity in the mutant p53 group, we focused on mutations in hotspot codons 175, 248, and 273 (11 cell lines), whereas the control group was composed of sixteen p53 wild-type cell lines. Applying this methodology, we observed that three of the highest scoring compounds belonged to the thiosemicarbazone family (NSC319725, NSC319726, and NSC328784), which preferentially inhibited p53 mutant cell lines (Figure 1B). When comparing the IC₅₀s of these compounds by p53 mutational status, we see that the low IC₅₀s are enriched of cells with a p53 mutation (Figure 1B, red), whereas the majority of p53 wild-type cells exhibit high IC₅₀s (Figure 1B, blue). In contrast, two reported mutant p53 reactivators (PRIMA-1 and MIRA-1), as well as an additional thiosemicarbazone currently in clinical trials (Triapine), scored poorly using this methodology in comparison to NSC319726 (Figures S1A–S1D).

We validated two of our screened compounds (NSC319725 and NSC319726) using a mouse fibroblast cell line containing no functional *TP53* gene (10(3)), from which several stable human cytomegalovirus-driven mutant p53 transfectants (175, 248, and 273) were derived (Dittmer et al., 1993). Balb/c 3T3 fibroblasts were used as a p53 WT control because this is the same background as the 10(3) and its derived cell lines. Both compounds exhibited growth inhibition at markedly lower concentrations in cells expressing mutant p53 as compared to the WT control, particularly in the 175 allele (Figure 1C). The IC₅₀ for the NSC319725 treated 175 mutant was ≥ 100 -fold lower than the WT. For NSC319726, the effect was even greater as the IC₅₀ for the 175 mutant was 8 nM, whereas the IC₅₀ of the WT was not reached. Similar to the Balb/c 3T3, these two compounds were remarkably nontoxic to WI38 human fibroblasts (p53 WT), as an IC₅₀ for both compounds was not obtained (Figure 1D). Furthermore, NSC319726 did not induce WT p53 protein levels or transcriptional activity as common cytotoxic agents, such as etoposide, do in vitro (Figure S1E).

We further validated NSC319726 by employing additional p53 mutant cell line systems. In a set of isogenic mouse embryonic fibroblast (MEF) cell lines from p53^{+/+}, p53^{-/-}, and p53^{R172H/R172H} mice, we found that NSC319726 exhibited a much higher sensitivity for the MEF-p53^{R172H/R172H} cell line as compared to the p53^{+/+} and p53^{-/-} controls (Figure 1E). We compared the sensitivities across human tumor cell lines with

different p53 “hot spot” mutations (175, 248, and 273). With the exception of one p53^{R175} cell line (RXF393), the 175 cells exhibited similar IC₅₀'s that were approximately 10-fold and in some instances 100-fold lower than the other hotspot mutants, indicating a 175 allele preference of growth inhibition by NSC319726 (Figure 1F). It is important to emphasize that the results of these assays depend to a significant degree on a number of factors, including the method of assaying cell viability, the proliferation rates of the cells, and the confluency at the time of drug exposure, as well as differences in redox in tumor cells. To diminish intra-assay variability, we used the Guava-ViaCount assay to compare the effects of NSC319726 across tumor cell lines that varied by p53 status given the heterogeneity of these cell lines. In both the MTS and Guava-ViaCount assay, we found it to be important to have the cells at 50%–60% confluency at the time of drug exposure. Cell growth inhibition assays carried out under different conditions can and do give different IC₅₀s.

Induction of p53^{R175}-Dependent Apoptosis by NSC319726

To determine if the inhibition of cell growth was mediated by apoptosis, we performed Annexin-V staining of different cell lines treated with NSC319726. We observed an increase in the number of Annexin-V-stained cells with a maximum increase in the 175 mutant (Figure 2A). Similarly, treatment of three different ovarian carcinoma cell lines (TOV112D [p53^{R175H}], OVCAR3 [p53^{R248W}], and SKOV3 [p53^{-/-}]) with NSC319726 resulted in an induction of apoptosis in the p53^{R175} mutant more than 2-fold higher than the other two mutant cell lines (Figure 2B). When we silenced expression of the p53^{R175} mutant protein by siRNA, we observed a marked reduction in sensitivity to cell growth inhibition, demonstrating that the NSC319726 mechanism is at least partially dependent on the p53^{R175} mutant protein (Figure 2C).

NSC319726 Induction of a “WT-like” Conformational Change in the p53^{R175} Mutant Protein

Because NSC319726 induced a p53 apoptotic function in p53^{R175} cells, we investigated if NSC319726 restored WT conformation to the mutant p53^{R175} protein. Using conformation-specific antibodies by immunofluorescence, we observed that NSC319726 induced a conformation change in the p53^{R175} mutant to a structure that was recognized by the WT-specific antibody (PAB1620) and was no longer recognized by the mutant-specific antibody (PAB240; Figure 3A). Quantification of the fluorescence intensity for PAB240 was reduced by 5-fold, whereas that of PAB1620 was increased by 2-fold (Figure 3B). We confirmed this conformation change by PAB240 immunoprecipitation of NSC319726-treated TOV112D lysates, indicating a more than 85% decrease in PAB240 immunoreactivity (Figure 3C). Next, we sought to confirm this conformation change in an additional cell line. NSC319726 treatment of a MEF cell line derived from p53^{R172H/R172H} mice resulted in a loss of PAB240 immunofluorescence staining (Figure 3D). The PAB1620 antibody staining is not shown because this antibody is human-specific. This demonstrates that the conformation change induced by NSC319726 occurs in both human (p53^{R175}) and mouse (p53^{R172}) proteins.

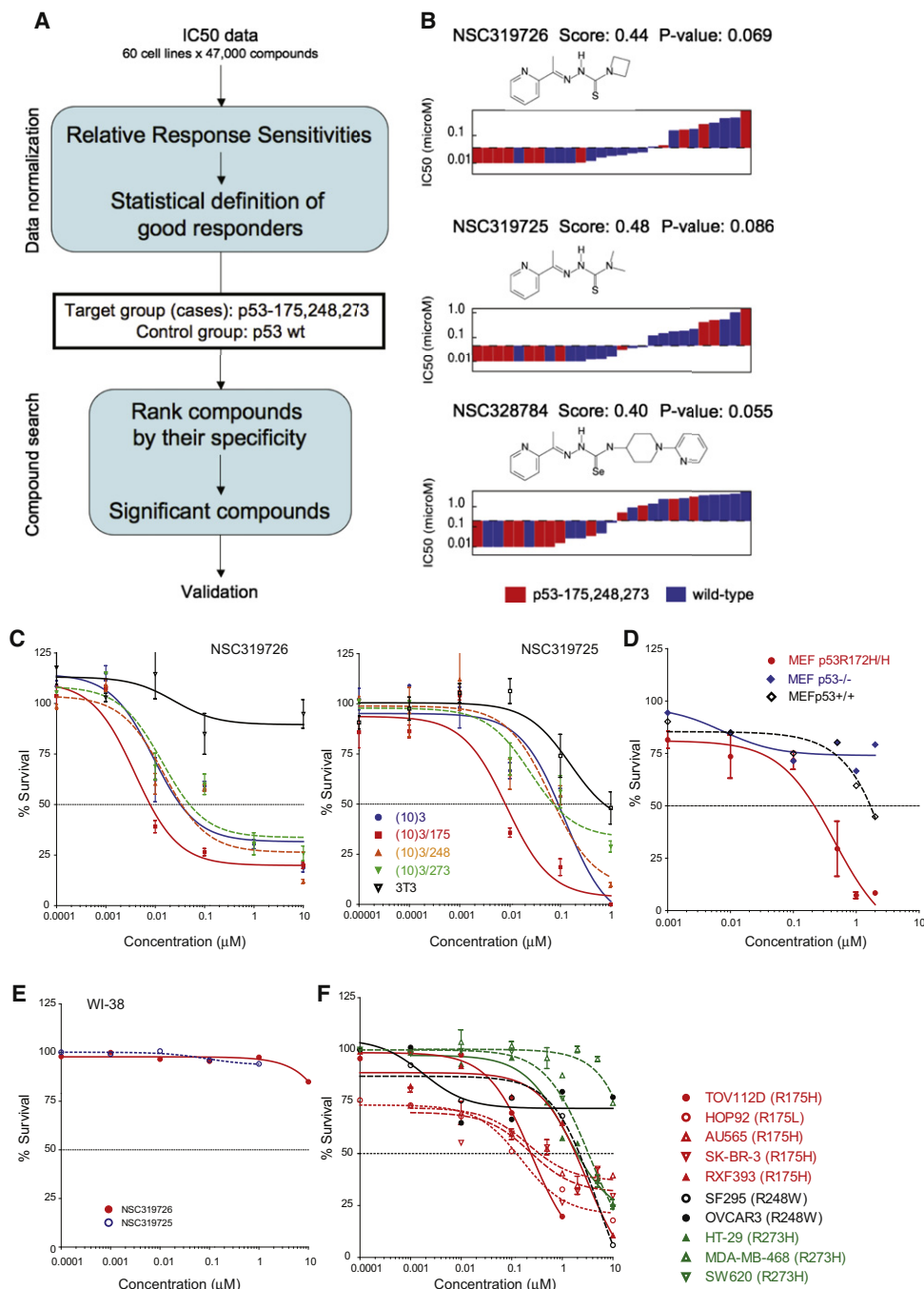


Figure 1. Identification of Thiosemicarbazones with Activity in Cell Lines Expressing Mutant p53

(A) Flow diagram of the in silico screen methodology.

(B) IC₅₀ distribution and chemical structure of the thiosemicarbazones aligning lower IC₅₀s to higher IC₅₀s in cells with mutant p53 (red) and WT p53 (blue), analyzed with the NCI60 data set. In the NCI60 data set, the human tumor cell lines are treated with five serial dilutions of each compound for 48 hr at 37°C.

(C) Validation of the sensitivity of the compounds in the cell lines expressing mutant p53. Cell growth inhibition assays using a mouse embryonic fibroblast (MEF) cell line system consisting of (10)3 (p53^{-/-}), (10)3/175, (10)3/248, (10)3/273, and 3T3 (p53^{+/+}). (Left panel) Growth inhibition with NSC319726. (Right panel) Growth inhibition with NSC319725.

(D) Sensitivity to NSC319726 in a set of isogenic MEF cell lines from p53^{+/+}, p53^{-/-}, and p53^{R172H/R172H} mice.

(E) NSC319725 and NSC319726 do not inhibit cell growth of WI38 (p53^{+/+}) human fibroblasts.

(F) The sensitivity of NSC319726 in human tumor cell lines with hotspot p53 mutations. Cell growth inhibition was analyzed by MTS assay (C) or by Guava ViaCount assay (D–F). In both the MTS and Guava ViaCount assays, cells were treated with five to seven serial dilutions of the compounds (0.00001 to 10 μM) for 3 days. The error bars are ± SD.

See also Figure S1.

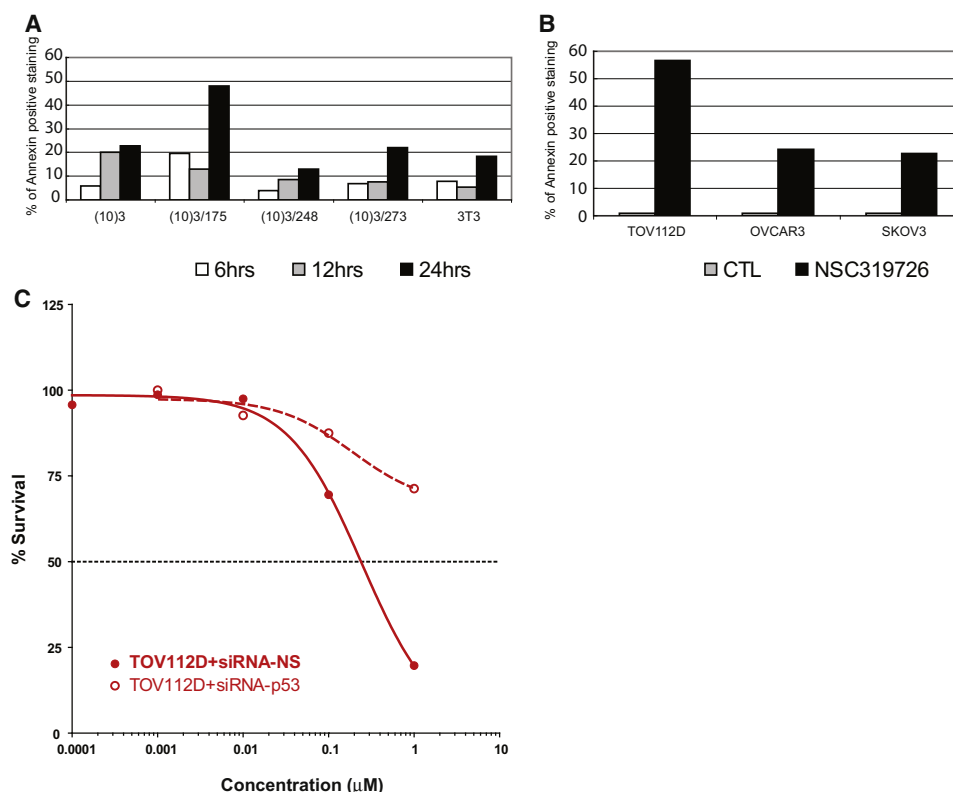


Figure 2. The p53-175-Mutant-Dependent Apoptosis Induced by NSC319726

The apoptosis is measured with Annexin-V staining using Guava Nexin reagent and Guava PCA instrument.

(A) Apoptosis is measured in the (10)3-derived MEF cells.

(B) Apoptosis is measured in a panel of ovarian cancer cell lines, TOV112D (p53^{R175H}), OVCAR3 (p53^{R248W}), and SKOV3 (p53^{-/-}). The treatment is 1 μM NSC319726 (as in the other figures, unless described differently) for 24 hr.

(C) Growth inhibition by NSC319726 in TOV112D cells with siRNA knockdown of p53^{R175H} mutant protein, measured as in Figure 1E.

Restoration of p53 Transactivational Function through the “WT-like” Conformational Change Induced by NSC319726

To determine if the conformation change observed with the p53^{R175} mutant resulted in restoration of p53 transcriptional function, we examined p21 protein levels after NSC319726 treatment in TOV112D and SKOV3 cells. We found that NSC319726 induced p21 in the TOV112D cell line but not in the SKOV3 (Figure 4A). Treatment of the TOV112D cells with the DNA damaging agent etoposide failed to induce p21 (Figure 4A). This suggests that the p21 induction in NSC319726-treated TOV112D cells was p53^{R175}-mutant-dependent.

We note NSC319726 caused a reduction in the levels of the mutant protein (Figure 4A). We examined this further by measuring the mutant protein levels at different time points over a 24 hr period. Treatment of TOV112D cells with NSC319726 decreased the stabilization of the mutant protein with the lowest levels seen at 6 hr with a return to pretreatment levels by 24 hr. This p53 mutant protein destabilization was not seen when we treated two cell lines containing the p53 DNA contact mutants R248 (OVCAR3) and R273 (SW620) with NSC319726. This indicates allele specificity to the NSC319726-mediated effect on p53 mutant protein levels. We hypothesized that the decrease in p53^{R175} protein stability was due to restora-

tion of Mdm2 negative regulation of the “WT-like” p53^{R175} mutant. To test this, we performed this experiment in the presence of Nutlin-3 (small-molecule antagonist of Mdm2) and found that Nutlin-3 abrogated the decrease in stability of the p53-175 mutant induced by NSC319726 (Figure 4B). This restoration of Mdm2-negative regulation is the result of transactivation of the *MDM2* promoter by the “WT”-like p53^{R175} mutant (Figures 4C and 4D).

We confirmed the ability of NSC319726 to restore DNA binding properties to the p53^{R175} mutant protein by chromatin immunoprecipitation (ChIP). Using the p53 antibody, DO-1, ChIP analysis of NSC319726-treated TOV112D cells revealed the restoration of site-specific DNA binding of p53^{R175} mutant to the promoters of *p21*, *PUMA*, and *MDM2* (Figure 4C). HCT116 cells treated with etoposide, as well as RNA polymerase II binding of the *GAPDH* promoter, were used as controls (Figure 4C). We compared the mRNA levels of several p53 targets (*p21*, *PUMA*, and *MDM2*) in the TOV112D (p53^{R175H}), OVCAR3 (p53^{R248W}), and SKOV3 (p53^{-/-}) cells upon treatment and found that NSC319726 increased the levels of all three p53 target genes in TOV112D cells, particularly the apoptotic gene *PUMA* (Figure 4D). To provide further evidence that NSC319726 restored site-specific p53 transactivational function, we transfected the TOV112D cells with a luciferase reporter plasmid

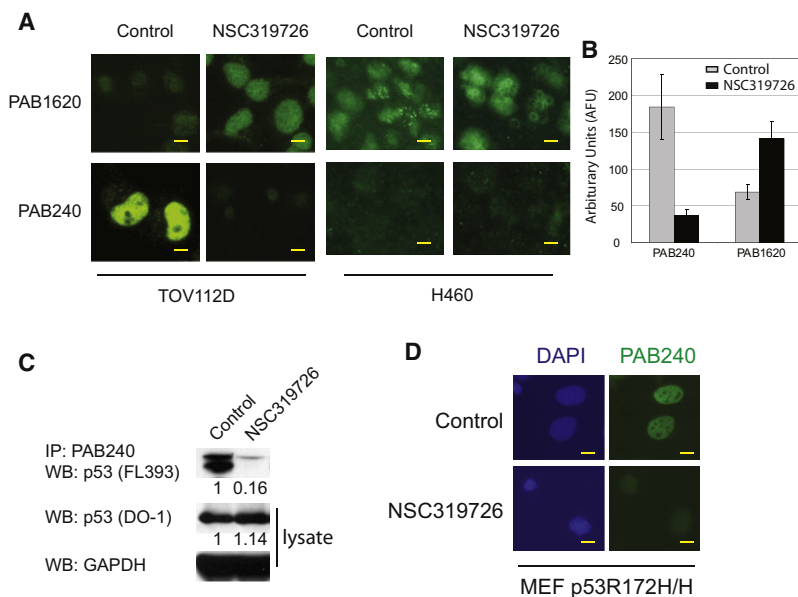


Figure 3. A “WT-like” Conformational Change in the p53-175 Mutant Protein Induced by NSC319726

(A) Immunofluorescence of TOV112D (p53^{R175H}) cells using p53-conformation-specific antibodies (PAB1620 for WT conformation and PAB240 for mutant conformation). The H460 cell line is used as a control to show that the WT p53 conformation is not changed by NSC319726. All scale bars represent a size of 25 μ m.

(B) Quantification of PAB240 and PAB1620 staining indicates significant differences upon treatment with NSC319726 ($p < 0.0001$, t test). The error bars are \pm SD.

(C) Immunoprecipitation of mutant p53 protein in TOV112D cells using PAB240 and detected by p53 (FL393) by western blot.

(D) Immunofluorescence of MEF p53^{R172H/H} cells using the PAB240-mutant-specific antibody.

In all experiments (A, C, and D), cells are treated with NSC319726 (1 μ M) for 6 hr before harvesting for immunostaining or immunoprecipitation.

containing 20 base pairs of the p53 response element in the *p21* promoter. NSC319726 treatment induced a 2.5-fold increase in luciferase activity that was not seen in MEF cells expressing the 248 and 273 alleles, indicating that the restoration of transcriptional function is allele-specific (Figure 4E). We next utilized gene expression microarrays to examine the transcriptional activity of a larger cohort of p53 targets in TOV112D cells. NSC319726 treatment produced a p53 target expression signature remarkably different from the untreated controls, confirming that the conformation change of the p53^{R175} mutant results in a transcriptionally active protein (Figure 4F). Table S1 reports the average expression log₂-ratios between cells treated with NSC319726 and untreated controls, focusing on probes that map to p53 target genes. The list of p53 targets were selected from a literature review, providing a comprehensive list of experimentally verified targets of p53 (Riley et al., 2008).

In Vivo Allele-Specific p53^{R175H} Mutant Reactivation by NSC319726

To investigate the p53 mutant's reactivation in vivo, we performed toxicity assays in p53^{+/+}, p53^{-/-}, and p53^{R172H} knockin mice (Lang et al., 2004). Mice were housed and treated according to guidelines and all the mouse experiments are done with the approval of the Institutional Animal Care and Use Committee (IACUC) of UMDNJ-Robert Wood Johnson Medical School. We hypothesized that p53^{R172H} mice would experience greater toxicity for a given dose of NSC319726 as compared to p53^{+/+} mice. By day 3 of treatment (10 mg/kg/day), all seven of the p53^{R172H/R172H} mice had died, whereas only one of nine p53^{+/+} mice had died. By day 4, the survival of the p53^{+/+} mice was 70%, whereas the survival of p53^{+/R172H} was 30%, suggesting a clear dosage effect that is dependent on the *TP53*^{R175} genotype (Figure 5A). Next, we lowered the dose to 5 mg/kg and found that by day 7, the p53^{+/+} and p53^{-/-} mice exhibited a 100% survival compared to only 30% of the p53^{R172H/R172H} mice (Figure 5A).

We examined the tissues of p53^{+/+} and p53^{R172H/R172H} mice after treatment for evidence of apoptosis as well as gene expression of a panel of p53 targets. We detected abundantly more apoptotic cells in the sections of the spleen and thymus of p53^{R172H/R172H} mice as compared with the p53^{+/+} controls (Figure 5B). We also detected elevated mRNA levels of a number of p53 targets in a tissue specific fashion in the p53^{R172H/R172H} mice as compared with the p53^{+/+} controls, most notably in the lung, spleen, thymus, and small intestine (Figure 5C).

We tested the ability of NSC319726 to inhibit the growth of xenograft mouse tumors derived from human tumor cell lines carrying different p53 alleles. At a dose of 1 mg/kg, tumor growth of the H460 (p53^{+/+}) and MDAMB468 (p53^{R273W}) xenografts was not inhibited relative to the vehicle control, whereas tumor growth was significantly inhibited in the TOV112D (p53^{R175H}) xenografts (Figure 5D). When we lowered the dose 10-fold to 0.1 mg/kg in the TOV112D mice, we observed only a small difference in tumor growth inhibition, demonstrating both a dosage effect of the drug and a larger therapeutic window. Taken together, these findings provide in vivo evidence for allele-specific p53 mutant reactivation.

Zinc Ion Chelation and Redox Changes Are Important for the NSC319726-Mediated p53^{R175} Reactivation Mechanism

Thiosemicarbazones are metal ion chelators with a strong affinity for iron, copper, and zinc (Yu et al., 2009). They have been investigated as anticancer agents and have been shown to inhibit DNA synthesis by inhibiting the iron-dependent enzyme ribonucleotide reductase (RR) but at much higher concentrations than are employed to inhibit the growth of p53^{R175} mutant cells. To determine if the metal ion chelating property of NSC319726 is important to its p53^{R175} mutant activity we added NSC319726 to TOV112D cells in the presence of various concentrations of FeSO₄. We found that FeSO₄ at concentrations above 15 μ M completely abrogated the activity

of NSC319726. At concentrations below 15 μM , the activity of NSC319726 was inhibited in a dose-dependent manner (Figure 6A).

We suspected iron was not the relevant metal ion, because iron is not associated with the p53 protein, and the treatment of the TOV112D cells with another iron chelator, desferrioxamine (DFO), had no apoptotic effect (Figure S2A). However, zinc is required for proper folding of WT p53, and the 175 mutant is classified as a non-zinc-binding mutant because it fails to coordinate zinc (Butler and Loh, 2003; Joerger and Fersht, 2007). When we added NSC319726 to TOV112D cells in the presence of different concentrations of ZnCl_2 , we found that there was an optimal zinc concentration range (5–15 μM) in which the activity of NSC319726 increased 2-fold (Figure 6B). We did not test higher concentrations over 100 μM of ZnCl_2 in combination with NSC319726 because we found that concentrations above 100 μM of ZnCl_2 (by itself) were toxic to cells. This toxicity was independent of p53 status (Figures S2B and S2C).

Another property of thiosemicarbazones is their effect on the redox state of the cell. Thiosemicarbazone:Fe complexes cause oxidative stress by the creation of hydroxyl radicals through Fenton chemistry (Kalinowski and Richardson, 2007; Richardson et al., 2006, 2009). This is relevant to the mechanism of NSC319726 as redox changes have been reported to influence WT p53 folding (Hainaut and Milner, 1993a). In support of this, we observed a statistically significant decrease in the levels of the cellular reductant glutathione upon NSC319726 treatment of TOV112D cells at 1, 3, and 24 hr (Figure 6C). To determine the importance of these redox changes to the activity of NSC319726 we treated TOV112D cells in the presence of the reducing agent N-acteyl-cysteine (NAC) and the oxidizing agent diamide. We found that 5 mM NAC inhibited the apoptotic activity of NSC319726, whereas diamide (100 μM) enhanced it (Figure 6D). These data suggest that ROS changes are important for the apoptotic mechanism of NSC319726 on p53^{R175} mutant cells.

DISCUSSION

The reactivation of p53 in mouse tumor models has been shown to be a highly effective therapeutic strategy (Martins et al., 2006; Ventura et al., 2007; Xue et al., 2007). Several small molecules have been claimed to reactivate mutant p53, including CP-31398, WR-1065, PRIMA-1, and MIRA-1 (Bykov et al., 2002, 2005; Foster et al., 1999; North et al., 2002). With the exception of one compound, WR1065, all have been identified using traditional chemical screens (Bykov et al., 2002, 2005). Traditional chemical screens favor the use of matched case/control cell lines derived from the same parental cell line, engineered such that the case cell line carries the molecular alteration under consideration. This can be a fundamental caveat, because cancers are known to be heterogeneous in nature. Here, we demonstrate our methodology to screen for compounds manifesting increased sensitivity in a panel of cell lines carrying p53 mutations independently of their diverse genetic backgrounds and cell type specificity, which is a more realistic model of what is observed in the clinic. Applying this methodology to the NCI60 screen we identified three compounds from the thiosemicarbazone family. Follow up experiments with two of these

compounds (NSC319725 and NSC319726) corroborated the predicted p53-mutant-specific growth inhibitory properties. It is possible that this methodology could be used to identify compounds with increased sensitivity in tumor cell lines carrying mutations in other major oncogene/tumor suppressor pathways.

It is important to note that cell viability assays in Figure 1C and the apoptosis assays in Figure 2A indicate that there is an apoptotic mechanism that is independent of p53 mutational status (null, mis-sense mutant). What initiates this apoptosis is unclear but may be related to either an increase in ROS levels or ribonucleotide reductase (RR) inhibition, two reported mechanisms of action for thiosemicarbazones. Nontumor cell lines with a WT p53 gene (Balb/c 3T3, WI38) showed relatively little to no growth inhibition by NSC319726 at these same doses, which would argue against the inhibition of RR as the explanation. If increased ROS levels are the reason, we speculate that this apoptosis may be due to the inability to compensate for these oxidative changes in a cell lacking a functional p53 transcription factor.

In distinction, the mechanism of apoptosis in a p53^{R175} mutant cell is dependent on the mutant p53^{R175} mutant protein. NSC319726 treatment induces a WT-like conformational change in the p53^{R175} mutant protein that restores sequence-specific p53 transcription. This is best observed in the *in vivo* experiments employing both knockin p53 mutant mice and xenografts.

We have demonstrated that the metal ion chelating properties of NSC319726 are required for the mutant-p53-mediated apoptotic activity. Interestingly, metal ion chelation has been shown to induce p53 conformational changes (Hainaut and Milner, 1993b; Yu et al., 2009). The fact that the 175 mutant fails to bind zinc and that zinc chloride at low concentrations (5–15 μM) enhances the activity leads us to hypothesize that NSC319726 may serve as a source of zinc to allow the 175 mutant to refold. Such a metallochaperone function was demonstrated for another zinc chelator, Nitriloacetate, which facilitated refolding of the p53 WT DNA binding domain (that was previously unfolded by removing the zinc; Butler and Loh, 2007). Further biophysical studies are needed to confirm this.

Structural studies of the p53 DNA binding domain indicate that the zinc ion is coordinated by four amino acids (C176, H179, C238, and C242; Cho et al., 1994; Joerger et al., 2005; Wong et al., 1999). Mutations in any of these residues result in the inability to coordinate zinc. In contrast, the R175H mutant is not directly involved in zinc binding. It is generally believed that a histidine residue at this location induces structural distortions in the protein that prevent it from binding zinc (Joerger and Fersht, 2007). If the metallochaperone hypothesis is correct then it is plausible that NSC319726 may reactivate other zinc binding mutants.

The question of what activates mutant p53 to become a better transcription factor and induce an apoptotic mechanism after a WT conformational change is an important one. Most likely this is due to the elevated oxidative state in the mutant p53 cell. This oxidative state is the result of the combination of NSC319726 treatment and elevated ROS levels in p53 mutant cells (due to loss of p53-mediated regulation of the redox state; Sablina et al., 2005). In support of this is the observation that an oxidizing agent, diamide, enhances the apoptotic activity of NSC319726, whereas NAC inhibits it.

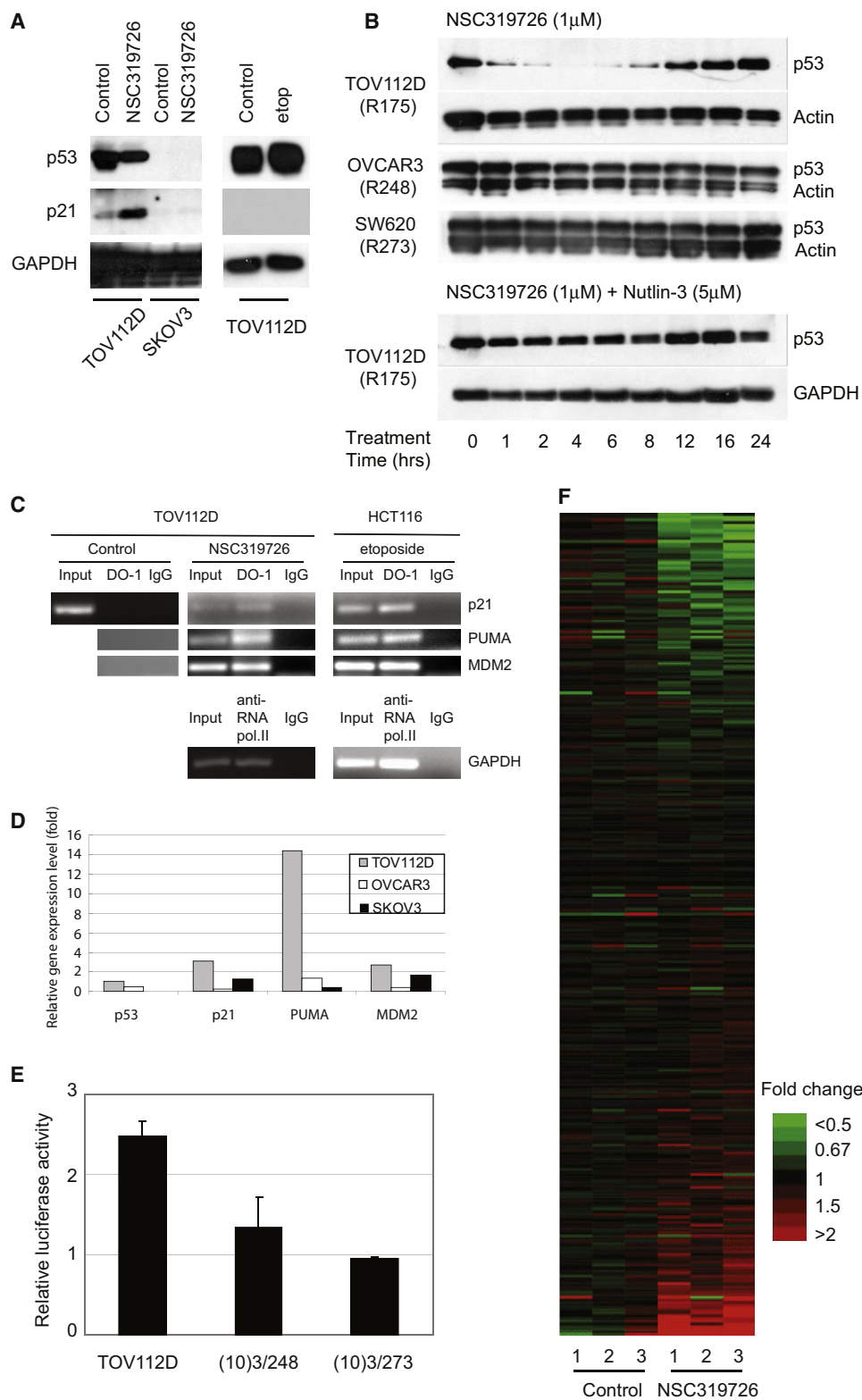


Figure 4. Restoration of Site-Specific p53-175 Mutant Protein Transactivational Function by NSC319726

(A) TOV112D and SKOV3 cells are treated with NSC319726 or etoposide and protein extracts are analyzed by western blot with antibodies directed against p21, p53. GAPDH is used as the internal (loading) control.
(B) Stability of p53 mutant protein in TOV112D (p53^{R175}), OVCAR3 (p53^{R248}), and SW620 (p53^{R273}) cells treated with NSC319726 (1 μ M) with/without Nutlin-3 (5 μ M) over a 24 hr time course. Protein levels are shown by western blot using antibodies to p53 (DO-1) or either actin or GAPDH.

Whereas inhibition of RR activity is a known mechanism of action of thiosemicarbazones, we feel this is unlikely involved in the p53^{R175} reactivation mechanism because (1) the drug is completely nontoxic to human fibroblasts at the IC₉₀ for p53^{R175} mutant cells and (2) the dose that inhibited p53^{R175} mutant xenograft tumor growth was completely nontoxic to mice. However, the doses we used in our mouse toxicity experiments were considerably higher, and RR inhibition may explain some of the toxicity observed in WT mice.

NSC319726 is an attractive lead compound for drug development for three reasons:

- (1) In vivo p53^{R175} mutant reactivation can be observed at doses that are nontoxic to WT animals;
- (2) The compound exhibits a wide therapeutic window when given intravenously; and
- (3) The target (p53 mutant protein) is found at high levels in cells.

The pool of potential patients for such a drug would be fairly large given the fact that the 175 mutant is the third most commonly found p53 mis-sense mutant, making up an estimated 5.5% of all mis-sense mutants (Olivier et al., 2010). Using the IARC TP53 database (<http://www-p53.iarc.fr/>), we estimate the annual incidence in the United States of cancer patients carrying the TP53^{R175} allele to be more than 32,000. Our findings support the growing trend in developmental therapeutics in which the efficacy of future cancer drugs will depend upon the knowledge of the patient's tumor genotype.

EXPERIMENTAL PROCEDURES

Cell Lines and Culture Conditions

The mouse embryonic fibroblasts (MEFs) (10)3 and its derived cell lines with various human p53 mutations (R175, R248, and R273) were previously derived (Dittmer et al., 1993). 3T3 is derived from Balb/c and has p53^{+/+} alleles. MEF p53^{R172H/R172H}, MEF p53^{+/+} and MEF p53^{-/-} cells are derived from C57BL/6 mice. All MEF cells are cultured in Dulbecco's modified Eagle's medium (DMEM) with 10% FBS. TOV112D and WI38 are cultured in DMEM with 10% FBS. SKOV3 is cultured in McCoy's 5A with 5% FBS. H460 and MCF7 are cultured in RPMI with 10% FBS. HCT116 is cultured in McCoy's 5A with 10% FBS. OVCAR3 is cultured in RPMI1640 with 20% FBS.

MTS Assay and Viability Assay

MTS assay is done in accordance with the manufacturer's instructions (Promega, Madison, WI, USA). In brief, 5,000 cells of TOV112D cells (5,000 cells/well, in 100 μ l culture) are cultured in 96-well plate to reach the 50%–60% confluence on the second day when treated with serial dilutions of the

compounds. The growth is measured by MTS reagent and Victor Plate reader instrument (PerkinElmer, Waltham, MA, USA) after incubation for 3 days. Viability assays are done in accordance with the manufacturer's instructions for Guava ViaCount (Millipore, Billerica, MA, USA). In brief, the cells (5×10^4 cells/well, in 1 ml culture) are cultured in a 12-well plate to reach the 50%–60% confluence on the second day when treated with serial dilutions of the compound. The growth is measured by Guava ViaCount reagent and Guava PCA instrument after incubation for 3 days.

Apoptosis Assay Using Annexin Staining

The Annexin staining is done in accordance with the manufacturer's instructions (Millipore). In brief, the cells are cultured in 12-well plate, followed by treatment with the compound for different time periods. The cells are stained with the Nexin staining reagent and Annexin-positive cells are detected with the Guava PCA instrument.

Transfection of p53 siRNA

The siRNA transfection is done with Lipofectamine 2000 (Invitrogen, Carlsbad, CA, USA), following the manufacturer's instructions. The p53 siRNA is from SMARTpool (Thermo Scientific/Dharmacon, Lafayette, CO, USA).

Immunofluorescent Staining

The cells are grown on the coverslip, followed by various treatments. The coverslips are fixed with 4% paraformaldehyde for 10 min and then permeabilized with 0.5% Triton X-100 for 5 min. The conformation of the mutant and WT p53 proteins can be recognized specifically by the antibodies PAB1620 (1:50, recognizing WT conformation) and PAB240 (1:200, recognizing mutant conformation) stained overnight, respectively. The secondary antibody, goat anti-mouse IgG is incubated for 40 min. PAB1620 and PAB240 are from EMD Chemicals (Gibbstown, NJ, USA). Fluorescent staining intensity was quantified using Adobe Photoshop.

Immunoprecipitation

The cell lysates (500 μ g) with various treatments are subjected to immunoprecipitation with ExctaCruz matrix (Santa Cruz Biotechnology, Santa Cruz, CA, USA) using the antibody PAB240 (4 μ g). The pull-down is detected by western blot with p53 (FL393; Santa Cruz Biotechnology), which recognizes all formats of the p53 protein. The density of the image relative to the control is determined using Adobe Photoshop.

Immunohistochemistry Staining

The mouse tissues are harvested and are subjected to immunohistochemistry (IHC) staining with cleaved caspase-3 (CC3, 1:100; Cell Signaling, Danvers, MA, USA).

Western Blot

The lysates (or immunoprecipitated products) are run on SDS-PAGE and transferred onto polyvinylidene fluoride membranes. The detection of the protein level is done with the manufacturer's instructions (ECL, GE Healthcare, Waukesha, WI, USA). The p21 antibody is from EMD Chemicals. The GAPDH, p53 (DO-1) and actin antibodies are from Santa Cruz Biotechnology. The density is determined using Adobe Photoshop and is expressed as the ratio to the loading control (GAPDH) relative to the control.

(C) Chromatin immunoprecipitation (ChIP) assay. Lysates from TOV112D cells treated with NSC319726 (1 μ M) and HCT116 cells treated with etoposide (20 μ M) for 6 hr are subject to immunoprecipitation using anti-p53 antibody (DO-1) followed by PCR of p53 recognition elements (p53REs) of *p21*, *PUMA*, and *MDM2*. HCT116 treated with etoposide is used as a positive control for functional p53 DNA-binding property. ChIP with anti-RNA polymerase II antibody and PCR for *GAPDH* is also used as a positive control.

(D) qRT-PCR of *p21*, *MDM2*, and *PUMA* in TOV112D, OVCAR3, and SKOV3 cells with treatment of NSC319726 (1 μ M) for 24 hr. The RNA is extracted from the cells using a Qiagen RNeasy kit, and the gene expression level is measured by quantitative RT-PCR using TaqMan gene expression assays.

(E) TOV112D cells are transfected with a plasmid bearing the 20 bp p53 response element (p53RE) in *p21* promoter region and then treated with NSC319726 (1 μ M) for 24 hr, followed by luciferase reporter assay. The error bars are \pm SD.

(F) Microarray analysis of NSC319726 (1 μ M, 24 hr) treated and control TOV112D cells comparing gene expression levels of p53 targets. The list of the genes is presented in Table S1. The heatmap is shown with the color scale indicating fold change. The data from the microarrays have been deposited in the GEO database with accession number GSE35972.

See also Table S1.

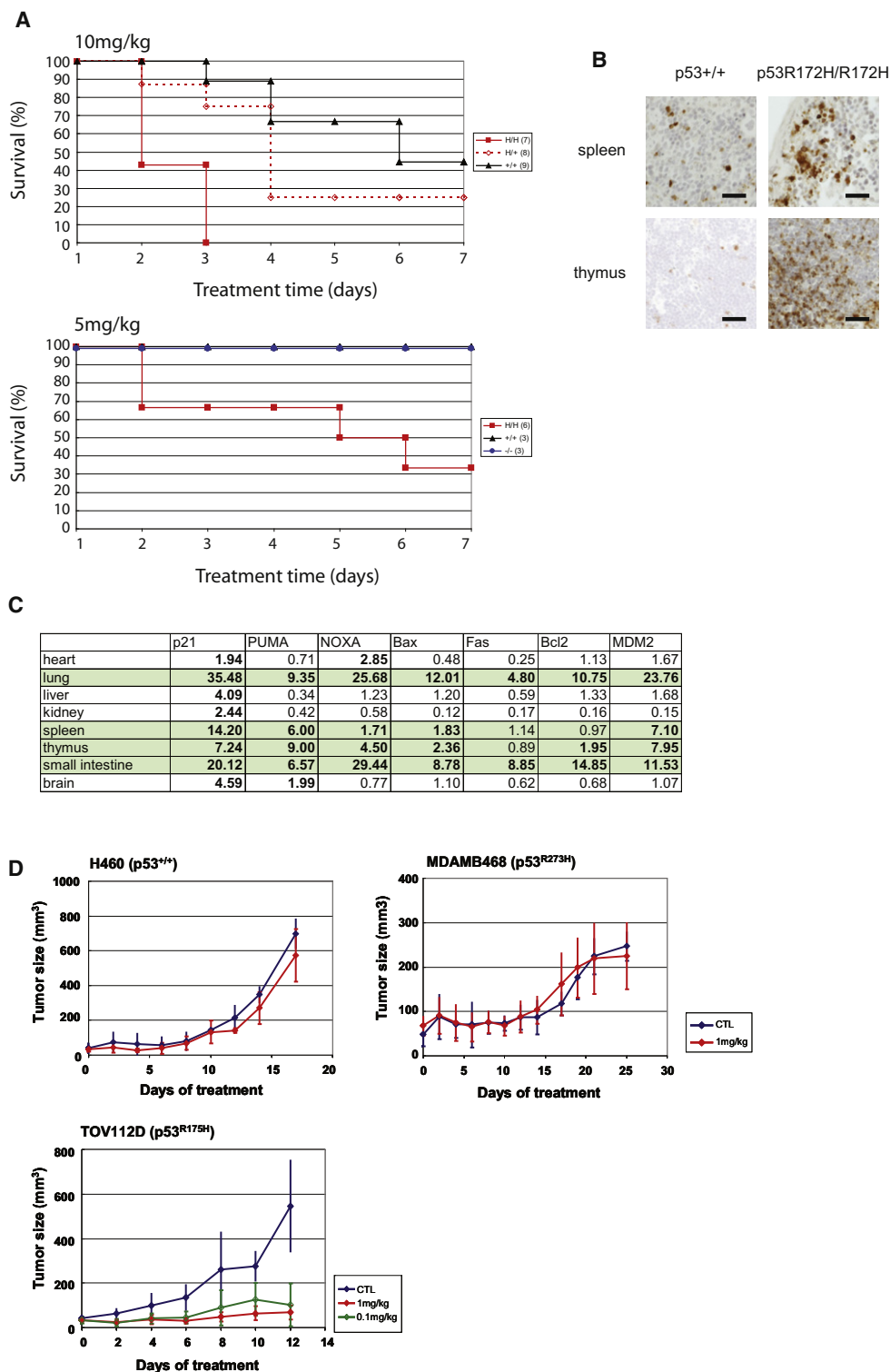


Figure 5. In Vivo Evidence of NSC319726-Mediated p53-175 Mutant Reactivation

(A) Toxicity assays of NSC319726 in p53^{R172H/R172H}, p53^{+/+}, and p53^{-/-} mice. Mice in the top panel are administered 10 mg/kg by daily intraperitoneal (i.p.) injection for up to 7 days. Mice in the bottom panel are administered 5 mg/kg daily (i.p.) for up to 7 days.

(B) Immunohistochemical staining with cleaved caspase-3 antibody of spleen and thymic tissues in p53^{+/+} and p53^{R172H/R172H} mice. All scale bars represent a size of 100 μ m.

(C) qRT-PCR of mRNA levels of several p53-regulated genes in p53^{+/+} and p53^{R172H/R172H} mouse tissues. The inductions of over 1.7 \times are highlighted in bold.

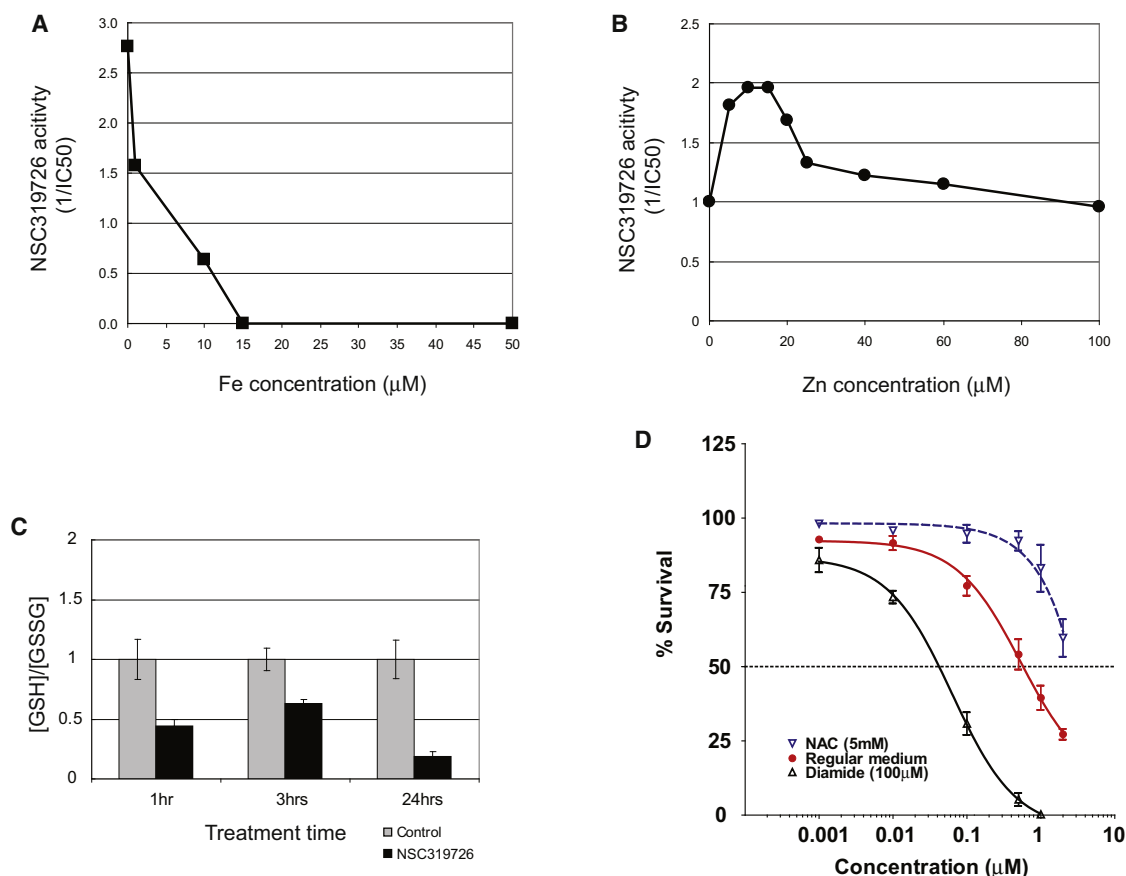


Figure 6. Zinc Ion Chelation and Redox Changes Are Important for the NSC319726-Mediated p53-175 Mutant Reactivation

(A) TOV112D cells are treated with NSC319726 with or without the presence of various concentrations of FeSO_4 , followed by measurement of growth inhibition. The NSC319726 activity is shown as $1/\text{IC}_{50}$ for cell growth inhibition.

(B) TOV112D cells are treated with NSC319726 with or without addition of various concentrations of ZnCl_2 , followed by measurement of growth inhibition. The NSC319726 activity is shown as $1/\text{IC}_{50}$ for cell growth inhibition.

(C) Ratio of reductant GSH and oxidative GSSG in the $\text{p53}^{\text{R175H}}$ cells upon NSC319726 (1 μM) treatment is measured at several time points ($p = 0.0057$ at 1 hr, $p = 0.0027$ at 3 hr, and $p = 0.001$ at 24 hr, t test). The error bars are \pm SD.

(D) TOV112D cells are treated with NSC319726 using six serial dilutions (0.001 to 2 μM) with either N-acetyl cysteine (NAC, 5 mM) or diamide (100 μM) for 3 days. The growth inhibition was analyzed by MTS assay as in Figure 1C. The error bars are \pm SD.

See also Figure S2.

Luciferase Reporter Assay

The p53 recognition element (p53RE) in the *p21* promoter region, constructed in pGL3 vector, is from Dr. Prives' laboratory (Columbia University, New York, NY, USA). It is transfected into the cells, followed by the treatment of NSC319726. The cell lysate is made and the luciferase reporter assay is done in accordance with the manufacturer's instructions (Promega).

Chromatin Immunoprecipitation and PCR

ChIP experiments are done using an EpiTect Chip One-Day Kit in accordance with the manufacturer's instructions (Qiagen, Venlo, The Netherlands). The recovered ChIP DNA is subject to PCR using primers flanking the p53 response elements (p53REs) in the *p21*, *PUMA*, and *MDM2* genes. They are *p21*-F: 5'-GTGGCTCTGATTGGCTTTCTG, *p21*-R: 5'-CTGAAACAGGCAGC CCAAGG; *PUMA*-F: 5'-TCCTTGCCCTGGGCTAGGCC, *PUMA*-R: 5'-CGCGG ACAAGTCAGGACTTG; and *MDM2*-F: 5'-GGTTGACTCAGCTTTCTCTTG,

MDM2-R: 5'-GGAAAATGCATGGTTTAAATAGCC. The control primers are used for PCR of *GAPDH* provided by the kit.

RNA Extraction and Quantitative RT-PCR

RNA is extracted from the cells or mouse tissues using a Qiagen RNeasy Kit, and the gene expression level is measured by quantitative RT-PCR using TaqMan gene expression assays (Applied BioSciences, Carlsbad, CA, USA). The gene expression level is normalized with β -actin, and the average is presented with standard deviation from duplicates or triplicates of repeated experiments.

Microarray Assay

GeneChip Human Genome U133 Plus 2.0 array is from Affymetrix (Santa Clara, CA, USA). The RNA is extracted from the cells with or without treatment with NSC319726 and subject to microarray assay. The list of p53 targets were

(D) Efficacy assays of NSC319726. Xenograft tumors are generated using H460, MDAMB468, and TOV112D cells and are allowed to grow to 60 mm^3 prior to daily intravenous administration of NSC319726 at 1 or 0.1 mg/kg (TOV112D only). Tumor measurements are mean \pm SD. The following number of animals were used, H460 (Control-5, Treatment-5), MDAMB468 (Control-9, Treatment-8), TOV112D (Control-7, Treatment 1mg/kg-7, 0.1 mg/kg-7). CTL is control. The error bars are \pm SD.

selected from a literature review, providing a comprehensive list of experimentally verified targets of p53 (Riley et al., 2008).

Measurement of Level of Glutathione

The levels of reduced glutathione (GSH) and oxidized glutathione (GSSG) are measured using the GSH-Glo Glutathione Assay in accordance with the manufacturer's instructions (Promega).

Mouse Experiments

Mice are housed and treated in accordance with guidelines and all the mouse experiments are done with the approval of Institutional Animal Care and Use Committee (IACUC) of the UMDNJ-Robert Wood Johnson Medical School. The mice with p53^{R172H/+} are a gift of Dr. Lozano (MD Anderson Cancer Center, Houston, TX, USA). The nude mice NCR nu/nu were purchased from Taconic. For the toxicity assays, 6- to 10-week-old mice were of the following genotypes, p53^{R172H/R172H} (n = 8), p53^{R172H/+} (n = 8), p53^{+/+} (n = 9), and p53^{-/-} (n = 3). Mice were treated with either NSC319726 at 10 or 5 mg/kg or vehicle control (dimethyl sulfoxide) by intraperitoneal injection daily for up to 7 days, followed by harvesting the mouse tissues. Xenografts tumor assays are derived from the human tumor cell lines, TOV112D, H460, and MDAMB468 (6 × 10⁶ cells/mouse). Tumor dimensions were measured every other day, and their volumes were calculated by length (L) and width (W) by using the formula: volume = L × W² × π/6. Tumors were allowed to grow to 60 mm³ prior to daily intravenous administration of NSC319726 at 1 or 0.1 mg/kg (TOV112D only). The following number of animals were used, H460 (Control-5, Treatment-5), MDAMB468 (Control-9, Treatment-8), and TOV112D (Control-7, Treatment 1 mg/kg-7, 0.1 mg/kg-7). The experiment was repeated two to three times with similar results.

ACCESSION NUMBERS

The data from the microarrays have been deposited in the GEO database with the accession number GSE35972.

SUPPLEMENTAL INFORMATION

Supplemental Information includes two figures, one table, and Supplemental Experimental Procedures and can be found with this article online at doi:10.1016/j.ccr.2012.03.042.

ACKNOWLEDGMENTS

We would like to thank Dr. Guillermina Lozano (MD Anderson Cancer Center, Houston, TX, USA) for the p53^{R172H} mice, Dr. Carol Prives (Columbia University, New York, NY, USA) for the p21RE-luciferase reporter plasmid, and the National Cancer Institute (Developmental Therapeutics Program) for the compounds NSC319725 and NSC319726. This work was supported by grants from the Cancer Institute of New Jersey (to D.R.C.), the Breast Cancer Research Foundation (to A.J.L.) and the National Institutes of Health (P01CA87497 to A.J.L.).

Received: September 28, 2011

Revised: January 5, 2012

Accepted: March 12, 2012

Published: May 14, 2012

REFERENCES

- Adorno, M., Cordenonsi, M., Montagner, M., Dupont, S., Wong, C., Hann, B., Solari, A., Bobisse, S., Rondina, M.B., Guzzardo, V., et al. (2009). A Mutant-p53/Smad complex opposes p63 to empower TGFβ-induced metastasis. *Cell* 137, 87–98.
- Butler, J.S., and Loh, S.N. (2003). Structure, function, and aggregation of the zinc-free form of the p53 DNA binding domain. *Biochemistry* 42, 2396–2403.
- Butler, J.S., and Loh, S.N. (2007). Zn(2+)-dependent misfolding of the p53 DNA binding domain. *Biochemistry* 46, 2630–2639.
- Bykov, V.J., Issaeva, N., Shilov, A., Hultcrantz, M., Pugacheva, E., Chumakov, P., Bergman, J., Wiman, K.G., and Selivanova, G. (2002). Restoration of the tumor suppressor function to mutant p53 by a low-molecular-weight compound. *Nat. Med.* 8, 282–288.
- Bykov, V.J., Issaeva, N., Zache, N., Shilov, A., Hultcrantz, M., Bergman, J., Selivanova, G., and Wiman, K.G. (2005). Reactivation of mutant p53 and induction of apoptosis in human tumor cells by maleimide analogs. *J. Biol. Chem.* 280, 30384–30391.
- Cho, Y., Gorina, S., Jeffrey, P.D., and Pavletich, N.P. (1994). Crystal structure of a p53 tumor suppressor-DNA complex: understanding tumorigenic mutations. *Science* 265, 346–355.
- Dittmer, D., Pati, S., Zambetti, G., Chu, S., Teresky, A.K., Moore, M., Finlay, C., and Levine, A.J. (1993). Gain of function mutations in p53. *Nat. Genet.* 4, 42–46.
- Foster, B.A., Coffey, H.A., Morin, M.J., and Rastinejad, F. (1999). Pharmacological rescue of mutant p53 conformation and function. *Science* 286, 2507–2510.
- Hainaut, P., and Milner, J. (1993a). Redox modulation of p53 conformation and sequence-specific DNA binding in vitro. *Cancer Res.* 53, 4469–4473.
- Hainaut, P., and Milner, J. (1993b). A structural role for metal ions in the “wild-type” conformation of the tumor suppressor protein p53. *Cancer Res.* 53, 1739–1742.
- Haupt, Y., Maya, R., Kazanietz, A., and Oren, M. (1997). Mdm2 promotes the rapid degradation of p53. *Nature* 387, 296–299.
- Hingorani, S.R., Wang, L., Murtani, A.S., Combs, C., Deramandt, T.B., Hruban, R.H., Rustgi, A.K., Chang, S., and Tuveson, D.A. (2005). Trp53R172H and KrasG12D cooperate to promote chromosomal instability and widely metastatic pancreatic ductal adenocarcinoma in mice. *Cancer Cell* 7, 469–483.
- Ikediobi, O.N., Davies, H., Bignell, G., Edkins, S., Stevens, C., O'Meara, S., Santarius, T., Avis, T., Barthorpe, S., Brackenbury, L., et al. (2006). Mutation analysis of 24 known cancer genes in the NCI-60 cell line set. *Mol. Cancer Ther.* 5, 2606–2612.
- Joerger, A.C., and Fersht, A.R. (2007). Structure-function-rescue: the diverse nature of common p53 cancer mutants. *Oncogene* 26, 2226–2242.
- Joerger, A.C., Ang, H.C., Veprintsev, D.B., Blair, C.M., and Fersht, A.R. (2005). Structures of p53 cancer mutants and mechanism of rescue by second-site suppressor mutations. *J. Biol. Chem.* 280, 16030–16037.
- Kalinowski, D.S., and Richardson, D.R. (2007). Future of toxicology—iron chelators and differing modes of action and toxicity: the changing face of iron chelation therapy. *Chem. Res. Toxicol.* 20, 715–720.
- Lang, G.A., Iwakuma, T., Suh, Y.A., Liu, G., Rao, V.A., Parant, J.M., Valentin-Vega, Y.A., Terzian, T., Caldwell, L.C., Strong, L.C., et al. (2004). Gain of function of a p53 hot spot mutation in a mouse model of Li-Fraumeni syndrome. *Cell* 119, 861–872.
- Liu, G., McDonnell, T.J., Montes de Oca Luna, R., Kapoor, M., Mims, B., El-Naggar, A.K., and Lozano, G. (2000). High metastatic potential in mice inheriting a targeted p53 missense mutation. *Proc. Natl. Acad. Sci. USA* 97, 4174–4179.
- Martins, C.P., Brown-Swigart, L., and Evan, G.I. (2006). Modeling the therapeutic efficacy of p53 restoration in tumors. *Cell* 127, 1323–1334.
- Midgley, C.A., and Lane, D.P. (1997). p53 protein stability in tumour cells is not determined by mutation but is dependent on Mdm2 binding. *Oncogene* 15, 1179–1189.
- Muller, P.A., Caswell, P.T., Doyle, B., Iwanicki, M.P., Tan, E.H., Karim, S., Lukashchuk, N., Gillespie, D.A., Ludwig, R.L., Gosselin, P., et al. (2009). Mutant p53 drives invasion by promoting integrin recycling. *Cell* 139, 1327–1341.
- Cancer Genome Atlas Research Network. (2011). Integrated genomic analyses of ovarian carcinoma. *Nature* 474, 609–615.
- North, S., Pluquet, O., Maurici, D., El-Ghissassi, F., and Hainaut, P. (2002). Restoration of wild-type conformation and activity of a temperature-sensitive mutant of p53 (p53(V272M)) by the cytoprotective aminothiol WR1065 in the esophageal cancer cell line TE-1. *Mol. Carcinog.* 33, 181–188.

- Olivier, M., Hollstein, M., and Hainaut, P. (2010). TP53 mutations in human cancers: origins, consequences, and clinical use. *Cold Spring Harb. Perspect. Biol.* 2, a001008.
- Petitjean, A., Mathe, E., Kato, S., Ishioka, C., Tavtigian, S.V., Hainaut, P., and Olivier, M. (2007). Impact of mutant p53 functional properties on TP53 mutation patterns and tumor phenotype: lessons from recent developments in the IARC TP53 database. *Hum. Mutat.* 28, 622–629.
- Richardson, D.R., Sharpe, P.C., Lovejoy, D.B., Senaratne, D., Kalinowski, D.S., Islam, M., and Bernhardt, P.V. (2006). Dipyridyl thiosemicarbazone chelators with potent and selective antitumor activity form iron complexes with redox activity. *J. Med. Chem.* 49, 6510–6521.
- Richardson, D.R., Kalinowski, D.S., Richardson, V., Sharpe, P.C., Lovejoy, D.B., Islam, M., and Bernhardt, P.V. (2009). 2-Acetylpyridine thiosemicarbazones are potent iron chelators and antiproliferative agents: redox activity, iron complexation and characterization of their antitumor activity. *J. Med. Chem.* 52, 1459–1470.
- Riley, T., Sontag, E., Chen, P., and Levine, A. (2008). Transcriptional control of human p53-regulated genes. *Nat. Rev. Mol. Cell Biol.* 9, 402–412.
- Sablina, A.A., Budanov, A.V., Ilyinskaya, G.V., Agapova, L.S., Kravchenko, J.E., and Chumakov, P.M. (2005). The antioxidant function of the p53 tumor suppressor. *Nat. Med.* 11, 1306–1313.
- Shoemaker, R.H. (2006). The NCI60 human tumour cell line anticancer drug screen. *Nat. Rev. Cancer* 6, 813–823.
- Sigal, A., and Rotter, V. (2000). Oncogenic mutations of the p53 tumor suppressor: the demons of the guardian of the genome. *Cancer Res.* 60, 6788–6793.
- Terzian, T., Suh, Y.A., Iwakuma, T., Post, S.M., Neumann, M., Lang, G.A., Van Pelt, C.S., and Lozano, G. (2008). The inherent instability of mutant p53 is alleviated by Mdm2 or p16INK4a loss. *Genes Dev.* 22, 1337–1344.
- Ventura, A., Kirsch, D.G., McLaughlin, M.E., Tuveson, D.A., Grimm, J., Lintault, L., Newman, J., Reczek, E.E., Weissleder, R., and Jacks, T. (2007). Restoration of p53 function leads to tumour regression in vivo. *Nature* 445, 661–665.
- Wong, K.B., DeDecker, B.S., Freund, S.M., Proctor, M.R., Bycroft, M., and Fersht, A.R. (1999). Hot-spot mutants of p53 core domain evince characteristic local structural changes. *Proc. Natl. Acad. Sci. USA* 96, 8438–8442.
- Xue, W., Zender, L., Miething, C., Dickins, R.A., Hernando, E., Krizhanovsky, V., Cordon-Cardo, C., and Lowe, S.W. (2007). Senescence and tumour clearance is triggered by p53 restoration in murine liver carcinomas. *Nature* 445, 656–660.
- Yu, Y., Kalinowski, D.S., Kovacevic, Z., Siafakas, A.R., Jansson, P.J., Stefani, C., Lovejoy, D.B., Sharpe, P.C., Bernhardt, P.V., and Richardson, D.R. (2009). Thiosemicarbazones from the old to new: iron chelators that are more than just ribonucleotide reductase inhibitors. *J. Med. Chem.* 52, 5271–5294.

Lunatic Fringe Deficiency Cooperates with the Met/Caveolin Gene Amplicon to Induce Basal-like Breast Cancer

Keli Xu,^{1,11} Jerry Usary,³ Philaretos C. Kousis,¹ Aleix Prat,³ Dong-Yu Wang,⁴ Jessica R. Adams,^{1,6} Wei Wang,¹ Amanda J. Loch,¹ Tao Deng,⁵ Wei Zhao,³ Robert Darrell Cardiff,⁸ Keejung Yoon,^{9,12} Nicholas Gaiano,⁹ Vicki Ling,^{1,2} Joseph Beyene,^{2,13} Eldad Zacksenhaus,⁵ Tom Gridley,¹⁰ Wey L. Leong,⁴ Cynthia J. Guidos,^{1,7} Charles M. Perou,³ and Sean E. Egan^{1,4,*}

¹Program in Developmental and Stem Cell Biology

²Child Health Evaluative Sciences

The Hospital for Sick Children, Toronto, ON, M5G 1L7, Canada

³Lineberger Comprehensive Cancer Center, Departments of Genetics and Pathology, University of North Carolina, Chapel Hill, NC 27599, USA

⁴The Campbell Family Cancer Research Institute and Surgical Oncology Princess Margaret Hospital, and the Department of General Surgery

⁵Division of Cell and Molecular Biology, Toronto General Research Institute

University Health Network, Toronto, ON M5S 1A1, Canada

⁶Department of Molecular Genetics

⁷Department of Immunology

University of Toronto, Toronto, ON M5S 1A1, Canada

⁸Center for Comparative Medicine, University of California, Davis, CA 95616, USA

⁹Institute for Cell Engineering, Johns Hopkins University School of Medicine, Baltimore, MD 21205, USA

¹⁰Center for Molecular Medicine, Maine Medical Center Research Institute, 81 Research Drive, Scarborough, ME 04074, USA

¹¹Present address: Cancer Institute, University of Mississippi Medical Center, 2500 North State Street, Jackson, MS 39216, USA

¹²Present address: College of Biotechnology and Bioengineering, Sungkyunkwan University, Suwon, Gyeonggi-do 440-746, Republic of Korea

¹³Present address: Program in Population Genomics, Department of Clinical Epidemiology and Biostatistics, McMaster University, Hamilton, ON L8S 4L8, Canada

*Correspondence: segan@sickkids.ca

DOI 10.1016/j.ccr.2012.03.041

SUMMARY

Basal-like breast cancers (BLBC) express a luminal progenitor gene signature. Notch receptor signaling promotes luminal cell fate specification in the mammary gland, while suppressing stem cell self-renewal. Here we show that deletion of *Lfng*, a sugar transferase that prevents Notch activation by Jagged ligands, enhances stem/progenitor cell proliferation. Mammary-specific deletion of *Lfng* induces basal-like and claudin-low tumors with accumulation of Notch intracellular domain fragments, increased expression of proliferation-associated Notch targets, amplification of the *Met/Caveolin* locus, and elevated Met and Igf-1R signaling. Human BL breast tumors, commonly associated with JAGGED expression, elevated MET signaling, and CAVEOLIN accumulation, express low levels of *LFNG*. Thus, reduced *LFNG* expression facilitates JAG/NOTCH luminal progenitor signaling and cooperates with MET/CAVEOLIN basal-type signaling to promote BLBC.

INTRODUCTION

Patients with BLBC show reduced survival compared to those with more common luminal tumors, and this disease frequently

occurs in young patients, as well as in women with African ancestry. Basal-like tumors express markers of myoepithelium, but show a gene expression signature related to that of luminal progenitor cells (Cheang et al., 2008; Lim et al., 2009; Perou

Significance

Here we report that *LFNG*, which suppresses Jagged/Notch signaling in vivo, is consistently expressed at a low level in basal-like tumors and deletion of this gene in the mouse mammary gland enhances accumulation of activated Notch intracellular domain polypeptides, increases proliferation, and induces basal-like mammary tumors in cooperation with amplification of the *Met/Caveolin* gene locus. These mutations interact to promote a specific BLBC signaling network with increased Notch pathway activation, as well as elevated Met and Igf-1R signaling. Patients with *MET/CAV*-overexpressing BLBC may therefore benefit from combination therapy targeting Notch, MET, and IGF1R.

and Børresen-Dale, 2011; Prat et al., 2010). Indeed, luminal progenitors may be the cell-of-origin for most BLBC (Molyneux et al., 2010). In the mouse system, activated Notch1 can induce commitment of mammary stem cells (MaSC) into luminal progenitors, and promote proliferation of luminal progenitor cells in vitro and in vivo (Bouras et al., 2008). Similarly in humans, increased *NOTCH3* expression and function can promote luminal progenitor cell fate specification, at least in vitro (Raouf et al., 2008).

On the basis of studies with the Mouse Mammary Tumor Virus (MMTV), which can induce mammary tumor formation through insertional activation of Notch genes, a role for Notch signaling in human breast cancer was anticipated (Callahan and Smith, 2000). Most human breast tumors express Notch ligands and receptors (Parr et al., 2004; Pece et al., 2004; Reedijk et al., 2005; Stylianou et al., 2006). High-level expression of the *JAGGED1* ligand, as well as *NOTCH1* and/or *NOTCH3*, is associated with poor overall survival (Reedijk et al., 2005). Recent studies reveal that signaling through multiple Notch receptors activates proliferation and/or survival of breast cancer cells (Harrison et al., 2010; Haughian et al., 2012; Osipo et al., 2008; Sansone et al., 2007; Yamaguchi et al., 2008). Interestingly, *JAGGED*-dependent Notch pathway activation has been associated with triple negative (ER α [−], PR[−] and HER2[−]) tumors, and specifically with basal-like tumors and cell lines (Cohen et al., 2010; Dong et al., 2010; Haughian et al., 2012; Lee et al., 2008a, 2008b; Leong et al., 2007; Reedijk et al., 2008; Sansone et al., 2007).

Met, a cell surface tyrosine kinase receptor involved in epithelial-mesenchymal transition, is frequently expressed at high levels in BLBC (Elsheikh et al., 2008; Gastaldi et al., 2010; Lu et al., 2008; Ponzo and Park, 2010; Ravid et al., 2005; Salani et al., 2008; Savage et al., 2007), and many basal-like tumors show elevated Met signaling (Hochgräfe et al., 2010). In addition, Caveolin1 and 2, which facilitate Igf-1R signaling, are also overexpressed (Elsheikh et al., 2008; Gastaldi et al., 2010; Lu et al., 2008; Ponzo and Park, 2010; Ravid et al., 2005; Salani et al., 2008; Savage et al., 2007). Interestingly, the genes coding for MET, CAV1, and CAV2 are located in the same region of Chromosome 7q31 and this locus is overexpressed in many BLBC (Elsheikh et al., 2008; Gastaldi et al., 2010; Ponzo and Park, 2010; Savage et al., 2007).

Fringe proteins are N-acetylglucosamine transferases that modify Notch receptors to control ligand-mediated activation (Haines and Irvine, 2003). These proteins enhance Notch activation by Delta-family ligands, while inhibiting Notch activation by Serrate/Jagged ligands (Haines and Irvine, 2003). *Lfrng*, one of three Fringe genes in mammals, controls Notch signaling in many developing tissues (Cohen et al., 1997; Johnston et al., 1997). Interestingly, *LFNG* is expressed at high levels in MaSC and/or bipotent progenitor cells of the human breast (Raouf et al., 2008). However, its role in the regulation of Notch signaling of the developing or adult mammary gland remains unknown, as is its potential for restricting Notch-dependent oncogenic signaling in this context. In this study, we used conditional mutant mice to define the function of *Lfrng* in mammary epithelium. In addition, we tested for its expression and potential role in human breast cancer.

RESULTS

A Lfrng Expression Boundary in Mammary Development

To define where and when Notch is activated in the developing mammary gland, we used LacZ knock-in mice for various Notch pathway genes. Typically, boundaries between Fringe-expressing cells and nonexpressing cells are sites of consequential Notch signaling (Irvine, 1999). Therefore, we examined *Lfrng* expression by performing X-gal staining on mammary glands from six-week-old *Lfrng*^{LacZ/+} virgin females (Zhang and Gridley, 1998). Interestingly, *Lfrng* expression was restricted to basal cells, in particular to cap cells of terminal end buds (TEBs) (Figure 1A), which have MaSC activity (Bai and Rohrschneider, 2010). This result is consistent with studies on cells purified from the human mammary gland, which show that *LFNG* expression is > 20-fold enriched in stem and/or bipotent progenitor cells as compared with luminal restricted progenitors (Raouf et al., 2008). Two Notch ligands, *Dll1* and *Jagged1*, show distinct expression at this stage. Weak X-gal staining from a *Dll1*^{LacZ/+} allele (Hrabě de Angelis et al., 1997) was observed in cap cells of the mammary TEB. In contrast, their basally located myoepithelial descendants showed intense staining. X-gal staining in pubescent *Jagged1* ^{β -Geo/+} (Xu et al., 2010) mice was strongest in stromal cells surrounding each TEB (Figure 1A).

In mature adults, after TEB regression, *Lfrng*^{LacZ} expression was barely detected, while *Dll1*^{LacZ} expression remained strong in myoepithelial cells. Interestingly, *Jagged1* expression switched from stroma to myoepithelium in the mature gland (Figure 1A). *JAGGED1* expression is also high in basal cells of the mature human gland (Reedijk et al., 2005). Next, we used antibodies to stain for Notch1 and Notch4, which were expressed at low levels in luminal and basal cells, respectively (Figure S1A available online). Using β -Geo/+ knock-in mice (Xu et al., 2010), *Notch3* expression was found to be high in body cells of the TEB, as well as in luminal epithelial cells of mature ducts, whereas *Notch2* expression was strong in stroma and weak in epithelium (Figure S1B). These data are consistent with recent Notch ligand and receptor expression analysis by rtPCR and immunohistochemistry (Bouras et al., 2008; Raafat et al., 2011; Raouf et al., 2008).

Lfrng Controls Notch Activation and Suppresses Mammary Epithelial Proliferation

Fringe controls Notch activation at compartment boundaries in the developing fruit fly (Irvine, 1999). Our expression analysis in the mammary gland reveals a similar boundary at the TEB-ductal junction, where *Lfrng* may differentially regulate Notch activation induced by *Dll1* and/or *Jagged1*. To define *Lfrng* function in this context, we analyzed mammary development in *Lfrng* mutant mice. Whole-mount analysis showed evidence of epithelial hyperplasia in virgin mammary glands from *Lfrng* mutants (Figure 1B). Sections from mutant and control glands were stained with antibodies against luminal and basally restricted cytokeratins, keratin 8 (K8) and 14 (K14), respectively. Most mutant glands showed decreased K8 expression in body cells of the TEB. Also, multiple layers of K14⁺ basal cells were observed in some locations. Cells did not co-express K8 and K14 in wild-type or mutant glands during puberty (Figure 1C). We next tested for altered cell proliferation by staining for Ki67. Indeed, *Lfrng* mutant glands showed increased cell proliferation in mature ducts (Figure 1D).

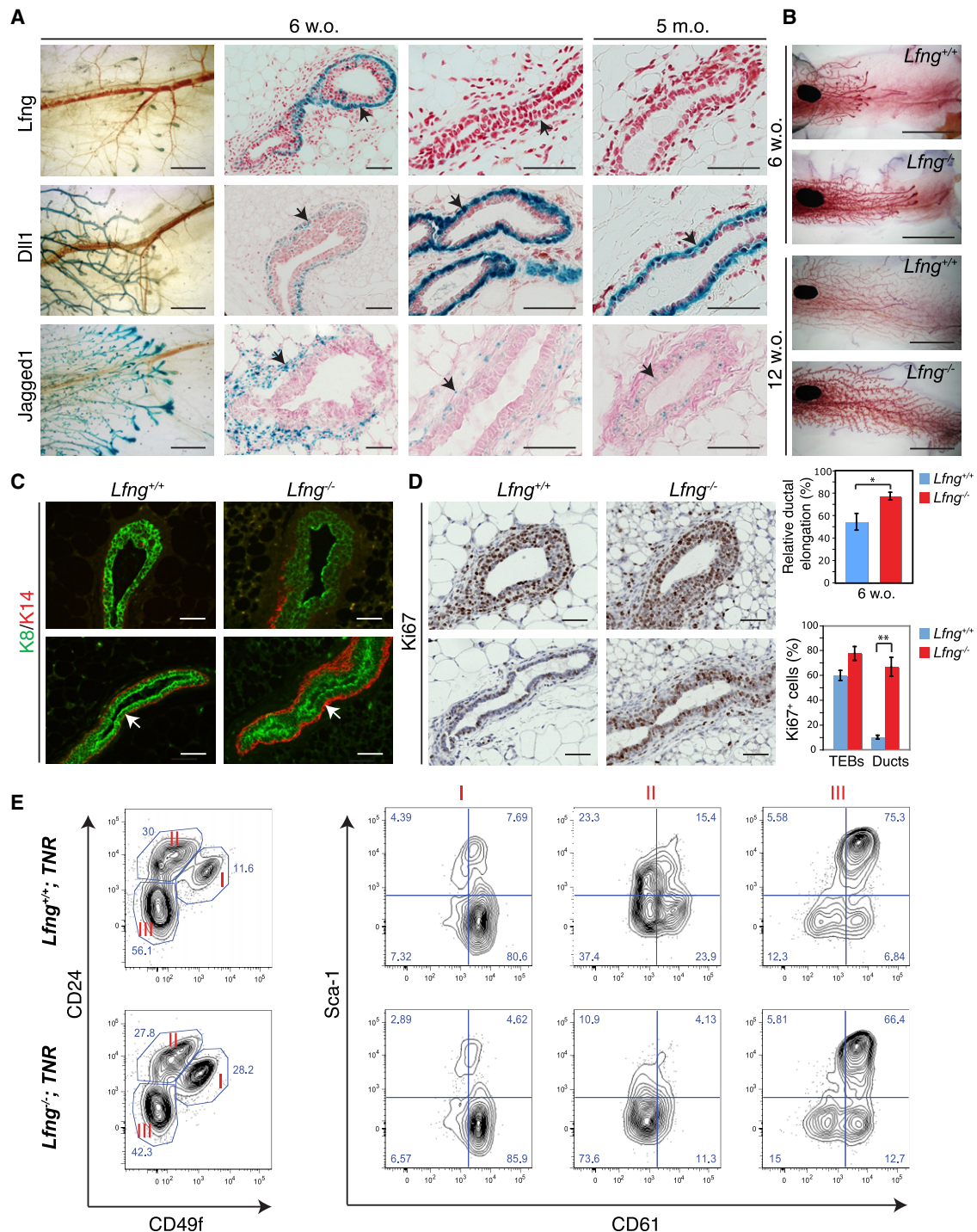


Figure 1. *Lfng* Is Expressed in Mammary Basal Cells and Its Deletion Causes Increased Proliferation and Expansion of the CD24⁺ CD49f^{hi}CD61⁺Sca1⁻ Population in the Pubescent Mammary Gland

(A) Expression of *Lfng*, *Dll1*, and *Jagged1* in the mouse mammary gland. Shown are representative photomicrographs of whole-mount (left column) and sectioned X-Gal staining of mammary glands from *Lfng*^{LacZ/+}, *Dll1*^{LacZ/+}, and *Jagged1*^{B-Geo/+} virgin mice at 6 weeks and 5 months of age. Sections for the TEBS are shown in the second column from left.

(B) Mammary hyperplasia in the *Lfng*^{-/-} mutant. Shown are representative photomicrographs of whole-mount mammary glands from 6- and 12-week-old virgins. (C) Representative photomicrographs of anti-K8, -K14 immunofluorescence staining in mammary sections from 6-week-old virgins of *Lfng*^{+/+} and *Lfng*^{-/-} mice. TEBS and ducts are shown in upper and lower panels, respectively.

(D) Ductal elongation at 6 weeks old, measured as the distance between the lymph node and the ductal front line normalized to the distance between the lymph node and the end of the fat pad, are presented as mean values ± standard error. *p < 0.05. Note, the *Lfng* null allele was generated through expression of Cre in the

Fringe proteins control Notch signaling by enhancing Delta-while inhibiting Serrate/Jagged-mediated activation (Haines and Irvine, 2003). Based on high-level *Lfng* expression in cap cells of the TEB, and the known cell autonomous function of Fringe proteins (Panin et al., 1997), *Lfng* likely facilitates Dll-mediated Notch signaling or blocks Jagged1-mediated Notch activation in MaSC and/or bipotential progenitors of the cap layer. The Transgenic Notch Reporter (TNR) mouse has an artificial Notch-responsive promoter with multiple RBPJk-binding sites regulating expression of eGFP (Duncan et al., 2005). This mouse has been used successfully to study Notch/p63 interaction in the developing mammary gland (Yalcin-Ozuysal et al., 2010). Therefore, to test for alterations in Notch signaling associated with *Lfng* deletion, we crossed TNR reporter mice with *Lfng* mutants. To follow Notch signaling at multiple levels within the developmental hierarchy, lineage-depleted mammary epithelial cells were stained for surface markers CD24, CD49f, CD61, and Sca1. Remarkably, *Lfng* null glands showed a more than 2-fold (2.37 ± 0.07 , $p < 0.05$) enrichment of CD24⁺CD49f^{hi} cells, a population known to contain mammary stem/early progenitor cells (Figure 1E). We gated on this population and found that most cells were CD61⁺Sca1⁻, characteristic of MaSC (Visvader, 2009) (Figure 1E). In some cases this was associated with decreased numbers of CD24^{hi}CD49f⁺ CD61⁺ luminal progenitor cells (Figure 1E). Thus, our flow cytometry analysis indicated that deletion of *Lfng* caused accumulation of stem/bipotent progenitor cells, likely at the expense of luminal progenitor cells in the developing mammary gland. Interestingly, *Lfng*^{-/-}; TNR mutants showed 40% decrease in GFP⁺ lineage-depleted mammary epithelial cells as compared to *Lfng*^{+/+} or *Lfng*^{+/-}; TNR controls (Figure S1C). Specifically, in mutant mice, fewer cells with active Notch signaling were observed in MaSC/early progenitor-containing (CD24⁺CD49f^{hi}) and luminal progenitor-containing (CD24^{hi}CD49f⁺) compartments (Figure S1D) (Shackleton et al., 2006; Stingl et al., 2006). Thus, deletion of *Lfng* leads to decreased Notch signaling in MaSC and progenitors in puberty (likely as a result of reduced Dll1-mediated Notch activation at this stage), and is associated with expansion of the immature cell compartment. These data are consistent with those of Bouras et al., who showed that shRNA-mediated knock-down of *RBPJk*, and thus disruption of canonical Notch signaling, caused expansion of the CD24⁺CD29^{hi} compartment (note: this is the same as the CD24⁺CD49f^{hi} compartment), and promotion of MaSC self-renewal (Bouras et al., 2008).

Lfng Is a Suppressor of Basal-like Tumor Formation in the Mouse Mammary Gland

Next, we tested for *Lfng* function by generating a Cre-conditional *Lfng* mutant mouse (Xu et al., 2010). This mouse was crossed to MMTV-Cre line A, which shows robust expression in mammary

epithelium (Wagner et al., 1997). Many *Lfng*^{flox/flox}; MMTV-Cre mutant mice developed mammary tumors starting at 10 months of age (Figure 2A). Histological analysis revealed three types of *Lfng* mutant tumors: approximately 60% showed glandular differentiation (type I); one-third mainly consisted of mesenchymal/spindle-shaped cells (type II); and about 5% had areas containing multinucleated giant cells (type III) (Figure 2B). All three histological types were triple-negative (ERα-, PR-, Her2/Neu-negative) (Figure 2C and data not shown), and highly proliferative (Figure 2D). Interestingly, tumors of all three types had cells co-expressing luminal (K8) and basal markers (K14). Notably, type I tumors contained a higher percentage (75.3% versus 16.8% in type II) of cells expressing one or both lineage-specific keratin (Figure 2E).

Next, we used transcriptional profiling to define molecular subtype for 11 *Lfng* mutant tumors (Herschowitz et al., 2007). Interestingly, in unsupervised cluster analysis, these tumors grouped with basal-like and claudin-low models but were otherwise quite unique. Specifically, six type I tumors clustered together with *Brca1/p53* tumors, DMBA-induced tumors and Wap-SV40T¹²¹-induced tumors, all of which are related to BLBC, whereas five spindle/EMT or type II *Lfng* mutant mammary tumors clustered nearby, together with DMBA-induced spindle tumors as well as with *Brca1/p53* tumors, which have previously been identified as claudin-low (Herschowitz et al., 2007) (Figures 3A and 3B). The claudin-low signature is related to that observed in MaSCs (Hennessy et al., 2009). Interestingly, many mouse mammary tumors that were induced by activated Met cluster with similar basal-like mouse models (Ponzo et al., 2009). We also performed enrichment map analysis to identify differentially expressed gene sets in *Lfng*^{flox/flox}; MMTV-Cre mammary tumors as compared to those expressed in other mouse breast cancer models. Interestingly, gene sets implicated in leukocyte activation and proliferation, inflammation, cytokine and chemokine signaling, as well as extracellular matrix remodeling were overrepresented in *Lfng* mutant tumors (Figure 3C and Table S1).

We next analyzed tumors by flow cytometry. *Lfng* mutant tumors were composed of cells with marker profiles that were distinct from profiles seen in the normal mammary gland. As discussed previously, the characteristic mammary epithelial profile includes CD24⁺CD49f^{hi} cells enriched for MaSC/bipotent progenitors, CD24^{hi}CD49f⁺ cells that are enriched for luminal progenitors, with a third compartment of CD24⁻CD49f⁻ cells. In contrast, type I *Lfng* mutant tumors had an increased fraction of CD49f⁺ cells, approximately half of which expressed CD24 (Figure 4A). Most of the CD49f⁺ cells also expressed CD61, with lower expression of Sca1 noted. Finally, there was an increased number of CD24⁺CD61⁺ cells and most of these were CD49f⁺Sca1⁻, suggesting that a luminal progenitor-like compartment is expanded in these tumors (Figures 4B and

germline of female *Lfng*^{flox/+}; MMTV-Cre mice. Increased mammary epithelial proliferation in *Lfng*^{-/-} compared with control *Lfng*^{+/-} littermates. Shown are representative photomicrographs of anti-Ki67 immunostaining in mammary sections same as (C). Numbers of Ki67⁺ cells are normalized to the total number of epithelial cells in TEBs or in ductal areas, presented as mean values \pm standard error. ** $p < 0.005$.

(E) Representative flow cytometry analyses of lineage-depleted mammary cells from *Lfng*^{-/-}; TNR mutants compared with *Lfng*^{+/-}; TNR littermates at 6 weeks old. Shown are CD24/CD49f plots and Sca1/CD61 plots on populations I, II, III gated as in CD24/CD49f plots.

Scale bars correspond to 1 mm in left panels of (A), 5 mm in (B), and 50 μ m in all others.

See also Figure S1.

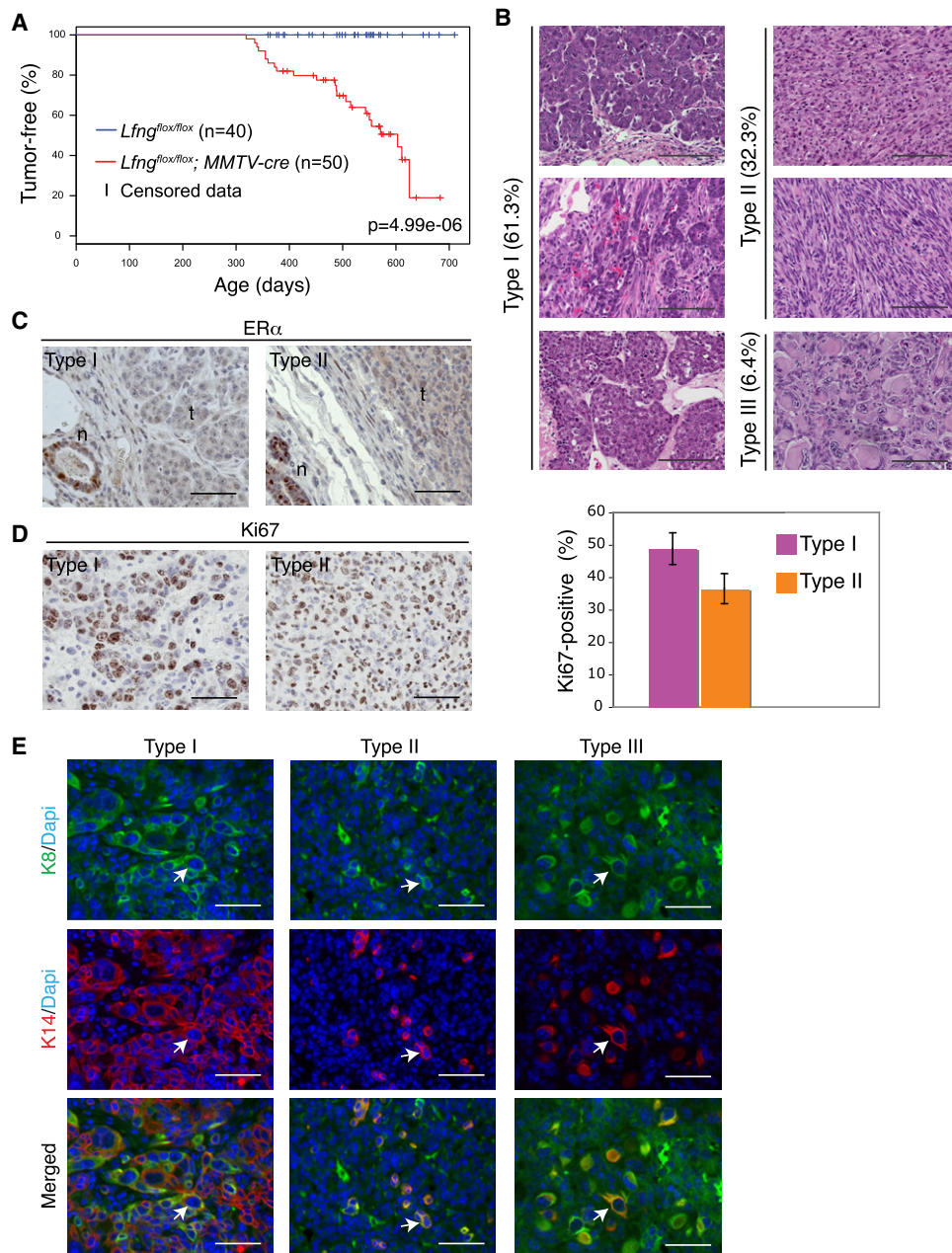


Figure 2. Deletion of *Lfng* Induced Mammary Tumors in Mice

(A) Kaplan-Meier mammary tumor-free survival curve for control *Lfng*^{flox/flox} and *Lfng*^{flox/flox}; MMTV-cre conditional mutant mice.

(B) Representative photomicrographs of H&E stained sections showing three histological types of *Lfng*^{flox/flox}; MMTV-cre mammary tumors.

(C) Anti-ERα immunostaining on two main types of *Lfng*^{flox/flox}; MMTV-cre mammary tumors. n: normal tissue; t: tumor. Note positive ERα staining in normal tissue adjacent to the tumor.

(D) Representative photomicrographs and quantification of anti-Ki67 immunostaining on two main types of *Lfng*^{flox/flox}; MMTV-cre mammary tumors. Data are derived from two sections in each of three Type I and Type II tumors presented as mean values ± standard error.

(E) Representative photomicrographs of anti-K8, -K14 immunofluorescence staining on three types of *Lfng*^{flox/flox}; MMTV-cre mammary tumors. Arrows point to cells showing co-expression of K8 and K14.

Scale bars correspond to 100 μm in (B), 50 μm in (C), (D) and (E).

S2A) (Visvader, 2009; Visvader and Smith, 2011). Next, fluorescence-activated cell sorting was used to fractionate tumor cells and to test for tumor initiating activity. Specifically, we separated type I tumors into three distinct populations (CD24⁺CD49f⁺,

CD24⁻CD49f⁻, and CD24⁻CD49f⁺) and injected matrigel suspensions of each into mammary fat pads of FVB recipient mice. Most tumor initiating activity was found within the CD24⁺CD49f⁺ luminal progenitor-like population (Figure 4C).

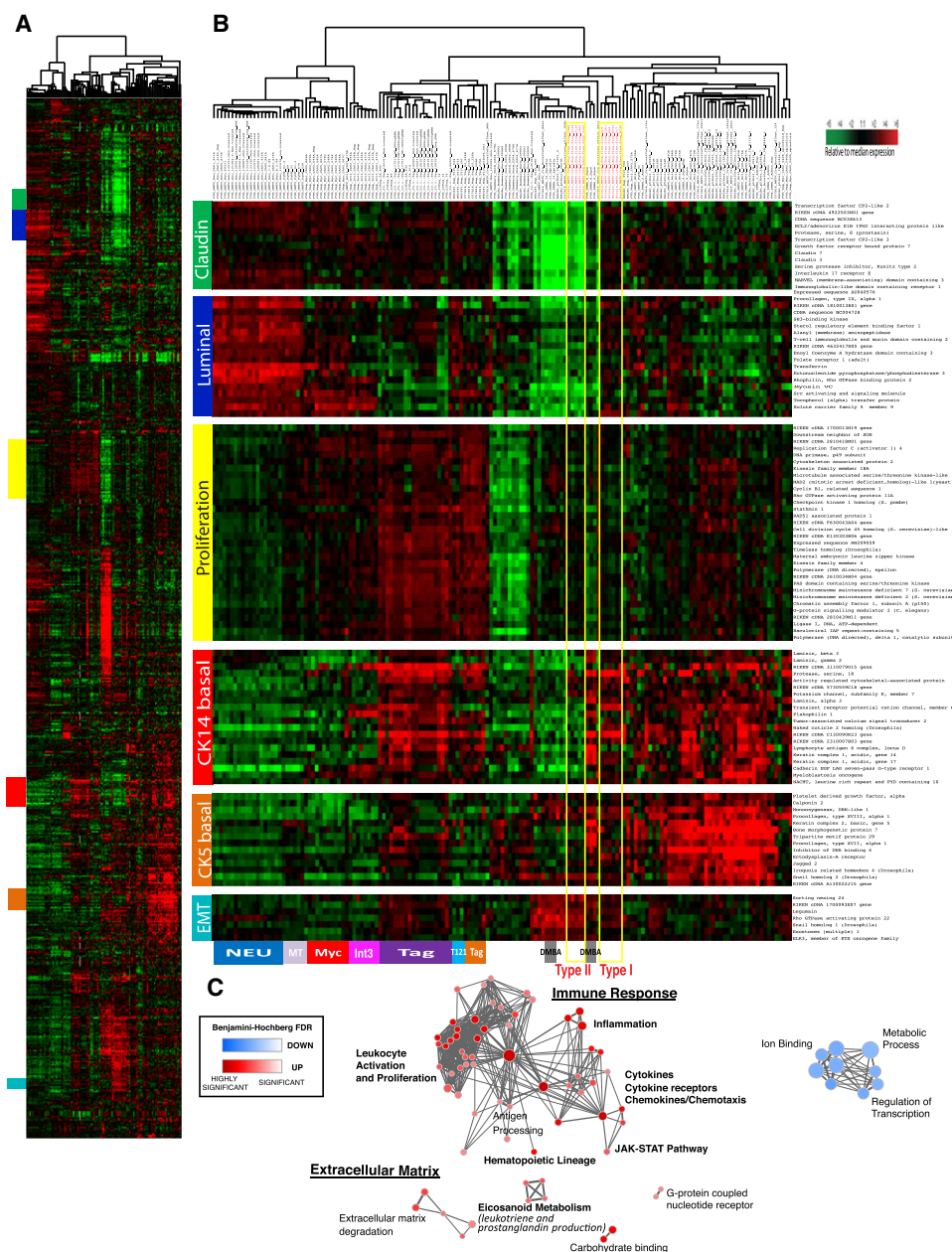


Figure 3. *Lfng*^{flox/flox}; MMTV-Cre Tumors Cluster with Basal-like and Claudin-Low Mouse Mammary Tumor Models

(A) Overview of expression of reference genes in tumors from various mouse models of breast cancer, including 11 tumors from *Lfng*^{flox/flox}; MMTV-Cre mice. Colored bars at left correspond to regions shown in (B).

(B) Expression of selected genes representing the Claudin gene cluster, luminal gene cluster, proliferation-associated gene cluster, CK14 basal-like gene cluster, CK5 basal-like gene cluster, and EMT gene cluster. Expression data from type I and type II *Lfng*^{flox/flox}; MMTV-Cre tumors are contained within yellow boxes. Clusters of tumor models are highlighted at the bottom. DMBA, 7,12-dimethylbenz[a]-anthracene.

(C) Enrichment map for gene sets over-represented in list of genes that are differentially expressed comparing *Lfng*^{flox/flox}; MMTV-Cre mouse mammary tumors to other mouse models of breast cancer.

See also Table S1.

Immunohistochemical analysis showed type I tumors also expressed high levels of CD61, contained Aldh1⁺ cells, and expressed low levels of Gata3 (Figures 4D and S2B) (Ginestier et al., 2007; Visvader, 2009; Visvader and Smith, 2011). Type II tumors show fewer CD61⁺ cells, and were almost completely

negative for Aldh1. However, Vimentin and Twist, two markers associated with EMT, were broadly expressed in type II, but not type I, tumors (Figure 4D). Phospho-Akt, a marker of PI3K signaling, was evident in type II tumors and at a somewhat lower level in type I tumors (Figure 4D). Thus, based on histology,

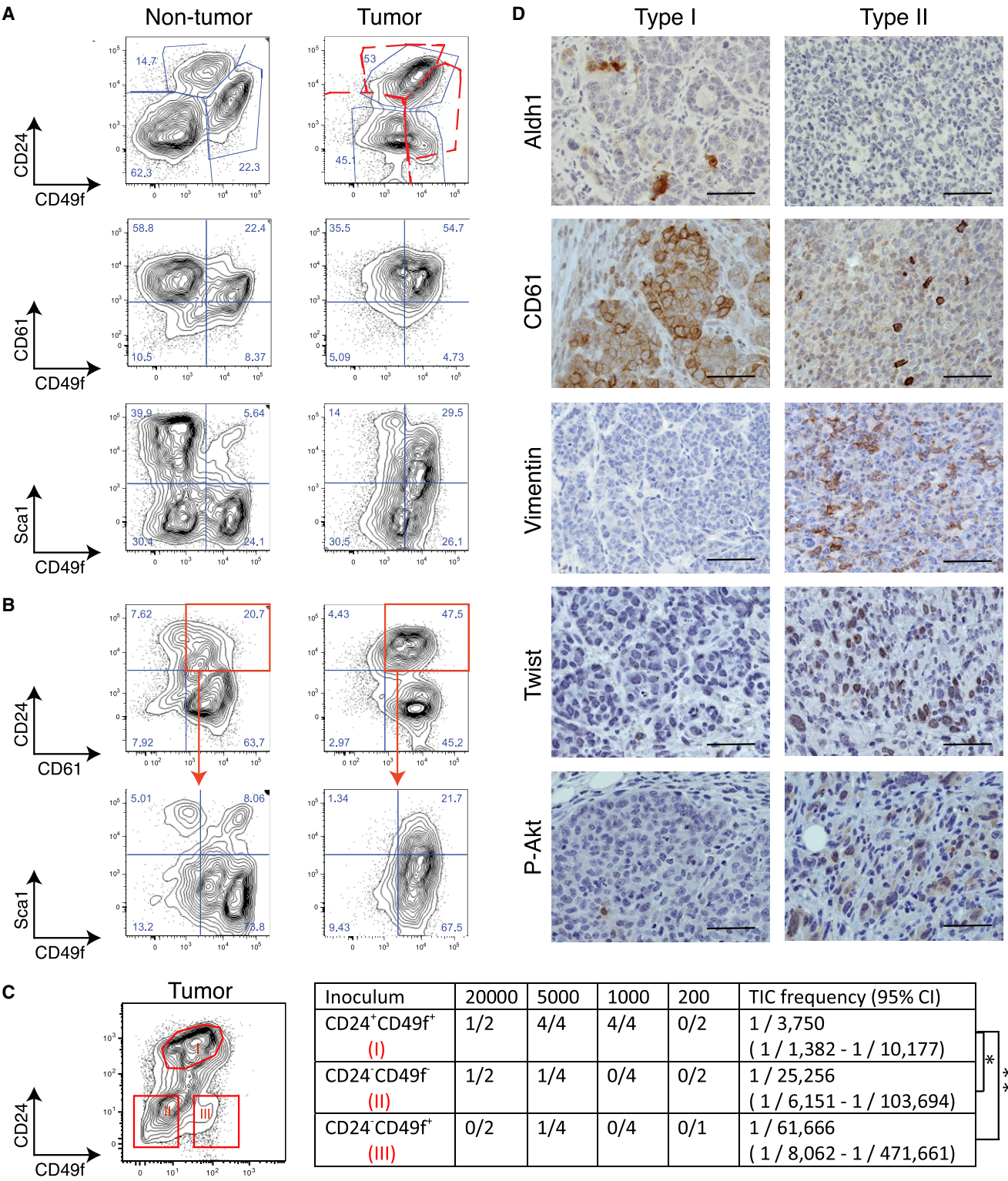


Figure 4. Flow Cytometry and Immunohistological Analysis of *Lfng*^{flx/flx}; MMTV-Cre Tumors

(A) Representative flow cytometry contour plots for lineage-depleted mammary tumor cells compared with non-tumor lineage-depleted mammary cells from a *Lfng*^{flx/flx}; MMTV-Cre mouse. Shown are CD24/CD49f, CD61/CD49f, and Sca1/CD49f plots from a Type I tumor.

(B) Additional analysis of the flow cytometry data as shown in (A): CD24/CD61 plots and Sca1/CD49f plots on the CD24⁺CD61⁺ populations as gated in the upper panels.

transcriptional profiling, flow cytometry and marker analysis, type I lesions were basal-like tumors with features of luminal progenitors (Cheang et al., 2008; Perou and Børresen-Dale, 2011), and type II were similar to claudin-low tumors with EMT-like features, a phenotype associated with MaSC-like cells (Car-diff, 2010; Taube et al., 2010).

Because Lfrng regulates Notch signaling in mammary epithelium as shown previously, we tested for altered expression of known Notch target genes in these tumors. Indeed, all 11 *Lfrng*^{flox/flox}; MMTV-Cre mammary tumors showed reduced expression of *Hey1*, *Hey2*, and *Notch3*, but elevated expression of *Dll4* and the Notch target genes *uPA*, *c-Myc*, and *Cyclin D1* (Cohen et al., 2010; Klinakis et al., 2006; Shimizu et al., 2011) (Figure 5A). As for other models, high-level expression of *Hey1*, *Hey2*, *Notch3*, *c-Myc*, *Cyclin D1*, and *Notch4* (*Int3*), as well as low-level expression of *p63* and *Dll1* was observed in tumors induced by activated Notch4 (Wap-*Int-3*). In contrast, low-level expression of *Hey1*, *Notch1*, *c-Myc* (endogenous), *Cyclin D1*, *p63*, and *Dll1* was observed in MMTV-Myc tumors. Finally, *Hey1* was highly expressed in Her2/Neu and Polyoma Middle T-induced tumors (Figure 5A).

To directly test for activation of Notch signaling in *Lfrng*^{flox/flox}; MMTV-Cre mammary tumors, we performed western blot analysis using antibodies that recognize N-terminal sequences of cleavage-generated intracellular domain (ICD) fragments from Notch1 and 2. Indeed, higher levels of Notch1^{ICD} and Notch2^{ICD} were present in *Lfrng* mutant tumors as compared to control non-tumor-bearing glands from the same animal (Figure 5B). Specific antibodies to detect murine Notch3^{ICD} and Notch4^{ICD} are currently unavailable; however, expression and processing of both proteins were changed in *Lfrng* mutant tumors (Figure S3). For Notch4, increased accumulation of a C-terminal fragment consistent with Notch4^{ICD} was observed (Figure S3). Finally, Jagged1 protein was expressed in *Lfrng* mutant tumors, as were the protein products of Notch target genes, *Cyclin D1* and *c-Myc* (Figure 5C). Thus, *Lfrng* gene deletion results in Notch activation in these tumors, and is consistent with induction of Jagged/Notch target genes, *CyclinD1* and *c-Myc*.

Met/Caveolin Gene Amplification and Signaling in Lfrng Mutant Tumors

Next, to identify cooperative events in *Lfrng* mutant tumors, we performed aCGH (array comparative genomic hybridization) on DNA isolated from 5 *Lfrng* conditional mutant tumors as compared to non-tumor DNA isolated from control tissue. While copy number gains and losses were noted in many regions across the genome, the only common abnormality involved amplification of a small locus at chromosome 6A2 (Figures S4A and S4B). This was observed in 4 out of 5 tumor samples, the exception being a *Lfrng*^{flox/+}; MMTV-Cre mammary tumor. The overlapping region with copy number gains in each of the four tumors contained 13 genes including the tyrosine kinase *Met*,

and neighboring *Cav1* and 2 genes (Figure 6A). This locus is amplified and/or overexpressed in BLBC in humans and in mammary tumors from *Brca1*^{Δ11/co}; *p53*^{+/-}; MMTV-Cre mice (Savage et al., 2007; Smolen et al., 2006). To determine which, if any, of these genes were overexpressed in *Lfrng* mutant tumors, we screened our transcriptional profiling data for expression of genes within this region. Indeed, expression of several, including *Met*, *Cav1* and 2, was significantly elevated in *Lfrng* mutant tumors (Figure 6B). Interestingly, high-level *MET* expression has been noted in aggressive human breast cancer, particularly in breast tumors with EMT features (Gastaldi et al., 2010; Ponzo and Park, 2010), and expression of oncogenic *Met* can induce basal-like mammary tumors in transgenic mice (Graveel et al., 2009; Ponzo et al., 2009). We next used western analysis to test for elevated Met accumulation and activation in *Lfrng* mutant tumors. As shown in Figure 6C, *Lfrng* mutant tumors showed dramatically increased Met expression and activation. Overexpressed Met could still depend on HGF ligand for activation. Indeed, *Hgfα* was identified as overrepresented in gene expression signatures from *Lfrng* mutant tumors in comparison to other mouse models of breast cancer analyzed (Table S1), and HGFα expression was detected by western analysis of *Lfrng* mutant tumors (data not shown). Next, we analyzed Caveolin 1/2 expression in *Lfrng* tumors. In the normal mammary gland, Caveolin 1 is very highly expressed in endothelial cells, adipocytes, and basally localized myoepithelium. High-level expression was also seen in type I and II tumor cells (Figure 6D). We analyzed Caveolin 2 expression by western blot, and in each case, it was elevated in tumor cells in comparison to nontumorous mammary tissue from the same animal (Figure 6E). Caveolin expression has been linked to enhanced Insulin and Igf-1R signaling (Lu et al., 2008; Ravid et al., 2005; Salani et al., 2008), and elevated Igf-1R signaling can induce mammary tumors in mice (Jones et al., 2007). We therefore analyzed InsR and Igf-1R signaling at the level of Irs1/2 tyrosine phosphorylation. Indeed, Irs tyrosine phosphorylation was elevated in *Lfrng* mutant mammary tumors (Figure 6E). Thus, *Lfrng* mutant tumors have selected for activation of receptors that are more highly expressed or active in basal cells (Hvid et al., 2011; Niranjan et al., 1995).

Low-Level LFNG Expression Is a Hallmark of Basal-like Breast Cancer in Humans

Because deletion of *Lfrng* caused basal-like and claudin-low mammary tumors in mice, we analyzed *LFNG* expression in human breast cancer. First, we screened publically available gene expression data from 676 human breast cancers with linked clinical-pathological information. Interestingly, reduced *LFNG* expression was associated with high tumor grade, with ERα/PR/HER2 triple-negative status, and most significantly, with the basal-like molecular subtype (Figures S5A and S5B). To the contrary, elevated *LFNG* expression was noted in ER⁺

(C) Limiting dilution transplantation assay on CD24⁺CD49f⁺, CD24⁺CD49f⁻ and CD24⁻CD49f⁺ tumor cells as gated in a CD24/CD49f plot. Data are derived from two independent experiments using two donors of type I tumor. TIC: Tumor-Initiating Cells. *p = 0.0307 (CD24⁺CD49f⁺ versus CD24⁻CD49f⁻), **p = 0.0155 (CD24⁺CD49f⁺ versus CD24⁻CD49f⁺)

(D) Representative photomicrographs of anti-Aldh1, anti-CD61, anti-Vimentin, anti-Twist and anti-Phospho-Akt immunostaining in two main types of *Lfrng*^{flox/flox}; MMTV-Cre mammary tumors. Scale bars correspond to 50 μm.

See also Figure S2.

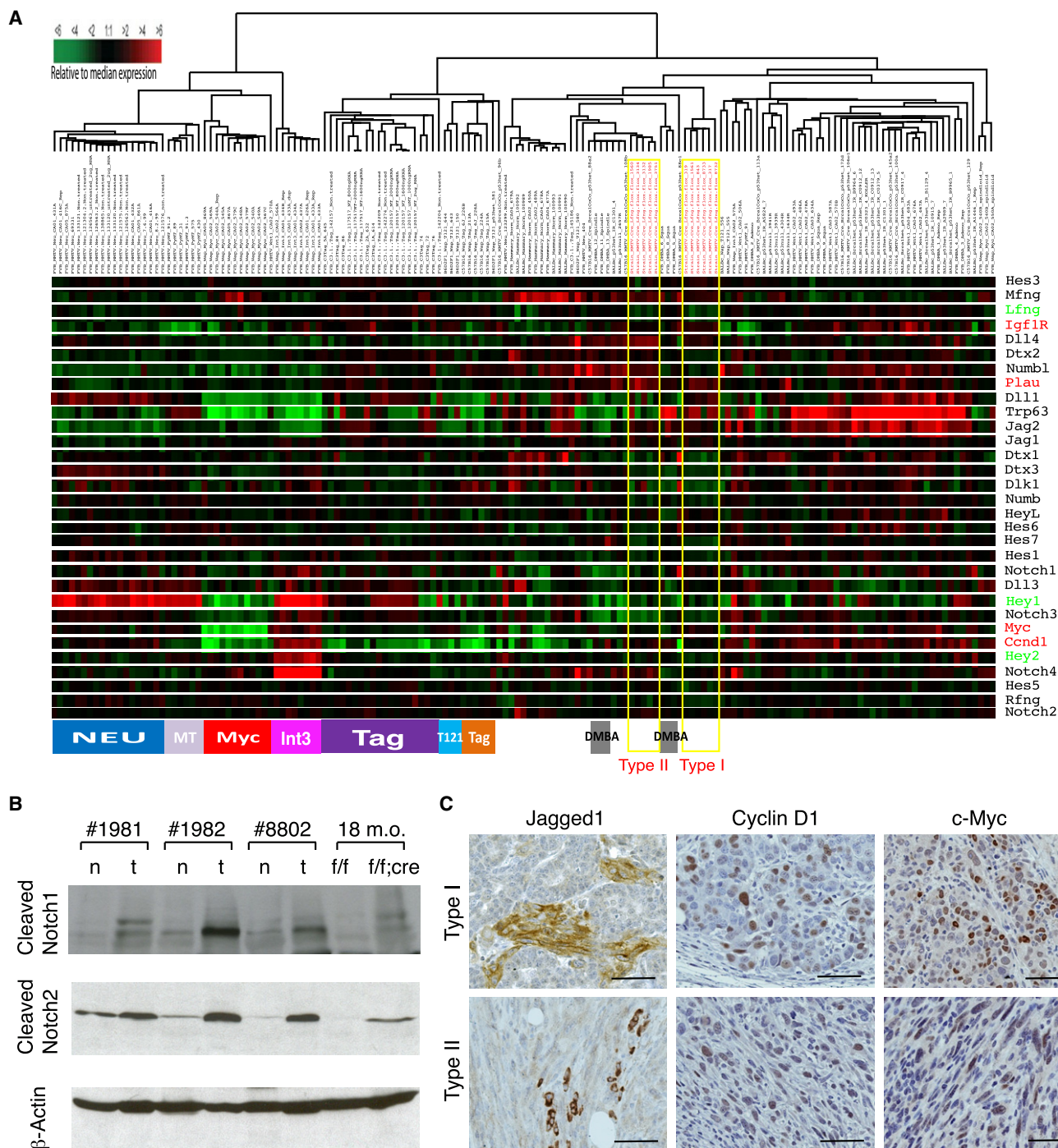


Figure 5. Dysregulation of Notch Signaling Pathway and Downstream Target Genes in *Lfng*^{flox/flox}; MMTV-Cre Tumors

(A) Expression of selected Notch signaling pathway and downstream target genes in tumors from various mouse models of breast cancer, including 11 tumors from *Lfng*^{flox/flox}; MMTV-Cre mice. Expression data from type I and type II *Lfng*^{flox/flox}; MMTV-Cre tumors are contained within yellow boxes. Genes with lower expression in *Lfng*^{flox/flox}; MMTV-Cre tumors are highlighted in green, with higher expression in red. Clusters of tumor models are highlighted at the bottom. DMBA, 7,12-dimethylbenz[a]anthracene.

(B) Western blot analysis of cleaved Notch1 and cleaved Notch2 in mammary tumors (t) and non-tumor mammary tissue (n) from *Lfng*^{flox/flox}; MMTV-Cre mice (#1981, #1982, #8802), as well as in non-tumor mammary tissues from 18-month old *Lfng*^{flox/flox} and *Lfng*^{flox/flox}; MMTV-Cre littermate mice. β -actin served as loading control.

(C) Representative photomicrographs of anti-Jagged1, anti-Cyclin D1 and anti-C-Myc, immunostaining in two main types of *Lfng*^{flox/flox}; MMTV-Cre mammary tumors. Scale bars correspond to 50 μ m.

See also Figure S3.

tumors and HER2⁺ tumors (Figures S5A and S5B). Nevins and colleagues have recently identified gene expression signatures for activation of signaling pathways in breast cancer (Gatza et al., 2010). We therefore tested for activation of these pathways in relation to *LFNG* gene expression. Several oncogenic pathways including those associated with a high rate of proliferation (Myc and E2F1), as well as stem cell signaling (β -catenin), show increased activity in tumors with low *LFNG* expression, whereas the p53 pathway activity is significantly depressed in *LFNG*^{low} tumors (Figure S5B). As *Met* was amplified and overexpressed in our *Lfng* mutant mammary tumors, we also tested for *MET* expression. As previously noted, basal-like and triple negative breast tumors expressed elevated levels of MET (Figure S5B and S5C) (Graveel et al., 2009; Ponzo et al., 2009). Perhaps not surprisingly, low *LFNG* expression was correlated with elevated *MET* levels (Figure S5C).

Finally, a number of studies have highlighted a potential role for Notch receptor signaling in human breast cancer. Therefore, we performed cluster analysis on the UNC publicly available microarray data set (UNC337, GSE18229), and evaluated expression of NOTCH pathway genes in each subtype (Prat et al., 2010). Once again, low-level *LFNG* expression was noted in basal-like tumors from this cohort, and also in a group of claudin-low tumors (Figures 7A and 7B). *HES1*, and to a lesser extent *HEY1*, showed reduced expression in a subset of basal tumors (Figure 7A). In contrast, *c-Myc* and *NOTCH1* expression were elevated in BLBC (Figures 7A and 7B). Thus, *LFNG* expression is consistently low in human basal-like and a subset of claudin-low breast cancers. These data help explain how Jagged-mediated Notch activation stimulates proliferation (Cohen et al., 2010) as well as invasion (Shimizu et al., 2011) of BLBC and other triple-negative breast tumors.

DISCUSSION

With the discovery of Notch4 as a target in MMTV-induced mammary tumor formation, it became clear that elevated Notch signaling was oncogenic in mammary epithelium (Callahan and Smith, 2000). Indeed, translocations that activate *NOTCH1* or 2 have been identified in some triple-negative breast cancers and cell lines (Robinson et al., 2011). In this study we have identified a role for *Lfng* deletion (mouse) or downregulation (human) in BLBC, associated with activation of Notch^{CD} accumulation and induction of oncogenic Notch target gene expression. Multiple Notch receptors are expressed in the mammary gland and several of these are believed to function in breast cancer (Harrison et al., 2010; Haughian et al., 2012; Osipo et al., 2008; Sansone et al., 2007; Yamaguchi et al., 2008). Based on accumulation of luminal progenitor-like cells in *Lfng* mutant basal-like tumors, our data reinforce the finding that elevated Notch signaling enhances proliferation of this compartment (Bouras et al., 2008). Interestingly, a low level of *LFNG* is observed in the vast majority of BLBCs (Figure 7). It will be important to see how these tumors compare in phenotype to the small fraction of triple-negative tumors with Notch-activating translocations (Robinson et al., 2011).

Deletion of *Lfng* in our conditional mutant mice results in reduced expression of the Notch reporter gene during puberty. Based on the known function of Fringe proteins to enhance

Delta ligand-mediated signaling, these data suggest that Dll1, expressed in myoepithelial cells, functions to activate Notch in *Lfng*-expressing MaSCs or bipotent progenitors. In adults, *Jagged1* expression is enhanced within the epithelial compartment (Figure 1) (Reedijk et al., 2005). Loss of *Lfng* in this setting would be expected to increase Jagged/Notch signaling and to induce luminal cell fate commitment as well as proliferation of luminal progenitors (Bouras et al., 2008). It is this effect, in older animals, that is likely responsible for establishing both lineage bias and progenitor compartment expansion to set the stage for transformation.

Human BLBCs contain dozens of mutations that presumably cooperate to transform mammary progenitor cells (Ding et al., 2010). Recent data indicate that cooperative interactions occur between mutations in a number of tumor suppressors, including *RB1*, *TP53*, *BRCA1*, *PTEN*, and *PTPN12* (Carey et al., 2010; Foulkes et al., 2010; Herschkowitz et al., 2008; Holstege et al., 2010; Jiang et al., 2010, 2011; Kobayashi, 2008; Rakha et al., 2008; Saal et al., 2008; Sun et al., 2011). Despite this, it has not been clear how oncogenic pathways interact to control lineage in basal tumors. As a first step to define cooperative pathways in *Lfng* mutant tumors, we performed aCGH analysis and found *Met/Cav* gene amplification and enhanced signaling to represent a common event in this context. Indeed, low-level *LFNG* expression and elevated MET signaling are both associated with BLBC in humans (Gastaldi et al., 2010; Ponzo and Park, 2010). Interestingly, this same amplicon is selected for in brain tumors that occur in *Pten/p53* conditional mutant mice, but not in brain tumors from mice with conditional deletion of *Pten*, *p53*, and *Rb* (Chow et al., 2011), suggesting that *Met/Cav* gene amplification/overexpression may perform similar oncogenic functions as *Rb* gene deletion, an event also associated with BLBC in humans and mice (Herschkowitz et al., 2008; Jiang et al., 2010). The consistent selection for amplification of the *Met/Cav* locus in *Lfng* mutant tumors is striking, and speaks to an emerging concept in cancer whereby genes that function synergistically to enhance signaling through a specific oncogenic signaling pathway will frequently be co-selected during tumor formation or progression. For example, the chromosome 17q amplicon in HER2⁺ breast tumors encodes the HER2 receptor and also the Grb7 adaptor protein, which binds to HER2 protein to facilitate signal transduction (Andrechek et al., 2003; Stein et al., 1994). In addition, the 9p24 amplicon associated with mediastinal B cell lymphoma contains several genes that interact synergistically to enhance IL-13 signaling (Rui et al., 2010). The consistent selection for amplification of the *Met/Cav* gene locus in *Lfng* mutant tumors, and common overexpression of this locus in human BLBC, also leads to synergistic interactions. As depicted in Figure 8, *Lfng* gene loss or reduced expression of *LFNG* in human tumors cooperates with *Met* and *Cav1/2* gene amplification at multiple levels. First, elevated Notch signaling as a result of decreased *Lfng* function, promotes specification and proliferation of luminal progenitors (Bouras et al., 2008). In addition, *Met* amplification would naturally result in elevated *Met* signaling. This effect should be enhanced through absence of Hes/Hey-mediated silencing of the *Met* gene promoter (Stella et al., 2005). Finally, Caveolin1/2 overexpression would be expected to enhance signaling through the insulin receptor and/or Igf-1R (Lu et al., 2008; Ravid et al.,

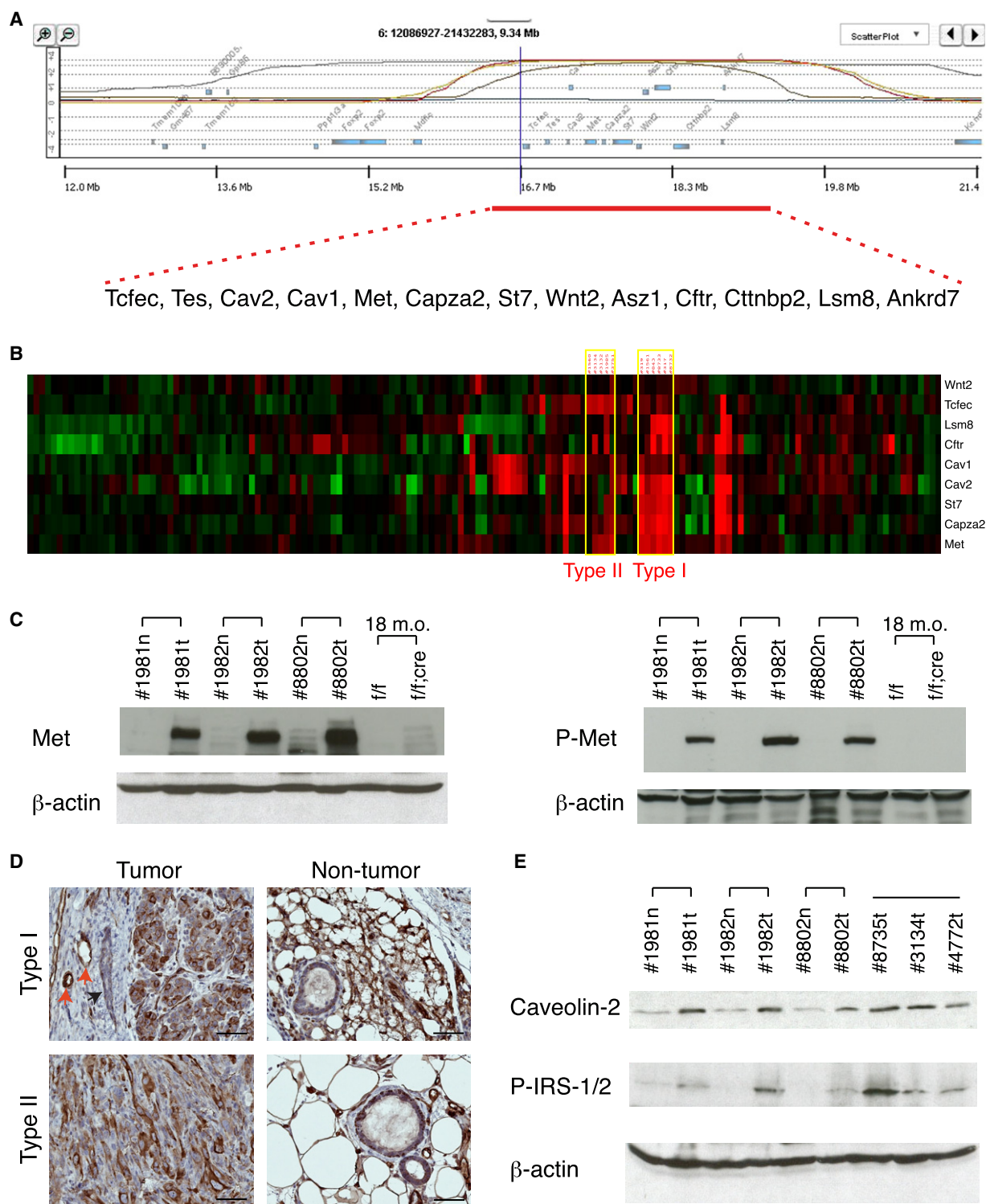


Figure 6. Met/Caveolin Amplicon and Signaling of Met and IgfR in *Lfn^{flox/flox}*; MMTV-Cre Mammary Tumors

(A) aCGH analysis of DNA isolated from four *Lfn^{flox/flox}*; MMTV-Cre mouse tumors and one *Lfn^{flox/+}*; MMTV-Cre tumor showing a commonly amplified locus among all four *Lfn^{flox/flox}*; MMTV-Cre tumors on chromosome 6. Red bar corresponds to the overlapping region containing 13 genes.

(B) Expression of the commonly amplified genes as shown in (A) in 11 *Lfn^{flox/flox}*; MMTV-Cre tumors in comparison with expression of these genes in other mouse models of breast cancer. Expression data from type I and type II *Lfn^{flox/flox}*; MMTV-Cre tumors are contained within yellow boxes.

(C) Western blot analysis of Met and phospho-Met in mammary tumors (t) and non-tumor mammary tissue (n) from *Lfn^{flox/flox}*; MMTV-Cre mice (#1981, #1982, #8802), as well as in mammary tissue from 18-month old *Lfn^{flox/flox}* and *Lfn^{flox/flox}*; MMTV-Cre littermate mice. β-actin served as loading control.

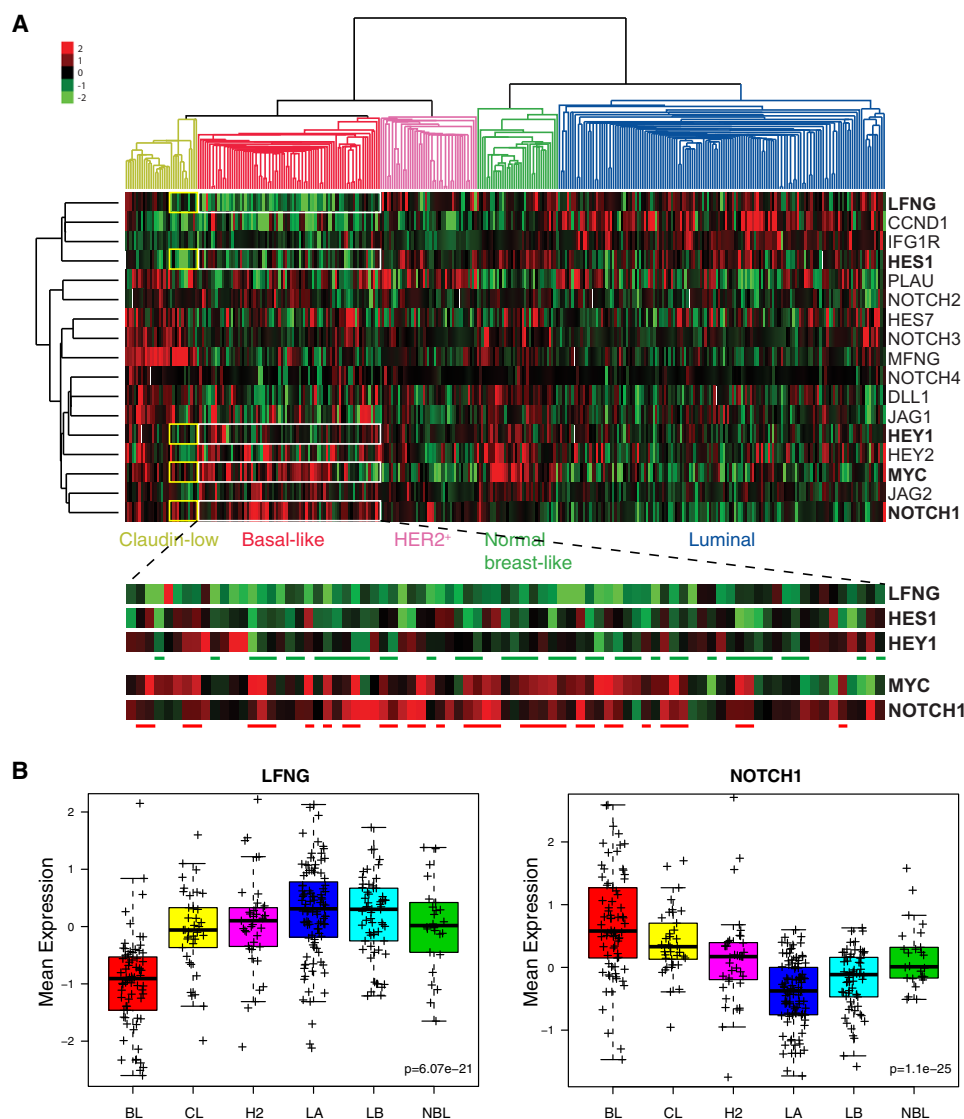


Figure 7. Human Basal-like and A Subset of Claudin-Low Breast Cancers Exhibit Low Levels of *LFNG*, *HES1*, and *HEY1* Gene Expression, but High Levels of *NOTCH1* and *MYC* Gene Expression

(A) Expression of selected Notch pathway genes and proliferation-associated Notch target genes in 320 breast tumors and 17 normal breast samples from the North Carolina data set. 5 subtypes of human breast cancers are highlighted. Expression of *LFNG*, *HES1*, *HEY1*, *MYC* and *NOTCH1* in basal-like breast cancers are boxed in white and shown in enlarged view (bottom of panel A). Expression levels for these five genes in a subset of Claudin-low breast cancers (with lower *LFNG* levels) are boxed in yellow. Green bars mark individual tumors showing decreased expression of all three genes (*LFNG*, *HES1*, *HEY1*). Red bars mark tumors with increased expression of both *NOTCH1* and *MYC*.

(B) Mean expression values for *LFNG* and *NOTCH1* from the North Carolina data set. BL, basal-like; CL, Claudin-low; H2, HER2-positive; LA, luminal A; LB, luminal B; NBL, normal breast-like. p values were calculated by comparing expression means across all subtypes.

See also Figure S5.

2005; Salani et al., 2008). Indeed, our *Lfng* mutant model of BLBC shows elevated Notch signaling to proliferation/invasion Notch target genes as well as reduced Hes/Hey expression,

together with elevated Met and InsR/Igf-1R signaling. Interestingly, elevated Notch signaling and *Met/Cav* overexpression could potentially also connect through induction of uPA (Lee

(D) Representative photomicrographs of anti-Caveolin-1 immunostaining in two main types of *Lfng*^{flax/flax}; *MMTV-Cre* mammary tumors. Red arrows indicate positive staining in blood vessels. Black arrow points to a mammary duct adjacent to the tumor. Note, non-tumor mammary tissues show strong staining in adipocytes and weak staining in myoepithelial cells. Scale bars correspond to 50 μ m.

(E) Western blot analysis of Caveolin-2 and Phospho-IRS-1/2 in mammary tumors (t) and non-tumor mammary tissue (n) from *Lfng*^{flax/flax}; *MMTV-Cre* mice. See also Figure S4.

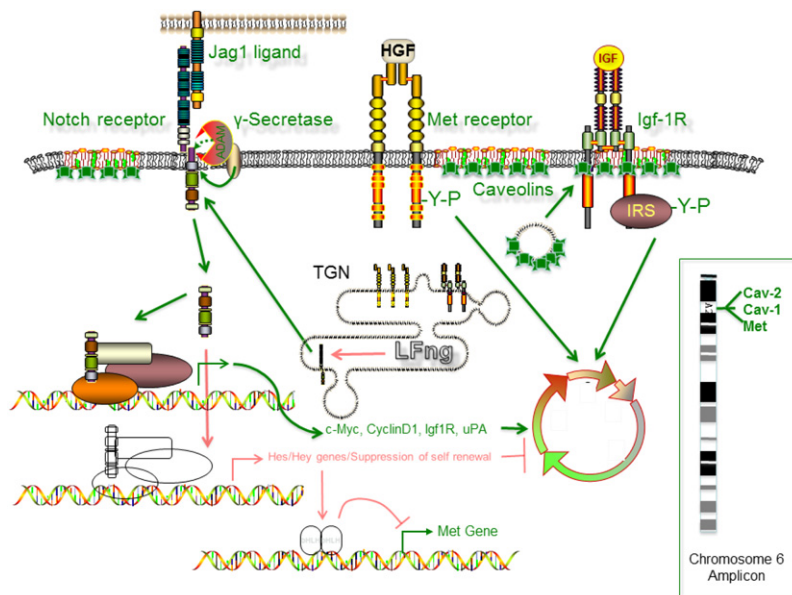


Figure 8. Model of Cooperation between Lfng Deficiency and Met/Caveolin Amplification/Overexpression in Basal-like Breast Cancer

Lfng modifies Notch receptor to inhibit its activation by Jagged ligand and enhance its activation by Dll1 ligand. Loss of *Lfng* results in increased Jagged1-mediated Notch activation and upregulation of c-Myc, Cyclin D1, Igf1R and uPA, leading to increased proliferation. Loss of *Lfng* may decrease Dll1-mediated Notch activation in bipotent mammary progenitor cells, causing expansion of basal cells. Decreased expression of Hes/Hey Notch target genes may de-repress the Met promoter. Selected as cooperative event in *Lfng* deficiency induced mammary tumorigenesis, the Met/caveolin amplicon increases abundance of Met and Caveolin1/2, the latter proteins are predicted to enhance signaling through Igf-1R and IRS. Signaling through Met and Igf-1R stimulate proliferation. TGN, trans Golgi network.

et al., 2006; Monaghan-Benson et al., 2008; Shimizu et al., 2011) and activation of HGF (Naldini et al., 1995). The specific combination of oncogenic mutations would therefore have the effect of promoting a luminal progenitor fate with lower integrin expression, and therefore reduced survival signaling from the basement membrane. The selection for elevated Met and InsR/Igf-1R signaling can thus provide a basal survival-type signal for these luminal progenitor tumor cells. Thus, combination therapy targeting Notch, Met and InsR/Igf-1R or other elements in this hybrid luminal/basal signaling network may prove effective for treatment of BLBC with low *LFNG* gene expression plus overexpression of the *MET/CAV* locus on chromosome 7q31.

EXPERIMENTAL PROCEDURES

Mice

Mice were housed under standard condition and protocols approved by animal care committees at the Hospital for Sick Children and Toronto Center for Phenogenomics. The specific mice used for this study are described elsewhere (Duncan et al., 2005; Hrabě de Angelis et al., 1997; Xu et al., 2010; Zhang and Gridley, 1998). Note, the *Lfng*^{-/-} null allele was generated through expression of Cre in the germline of female *Lfng*^{fllox/+}; MMTV-Cre mice. *Lfng*^{fllox/fllox}, MMTV-Cre experimental animals were generated by crossing *Lfng*^{fllox/fllox} females with *Lfng*^{fllox/fllox}; MMTV-Cre males, which did not result in Cre-mediated deletion in the germline.

Mammary Gland Whole-Mounts, X-Gal Staining, Immunohistochemistry, and Western Analysis

These techniques were performed as per standard protocols and are described in Supplemental Experimental Procedures.

Flow Cytometry and Tumor Cell Transplantation

Mouse mammary tissues were dissociated in Epicult-B medium plus collagenase/hyaluronidase (StemCell Technologies), and single cell suspensions were generated according to manufacturer's protocols. Lineage-depleted (Lin⁻) mammary epithelial cells were prepared using a Mouse Mammary Stem Cell Enrichment Kit (StemCell Technologies). Lin⁻ single cells were suspended in HBSS with calf serum and HEPES, and stained with saturating concentrations of fluorochrome-conjugated antibodies as listed in Supple-

mental Experimental Procedures. Fluorescence was recorded using BD LSR-II flow cytometer and analyzed with FlowJo 9.1 (TreeStar). Dead cells were excluded based on propidium iodide staining. Distinct populations of tumor cells were serially diluted, suspended in matrigel, and then injected into the mammary fat pad of 4-week-old FVB mice (Liu et al., 2007).

Array Comparative Genomic Hybridization

Genomic DNAs were purified using DNAeasy kits (QIAGEN) combined with phenol-chloroform extraction. Array CGH was conducted at the Center for Applied Genomics, Hospital for Sick Children. Briefly, 2.0 µg genomic DNA was labeled using a BioPrime kit (Invitrogen), hybridized to Agilent mouse 1 × 1M CGH arrays, and scanned. Genomic DNA from non-tumor mammary tissue of the same animal was used as reference for tumor samples.

Microarray Gene Expression Analysis

Mouse mammary tumor RNA was purified using an RNeasy mini Kit (QIAGEN). Microarray hybridizations were performed as described in Herschkowitz et al. except that samples were hybridized to custom 180K Agilent microarrays (BARCODE25503) and were scanned using an Agilent Microarray Scanner with Feature Extraction software (Herschkowitz et al., 2007). Analysis of the North Carolina breast cancer data set has been described (Prat et al., 2010). See Supplemental Experimental Procedures for gene expression analysis of mouse mammary tumors and analysis of LFNG expression in 676 human breast cancers.

Statistics

All data are presented as mean ± standard error (SE). For two group comparisons, two-tailed Student's t test was used. For fold changes compared to 1, one-tailed one sample t test was used. A p value of 0.05 or less was considered statistically significant. Mouse tumor-free survival was analyzed by the Kaplan-Meier method and compared by a nonparametric log-rank test. Frequency of tumor-initiating cells was calculated using L-Calcul software (StemCell Technologies).

ACCESSION NUMBERS

Transcriptional profiling data and aCGH data have been deposited in the GEO database (<http://www.ncbi.nlm.nih.gov/geo/>; accession numbers GSE28712 and GSE35855, respectively).

SUPPLEMENTAL INFORMATION

Supplemental Information includes five figures, one table, and Supplemental Experimental Procedures and can be found with this article online at doi:10.1016/j.ccr.2012.03.041.

ACKNOWLEDGMENTS

The authors thank Chao Lu, Jo-Anne Herbrick, Steve Scherer, and Jeff MacDonald in the Center for Applied Genomics at the Hospital for Sick Children as well as technicians at The Toronto Center for Phenogenomics. We also thank members of the Egan and Zacksenhaus labs and colleagues at the Hospital for Sick Children. Finally, we thank Dr. Daniele Merico for bioinformatic analysis, Dr. Jeff Liu for TIC calculations, Drs. Morag Park and Sam Aparicio for discussions on BLBC, and anonymous reviewers for helpful comments on the manuscript. K.X. was supported by a CIHR fellowship. S.E.E.'s lab has been supported by funds from the Canadian Cancer Society Research Institute, from Susan G. Komen for the Cure, and from Genome Canada. Work in C.M.P.'s lab has been supported by funds from the NCI Breast SPORE program (P50-CA58223-09A1), by R01-CA138255 and R01-CA148761, by the Sociedad Española de Oncología Médica (SEOM), and by the Breast Cancer Research Foundation.

Received: January 14, 2011

Revised: October 31, 2011

Accepted: March 8, 2012

Published: May 14, 2012

REFERENCES

- Andrechek, E.R., Laing, M.A., Girgis-Gabardo, A.A., Siegel, P.M., Cardiff, R.D., and Muller, W.J. (2003). Gene expression profiling of neu-induced mammary tumors from transgenic mice reveals genetic and morphological similarities to ErbB2-expressing human breast cancers. *Cancer Res.* 63, 4920–4926.
- Bai, L., and Rohrschneider, L.R. (2010). s-SHIP promoter expression marks activated stem cells in developing mouse mammary tissue. *Genes Dev.* 24, 1882–1892.
- Bouras, T., Pal, B., Vaillant, F., Harburg, G., Asselin-Labat, M.L., Oakes, S.R., Lindeman, G.J., and Visvader, J.E. (2008). Notch signaling regulates mammary stem cell function and luminal cell-fate commitment. *Cell Stem Cell* 3, 429–441.
- Callahan, R., and Smith, G.H. (2000). MMTV-induced mammary tumorigenesis: gene discovery, progression to malignancy and cellular pathways. *Oncogene* 19, 992–1001.
- Cardiff, R.D. (2010). The pathology of EMT in mouse mammary tumorigenesis. *J. Mammary Gland Biol. Neoplasia* 15, 225–233.
- Carey, L., Winer, E., Viale, G., Cameron, D., and Gianni, L. (2010). Triple-negative breast cancer: disease entity or title of convenience? *Nat. Rev. Clin. Oncol.* 7, 683–692.
- Cheang, M.C., Voduc, D., Bajdik, C., Leung, S., McKinney, S., Chia, S.K., Perou, C.M., and Nielsen, T.O. (2008). Basal-like breast cancer defined by five biomarkers has superior prognostic value than triple-negative phenotype. *Clin. Cancer Res.* 14, 1368–1376.
- Chow, L.M., Endersby, R., Zhu, X., Rankin, S., Qu, C., Zhang, J., Broniscer, A., Ellison, D.W., and Baker, S.J. (2011). Cooperativity within and among Pten, p53, and Rb pathways induces high-grade astrocytoma in adult brain. *Cancer Cell* 19, 305–316.
- Cohen, B., Bashirullah, A., Dagnino, L., Campbell, C., Fisher, W.W., Leow, C.C., Whiting, E., Ryan, D., Ziyk, D., Boulianne, G., et al. (1997). Fringe boundaries coincide with Notch-dependent patterning centres in mammals and alter Notch-dependent development in *Drosophila*. *Nat. Genet.* 16, 283–288.
- Cohen, B., Shimizu, M., Izrailit, J., Ng, N.F., Buchman, Y., Pan, J.G., Dering, J., and Reedijk, M. (2010). Cyclin D1 is a direct target of JAG1-mediated Notch signaling in breast cancer. *Breast Cancer Res. Treat.* 123, 113–124.
- Ding, L., Ellis, M.J., Li, S., Larson, D.E., Chen, K., Wallis, J.W., Harris, C.C., McLellan, M.D., Fulton, R.S., Fulton, L.L., et al. (2010). Genome remodelling in a basal-like breast cancer metastasis and xenograft. *Nature* 464, 999–1005.
- Dong, Y., Li, A., Wang, J., Weber, J.D., and Michel, L.S. (2010). Synthetic lethality through combined Notch-epidermal growth factor receptor pathway inhibition in basal-like breast cancer. *Cancer Res.* 70, 5465–5474.
- Duncan, A.W., Rattis, F.M., DiMascio, L.N., Congdon, K.L., Pazianos, G., Zhao, C., Yoon, K., Cook, J.M., Willert, K., Gaiano, N., and Reya, T. (2005). Integration of Notch and Wnt signaling in hematopoietic stem cell maintenance. *Nat. Immunol.* 6, 314–322.
- Elsheikh, S.E., Green, A.R., Rakha, E.A., Samaka, R.M., Ammar, A.A., Powe, D., Reis-Filho, J.S., and Ellis, I.O. (2008). Caveolin 1 and Caveolin 2 are associated with breast cancer basal-like and triple-negative immunophenotype. *Br. J. Cancer* 99, 327–334.
- Foulkes, W.D., Smith, I.E., and Reis-Filho, J.S. (2010). Triple-negative breast cancer. *N. Engl. J. Med.* 363, 1938–1948.
- Gastaldi, S., Comoglio, P.M., and Trusolino, L. (2010). The Met oncogene and basal-like breast cancer: another culprit to watch out for? *Breast Cancer Res.* 12, 208.
- Gatza, M.L., Lucas, J.E., Barry, W.T., Kim, J.W., Wang, Q., Crawford, M.D., Datto, M.B., Kelley, M., Mathey-Prevot, B., Potti, A., and Nevins, J.R. (2010). A pathway-based classification of human breast cancer. *Proc. Natl. Acad. Sci. USA* 107, 6994–6999.
- Ginestier, C., Hur, M.H., Charafe-Jauffret, E., Monville, F., Dutcher, J., Brown, M., Jacquemier, J., Viens, P., Kleer, C.G., Liu, S., et al. (2007). ALDH1 is a marker of normal and malignant human mammary stem cells and a predictor of poor clinical outcome. *Cell Stem Cell* 1, 555–567.
- Graveel, C.R., DeGroot, J.D., Su, Y., Koeman, J., Dykema, K., Leung, S., Snider, J., Davies, S.R., Swiatek, P.J., Cottingham, S., et al. (2009). Met induces diverse mammary carcinomas in mice and is associated with human basal breast cancer. *Proc. Natl. Acad. Sci. USA* 106, 12909–12914.
- Haines, N., and Irvine, K.D. (2003). Glycosylation regulates Notch signalling. *Nat. Rev. Mol. Cell Biol.* 4, 786–797.
- Harrison, H., Farnie, G., Howell, S.J., Rock, R.E., Stylianou, S., Brennan, K.R., Bundred, N.J., and Clarke, R.B. (2010). Regulation of breast cancer stem cell activity by signaling through the Notch4 receptor. *Cancer Res.* 70, 709–718.
- Haughian, J.M., Pinto, M.P., Harrell, J.C., Bliesner, B.S., Joensuu, K.M., Dye, W.W., Sartorius, C.A., Tan, A.C., Heikkila, P., Perou, C.M., and Horwitz, K.B. (2012). Maintenance of hormone responsiveness in luminal breast cancers by suppression of Notch. *Proc. Natl. Acad. Sci. USA* 109, 2742–2742.
- Hennessy, B.T., Gonzalez-Angulo, A.M., Stemke-Hale, K., Gilcrease, M.Z., Krishnamurthy, S., Lee, J.S., Fridlyand, J., Sahin, A., Agarwal, R., Joy, C., et al. (2009). Characterization of a naturally occurring breast cancer subset enriched in epithelial-to-mesenchymal transition and stem cell characteristics. *Cancer Res.* 69, 4116–4124.
- Herschkowitz, J.I., Simin, K., Weigman, V.J., Mikaelian, I., Usary, J., Hu, Z., Rasmussen, K.E., Jones, L.P., Assefnia, S., Chandrasekharan, S., et al. (2007). Identification of conserved gene expression features between murine mammary carcinoma models and human breast tumors. *Genome Biol.* 8, R76.
- Herschkowitz, J.I., He, X., Fan, C., and Perou, C.M. (2008). The functional loss of the retinoblastoma tumour suppressor is a common event in basal-like and luminal B breast carcinomas. *Breast Cancer Res.* 10, R75.
- Hochgräfe, F., Zhang, L., O'Toole, S.A., Browne, B.C., Pinese, M., Porta Cubas, A., Lehrbach, G.M., Croucher, D.R., Rickwood, D., Boulghourjian, A., et al. (2010). Tyrosine phosphorylation profiling reveals the signaling network characteristics of Basal breast cancer cells. *Cancer Res.* 70, 9391–9401.
- Holstege, H., Horlings, H.M., Velds, A., Langerød, A., Børresen-Dale, A.L., van de Vijver, M.J., Nederlof, P.M., and Jonkers, J. (2010). BRCA1-mutated and basal-like breast cancers have similar aCGH profiles and a high incidence of protein truncating TP53 mutations. *BMC Cancer* 10, 654.
- Hrabě de Angelis, M., McIntyre, J., 2nd, and Gossler, A. (1997). Maintenance of somite borders in mice requires the Delta homologue Dll1. *Nature* 386, 717–721.
- Hvid, H., Fels, J.J., Kirk, R.K., Thorup, I., Jensen, H.E., Hansen, B.F., and Oleksiewicz, M.B. (2011). In situ phosphorylation of Akt and ERK1/2 in rat mammary gland, colon, and liver following treatment with human insulin and IGF-1. *Toxicol. Pathol.* 39, 623–640.
- Irvine, K.D. (1999). Fringe, Notch, and making developmental boundaries. *Curr. Opin. Genet. Dev.* 9, 434–441.

- Jiang, Z., Deng, T., Jones, R., Li, H., Herschkowitz, J.I., Liu, J.C., Weigman, V.J., Tsao, M.S., Lane, T.F., Perou, C.M., and Zacksenhaus, E. (2010). Rb deletion in mouse mammary progenitors induces luminal-B or basal-like/EMT tumor subtypes depending on p53 status. *J. Clin. Invest.* 120, 3296–3309.
- Jiang, Z., Jones, R., Liu, J.C., Deng, T., Robinson, T., Chung, P.E.D., Wang, S., Herschkowitz, J.I., Egan, S.E., Perou, C.M., and Zacksenhaus, E. (2011). RB1 and p53 at the crossroad of EMT and triple-negative breast cancer. *Cell Cycle* 10, 1563–1570.
- Johnston, S.H., Rauskolb, C., Wilson, R., Prabhakaran, B., Irvine, K.D., and Vogt, T.F. (1997). A family of mammalian Fringe genes implicated in boundary determination and the Notch pathway. *Development* 124, 2245–2254.
- Jones, R.A., Campbell, C.I., Gunther, E.J., Chodosh, L.A., Petrik, J.J., Khokha, R., and Moorehead, R.A. (2007). Transgenic overexpression of IGF-IR disrupts mammary ductal morphogenesis and induces tumor formation. *Oncogene* 26, 1636–1644.
- Klinakis, A., Szabolcs, M., Politi, K., Kiaris, H., Artavanis-Tsakonas, S., and Efstratiadis, A. (2006). Myc is a Notch1 transcriptional target and a requisite for Notch1-induced mammary tumorigenesis in mice. *Proc. Natl. Acad. Sci. USA* 103, 9262–9267.
- Kobayashi, S. (2008). Basal-like subtype of breast cancer: a review of its unique characteristics and their clinical significance. *Breast Cancer* 15, 153–158.
- Lee, C.W., Raskett, C.M., Prudovsky, I., and Altieri, D.C. (2008a). Molecular dependence of estrogen receptor-negative breast cancer on a notch-survivin signaling axis. *Cancer Res.* 68, 5273–5281.
- Lee, C.W., Simin, K., Liu, Q., Plescia, J., Guha, M., Khan, A., Hsieh, C.C., and Altieri, D.C. (2008b). A functional Notch-survivin gene signature in basal breast cancer. *Breast Cancer Res.* 10, R97.
- Lee, K.H., Choi, E.Y., Kim, M.K., Hyun, M.S., Jang, B.I., Kim, T.N., Kim, S.W., Song, S.K., Kim, J.H., and Kim, J.R. (2006). Regulation of hepatocyte growth factor-mediated urokinase plasminogen activator secretion by MEK/ERK activation in human stomach cancer cell lines. *Exp. Mol. Med.* 38, 27–35.
- Leong, K.G., Niessen, K., Kulic, I., Raouf, A., Eaves, C., Pollet, I., and Karsan, A. (2007). Jagged1-mediated Notch activation induces epithelial-to-mesenchymal transition through Slug-induced repression of E-cadherin. *J. Exp. Med.* 204, 2935–2948.
- Lim, E., Vaillant, F., Wu, D., Forrest, N.C., Pal, B., Hart, A.H., Asselin-Labat, M.L., Gyorki, D.E., Ward, T., Partanen, A., et al; kConFab. (2009). Aberrant luminal progenitors as the candidate target population for basal tumor development in BRCA1 mutation carriers. *Nat. Med.* 15, 907–913.
- Liu, J.C., Deng, T., Lehal, R.S., Kim, J., and Zacksenhaus, E. (2007). Identification of tumorsphere- and tumor-initiating cells in HER2/Neu-induced mammary tumors. *Cancer Res.* 67, 8671–8681.
- Lu, X., Kambe, F., Cao, X., Yamauchi, M., and Seo, H. (2008). Insulin-like growth factor-I activation of Akt survival cascade in neuronal cells requires the presence of its cognate receptor in caveolae. *Exp. Cell Res.* 314, 342–351.
- Molyneux, G., Geyer, F.C., Magnay, F.A., McCarthy, A., Kendrick, H., Natrajan, R., Mackay, A., Grigoriadis, A., Tutt, A., Ashworth, A., et al. (2010). BRCA1 basal-like breast cancers originate from luminal epithelial progenitors and not from basal stem cells. *Cell Stem Cell* 7, 403–417.
- Monaghan-Benson, E., Mastick, C.C., and McKeown-Longo, P.J. (2008). A dual role for caveolin-1 in the regulation of fibronectin matrix assembly by uPAR. *J. Cell Sci.* 121, 3693–3703.
- Naldini, L., Vigna, E., Bardelli, A., Follenzi, A., Galimi, F., and Comoglio, P.M. (1995). Biological activation of pro-HGF (hepatocyte growth factor) by urokinase is controlled by a stoichiometric reaction. *J. Biol. Chem.* 270, 603–611.
- Niranjan, B., Buluwela, L., Yant, J., Perusinghe, N., Atherton, A., Phippard, D., Dale, T., Gusterson, B., and Kamalati, T. (1995). HGF/SF: a potent cytokine for mammary growth, morphogenesis and development. *Development* 121, 2897–2908.
- Osipo, C., Patel, P., Rizzo, P., Clementz, A.G., Hao, L., Golde, T.E., and Miele, L. (2008). ErbB-2 inhibition activates Notch-1 and sensitizes breast cancer cells to a gamma-secretase inhibitor. *Oncogene* 27, 5019–5032.
- Panin, V.M., Papayannopoulos, V., Wilson, R., and Irvine, K.D. (1997). Fringe modulates Notch-ligand interactions. *Nature* 387, 908–912.
- Parr, C., Watkins, G., and Jiang, W.G. (2004). The possible correlation of Notch-1 and Notch-2 with clinical outcome and tumour clinicopathological parameters in human breast cancer. *Int. J. Mol. Med.* 14, 779–786.
- Pece, S., Serresi, M., Santolini, E., Capra, M., Hulleman, E., Galimberti, V., Zurrida, S., Maisonneuve, P., Viale, G., and Di Fiore, P.P. (2004). Loss of negative regulation by Numb over Notch is relevant to human breast carcinogenesis. *J. Cell Biol.* 167, 215–221.
- Perou, C.M., and Børresen-Dale, A.L. (2011). Systems Biology and Genomics of Breast Cancer. Cold Spring Harb. Perspect. Biol. 3.
- Ponzo, M.G., Lesurf, R., Petkiewicz, S., O'Malley, F.P., Pinnaduwa, D., Andrulis, I.L., Bull, S.B., Chughtai, N., Zuo, D., Souleimanova, M., et al. (2009). Met induces mammary tumors with diverse histologies and is associated with poor outcome and human basal breast cancer. *Proc. Natl. Acad. Sci. USA* 106, 12903–12908.
- Ponzo, M.G., and Park, M. (2010). The Met receptor tyrosine kinase and basal breast cancer. *Cell Cycle* 9, 1043–1050.
- Prat, A., Parker, J.S., Karginova, O., Fan, C., Livasy, C., Herschkowitz, J.I., He, X., and Perou, C.M. (2010). Phenotypic and molecular characterization of the claudin-low intrinsic subtype of breast cancer. *Breast Cancer Res.* 12, R68.
- Raafat, A., Goldhar, A.S., Klauzinska, M., Xu, K., Amirjazi, I., McCurdy, D., Lashin, K., Salomon, D., Vonderhaar, B.K., Egan, S., and Callahan, R. (2011). Expression of Notch receptors, ligands, and target genes during development of the mouse mammary gland. *J. Cell. Physiol.* 226, 1940–1952.
- Rakha, E.A., Reis-Filho, J.S., and Ellis, I.O. (2008). Basal-like breast cancer: a critical review. *J. Clin. Oncol.* 26, 2568–2581.
- Raouf, A., Zhao, Y., To, K., Stingl, J., Delaney, A., Barbara, M., Iscove, N., Jones, S., McKinney, S., Emerman, J., et al. (2008). Transcriptome analysis of the normal human mammary cell commitment and differentiation process. *Cell Stem Cell* 3, 109–118.
- Ravid, D., Maor, S., Werner, H., and Liscovitch, M. (2005). Caveolin-1 inhibits cell detachment-induced p53 activation and anoikis by upregulation of insulin-like growth factor-I receptors and signaling. *Oncogene* 24, 1338–1347.
- Reedijk, M., Odorcic, S., Chang, L., Zhang, H., Miller, N., McCready, D.R., Lockwood, G., and Egan, S.E. (2005). High-level coexpression of JAG1 and NOTCH1 is observed in human breast cancer and is associated with poor overall survival. *Cancer Res.* 65, 8530–8537.
- Reedijk, M., Pinnaduwa, D., Dickson, B.C., Mulligan, A.M., Zhang, H., Bull, S.B., O'Malley, F.P., Egan, S.E., and Andrulis, I.L. (2008). JAG1 expression is associated with a basal phenotype and recurrence in lymph node-negative breast cancer. *Breast Cancer Res. Treat.* 111, 439–448.
- Robinson, D.R., Kalyana-Sundaram, S., Wu, Y.M., Shankar, S., Cao, X., Ateeq, B., Asangani, I.A., Iyer, M., Maher, C.A., Grasso, C.S., et al. (2011). Functionally recurrent rearrangements of the MAST kinase and Notch gene families in breast cancer. *Nat. Med.* 17, 1646–1651.
- Rui, L., Emre, N.C., Kruhlak, M.J., Chung, H.J., Steidl, C., Slack, G., Wright, G.W., Lenz, G., Ngo, V.N., Shaffer, A.L., et al. (2010). Cooperative epigenetic modulation by cancer amplicon genes. *Cancer Cell* 18, 590–605.
- Saal, L.H., Gruvberger-Saal, S.K., Persson, C., Lövgren, K., Jumppanen, M., Staaf, J., Jönsson, G., Pires, M.M., Maurer, M., Holm, K., et al. (2008). Recurrent gross mutations of the PTEN tumor suppressor gene in breast cancers with deficient DSB repair. *Nat. Genet.* 40, 102–107.
- Salani, B., Briatore, L., Garibaldi, S., Cordera, R., and Maggi, D. (2008). Caveolin-1 down-regulation inhibits insulin-like growth factor-I receptor signal transduction in H9C2 rat cardiomyoblasts. *Endocrinology* 149, 461–465.
- Sansone, P., Storci, G., Tavolari, S., Guarnieri, T., Giovannini, C., Taffurelli, M., Ceccarelli, C., Santini, D., Paterini, P., Marcu, K.B., et al. (2007). IL-6 triggers malignant features in mammospheres from human ductal breast carcinoma and normal mammary gland. *J. Clin. Invest.* 117, 3988–4002.
- Savage, K., Lambros, M.B., Robertson, D., Jones, R.L., Jones, C., Mackay, A., James, M., Hornick, J.L., Pereira, E.M., Milanezi, F., et al. (2007). Caveolin 1 is overexpressed and amplified in a subset of basal-like and metaplastic breast

carcinomas: a morphologic, ultrastructural, immunohistochemical, and in situ hybridization analysis. *Clin. Cancer Res.* 13, 90–101.

Shackleton, M., Vaillant, F., Simpson, K.J., Stingl, J., Smyth, G.K., Asselin-Labat, M.L., Wu, L., Lindeman, G.J., and Visvader, J.E. (2006). Generation of a functional mammary gland from a single stem cell. *Nature* 439, 84–88.

Shimizu, M., Cohen, B., Goldvasser, P., Berman, H., Virtanen, C., and Reedijk, M. (2011). Plasminogen activator uPA is a direct transcriptional target of the JAG1-Notch receptor signaling pathway in breast cancer. *Cancer Res.* 71, 277–286.

Smolen, G.A., Muir, B., Mohapatra, G., Barmettler, A., Kim, W.J., Rivera, M.N., Haserlat, S.M., Okimoto, R.A., Kwak, E., Dahiya, S., et al. (2006). Frequent met oncogene amplification in a Brca1/Trp53 mouse model of mammary tumorigenesis. *Cancer Res.* 66, 3452–3455.

Stein, D., Wu, J., Fuqua, S.A., Roonprapunt, C., Yajnik, V., D'Eustachio, P., Moskow, J.J., Buchberg, A.M., Osborne, C.K., and Margolis, B. (1994). The SH2 domain protein GRB-7 is co-amplified, overexpressed and in a tight complex with HER2 in breast cancer. *EMBO J.* 13, 1331–1340.

Stella, M.C., Trusolino, L., Pennacchietti, S., and Comoglio, P.M. (2005). Negative feedback regulation of Met-dependent invasive growth by Notch. *Mol. Cell. Biol.* 25, 3982–3996.

Stingl, J., Eirew, P., Ricketson, I., Shackleton, M., Vaillant, F., Choi, D., Li, H.I., and Eaves, C.J. (2006). Purification and unique properties of mammary epithelial stem cells. *Nature* 439, 993–997.

Stylianou, S., Clarke, R.B., and Brennan, K. (2006). Aberrant activation of notch signaling in human breast cancer. *Cancer Res.* 66, 1517–1525.

Sun, T., Aceto, N., Meerbrey, K.L., Kessler, J.D., Zhou, C., Migliaccio, I., Nguyen, D.X., Pavlova, N.N., Botero, M., Huang, J., et al. (2011). Activation

of multiple proto-oncogenic tyrosine kinases in breast cancer via loss of the PTPN12 phosphatase. *Cell* 144, 703–718.

Taube, J.H., Herschkowitz, J.I., Komurov, K., Zhou, A.Y., Gupta, S., Yang, J., Hartwell, K., Onder, T.T., Gupta, P.B., Evans, K.W., et al. (2010). Core epithelial-to-mesenchymal transition interactome gene-expression signature is associated with claudin-low and metaplastic breast cancer subtypes. *Proc. Natl. Acad. Sci. USA* 107, 15449–15454.

Visvader, J.E. (2009). Keeping abreast of the mammary epithelial hierarchy and breast tumorigenesis. *Genes Dev.* 23, 2563–2577.

Visvader, J.E., and Smith, G.H. (2011). Murine Mammary Epithelial Stem Cells: Discovery, Function, and Current Status. *Cold Spring Harb. Perspect. Biol.* 3.

Wagner, K.U., Wall, R.J., St-Onge, L., Gruss, P., Wynshaw-Boris, A., Garrett, L., Li, M., Furth, P.A., and Hennighausen, L. (1997). Cre-mediated gene deletion in the mammary gland. *Nucleic Acids Res.* 25, 4323–4330.

Xu, K., Nieuwenhuis, E., Cohen, B.L., Wang, W., Canty, A.J., Danska, J.S., Coultas, L., Rossant, J., Wu, M.Y., Piscione, T.D., et al. (2010). Lunatic Fringe-mediated Notch signaling is required for lung alveogenesis. *Am. J. Physiol. Lung Cell. Mol. Physiol.* 298, L45–L56.

Yalcin-Ozuysal, O., Fiche, M., Guitierrez, M., Wagner, K.U., Raffoul, W., and Briskin, C. (2010). Antagonistic roles of Notch and p63 in controlling mammary epithelial cell fates. *Cell Death Differ.* 17, 1600–1612.

Yamaguchi, N., Oyama, T., Ito, E., Satoh, H., Azuma, S., Hayashi, M., Shimizu, K., Honma, R., Yanagisawa, Y., Nishikawa, A., et al. (2008). NOTCH3 signaling pathway plays crucial roles in the proliferation of ErbB2-negative human breast cancer cells. *Cancer Res.* 68, 1881–1888.

Zhang, N., and Gridley, T. (1998). Defects in somite formation in lunatic fringe-deficient mice. *Nature* 394, 374–377.

S1PR1-STAT3 Signaling Is Crucial for Myeloid Cell Colonization at Future Metastatic Sites

Jiehui Deng,¹ Yong Liu,¹ Heehyoung Lee,¹ Andreas Herrmann,¹ Wang Zhang,¹ Chunyan Zhang,¹ Shudan Shen,¹ Saul J. Priceman,¹ Maciej Kujawski,¹ Sumanta K. Pal,² Andrew Raubitschek,¹ Dave S.B. Hoon,⁵ Stephen Forman,³ Robert A. Figlin,⁶ Jie Liu,^{7,8} Richard Jove,⁴ and Hua Yu^{1,8,*}

¹Department of Cancer Immunotherapeutics and Tumor Immunology

²Department of Medical Oncology

³Department of Hematology and Hematopoietic Cell Transplantation

⁴Department of Molecular Medicine

Beckman Research Institute and City of Hope Comprehensive Cancer Center, Duarte, CA 91010, USA

⁵Department of Molecular Oncology, John Wayne Cancer Institute, Santa Monica, CA 90404, USA

⁶Department of Hematology-Oncology, Cedars-Sinai Medical Center, Los Angeles, CA 90048, USA

⁷Department of Digestive Diseases of Huashan Hospital, Department of Immunology of Shanghai Medical School, Fudan University, Shanghai, 200040, China

⁸Center for Translational Medicine, Zhangjiang High-Tech Park, Shanghai, 201203, China

*Correspondence: hyu@coh.org

DOI 10.1016/j.ccr.2012.03.039

SUMMARY

Recent studies underscore the importance of myeloid cells in rendering distant organs hospitable for disseminating tumor cells to colonize. However, what enables myeloid cells to have an apparently superior capacity to colonize distant organs is unclear. Here, we show that S1PR1-STAT3 upregulation in tumor cells induces factors that activate S1PR1-STAT3 in various cells in premetastatic sites, leading to premetastatic niche formation. Targeting either S1PR1 or STAT3 in myeloid cells disrupts existing premetastatic niches. S1PR1-STAT3 pathway enables myeloid cells to intravasate, prime the distant organ microenvironment and mediate sustained proliferation and survival of their own and other stromal cells at future metastatic sites. Analyzing tumor-free lymph nodes from cancer patients shows elevated myeloid infiltrates, STAT3 activity, and increased survival signal.

INTRODUCTION

Several seminal studies have documented the importance of myeloid cells in providing a sanctuary for tumor cells to adhere, survive, and colonize secondary sites (Erlor et al., 2009; Hiratsuka et al., 2006; Kaplan et al., 2005; Kim et al., 2009; Kowanetz et al., 2010; Psaila and Lyden, 2009). Although myeloid cells are mobile and produce chemokines and other molecules in response to the tumor environment thereby promoting cancer progression (Biswas and Mantovani, 2010; Coussens et al., 2000; Du et al., 2008; Fan and Malik, 2003; Mantovani et al.,

2008; Pollard, 2004; Shojaei et al., 2007), myeloid cells need to proliferate and evade apoptosis in order to establish colonies at future metastatic sites. However, mechanisms that enable myeloid cells to colonize in the hostile environment at future metastatic sites remain to be identified. In addition, the underlying molecular mechanism(s) that orchestrates tumor cells, myeloid cells, resident fibroblasts, and other stromal cell types to achieve outgrowths prior to tumor cell arrival at distant organs remains unknown. A more complete body of knowledge on such molecular mechanisms may facilitate translation of potentially paradigm-shifting therapeutic strategies for the treatment of

Significance

Conceptually, our results introduce the idea that S1PR1-STAT3 signaling axis is elevated in distant organs prior to tumor cell arrival, which empowers myeloid cells to invade, proliferate and resist apoptosis at premetastatic sites. We further identify a role of myeloid cells in regulating fibroblasts by producing factors similar to those of tumor cells, thereby facilitating formation of premetastatic niches. Additionally, we demonstrate the ability of STAT3 in regulating numerous genes crucial for premetastatic niche formation in bone marrow-derived cells. Perhaps the most significant aspect of our current studies is the therapeutic potential to target the S1PR1-STAT3 signaling axis to eliminate and/or reduce preformed premetastatic niches, thereby preventing tumor metastasis.

tumor metastasis: target premetastatic niches before clinical detection of metastasis.

Persistently activated STAT3 in tumor cells acting as a crucial oncogenic mediator and potent transcriptional factor has been widely documented (Bollrath et al., 2009; Bromberg et al., 1999; Catlett-Falcone et al., 1999; Chiarle et al., 2005; Fukuda et al., 2011; Grivennikov et al., 2009; Lee et al., 2010; Lesina et al., 2011; Yu et al., 2007, 2009). Recent studies have also demonstrated persistent activation of STAT3 in myeloid cells and T cells at primary tumor sites, promoting immunosuppression, tumor angiogenesis, tumor growth, and metastasis (Biswas and Mantovani, 2010; Kortylewski et al., 2005, 2009c; Kujawski et al., 2008; Wang et al., 2009). While many cytokines, chemokines, and growth factors can activate STAT3 in tumor cells and in tumor-associated stromal cells (Biswas and Mantovani, 2010; Bollrath et al., 2009; Catlett-Falcone et al., 1999; Grivennikov et al., 2009; Kortylewski et al., 2009c; Kujawski et al., 2008; Lee et al., 2010; Lesina et al., 2011; Wang et al., 2009; Yu et al., 2007), our recent studies showed a critical role of S1PR1 in maintaining persistent STAT3 activation in primary tumors, by regulating both tumor cells and tumor-infiltrating myeloid cells (Lee et al., 2010). S1PR1 and its ligand, S1P, play a fundamental role in endothelial cells for regulating tumor angiogenesis, which is also crucial for metastasis (Chae et al., 2004; Gao et al., 2008; Holmgren et al., 1995; Spiegel and Milstien, 2003; Visentin et al., 2006). Although the importance of tumor-infiltrating myeloid cells in facilitating tumor cell invasion and metastasis is well established, the role of myeloid cells in forming a sanctuary for tumor cells in distant organs prior to tumor cell arrival/outgrowth has only begun to be appreciated (Erler et al., 2009; Kaplan et al., 2005; Psaila and Lyden, 2009). Our current study investigates whether STAT3 is persistently activated at future metastatic sites prior to tumor cell arrival and whether S1PR1-STAT3 signaling in both tumor cells and myeloid cells is critical for tumor cell outgrowth/metastasis, and thus a potential therapeutic target.

RESULTS

S1PR1-STAT3-Induced Tumor Factors Activate S1PR1-STAT3 at Distant Premetastatic Sites

To investigate whether increased STAT3 signaling in tumor cells would induce production of factors that could prime distant premetastatic sites, we generated tumor conditioned media (TCM) from control or *S1pr1* overexpressing (*S1pr1^{high}*) mouse B16 melanoma and MB49 bladder tumor cells. The parental tumor cells display relatively low Stat3 activation in cultured cells, which was elevated by *S1pr1* overexpression (Lee et al., 2010). We examined several factors known to activate Stat3, and detected elevated levels of both IL-6 and IL-10 in the TCM derived from the *S1pr1^{high}* tumor cells (Figure S1A available online). We treated mice with TCMs from control and *S1pr1^{high}* tumor cells for 5 days prior to parental tumor cell challenge. Three days after tumor challenge when there were no detectable metastases, we observed extensive CD11b⁺ myeloid cell cluster formation in the lung (Figure 1A). Importantly, we also observed widespread Stat3 activation in lung-associated stromal cells by tumor-secreted factors (Figures S1B and S1C). Further analyses of CD11b⁺ myeloid cells indicated that changing Stat3 activity in

tumor cells altered the number of myeloid-derived suppressor cells (Figure S1D).

We next performed experiments to ensure that in the absence of tumor cell challenge, treatment with TCM derived from *S1pr1^{high}* tumor cells could activate Stat3 in future metastatic sites and induce premetastatic niche formation in distant future metastatic sites. Our results showed that treating mice with the TCM from *S1pr1^{high}* tumor cells for 5 days could induce strong Stat3 activation and myeloid infiltration without tumor cell challenge (Figure 1B). Stat3 activity was detectable in myeloid cells and also widespread in the lung (Figure 1B). Furthermore, treating mice with TCM generated from *S1pr1^{high}* tumor cells, but not TCM derived from control tumor cells, was able to induce *S1pr1* expression and phosphorylated Stat3 (p-Stat3) in both lung CD11b⁺ myeloid cells and metastatic nodules, which was accompanied by extensive metastasis at days 9 and 14 post-tumor cell challenge (Figure 1C). We also observed an increase in total Stat3 protein level, which is likely caused by autoregulation of p-Stat3.

Since resident fibroblasts at future metastatic sites play an important role in premetastatic niche formation (Kaplan et al., 2005; Orimo et al., 2005), and because we detected extensive Stat3 activation at the future metastatic sites (Figures 1A and 1B), we tested whether *S1pr1*-Stat3-induced tumor factors could activate fibroblasts to produce fibronectin, a factor crucial for premetastatic niche formation (Erler et al., 2009; Kaplan et al., 2005; Psaila and Lyden, 2009). Treating mouse embryonic fibroblasts (MEFs), as well as primary fibroblasts derived from mouse lungs, with TCM prepared from *S1pr1^{high}* tumor cells, but not that from control tumor cells, induced fibronectin expression and Stat3 activation (Figure 1D). Trypsin treatment of TCM for *S1pr1^{high}* tumor cells blocked fibronectin and Stat3 activation in the fibroblasts. Heat treatment of the same TCM also, to a lesser degree, reduced p-Stat3 level (Figure S1E).

Myeloid Cell S1PR1-STAT3 Is Crucial for Premetastatic Niche Formation

Since S1PR1-STAT3 signaling is activated at premetastatic sites and in myeloid clusters, we assessed whether Stat3 activation intrinsic to myeloid cells is required for maintaining *S1pr1*-Stat3 activity in the premetastatic sites and for formation of premetastatic niches. We induced *Stat3* ablation in the myeloid compartment with poly(I:C) treatment using *Mx1Cre-Stat3^{loxp/loxp}* mice. Relative to the control *Stat3^{loxp/loxp}* mice with intact *Stat3* alleles, ablating *Stat3* in the myeloid compartment of *Mx1Cre-Stat3^{loxp/loxp}* mice effectively reduced Stat3 activity in the entire lung and eliminated formation of premetastatic niches (Figure 2A), as well as lung metastasis (Figure 2B, upper panel). In addition to CD11b⁺ cells, endothelial cells and fibroblasts were among the p-Stat3-positive cells, which were reduced by ablating *Stat3* in the myeloid compartment (Figure 2B, lower panel).

In vivo ablating *S1pr1* in myeloid cells using *Mx1Cre-S1pr1^{loxp/loxp}* mice reduced Stat3 activity and myeloid clusters in the lung (Figure 2C). Additionally, increased *S1pr1* expression in tumor cells led to production of factors that elevated *S1pr1* and p-Stat3 levels in the lungs, which required myeloid cell-specific *S1pr1* expression (Figure S2A). The reduction in *S1pr1*

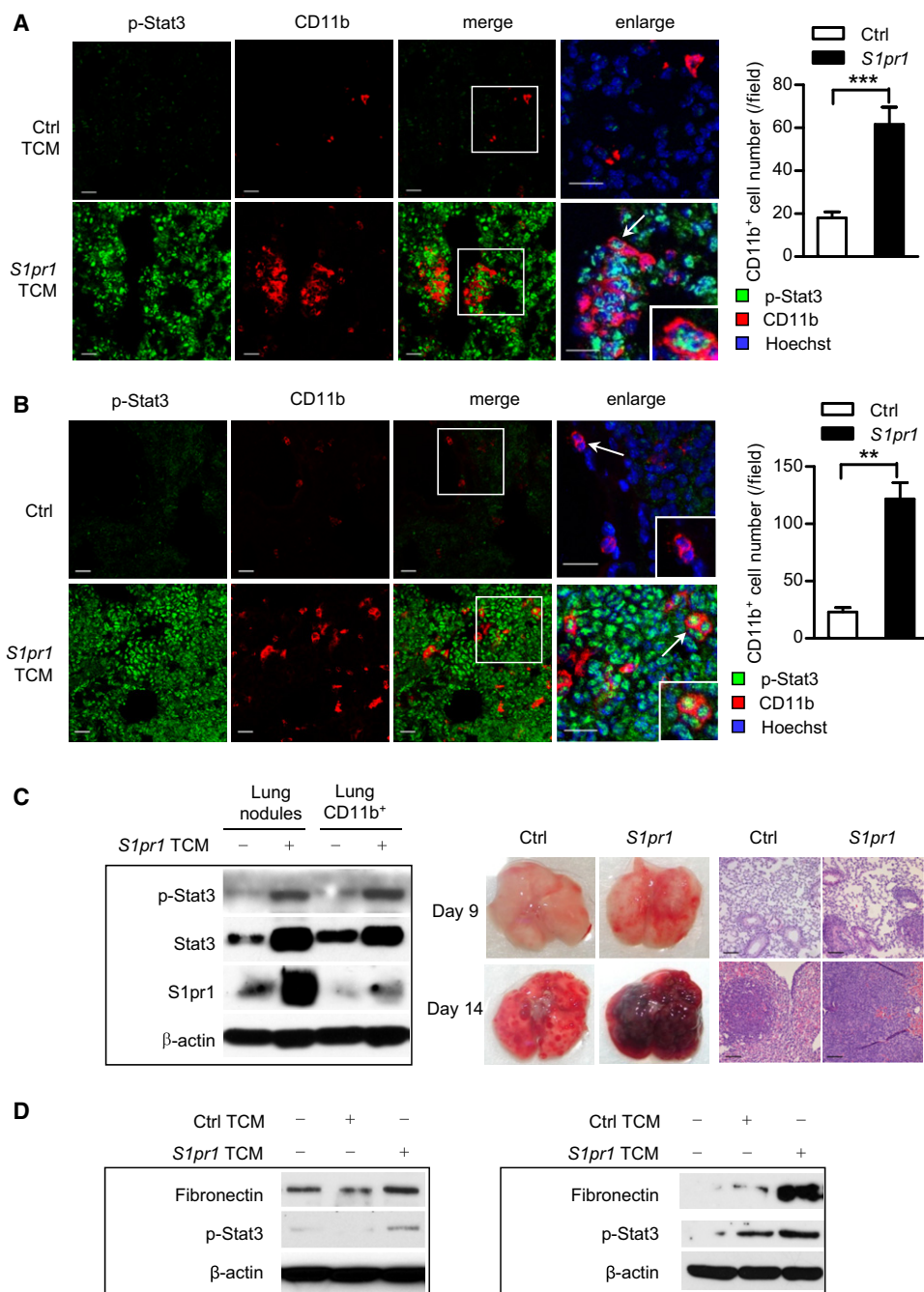


Figure 1. S1PR1-STAT3-Induced Tumor Factors Activate STAT3 at Premetastatic Sites

(A) Left: Confocal microscopy images show phospho-Stat3 (p-Stat3, green) in myeloid cell clusters (CD11b, red) and other cells in premetastatic lung tissue sections from mice treated with TCMs from control or *S1pr1* overexpressing tumor cells for 5 days, followed by systemic tumor challenge for 3 days. Scale bars, 20 μ m. Right, quantification of infiltrating CD11b⁺ cells shown on left ($n = 10$).

(B) Immunofluorescence (IF) staining measuring p-Stat3 and CD11b in lung sections from naive mice (upper panel) and mice treated with TCM from *S1pr1*^{high} MB49 tumor cells for 5 days without tumor challenge (lower panel). Left: representative confocal images from 4 mice per group. Right, quantification of infiltrating CD11b⁺ cells. Scale bars, 20 μ m.

(C) Left panel, western blotting showing *S1pr1*, Stat3, and p-Stat3 in lung CD11b⁺ myeloid cells and metastatic nodules in mice 14 days post-tumor injection. Right panel, representative lung metastasis and H&E staining ($n = 6$). Scale bars, 100 μ m.

(D) Western blotting showing expression levels of fibronectin and p-Stat3 in MEFs (left) and primary lung-derived fibroblasts (right) exposed to indicated media. Results represent means \pm SEM. ** $p < 0.01$, *** $p < 0.001$.

See also Figure S1.

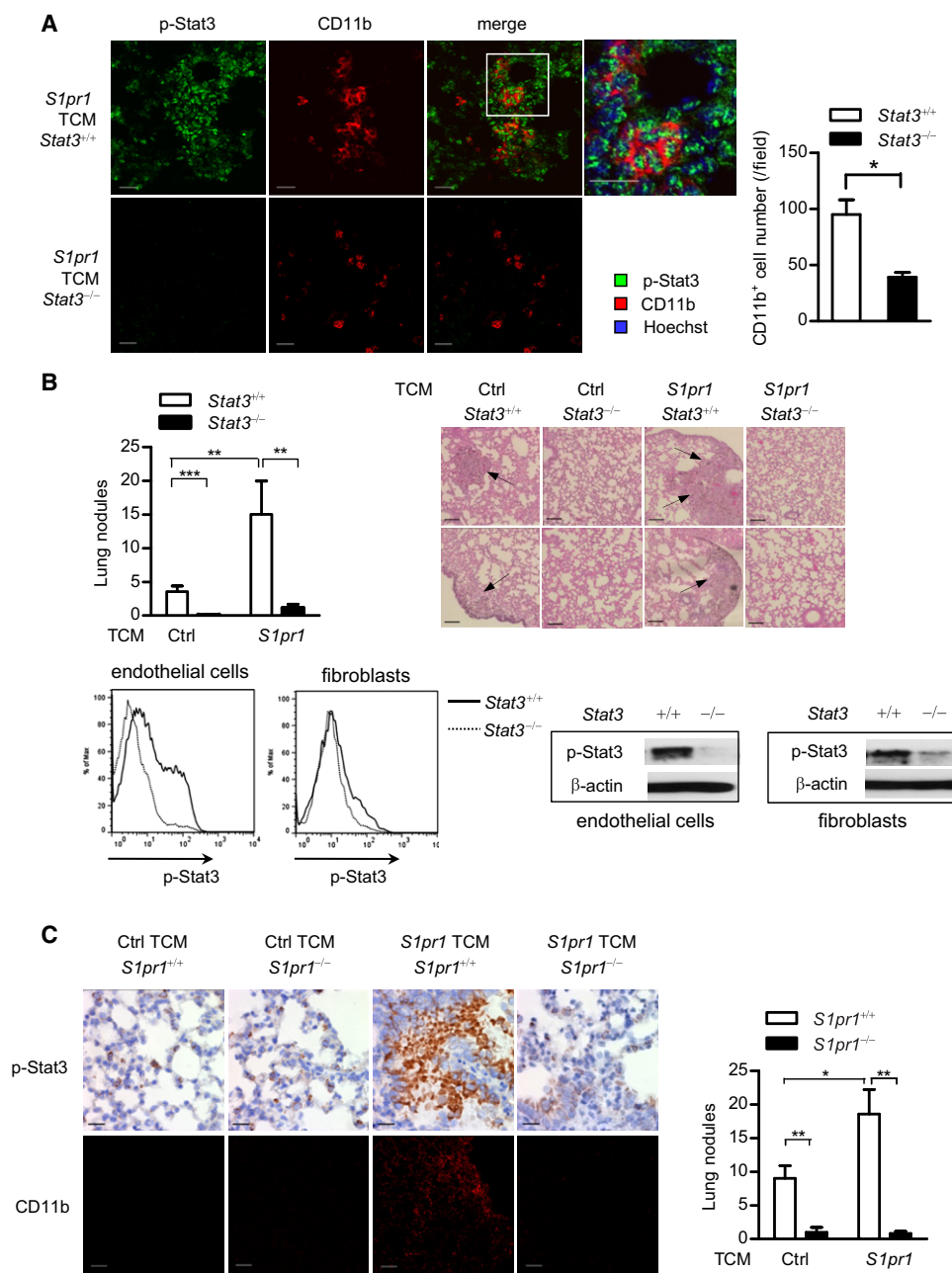


Figure 2. Ablating *S1pr1* or *Stat3* in Myeloid Cells Abrogates Tumor Factor-Induced Premetastatic Niches

(A) Representative immunofluorescence staining and confocal microscopy of p-Stat3 and CD11b⁺ myeloid cells in lung tissues harvested from mice with Stat3^{+/+} and Stat3^{-/-} myeloid compartment. Right, quantification of the images (n = 9). Scale bars, 20 μm.

(B) Upper left panel, enumeration of metastatic lung nodules in mice with Stat3^{+/+} and Stat3^{-/-} myeloid compartment treated with indicated TCMS followed by parental tumor cell challenge (n = 9). Upper right panel, H&E staining shows histology of lungs from representative mice in each group, arrows indicate lung metastasis. Scale bars, 100 μm. Lower panel, flow cytometric analysis and western blotting measuring p-Stat3 in endothelial cells (CD31⁺αSMA⁻) and fibroblasts (CD31⁻αSMA⁺) in premetastatic sites.

(C) Mice were treated with indicated TCMS, followed by systemic parental tumor cell challenge. Left upper panel, IHC staining evaluates p-Stat3 expression in lung tissues from mice with S1pr1^{+/+} or S1pr1^{-/-} myeloid compartment. Scale bars, 20 μm. Left lower panel, CD11b⁺ myeloid cell clusters were analyzed by confocal microscopy. Scale bars, 100 μm. Right panel, bar graph indicates number of lung nodules from mice with S1pr1^{+/+} and S1pr1^{-/-} myeloid compartment (n = 6).

Results represent means ± SEM. *p < 0.05, **p < 0.01, ***p < 0.001.

See also Figure S2.

expression and Stat3 activity in the lungs of *Mx1Cre-S1pr1^{loxp/loxp}* mice was accompanied by drastically reduced lung metastasis (Figure 2C, right). Collectively, these data suggest that S1pr1-Stat3 signaling in myeloid cells contributes to premetastatic niche formation, and extensive Stat3 activation in the lung, as well as tumor metastasis. We further analyzed the effects of *S1pr1* and *Stat3* ablation on subtypes of CD11b⁺ cells, such as M1 and M2, as well as N1 and N2, derived from the lung premetastatic sites (Figures S2B and S2C). Moreover, lack of Stat3 in myeloid cells did not significantly change the percentage of myeloid cells in bone marrow and spleen (Figure S2D). T cell subsets were affected by *Stat3* ablation in myeloid compartment at premetastatic niche sites (Figures S2E and S2F). Ablating *Stat3* in myeloid cells also increased T cell proliferation (Figures S2G and S2H).

Targeting S1PR1 or STAT3 in Myeloid Cells Reduces Preformed Metastatic Niches

For potential clinical translation of our results that S1PR1-STAT3 in myeloid cells is critical for premetastatic niche formation, we assessed whether in vivo targeting of *Stat3* or *S1pr1* in myeloid compartment by CpG-*Stat3* siRNA and CpG-*S1pr1* siRNA would effectively reduce preformed metastatic niches at distant organs and thereby prevent metastasis. CpG is a small oligonucleotide with methylated CpG dinucleotides that activate Toll-like receptor (TLR)-9, which is mainly expressed in the endosomal compartment of myeloid and B cells (Kortylewski et al., 2009b). CpG-siRNA can facilitate specific gene silencing in these cells in vivo (Kortylewski et al., 2009b). We first induced premetastatic niches using TCM from *S1pr1^{high}* B16 tumor cells, followed by parental tumor cell injection. The level of *S1pr1* expression was elevated in lungs of mice treated with TCM relative to lungs from control naive mice (Figure S3A). After myeloid cell cluster formation in the lung, mice were treated with CpG-*S1pr1* siRNA. We collected the lungs and analyzed CD11b⁺ myeloid cells by immunofluorescence staining 3 days after the last CpG-*S1pr1* siRNA treatment. In control CpG-*Luciferase* siRNA-treated mice, we observed abundant myeloid cell infiltration near the distal alveoli (Figure 3A, left), which are the common sites for cell infiltration and metastatic niche formation (Kaplan et al., 2005). In the CpG-*S1pr1* siRNA treatment group, myeloid cell infiltration and cluster formation were drastically reduced compared to those treated with control CpG-*Luciferase* siRNA (Figure 3A). *S1pr1* expression in the whole lung was reduced in the CpG-*S1pr1* siRNA-treated group relative to controls (Figure 3B, left). The number of lung metastatic nodules was also greatly reduced by treatment with CpG-*S1pr1* siRNA (Figure 3B, right). We also performed similar experiments with CpG-*Stat3* siRNA to test whether blocking *Stat3* in myeloid cells would reduce preformed premetastatic niches and tumor metastasis. Directly targeting *Stat3* in myeloid by CpG-*Stat3* siRNA further reduced tumor factor-induced lung metastasis (Figure 3C). The control CpG-*Luciferase* siRNA treatment also led to somewhat a decrease in lung metastasis compared to PBS treatment, which is likely due to the immune stimulatory effect of CpG (Kortylewski et al., 2009b). We also used inducible genetic ablation of *Stat3* in myeloid cells to confirm that targeting *Stat3* in myeloid cells can eliminate pre-existing metastatic niches and metastasis (Figure S3B). CpG-*Stat3* siRNA was

also able to eliminate premetastatic that were already formed in lungs after mice were treated with the TCM derived from *S1pr1^{high}* tumor cells (Figure S3C). To assess whether the maintenance of the premetastatic niche requires ongoing production of tumor factors, we performed experiments in which lung myeloid infiltrates were assessed at various time points after treatments with tumor conditioned media was stopped. Data generated from this set of experiments suggest that ongoing production of tumor factors is crucial for the maintenance of the myeloid cell infiltrates in the premetastatic niches (Figure 3D).

STAT3 Signaling Enables Myeloid Cell Invasion and Priming of Premetastatic Sites

Initiation of metastasis involves intravasation of tumor stromal cells, including myeloid cells, from primary tumor sites (Fidler, 2003). We determined whether increasing STAT3 activity intrinsic to myeloid cells could promote their intravasation capacity from primary tumor. We visualized, by multiphoton live imaging, interaction of myeloid cells with tumor endothelium, as a result of increasing Stat3 activity by *S1pr1^{high}* myeloid cells (Figure 4A; Figures S4A and S4B). To further validate that Stat3 activity is crucial for myeloid cells to intravasate at primary tumors, we performed time-lapsed two-photon imaging (Movies S1, S2, S3, and S4), as well as trans-endothelial migration assays with CD11b⁺ and CD11b⁺Gr1⁺ myeloid cells (Figure 4B).

Recent studies emphasize the importance of tumor-secreted factors for premetastatic niche formation (Erler et al., 2009; Hiratsuka et al., 2006; Kim et al., 2009). We next addressed whether myeloid cells, through the S1PR1-STAT3 signaling axis, could also produce factors to condition future metastatic sites. We treated MEFs and primary lung-derived fibroblasts with conditioned media from control and *S1pr1^{high}* myeloid cells and found that both p-Stat3 and fibronectin protein level were higher in fibroblasts treated with conditioned medium from *S1pr1^{high}* myeloid cells compared to those treated with control conditioned medium (Figure 4C). We also detected elevated expression of IL-6, IL-10, and S1P by *S1pr1^{high}* myeloid cells (Figure S4C). In addition, *S1pr1^{high}* myeloid cells mediated increased metastasis (Figure S4D) and produced elevated *Vegf* and *Hif-1 α* mRNA and secreted VEGF levels (Figure 4D).

Expression of the receptor for fibronectin, integrin $\alpha_4\beta_1$, by VEGFR1⁺ myeloid cells has been demonstrated to be critical for premetastatic niche formation (Kaplan et al., 2005). We therefore asked the question whether integrin $\alpha_4\beta_1$ and fibronectin are regulated by Stat3. Real-time PCR revealed that myeloid cells express *Fibronectin* (also known as *Fn1*) in a Stat3-dependent manner (Figure 5A). Tumor cell-produced lysyl oxidase (LOX) has recently been shown to be critical for premetastatic formation (Erler et al., 2009). Real-time PCR analysis indicated that Stat3 could upregulate *Lox* expression in myeloid cells (Figure 5A). We identified STAT-binding sites in the promoter regions of *ITGA4* (encoding integrin α_4), *Fibronectin*, and *LOX* using Transfected. Moreover, chromatin immunoprecipitation (ChIP) assays using chromatin prepared from bone marrow-derived macrophages (BMDMs) exposed to *S1pr1^{high}* TCM indicated that Stat3 protein can directly bind to these sites, suggesting that *Itga4*, *Fibronectin*, and *Lox* are Stat3-target genes, at least in mouse cells (Figure 5B; Figure S5A).

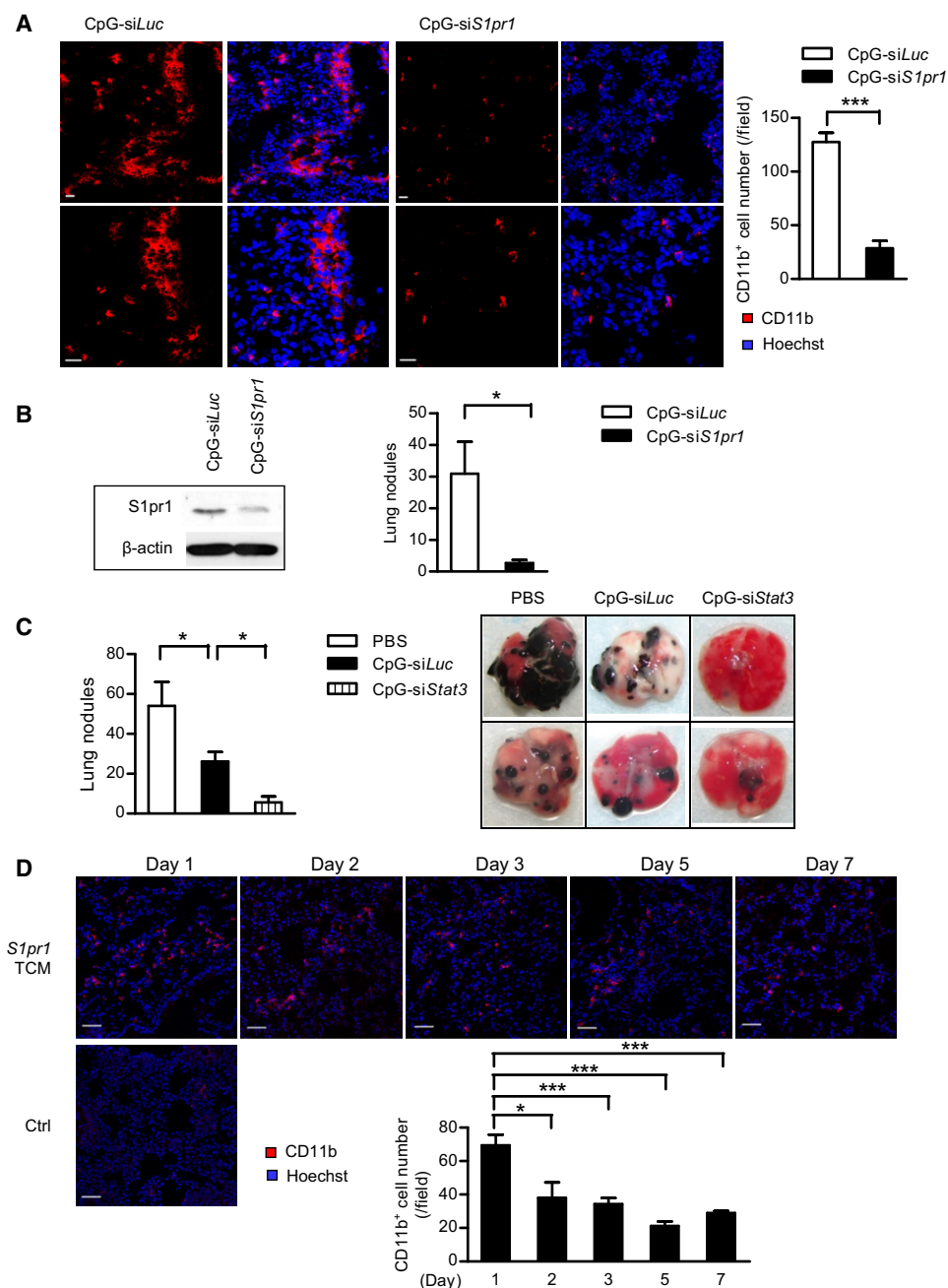


Figure 3. Targeting S1PR1 and STAT3 in Myeloid Cells Can Eliminate Preformed Metastatic Niches

(A) Immunofluorescence staining showing lung myeloid cell infiltrates in mice receiving indicated CpG-siRNA treatments. Left panel: representative images from each group. The images in the lower panel show magnification of upper row of images. Red, CD11b⁺ myeloid cells; blue, Hoechst staining for nuclei. Right panel: quantification of images on left (n = 8). Scale bars, 20 μ m.

(B) Left panel, western blotting measuring effects of CpG-*S1pr1* siRNA on S1pr1 protein expression levels in whole lungs. Right panel, lung metastasis was enumerated after tumor challenge and CpG-*S1pr1* siRNA treatment; shown are representative results from three experiments (n = 6).

(C) Left panel, lung metastatic colonies were enumerated from mice receiving indicated treatments (n = 5). Right panel, representative photos of lungs harvested from mice treated with indicated CpG-siRNA conjugates.

(D) Lung-infiltrating CD11b⁺ cells were assessed by confocal microscopy. Mice were treated with *S1pr1*^{high} TCM for 5 days. Upper panel, IF staining of CD11b⁺ cells in mouse lung tissues harvested at indicated time points after cessation of treatments. Lower left panel, IF staining of CD11b⁺ cells in a control mouse lung. Scale bars, 50 μ m. Lower right panel, quantification of lung infiltrating CD11b⁺ cells in upper panel (n = 4).

Results represent means \pm SEM. * $p < 0.05$, *** $p < 0.001$.

See also [Figure S3](#).

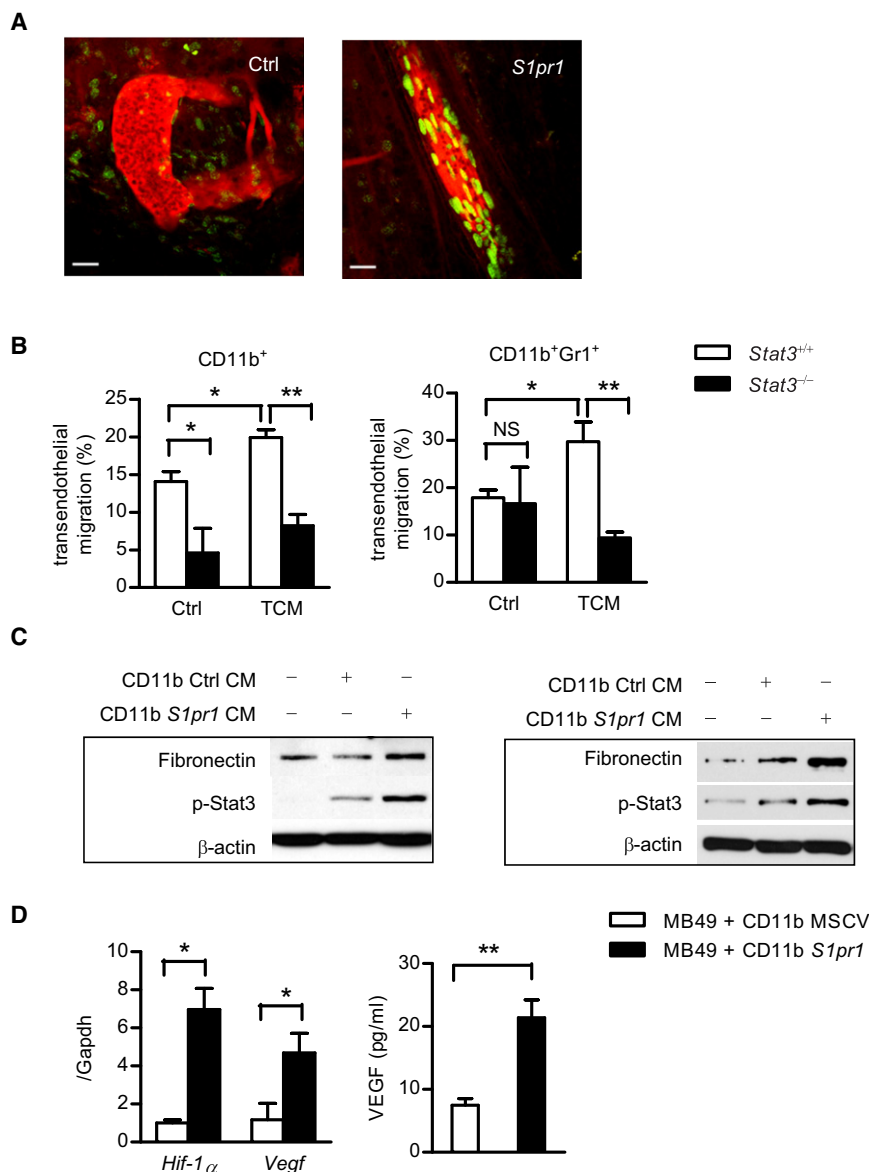


Figure 4. STAT3 in Myeloid Cells Increases Self Invasion and Tumor Metastasis

(A) Intravital two-photon live imaging of primary tumors, visualizing myeloid cell interaction with tumor endothelium. Green, CD11b⁺ myeloid cells transduced with either *S1pr1* expressing retrovirus or control retrovirus vector with eGFP tag; Red, blood vessels labeled with rhodamine-dextran. Scale bars, 100 μ m.

(B) Trans-endothelial migration assay of *Stat3*^{+/+} and *Stat3*^{-/-} myeloid cells to migrate across endothelial cells in response to *S1pr1*^{high} TCM. Migrated CD11b⁺ (left panel) and CD11b⁺Gr1⁺ (right panel) myeloid cells were further analyzed by flow cytometry and normalized by input total cell numbers; data represents one of three independent experiments.

(C) Western blotting showing Fibronectin and p-Stat3 proteins in MEFs (left) or primary lung-derived fibroblasts (right) incubated with conditioned media (CM) from myeloid cells with or without *S1pr1* overexpression.

(D) Left panel, real-time PCR analysis of whole tumor mixture showing *Hif-1 α* and *Vegf* mRNA expression levels, which is normalized by *Gapdh* expression ($n = 8$). Right panel, tumor secreted VEGF levels were assessed by ELISA using conditioned medium from whole tumors ($n = 10$).

Results represent means \pm SEM. * $p < 0.05$, ** $p < 0.01$.

See also Figure S4 and Movies S1, S2, S3, and S4.

We also evaluated expression levels of several known STAT3-regulated genes involved in invasion and matrix-remodeling, processes critical for premetastatic niche formation (Yu et al., 2009) in the BMDMs. Real-time PCR results confirmed that tumor factors can induce expression of *Cxcl2*, *Cxcl12*, *Cxcr4*, *Mmp2*, *Cox-2* in BMDMs in a Stat3-dependent manner (Figure 5A). Furthermore, we showed that tumor factors from *S1pr1*^{high} tumor cells induced expression of *Il6*, *Il1 β* , *Cxcl2*, *Cxcl12*, and *Mmp2* in lung-infiltrating myeloid cells, which is also Stat3-dependent (Figure S5B).

To determine whether myeloid cell production of these STAT3-dependent factors would impact their expression at metastatic sites, we performed ChIP assay using lung tissues collected from mice with *Stat3*^{+/+} and *Stat3*^{-/-} in myeloid compartment, challenged with tumor cells. Without Stat3 in the myeloid compartment, metastatic lungs exhibited lowered levels of p-Stat3 (Figure 5C, right). The lung tissue ChIP assays

indicated that Stat3 binds to the promoters of *Lox*, *Mmp2*, *Mmp9*, *Itga4*, and *Cxcl12* in the metastatic tissues (Figure 5C, left). Taken together, we show that through STAT3, whose persistent activation is contributed by S1PR1 in the tumor microenvironment, myeloid cells can express multiple key factors for various aspects of premetastatic niche formation, allowing them to prime

S1PR1-STAT3 Signaling Enables Myeloid Cells to Colonize at Premetastatic Sites

While invasion potential is critical for myeloid cells to colonize/form premetastatic niches at distal organs, myeloid cells must proliferate and evade apoptosis. We therefore assessed whether STAT3 signaling could upregulate expression of prosurvival and proliferative genes in myeloid cells. Real-time PCR analysis indicated that expression of several prosurvival and proliferative genes in BMDMs in response to tumor factors was Stat3 dependent (Figure 5A). Expression of the antiproliferative and proapoptotic gene, p53 (Niu et al., 2005), was inhibited by Stat3 in myeloid cells when exposed to the tumor milieu (Figure 5A). To test whether S1PR1-STAT3 signaling in myeloid cells leads to increased proliferation in future metastatic sites, we

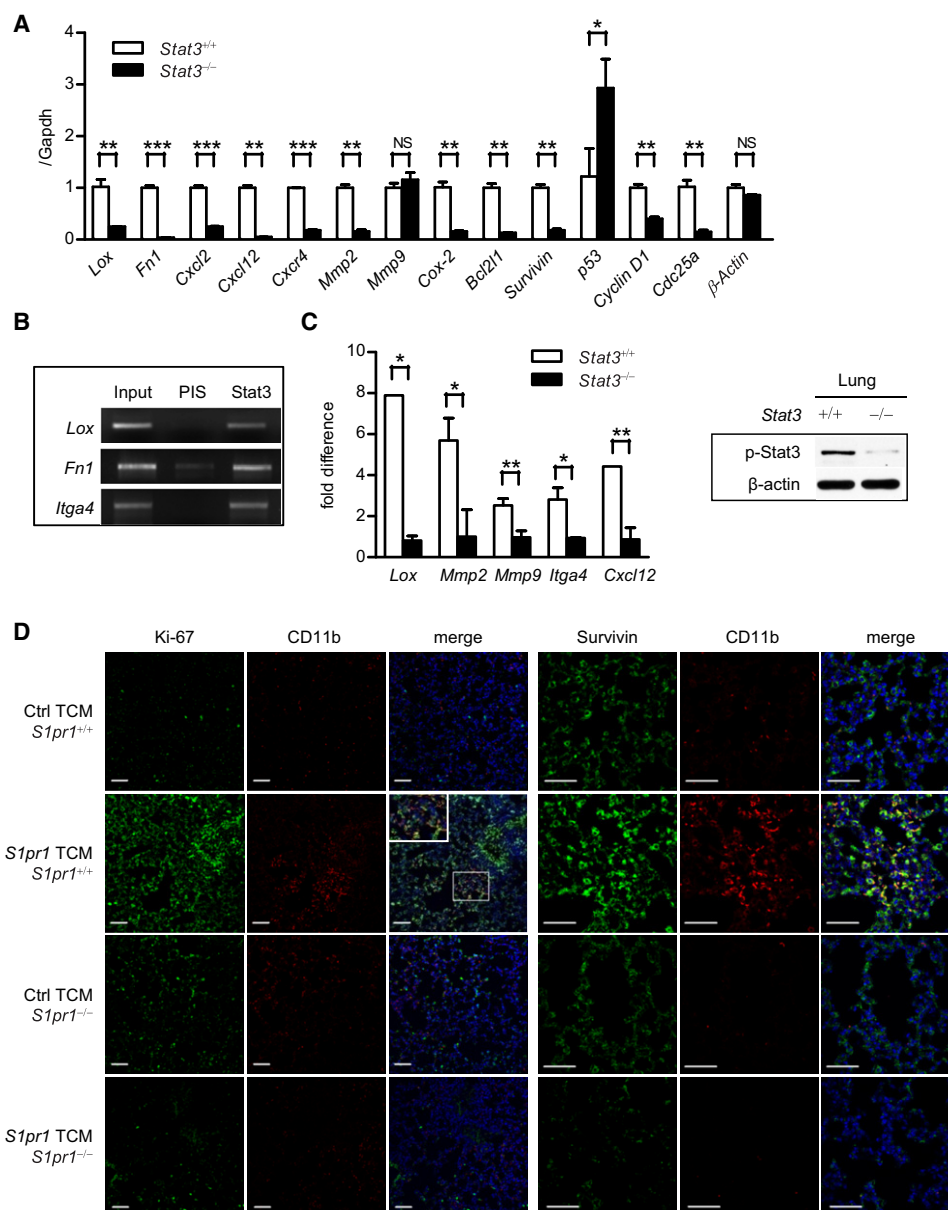


Figure 5. STAT3 Signaling Facilitates Myeloid Cell Colonization

(A) Real-time PCR showing Stat3-dependent expression of indicated genes in Stat3^{+/+} and Stat3^{-/-} bone marrow-derived macrophages (BMDMs) exposed to TCM (n = 3).

(B) ChIP using BMDMs showing *Itga4*, *Fibronectin* and *Lox* are direct Stat3 target genes. DNA electrophoresis shows DNA fragments within the indicated promoters detected by specific primers. PIS (preimmune serum) antibody was used for immunoprecipitation as a negative control (n = 10).

(C) In vivo ChIP assay of lung tissues collected from mice with Stat3^{+/+} or Stat3^{-/-} myeloid compartment treated with TCM prior to tumor cell challenge. All ChIP data were quantified by real-time PCR in comparison with input DNA, and normalized with Stat3^{-/-} samples set as one. ChIP assay performed in triplicate.

(D) Left panels: double immunofluorescence staining with proliferation marker Ki-67 and myeloid cells marker CD11b, of lung tissue sections prepared from mice with S1pr1^{+/+} or S1pr1^{-/-} myeloid compartment and treated with indicated TCMs. Inset shows magnification at specified region. Right panels: immunofluorescence staining for detection of Survivin and CD11b in the lungs of indicated mice. Scale bars, 50 μm.

Results represent means ± SEM. *p < 0.05, **p < 0.01, ***p < 0.001.

See also Figure S5.

assessed proliferation index (Ki-67) in the lungs of mice following systemic treatment with S1pr1^{high} TCM and found that tumor-derived soluble factors could promote proliferation of cells in premetastatic niches but it depended on S1pr1-Stat3 in the

myeloid compartment (Figure 5D, left panels). Notably, the increase in cell proliferation in the premetastatic sites was not restricted to myeloid cells, which was consistent with Stat3 activation in various cells in addition to the myeloid clusters (Figure 1;

Figure S1). We further showed that factors from *S1pr1*^{high} tumors cells induced Stat3-dependent expression of prosurvival/proliferation genes in lung-infiltrating myeloid cells (Figure S5B).

In order to colonize distant sites, myeloid cells must also be able to evade apoptosis in the hostile environment of distant organs. We therefore determined anti-apoptotic gene *Survivin* expression in lung tissue sections adjacent to those used for proliferation analysis. Our results indicated a significant increase in the number of Survivin-positive cells in lungs harvested from mice treated with *S1pr1*^{high} TCM (Figure 5D, right panels). Ablating *S1pr1* in the myeloid compartment abrogated Survivin induction by TCM (Figure 5D, right panels). Consistent with this, we observed Stat3-dependent *Survivin* expression in BMDMs exposed to TCM (Figure 5A).

STAT3 Signaling and Effects in Premetastatic Human Patient Tissues

To extend our findings to human cancers, we analyzed S1PR1 expression and STAT3 activity in uninvolved (tumor cell-free) lymph nodes from high-risk prostate cancer patients and melanoma patients, and from individual without malignancy. We were able to detect strong STAT3 activation in the primary tumor sites (data not shown), and heavy CD68⁺ myeloid infiltrates in 40 out of 50 uninvolved lymph nodes from the prostate cancer patients, and four out of five uninvolved lymph nodes from the melanoma patients (Figure 6A). CD68⁺ areas in the lymph nodes also displayed elevated S1PR1 expression and p-STAT3 (Figure 6A). Immunohistochemical staining with another myeloid cells marker, CD33, showed a similar staining pattern as CD68 (Figure S6A). As in mouse premetastatic sites, cells other than myeloid cells including those in the endothelium, also showed increased S1PR1 expression and p-STAT3 levels (Figure S6B). Similar to a prior report (Kaplan et al., 2005), we did not observe heavy CD68⁺ myeloid infiltrates in the lymph node sections from individual without cancer (Figure 6A). Only weak S1PR1 and p-STAT3 was detected inside normal control lymph nodes (Figure 6A). We further tested SURVIVIN expression in lymph nodes from individuals with prostate cancer and without cancer (Figure 6B, left panel). Quantification of relative expression levels of CD68 and SURVIVIN in the patient lymph nodes versus normal lymph node is also shown (Figure S6C). Expression of BCL2L1 in uninvolved lymph nodes from melanoma patients was associated with elevated p-STAT3 (Figure 6B, right panel).

DISCUSSION

Recent studies suggest a paradigm-shifting concept that non-neoplastic cell populations, such as myeloid cells, are crucial in providing tumor cells a conducive microenvironment to engraft and colonize in distant organs (Erler et al., 2009; Hiratsuka et al., 2006; Kaplan et al., 2005; Kim et al., 2009; Kowanetz et al., 2010; Psaila and Lyden, 2009). This current study introduces the concept that persistent activation of STAT3 occurs in distant organs before tumor cell arrival. *Stat3* or *S1pr1* ablation in myeloid cells also abrogated Stat3 activity in the entire future metastatic site, further suggesting an important role of myeloid cells in establishing premetastatic niches. While induced ablation in the Mx-Cre mice also, to a lesser degree, affects other types of cells in addition to hematopoietic cells, results from

CpG-siRNA treatments, which selectively targeting TLR-9⁺ cells (Kortylewski et al., 2009a, 2009b), support the notion that targeting STAT3/S1PR1 signaling in immune cells can reduce STAT3 activity and myeloid cell infiltrates in future metastatic sites. Consistent with previous studies (Erler et al., 2009; Kaplan et al., 2005; Kim et al., 2009), we show that tumor cell-produced factors, whose upregulation is contributed by S1PR1-STAT3 signaling, are critical in initiating premetastatic niche formation. Our results further indicate that the maintenance of the niche requires ongoing production of tumor factors, suggesting if the tumors are removed timely and completely there would not be premetastatic niches for therapeutic intervention. However, many patients cannot have their tumors removed timely and/or completely, causing relapses. Therefore, targeting premetastatic niches to prevent/reduce metastasis in these patients can be highly desirable. We show that S1PR1-STAT3 signaling-induced tumor factors can prime/activate fibroblasts, which are crucial for forming premetastatic niches at distant organs. These results, taken together, suggest a critical role of S1PR1-STAT3 not only in tumor cells, but also in myeloid cells, and likely in other types of stromal cells including fibroblasts and endothelial cells, in orchestrating premetastatic niche formation.

The focus on initiating distant organ metastasis through myeloid cells has been on tumor cell-produced factors (Erler et al., 2009; Kaplan et al., 2005; Kim et al., 2009). Our data suggest that once STAT3 is persistently activated, myeloid cells produce similar factors as tumor cells, including IL-6 and IL-10, capable of activating fibroblasts and upregulating key molecules, such as fibronectin (Kaplan et al., 2005; Kenny et al., 2008), for premetastatic niche formation. Being able to express integrins and produce chemokines, growth factors, angiogenic factors, and inflammatory mediators in response to tumor factors, is viewed as the primary function of myeloid cells in forming premetastatic niches (Psaila and Lyden, 2009). While these factors/molecules clearly play an important role in premetastatic niche formation, to achieve outgrowth in the hostile environment of distant organs, nonneoplastic cells must sustain proliferation and resist apoptosis. Our results suggest that persistent STAT3 signaling in myeloid cells can increase their proliferation and survival, as well as that of other stromal cells at future metastatic sites. It was previously reported that ablating Stat3 in myeloid cells could enhance the development and progression of colorectal cancer, presumably through inhibition of IL-10 signaling (Deng et al., 2010). In other colorectal cancer models, however, blocking Stat3 was associated with a decrease in tumor development/progression due to inhibition of Th17 (Wu et al., 2009). These results suggest the complexity of immunoregulation in colon cancer, which is greatly impacted by STAT3. At the same time, in many cancers, the role of STAT3 in promoting cancer development and progression has been demonstrated (Yu et al., 2009).

Prior publications suggest that myeloid cells migrate into distant organs from bone marrow without necessarily passing through the primary tumor site (Erler et al., 2009). Our data indicate that S1PR1-STAT3 upregulation in myeloid cells at primary tumor sites can promote their intravasation, which might facilitate their accumulation in future metastatic sites. Activation of Toll-like receptors, specifically TLR2, on myeloid cells by

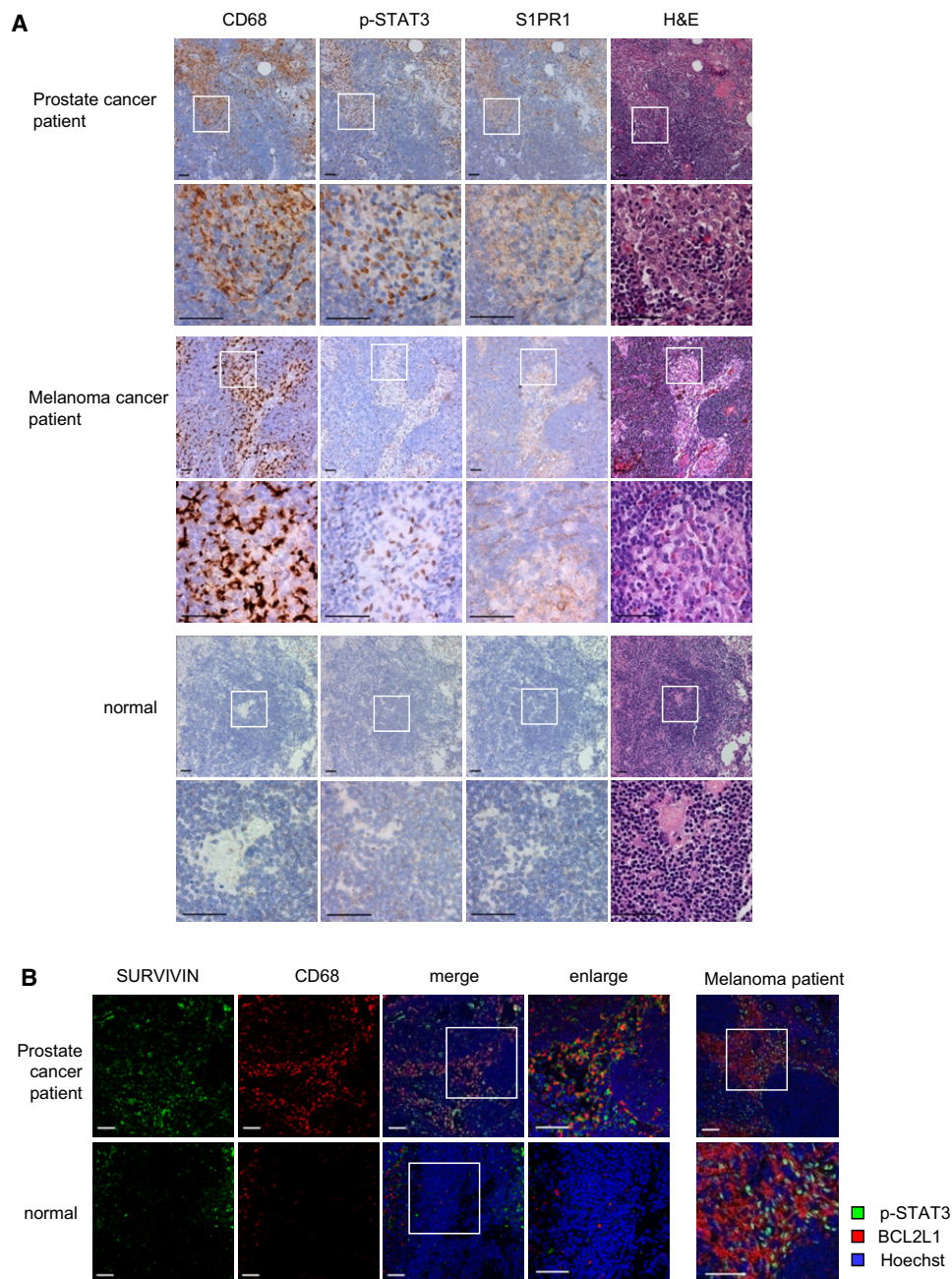


Figure 6. STAT3 Is Activated in Myeloid Clusters in Human Premetastatic Sites

(A) IHC staining of p-STAT3, S1PR1, and CD68 from uninvolved lymph nodes from prostate and melanoma cancer patients with high metastatic potential (upper and middle panels, respectively) or from a control lymph node from an individual without cancer (lower panels).

(B) Immunofluorescence staining from adjacent sections of the same tissues as in (A). Left panel, green, SURVIVIN; red, CD68 of human myeloid cells; blue, nuclei stained with Hoechst. Data on prostate cancer patient lymph nodes are representative of 15 independent patient samples. Right panel, uninvolved lymph nodes from melanoma patients are stained for p-STAT3 (green) and BCL2L1 (red). Nuclei counter stained with Hoechst (blue).

Data are representative of samples from five melanoma patients. Scale bars, 50 μ m.

See also Figure S6.

tumor-produced factors has been shown to create an inflammatory milieu that mediates distant-site metastasis (Kim et al., 2009). Because STAT3 can be activated by many inflammatory stimuli through various receptors including Toll-like receptors, and by smoking, carcinogen, radiation, and UV exposure, among

other external insults (Arredondo et al., 2006; Aziz et al., 2007; Biswas and Mantovani, 2010; Bronte-Tinkew et al., 2009; Chan et al., 2004; Psaila and Lyden, 2009; Wels et al., 2008; Yu et al., 2009), our findings support the concept that environmental conditions may contribute to cancer metastasis.

Metastasis remains the final frontier for cancer therapy (Klein, 2009; Psaila and Lyden, 2009; Steeg, 2006; Wels et al., 2008). Being able to prevent metastasis by eliminating premetastatic niches is an attractive approach for effective cancer treatment. Our study suggests that the S1PR1-STAT3 axis is operative in not only tumor cells, but also myeloid cells, and likely other types of stromal cells crucially involved in forming premetastatic niches. Our data further expand the STAT3-regulated downstream genes involved in premetastatic niche formation. These studies demonstrate that S1PR1-STAT3 is an effective target to disable both tumor cells and “nonneoplastic” cells from creating an environment that is crucial for malignant distant outgrowth.

EXPERIMENTAL PROCEDURES

Tumor and Myeloid Conditioned Media Preparation

Tumor cells (B16, MB49) were transduced with MSCV retrovirus with or without *S1pr1*. Control and *S1pr1* overexpressing tumor cell lines were incubated in serum-free medium for 24 hr and TCM was collected and filtered through 0.22 μ m SFCA membrane (Corning, Inc.). To obtain myeloid cell conditioned media, total splenocytes were harvested and transduced with *S1pr1*-expressing GFP-tagged retrovirus. GFP⁺CD11b⁺ myeloid cells were FACS sorted after a 24 hr infection, and supernatant was collected 24 hr after culture in RPMI medium supplied with 10% FBS. The supernatants were centrifuged at 3,000 rpm for 5 min.

In Vivo Experiments

Mouse care and experimental procedures were performed in accordance with established institutional guidance and approved protocols from Institutional Animal Care and Use Committee at Beckman Research Institute of City of Hope National Medical Center. We obtained *Mx1-Cre* mice from Jackson Laboratory and *Stat3^{loxP/loxP}* mice from Drs. Shizuo Akira and Kiyoshi Takeda (Osaka University). *Stat3^{-/-}* ablation in hematopoietic cells was accomplished as previously described (Kortylewski et al., 2005). *S1pr1^{loxP/loxP}* mice (generous gift from Dr. Richard Proia) were crossed with *Mx1-Cre* mice to generate *S1pr1* deletion in hematopoietic cells as previously described (Lee et al., 2010).

For TCM treatments, mice were treated by intraperitoneal injection of TCM (300 μ l) followed by parental tumor cell tail vein injection (1×10^5 /mouse). Lungs were perfused using HBSS, harvested and immediately embedded in OCT or fixed with formalin.

For tumor cell/myeloid cell co-administration, GFP⁺CD11b⁺ myeloid cells, transduced and sorted as described above, were mixed with either MB49 or B16 tumor cells (1:10 ratio), and subsequently injected into mice either subcutaneously or through tail vein injection.

CpG conjugated siRNA was synthesized as previously described (Kortylewski et al., 2009b). The sequences of CpG-*Luc* siRNA and CpG-*Stat3* siRNA conjugate molecules were reported elsewhere (Kortylewski et al., 2009b). C57BL/6 mice were treated with TCM for 5 consecutive days, followed by i.v. parental tumor cell challenge. Mice were first treated (i.v.) with CpG-siRNA conjugates (0.78 nmol/mice) at day 7 post-tumor challenge, followed by every other day treatment for 2 weeks. Lungs were perfused, harvested, and embedded in OCT for further analysis.

Immunohistochemistry and Immunofluorescent Staining and Analyses

Paraffin-embedded sections were deparaffinized, followed by staining with antibodies against pY705-Stat3 (Cell Signaling Technology), S1PR1 (Santa Cruz Biotechnology Inc.) or CD68 (AbD Serotec) and examined under Olympus AX70 automated upright microscope. Frozen or deparaffinized sections were stained with pY705-Stat3 (Santa Cruz Biotechnology Inc.), CD11b (BD PharMingen), Ki-67 (Abcam), and Survivin (Novus Biologicals) antibodies. For fluorescence detection, secondary antibodies were used (Alexa Fluor 488 and Alexa Fluor 546, Invitrogen) and counterstained with Hoechst 33342 (Invitrogen) for nuclei. Slides were mounted and examined using the Zeiss

clSM510Meta inverted confocal microscope. Image-Pro Plus (MediaCybernetics) software was used to count the number of stained cells as indicated in the figure legends for quantification purpose.

Intravital Two-Photon Imaging, Time-Lapse 3D Imaging, and Analysis

After injection of tumor cells mixed with myeloid cells (GFP-tagged) for 9 days, mice were retroorbitally injected with dextran-rhodamine (Invitrogen) and were anesthetized 30 min later. Live imaging was performed using Prairie Ultima microscope (Prairie Technologies, Madison, WI) as previously described (Kortylewski et al., 2009b). Both green and red channels were excited at 860 nm, with emission detected simultaneously between 500 and 550 nm (green/GFP) and between 570 and 620 nm (red/Dextran). Multidimensional images were created as previously reported (Wei et al., 2005). Z-stack images were acquired (20x/1.0W objective by Olympus, 1024 \times 1024 = 0.464 μ m/pixel) every 5 min for 13 time points to create a 4D data set (x, y, and z axes with time and different emission wavelengths). Fourteen Z-sections were collected at 3 μ m intervals for a total of 42 μ m. Z-stacks images were first assembled in Image Pro Plus software version 6.3 (Media Cybernetics), and then 3D data sets were generated using Amira software version 5.3.3 (Visage Imaging) using Volren projections. Time-lapse sequences were created using Amira Demo Maker and Movie Maker. Movies were saved in the MPG format with 200 frames at a rate of 24 fps.

Trans-Endothelial Migration Assay

Mouse prostate endothelial cells were seeded in 24-well transwell inserts (Corning Costar Corp.) with polycarbonate membranes (8.0 μ m pore). For trans-endothelial cell migration, myeloid cells were stained with CD11b and Gr1 antibodies and re-suspended in leukocyte migration buffer containing RPMI 1640 medium with 0.25% BSA (fatty acid free, Sigma), and added to the upper chamber at 1×10^5 /well. Cells were allowed to migrate toward TCM in lower chamber for 1 hr. The numbers of migrated cells into lower chamber were enumerated for different myeloid subpopulations by flow cytometry at a fixed flow rate for 1 min on Accuri C6 flow cytometer. The percentage of migrated cells was normalized by the total numbers of input cells for each sample.

Chromatin Immunoprecipitation Assay

ChIP assays for cells and tissues were performed based on the protocol from Millipore-Upstate Biotechnology. Rabbit anti-Stat3 (C-20, Santa Cruz Biotechnology, Inc.) was used for immunoprecipitation. Potential STAT-binding sites on mouse *Lox*, *Fibronectin*, *Vla-4*, *Mmp2* and *Mmp9* were analyzed by Transfec software. The potential Stat binding sites are: *Lox* (5'-TTCCCATAA-3', -405 bp); *Fibronectin* (5'-TTCCACAA-3', -574 bp); *Itga4* (5'-TTCCCCCAA-3', -229 bp); *Mmp2* (5'-TTCCTGGAA-3', -1,667 bp); *Mmp9* (5'-TTCCCCAA-3', -579 bp). ChIP primers were designed to flank these sites: for *Lox*, 5'-CGTAGCAAGCTTTGTTCCT-3', 5'-GGGAGTTGTGACTAAGGCTTATGCT-3'; *Fibronectin*, 5'-AAACCGAGGTCTGAGCCTACCTAA-3', 5'-AATTGGTGGCTGTGGTGGTGTG-3'; *Itga4*, 5'-CCCAAATTATTGGCCACTGGGACT-3', 5'-ACCTAGGTTGCATGGACTCACA-3'; *Mmp2*, 5'-ATTGCGAGGCCCATTTGGGTTGAT-3', 5'-TCAGGGATTCACGGTTGTACCTT-3'; *Mmp9*, 5'-ATAGGGACAAAGGCTTGAGCGACA-3', 5'-AGCAGGCTCTTTGAGCAGGATTT-3'. *Cxcl12* primer was used according to previous publication (Stat3 binding site 5'-TTCCCGGAA-3', -527 bp) (Olive et al., 2008), 5'-ACCTGTTGGTCTCTTTGCTCGGT-3', 5'-CTGTCAAAGGCACAAGCCGTGA-3'. The relative amount of precipitated DNAs were quantified by real-time PCR and normalized by input DNA.

Patient and Normal Lymph Node Specimens

Prostate cancer patient specimens were obtained through a City of Hope Institutional Review Board approved protocol (COH IRB 09213) with consent from patients. Briefly, 50 high-risk prostate cancer patients (defined by standard D'Amico criteria, i.e., baseline PSA >20 ng/ml, Gleason grade 8–10, or stage T3a–T4 disease), who were treated with prostatectomy, were selected. Paraffin-embedded tissue from benign pelvic lymph nodes were obtained and prepared as 4 μ m sections on unstained slides for subsequent analyses. Lymph node sections from melanoma were prepared for immunohistochemistry (IHC) analysis as previously described (de Maat et al., 2007), and were

provided by John Wayne Cancer Institute, with approval from Western Institutional Review Board and with patient consent. Lymph node tissue sections from individuals without cancer were purchased from Abcam. Tissue sections were stained and examined as described above. Paraffin-embedded tissue slides were stained with H&E and examined/ diagnosed by a licensed pathologist.

Statistics

Data are presented as means \pm SEM. Statistical comparisons between groups were performed using unpaired Student's *t* tests to calculate the two-tailed *p* value: **p* < 0.05, ***p* < 0.01, ****p* < 0.001.

SUPPLEMENTAL INFORMATION

Supplemental Information includes six figures, Supplemental Experimental Procedures, and four movies and can be found with this article online at doi:10.1016/j.ccr.2012.03.039.

ACKNOWLEDGMENTS

We would like to thank Dr. Brian Armstrong and other staff members of Light Microscopy Imaging Core, and Dr Bogdan Gabriel Gugiu at Mass Spectrometry and Proteomics Core, at Beckman Research Institute, City of Hope Comprehensive Cancer Center, for time-lapsed imaging and for measuring S1P, respectively. We are also grateful to staff members at Pathology Core, Flow Cytometry Core and Animal Facility Core at City of Hope for technical assistance. We would also like to thank Dr. Richard Proia (US National Institute of Health) for providing *Stat3^{loxP/loxP}* mice, Dr. Edouard Cantin at City of Hope for providing L929 cell line, Piotr Swiderski at City of Hope for CpG-siRNA construct synthesis. This work is funded by Markel fund and Tim Nesvick Fund at City of Hope Comprehensive Cancer Center, Keck Foundation and R01 CA115815, R01 CA122976 and R01 CA115674, P30 CA33572 from the NCI, as well as National Natural Science Foundation Grants of China (91129702, 81125001). Procurement of patient samples and normal lymph nodes were supported by NIH grant 2K12CA001727-16A1 and Abcam.

Received: April 21, 2011

Revised: November 28, 2011

Accepted: March 5, 2012

Published: May 14, 2012

REFERENCES

- Arredondo, J., Chernyavsky, A.I., Jolkovsky, D.L., Pinkerton, K.E., and Grando, S.A. (2006). Receptor-mediated tobacco toxicity: cooperation of the Ras/Raf-1/MEK1/ERK and JAK-2/STAT-3 pathways downstream of alpha7 nicotinic receptor in oral keratinocytes. *FASEB J.* 20, 2093–2101.
- Aziz, M.H., Manoharan, H.T., and Verma, A.K. (2007). Protein kinase C epsilon, which sensitizes skin to sun's UV radiation-induced cutaneous damage and development of squamous cell carcinomas, associates with Stat3. *Cancer Res.* 67, 1385–1394.
- Biswas, S.K., and Mantovani, A. (2010). Macrophage plasticity and interaction with lymphocyte subsets: cancer as a paradigm. *Nat. Immunol.* 11, 889–896.
- Bollrath, J., Pheesse, T.J., von Burstin, V.A., Putoczki, T., Bennecke, M., Bateman, T., Nebelsiek, T., Lundgren-May, T., Canli, O., Schwitalla, S., et al. (2009). gp130-mediated Stat3 activation in enterocytes regulates cell survival and cell-cycle progression during colitis-associated tumorigenesis. *Cancer Cell* 15, 91–102.
- Bromberg, J.F., Wrzeszczynska, M.H., Devgan, G., Zhao, Y., Pestell, R.G., Albanese, C., and Darnell, J.E., Jr. (1999). Stat3 as an oncogene. *Cell* 98, 295–303.
- Bronte-Tinkew, D.M., Terebiznik, M., Franco, A., Ang, M., Ahn, D., Mimuro, H., Sasakawa, C., Ropeleski, M.J., Peek, R.M., Jr., and Jones, N.L. (2009). Helicobacter pylori cytotoxin-associated gene A activates the signal transducer and activator of transcription 3 pathway in vitro and in vivo. *Cancer Res.* 69, 632–639.
- Catlett-Falcone, R., Landowski, T.H., Oshiro, M.M., Turkson, J., Levitzki, A., Savino, R., Ciliberto, G., Moscinski, L., Fernández-Luna, J.L., Nuñez, G., et al. (1999). Constitutive activation of Stat3 signaling confers resistance to apoptosis in human U266 myeloma cells. *Immunity* 10, 105–115.
- Chae, S.S., Paik, J.H., Furneaux, H., and Hla, T. (2004). Requirement for sphingosine 1-phosphate receptor-1 in tumor angiogenesis demonstrated by in vivo RNA interference. *J. Clin. Invest.* 114, 1082–1089.
- Chan, K.S., Sano, S., Kiguchi, K., Anders, J., Komazawa, N., Takeda, J., and DiGiovanni, J. (2004). Disruption of Stat3 reveals a critical role in both the initiation and the promotion stages of epithelial carcinogenesis. *J. Clin. Invest.* 114, 720–728.
- Chiarle, R., Simmons, W.J., Cai, H., Dhall, G., Zamo, A., Raz, R., Karras, J.G., Levy, D.E., and Inghirami, G. (2005). Stat3 is required for ALK-mediated lymphomagenesis and provides a possible therapeutic target. *Nat. Med.* 11, 623–629.
- Coussens, L.M., Tinkle, C.L., Hanahan, D., and Werb, Z. (2000). MMP-9 supplied by bone marrow-derived cells contributes to skin carcinogenesis. *Cell* 103, 481–490.
- de Maat, M.F., van de Velde, C.J., Umetani, N., de Heer, P., Putter, H., van Hoesel, A.Q., Meijer, G.A., van Grieken, N.C., Kuppen, P.J., Bilchik, A.J., et al. (2007). Epigenetic silencing of cyclooxygenase-2 affects clinical outcome in gastric cancer. *J. Clin. Oncol.* 25, 4887–4894.
- Deng, L., Zhou, J.F., Sellers, R.S., Li, J.F., Nguyen, A.V., Wang, Y., Orlofsky, A., Liu, Q., Hume, D.A., Pollard, J.W., et al. (2010). A novel mouse model of inflammatory bowel disease links mammalian target of rapamycin-dependent hyperproliferation of colonic epithelium to inflammation-associated tumorigenesis. *Am. J. Pathol.* 176, 952–967.
- Du, R., Lu, K.V., Petritsch, C., Liu, P., Ganss, R., Passequé, E., Song, H., Vandenberg, S., Johnson, R.S., Werb, Z., and Bergers, G. (2008). HIF1alpha induces the recruitment of bone marrow-derived vascular modulatory cells to regulate tumor angiogenesis and invasion. *Cancer Cell* 13, 206–220.
- Erlor, J.T., Bennewith, K.L., Cox, T.R., Lang, G., Bird, D., Koong, A., Le, Q.T., and Giaccia, A.J. (2009). Hypoxia-induced lysyl oxidase is a critical mediator of bone marrow cell recruitment to form the premetastatic niche. *Cancer Cell* 15, 35–44.
- Fan, J., and Malik, A.B. (2003). Toll-like receptor-4 (TLR4) signaling augments chemokine-induced neutrophil migration by modulating cell surface expression of chemokine receptors. *Nat. Med.* 9, 315–321.
- Fidler, I.J. (2003). The pathogenesis of cancer metastasis: the 'seed and soil' hypothesis revisited. *Nat. Rev. Cancer* 3, 453–458.
- Fukuda, A., Wang, S.C., Morris, J.P., 4th, Folas, A.E., Liou, A., Kim, G.E., Akira, S., Boucher, K.M., Firpo, M.A., Mulvihill, S.J., and Hebrok, M. (2011). Stat3 and MMP7 contribute to pancreatic ductal adenocarcinoma initiation and progression. *Cancer Cell* 19, 441–455.
- Gao, D., Nolan, D.J., Mellick, A.S., Bambino, K., McDonnell, K., and Mittal, V. (2008). Endothelial progenitor cells control the angiogenic switch in mouse lung metastasis. *Science* 319, 195–198.
- Grivennikov, S., Karin, E., Terzic, J., Mucida, D., Yu, G.Y., Vallabhapurapu, S., Scheller, J., Rose-John, S., Cheroutre, H., Eckmann, L., and Karin, M. (2009). IL-6 and Stat3 are required for survival of intestinal epithelial cells and development of colitis-associated cancer. *Cancer Cell* 15, 103–113.
- Hiratsuka, S., Watanabe, A., Aburatani, H., and Maru, Y. (2006). Tumour-mediated upregulation of chemoattractants and recruitment of myeloid cells pre-determine lung metastasis. *Nat. Cell Biol.* 8, 1369–1375.
- Holmgren, L., O'Reilly, M.S., and Folkman, J. (1995). Dormancy of micrometastases: balanced proliferation and apoptosis in the presence of angiogenesis suppression. *Nat. Med.* 1, 149–153.
- Kaplan, R.N., Riba, R.D., Zacharoulis, S., Bramley, A.H., Vincent, L., Costa, C., MacDonald, D.D., Jin, D.K., Shido, K., Kerns, S.A., et al. (2005). VEGFR1-positive haematopoietic bone marrow progenitors initiate the pre-metastatic niche. *Nature* 438, 820–827.
- Kenny, H.A., Kaur, S., Coussens, L.M., and Lengyel, E. (2008). The initial steps of ovarian cancer cell metastasis are mediated by MMP-2 cleavage of vitronectin and fibronectin. *J. Clin. Invest.* 118, 1367–1379.

- Kim, S., Takahashi, H., Lin, W.W., Descargues, P., Grivennikov, S., Kim, Y., Luo, J.L., and Karin, M. (2009). Carcinoma-produced factors activate myeloid cells through TLR2 to stimulate metastasis. *Nature* 457, 102–106.
- Klein, C.A. (2009). Parallel progression of primary tumours and metastases. *Nat. Rev. Cancer* 9, 302–312.
- Kortylewski, M., Kujawski, M., Wang, T., Wei, S., Zhang, S., Pilon-Thomas, S., Niu, G., Kay, H., Mulé, J., Kerr, W.G., et al. (2005). Inhibiting Stat3 signaling in the hematopoietic system elicits multicomponent antitumor immunity. *Nat. Med.* 11, 1314–1321.
- Kortylewski, M., Kujawski, M., Herrmann, A., Yang, C., Wang, L., Liu, Y., Salcedo, R., and Yu, H. (2009a). Toll-like receptor 9 activation of signal transducer and activator of transcription 3 constrains its agonist-based immunotherapy. *Cancer Res.* 69, 2497–2505.
- Kortylewski, M., Swiderski, P., Herrmann, A., Wang, L., Kowolik, C., Kujawski, M., Lee, H., Scuto, A., Liu, Y., Yang, C., et al. (2009b). In vivo delivery of siRNA to immune cells by conjugation to a TLR9 agonist enhances antitumor immune responses. *Nat. Biotechnol.* 27, 925–932.
- Kortylewski, M., Xin, H., Kujawski, M., Lee, H., Liu, Y., Harris, T., Drake, C., Pardoll, D., and Yu, H. (2009c). Regulation of the IL-23 and IL-12 balance by Stat3 signaling in the tumor microenvironment. *Cancer Cell* 15, 114–123.
- Kowanetz, M., Wu, X., Lee, J., Tan, M., Hagenbeek, T., Qu, X., Yu, L., Ross, J., Korsisaari, N., Cao, T., et al. (2010). Granulocyte-colony stimulating factor promotes lung metastasis through mobilization of Ly6G+Ly6C+ granulocytes. *Proc. Natl. Acad. Sci. USA* 107, 21248–21255.
- Kujawski, M., Kortylewski, M., Lee, H., Herrmann, A., Kay, H., and Yu, H. (2008). Stat3 mediates myeloid cell-dependent tumor angiogenesis in mice. *J. Clin. Invest.* 118, 3367–3377.
- Lee, H., Deng, J., Kujawski, M., Yang, C., Liu, Y., Herrmann, A., Kortylewski, M., Horne, D., Somlo, G., Forman, S., et al. (2010). STAT3-induced S1PR1 expression is crucial for persistent STAT3 activation in tumors. *Nat. Med.* 16, 1421–1428.
- Lesina, M., Kurkowski, M.U., Ludes, K., Rose-John, S., Treiber, M., Klöppel, G., Yoshimura, A., Reindl, W., Sipos, B., Akira, S., et al. (2011). Stat3/Socs3 activation by IL-6 transsignaling promotes progression of pancreatic intraepithelial neoplasia and development of pancreatic cancer. *Cancer Cell* 19, 456–469.
- Mantovani, A., Allavena, P., Sica, A., and Balkwill, F. (2008). Cancer-related inflammation. *Nature* 454, 436–444.
- Niu, G., Wright, K.L., Ma, Y., Wright, G.M., Huang, M., Irby, R., Briggs, J., Karras, J., Cress, W.D., Pardoll, D., et al. (2005). Role of Stat3 in regulating p53 expression and function. *Mol. Cell. Biol.* 25, 7432–7440.
- Olive, M., Mellad, J.A., Beltran, L.E., Ma, M., Cimato, T., Noguchi, A.C., San, H., Childs, R., Kovacic, J.C., and Boehm, M. (2008). p21Cip1 modulates arterial wound repair through the stromal cell-derived factor-1/CXCR4 axis in mice. *J. Clin. Invest.* 118, 2050–2061.
- Orimo, A., Gupta, P.B., Sgroi, D.C., Arenzana-Seisdedos, F., Delaunay, T., Naeem, R., Carey, V.J., Richardson, A.L., and Weinberg, R.A. (2005). Stromal fibroblasts present in invasive human breast carcinomas promote tumor growth and angiogenesis through elevated SDF-1/CXCL12 secretion. *Cell* 121, 335–348.
- Pollard, J.W. (2004). Tumour-educated macrophages promote tumour progression and metastasis. *Nat. Rev. Cancer* 4, 71–78.
- Psaila, B., and Lyden, D. (2009). The metastatic niche: adapting the foreign soil. *Nat. Rev. Cancer* 9, 285–293.
- Shojaei, F., Wu, X., Zhong, C., Yu, L., Liang, X.H., Yao, J., Blanchard, D., Bais, C., Peale, F.V., van Bruggen, N., et al. (2007). Bv8 regulates myeloid-cell-dependent tumour angiogenesis. *Nature* 450, 825–831.
- Spiegel, S., and Milstien, S. (2003). Sphingosine-1-phosphate: an enigmatic signalling lipid. *Nat. Rev. Mol. Cell Biol.* 4, 397–407.
- Steeg, P.S. (2006). Tumor metastasis: mechanistic insights and clinical challenges. *Nat. Med.* 12, 895–904.
- Visentin, B., Vekich, J.A., Sibbald, B.J., Cavalli, A.L., Moreno, K.M., Matteo, R.G., Garland, W.A., Lu, Y., Yu, S., Hall, H.S., et al. (2006). Validation of an anti-sphingosine-1-phosphate antibody as a potential therapeutic in reducing growth, invasion, and angiogenesis in multiple tumor lineages. *Cancer Cell* 9, 225–238.
- Wang, L., Yi, T., Kortylewski, M., Pardoll, D.M., Zeng, D., and Yu, H. (2009). IL-17 can promote tumor growth through an IL-6-Stat3 signaling pathway. *J. Exp. Med.* 206, 1457–1464.
- Wei, S.H., Rosen, H., Matheu, M.P., Sanna, M.G., Wang, S.K., Jo, E., Wong, C.H., Parker, I., and Cahalan, M.D. (2005). Sphingosine 1-phosphate type 1 receptor agonism inhibits transendothelial migration of medullary T cells to lymphatic sinuses. *Nat. Immunol.* 6, 1228–1235.
- Wels, J., Kaplan, R.N., Rafii, S., and Lyden, D. (2008). Migratory neighbors and distant invaders: tumor-associated niche cells. *Genes Dev.* 22, 559–574.
- Wu, S., Rhee, K.J., Albesiano, E., Rabizadeh, S., Wu, X., Yen, H.R., Huso, D.L., Brancati, F.L., Wick, E., McAllister, F., et al. (2009). A human colonic commensal promotes colon tumorigenesis via activation of T helper type 17 T cell responses. *Nat. Med.* 15, 1016–1022.
- Yu, H., Kortylewski, M., and Pardoll, D. (2007). Crosstalk between cancer and immune cells: role of STAT3 in the tumour microenvironment. *Nat. Rev. Immunol.* 7, 41–51.
- Yu, H., Pardoll, D., and Jove, R. (2009). STATs in cancer inflammation and immunity: a leading role for STAT3. *Nat. Rev. Cancer* 9, 798–809.

DNA Methylation Screening Identifies Driver Epigenetic Events of Cancer Cell Survival

Daniel D. De Carvalho,^{1,3} Shikhar Sharma,^{1,2,3} Jueng Soo You,¹ Sheng-Fang Su,^{1,2} Phillippa C. Taberlay,¹ Theresa K. Kelly,¹ Xiaojing Yang,¹ Gangning Liang,¹ and Peter A. Jones^{1,*}

¹Department of Urology, Biochemistry and Molecular Biology

²Program in Genetic, Molecular and Cellular Biology

University of Southern California/Norris Comprehensive Cancer Center Keck School of Medicine, University of Southern California, Los Angeles, CA 90089-9181, USA

³These authors contributed equally to this work

*Correspondence: pjones@med.usc.edu

DOI 10.1016/j.ccr.2012.03.045

SUMMARY

Cancer cells typically exhibit aberrant DNA methylation patterns that can drive malignant transformation. Whether cancer cells are dependent on these abnormal epigenetic modifications remains elusive. We used experimental and bioinformatic approaches to unveil genomic regions that require DNA methylation for survival of cancer cells. First, we surveyed the residual DNA methylation profiles in cancer cells with highly impaired DNA methyltransferases. Then, we clustered these profiles according to their DNA methylation status in primary normal and tumor tissues. Finally, we used gene expression meta-analysis to identify regions that are dependent on DNA methylation-mediated gene silencing. We further showed experimentally that these genes must be silenced by DNA methylation for cancer cell survival, suggesting these are key epigenetic events associated with tumorigenesis.

INTRODUCTION

During tumorigenesis cancer cells acquire, through a multistep process, a new set of properties that allows them to overcome physiological homeostasis. These properties include unlimited proliferation potential, self-sufficiency in growth signals, resistance to antiproliferative and apoptotic signals and immune system evasion, among others (Hanahan and Weinberg, 2000, 2011). These alterations, on the other hand, contribute to a process known as the stress phenotype of cancer (Luo et al., 2009), which includes DNA damage/replication stress, proteotoxic stress, mitotic stress, metabolic stress, and oxidative stress.

To survive the tumorigenic process, a cancer cell undergoes several modifications to its genomic circuitry, such as activating mutations in oncogenes and aberrant activation of nononcogenic pathways. These adaptations lead to oncogene addiction (Weinstein, 2002) and nononcogene addiction (Solimini et al.,

2007), respectively. Because of this aberrant circuitry, cancer cells become hypersensitive to the effects of classic tumor suppressor genes (TSGs) (Luo et al., 2009; Weinstein, 2002) and, potentially, to genes that can inhibit the nononcogenic signaling pathways that cancer cells rely on to survive.

Changes in the cancer cell transcriptome can be driven by genetic and epigenetic alterations (Baylin and Ohm, 2006; Jones and Baylin, 2007). DNA methylation is an epigenetic process that can heritably change gene expression without altering the DNA sequence. In normal somatic cells, most DNA methylation occurs at CpG dinucleotides within CpG poor sequences, whereas CpG-rich sequences, also known as CpG islands, are usually unmethylated (Sharma et al., 2010). DNA methylation is a vital mechanism of epigenetic gene silencing, playing key roles in X chromosome inactivation, genomic imprinting, embryonic development, silencing of repetitive elements and germ cell-specific genes, differentiation, and maintenance of pluripotency (De Carvalho et al., 2010; Meissner, 2010; Robertson,

Significance

Epigenetic modifications are potentially reversible, making them good “druggable” targets. Here, we show that cancer cells cannot survive in the absence of aberrant DNA methylation of specific promoter regions. This process may render cancer cells more susceptible to epigenetic therapy. We also found that physiological DNA methylation of germline-specific genes is necessary for somatic cell survival, suggesting a physiological dependence on continuous DNA methylation of these regions in somatic tissues. Moreover, by defining the promoter regions that must be methylated in order for cells to survive in culture, we found several genes that acquire de novo DNA methylation in cell lines, highlighting the importance of careful interpretation of epigenetic results obtained from cell culture experiments.

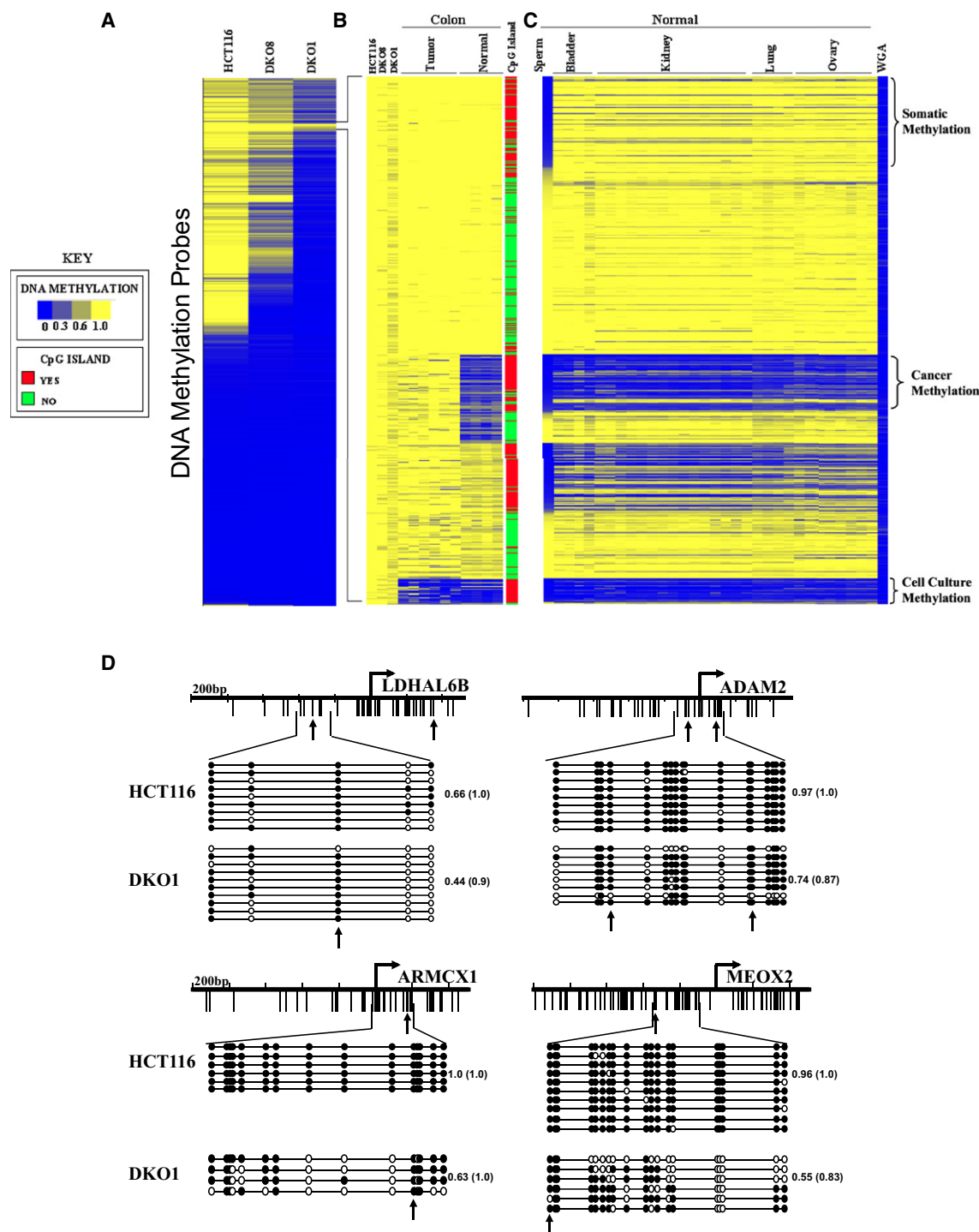


Figure 1. Clustering of DNMT-Deficient Cells Identifies Three Classes of Putative Driver Genes Marked by DNA Methylation

(A) One-dimensional hierarchical clustering using Euclidean distance and average linkage was performed with the ~24,000 Infinium DNA methylation probes located outside of repeats or known SNPs in HCT116 wild-type, DKO8, and DKO1 cell lines. Each row represents a probe; each column represents a sample. The β value (level of DNA methylation) for each probe is represented with a color scale as shown in the key.

(B) k Means ($K = 4$) clustering of the 566 Infinium DNA methylation probes that maintain DNA methylation in DKO1 sample (a β value of at least 0.6 and a difference between HCT116 and DKO1 smaller than 0.2) in (A) for 10 TCGA samples ($n = 4$ normal colon and $n = 6$ primary colon adenocarcinoma).

(C) Heat map of 566 Infinium DNA methylation probes in 32 normal tissues retaining the probe order from (B). Primary normal bladder ($n = 4$), sperm ($n = 1$), and primary normal TCGA kidney ($n = 15$), lung ($n = 4$), and ovary ($n = 8$). WGA DNA was used as a negative control for DNA methylation.

(D) Bisulfite-sequencing validation of Infinium DNA methylation data from two regions (*LDHAL6B* and *ADAM2*) from the somatic-specific DNA methylation cluster and two regions (*ARMCX1* and *MEOX2*) from the cancer-specific DNA methylation cluster. Arrow indicates the position of the Infinium probe. Empty and filled

2005). Besides these physiological roles, deregulated DNA methylation can also be a major driver of pathological conditions, including neurological and autoimmune diseases, as well as cancer (Kelly et al., 2010; Portela and Esteller, 2010; Taberlay and Jones, 2011). During tumorigenesis, global DNA methylation patterns change, resulting in hypomethylation of non-CpG islands and hypermethylation of CpG islands (Sharma et al., 2010). DNA hypermethylation has been shown to result in abnormal silencing of several TSGs in most types of cancer (Jones and Baylin, 2002, 2007).

Recently, several efforts to examine the cancer methylome, utilizing genome-wide techniques, have revealed that a large number of genes exhibit aberrant DNA methylation profiles in cancer (Figuerola et al., 2010; Irizarry et al., 2009). These changes can be used to stratify subtypes of cancers (Figuerola et al., 2010; Noushmehr et al., 2010) and to predict cancer outcomes (Portela and Esteller, 2010), among other uses. Distinguishing which genes play key “driver” roles via DNA methylation-mediated gene silencing in cancer initiation, progression, and maintenance and those genes that are only “passengers” in the tumorigenic process would be extremely useful in developing more targeted epigenetic therapies (Kelly et al., 2010). However, making this distinction has proven extremely difficult due to the large number of differentially DNA-methylated genes in human cancers (Kalari and Pfeifer, 2010).

We, and others, have suggested that cancer cells may become addicted to an aberrant epigenetic landscape, especially with respect to DNA methylation (Baylin and Ohm, 2006; Kelly et al., 2010). However, as of yet, and to our knowledge, there is no direct evidence for such an addiction. Furthermore, mining the thousands of genomic regions that are de novo DNA methylated in cancer and identifying those required for cancer cell survival have proven extremely challenging (Kalari and Pfeifer, 2010). Here, we describe an approach to identify driver epigenetic events associated with cancer cell survival. Our findings pave the way for new generations of epigenetic therapies, which target the genes cancer cells rely on being silenced by DNA methylation in order to survive.

RESULTS

Identification of the Minimum DNA Methylation Profile Required for Cancer Cell Survival

We hypothesized that cancer cells depend on DNA methylation of a few key regions for survival and that these regions would preferentially maintain methylation when artificially reducing global DNA methylation. To test this hypothesis, we profiled HCT116 colon cancer cells and HCT116 cells with a genetic disruption of *DNMT3B* and *DNMT1* (DKO) (Rhee et al., 2002). This genetic disruption led to a complete knockout of *DNMT3B* and a truncated *DNMT1* transcript, expressed at very low levels (Egger et al., 2006; Rhee et al., 2002; Spada et al., 2007). For this study we used two DKO subclones, DKO8 and DKO1, which

retain approximately 45% and 5% of the HCT116 wild-type global DNA methylation levels, respectively (Rhee et al., 2002; Sharma et al., 2011). It is important to note that a further reduction of *DNMT1* levels, by RNAi, in cells with a genetic disruption of *DNMT1* results in demethylation and a massive reduction of cell viability and immediate induction of cell death (Spada et al., 2007), suggesting that DNA methylation is required for cancer cell survival.

We profiled promoter DNA methylation of HCT116, DKO8, and DKO1 cell lines using the Illumina Infinium platform (HumanMethylation27) and observed a reduction in global DNA methylation levels in DKO8 cells compared to HCT116 wild-type cells and an even greater reduction in DKO1 cells (Figure 1A), consistent with previous data (Rhee et al., 2002; Sharma et al., 2011). Surprisingly, we found a collection of 566 CpG sites, spanning 490 genes that despite the strong impairment in DNA methyltransferase activity, still retained a high level of DNA methylation in DKO1 cells, with a β value higher than 0.6 (see Table S1 available online for gene/probe list). These regions were also highly methylated in HCT116 and DKO8 cells, and none showed a difference in their β values greater than 0.2 among the three cell lines.

Next, we sought to identify whether there was a cancer-specific DNA methylation profile at these regions that maintained DNA methylation even in DKO1 cells, which would potentially include important putative targets for epigenetic therapy. To accomplish this, we first compared the DNA methylation levels of the 566 CpG sites that retained DNA methylation in DKO1 cells to the DNA methylation profile of 6 primary colon adenocarcinoma tissue samples and 4 normal colon tissue samples obtained from The Cancer Genome Atlas (TCGA) database. Using k means clustering, we identified 92 CpG sites, spanning 77 genes that were unmethylated in normal colon and became hypermethylated in colon adenocarcinoma (Figure 1B; Table S1), consistent with a cancer-specific methylation profile.

We further compared these data to DNA methylation data of several normal tissues including sperm, bladder, kidney, lung, and ovary, which allowed us to identify clusters of gene regions highly enriched for somatic tissue-specific DNA methylation. Such genes were methylated in the somatic tissues analyzed and unmethylated in germ cells. This somatic tissue-specific cluster comprised 99 CpG sites, spanning 83 genes (Figure 1C; Table S1). Furthermore, we also identified genes that exhibit cell culture-specific DNA methylation, such that these regions are methylated in all cell lines analyzed but unmethylated in primary tissues (Figure 1C; Table S1). This cell culture-specific cluster comprised 29 CpG sites, spanning 25 genes. We focused only on these three groups because of their differential DNA methylation profiles. We speculate that the remaining 346 CpG sites might be regions that are more prone to methylation, remaining a good target for residual DNA methylation activity without functional relevance or, alternatively, may have a tissue-specific expression profile, being unmethylated only in

circles denote unmethylated and methylated CpG sites, respectively. Each horizontal row represents one sequenced DNA clone. The number on the right represents the mean DNA methylation score of each region, and the number in the parentheses represents the mean DNA methylation score of the specific Infinium CpG site.

See also Figure S1 and Table S1.

specific cell types that were not surveyed in this study. Whole Genome Amplified (WGA) DNA served as a negative control (Figure 1C) to confirm that the regions identified as being methylated in DKO1 cells were not false positives due to technical problems with the specific Infinium probes.

The distribution of probes, relative to transcription start sites (TSSs), in the cancer-specific and somatic tissue-specific clusters was found to be very similar to the distribution of the array itself, whereas the distribution in the cell culture-specific cluster tended to be slightly more concentrated at the TSS (Figure S1A). However, it should be noted that there was no association between distance to TSS and methylation cluster (somatic, cancer, cell line) as assessed by one-way ANOVA ($p > 0.05$).

We selected genomic regions from each cluster to validate the Infinium-based DNA methylation data using bisulfite sequencing. All of the sequences analyzed showed high levels of DNA methylation in HCT116 wild-type and DKO1 cells (Figure 1D), with the CpG site surveyed by the Infinium platform presenting a maximum difference between their β values of 0.17 in DKO1 when compared to HCT116 wild-type. These results demonstrate that even though DKO cells are globally DNA hypomethylated (Rhee et al., 2002; Sharma et al., 2011), the residual DNA methylation is focal and site specific, supporting the hypothesis that there is a functional role for some of the retained DNA methylation.

To further demonstrate the importance of the DNA methylation that is retained in the three identified clusters, we treated DKO1 cells with 1 μ M of 5-Aza-2'-deoxycytidine or PBS for 24 hr. After treatment, we allowed at least two population doublings (5 days) for demethylation to occur and then analyzed changes in the DNA methylation profile by the Illumina Infinium array. As expected, most of the regions in the three previously identified clusters were resistant to demethylation, with only eight regions from the somatic cluster, five regions from the cancer cluster, and one region from the cell culture cluster presenting a difference in the β value greater than 0.2 (Figure S1B). These regions we considered false positives and excluded them from subsequent analysis.

Residual Methylation in DKO1 Cannot Be Explained by an Inherent Susceptibility to DNA Methylation

Our working hypothesis is that the artificial impairment of DNA methyltransferase machinery in DKO1 cells will induce a strong selective pressure for any remaining DNA methylation to be maintained at the regions necessary for cancer cell survival. An equally plausible hypothesis is that the residual methylation reflects an inherent tendency for some genes to remain methylated. Indeed, previous studies suggest that certain genomic regions are more prone to DNA methylation (Estéicio et al., 2010; Ohm et al., 2007; Schlesinger et al., 2007; Widschwendter et al., 2007). Therefore, these regions may remain better targets for residual DNA methylation activity. To directly test this alternative hypothesis, we used two known approaches to predict whether a gene is more prone to DNA methyltransferase activity in cancer cells: one based on its chromatin structure (Ohm et al., 2007; Schlesinger et al., 2007; Widschwendter et al., 2007), and another based on its genomic architecture (Estéicio et al., 2010).

Genes marked by H3K27me3 in embryonic stem cells (ESCs) are known to be predisposed to DNA methylation in cancer cells (Ohm et al., 2007; Schlesinger et al., 2007; Widschwendter et al., 2007). Indeed, we found that the H3K27me3 status in ESCs can accurately predict the methylation levels in the wild-type HCT116 cells (Figure 2A). Then, we tested whether methylation-prone regions (H3K27me3 positive in ESCs) would preferentially retain methylation in DKO1 cells, compared to HCT116 cells. If this hypothesis was correct, we should observe an enrichment of methylation-prone genes in the cohort of genes that is methylated in DKO1 cells because they would be better targets for residual DNA methyltransferase activity. Yet, there was no such enrichment (Figure 2B). Rather, we observed a slight decrease in the proportion of methylation-prone genes that retain methylation in DKO1 cells. These data suggest that genes found to retain DNA methylation in DKO1 cells are not simply predisposed to DNA methylation in cancer cells.

To further test this hypothesis, we performed a similar analysis using a previously published algorithm to predict whether a genomic region is prone, intermediate, or resistant to DNA methylation in cancer cells, based on its genomic architecture (Estéicio et al., 2010). In our test this algorithm accurately predicted methylation levels in HCT116 cells (Figure 2C). Similar to the previous analysis, if the genes that maintain methylation in DKO1 cells were simply more prone to DNA methyltransferase activity, one would expect an enrichment of methylation-prone genes in the pool of genes that retains methylation in DKO1 cells. Again, we could not find such enrichment (Figure 2D).

Taken together, these data suggest that the targets of residual DNA methylation in DKO1 cells are not dictated by an inherent predisposition to DNA methylation based on either the chromatin structure or the genomic architecture. These findings further support our original hypothesis that these loci retain methylation due to a functional selection pressure.

Validation of the Findings in Other Types of Cancer and Association with Gene Expression

We next validated our findings in a larger test set of colon adenocarcinoma and normal colon samples. Using DNA methylation data available from TCGA, we observed a significant increase in DNA methylation in the majority of the CpG sites identified with cancer-specific DNA methylation in 168 primary colon adenocarcinoma samples relative to 16 normal colon samples (Figure 3A; Wilcoxon rank sum test followed by a FDR correction, $p < 0.05$). We next extended our findings to determine whether this cancer-specific DNA methylation profile was unique to colon adenocarcinoma or if it could also be observed in other tumor types. Using DNA methylation data available from TCGA, we analyzed DNA methylation from 19 lung adenocarcinoma samples against 4 normal samples. Again, the same pattern emerged, where the identified CpG sites presented an overall significant gain of DNA methylation in the tumor samples (Figure 3C; Wilcoxon rank sum test followed by a FDR correction, $p < 0.05$). Indeed, most of the genes statistically determined to be hypermethylated in lung adenocarcinoma were also hypermethylated in colon adenocarcinoma (Figure 3E). These data indicate that the CpG sites we identified as cancer specific are frequently hypermethylated in other types of human cancer relative to the normal cell counterparts, suggesting that these

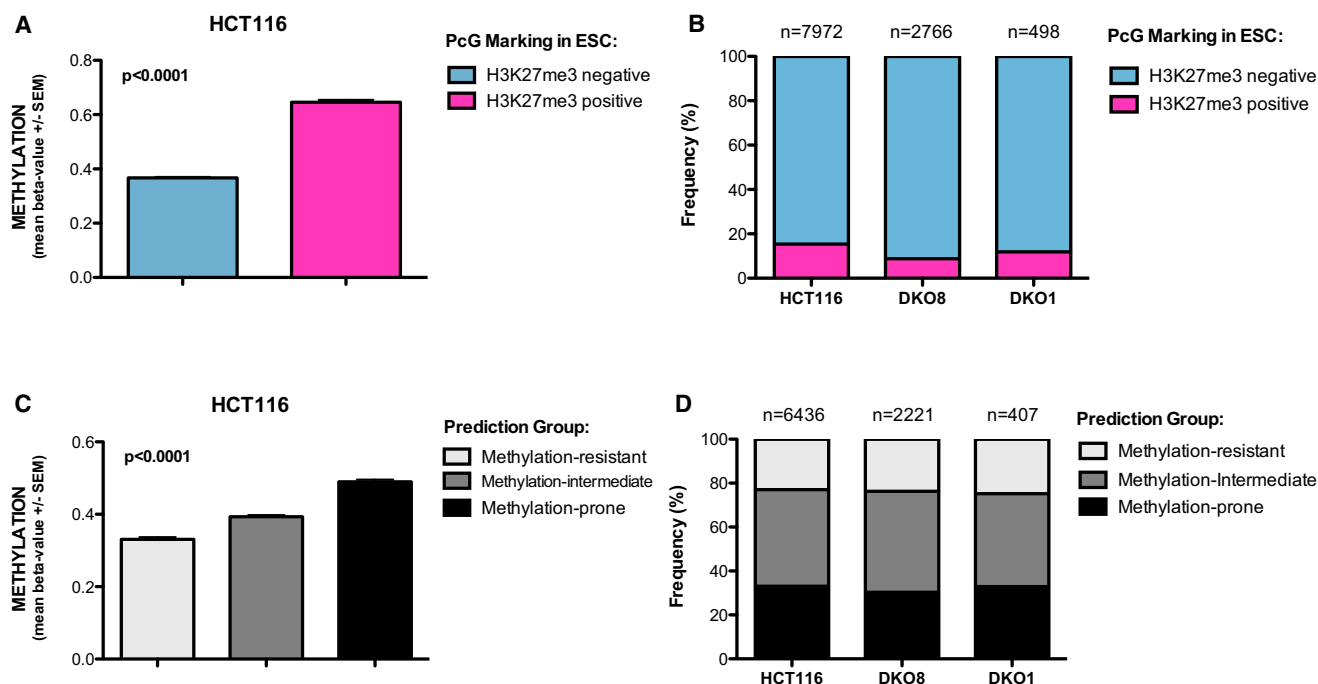


Figure 2. Residual Methylation in DKO1 Is Not Caused by an Inherent Susceptibility to DNA Methylation

(A) Validation of H3K27me3 status in ESCs as a predictive method for DNA methylation in HCT116 cells. Methylation status of ~27,000 CpG sites was determined by Infinium. A t test with Mann-Whitney U posttest was performed. Data represent the mean \pm SEM.

(B) Frequency of probes marked by H3K27me3 in ESCs in the cohort of DNA-methylated probes (β value > 0.6) in HCT116, DKO8, and DKO1 cells.

(C) Validation of the predictive method based on genomic architecture (Estéicio et al., 2010) in HCT116 cells. Methylation status of ~27,000 CpG sites was determined by Infinium. One-way ANOVA with Kruskal-Wallis test as performed. Data represent the mean \pm SEM.

(D) Frequency of methylation-prone genes in the cohort of DNA-methylated genes (β value > 0.6) in HCT116, DKO8, and DKO1 cells.

regions might have a more fundamental role in tumorigenesis, such as cell survival.

Because DNA methylation of CpG islands located in promoter regions is well known to be correlated with gene silencing (Cedar and Bergman, 2009; Jones and Baylin, 2007; Portela and Esteller, 2010), we investigated the expression state of the genes identified using independent data sets. We selected two microarray data sets from the Gene Expression Omnibus database (<http://www.ncbi.nlm.nih.gov/geo/>): colon adenocarcinoma against normal colon (GSE 8671) (Sabates-Bellver et al., 2007); and lung adenocarcinoma against normal lung (GSE7670) (Su et al., 2007).

We found an inverse correlation between DNA methylation and gene expression when we analyzed the gene expression data of 32 normal colon samples and 25 colon tumor samples. The majority of the genes subject to cancer-specific DNA methylation displayed decreased gene expression in colon cancer samples compared to normal colon (Figure 3B; t test followed by a FDR correction, $p < 0.05$). We also observed that some genes showed a similarly low level of expression in both samples, probably due to an epigenetic switch in the silencing mechanism where the gene was already silenced in the normal sample by another epigenetic mechanism and became de novo DNA methylated in cancer (Gal-Yam et al., 2008).

Moreover, we found a similar gene expression pattern in lung adenocarcinoma, where most of the cancer-specific DNA

methylation genes displayed decreased gene expression in the tumor when compared to the correspondent normal tissue (Figure 3D; t test followed by a FDR correction, $p < 0.05$). Again, most of the genes statistically repressed in lung adenocarcinoma were also repressed in colon adenocarcinoma (Figure 3F). These data further suggest that there is a functional relevance of identified DNA methylation.

Altogether, by combining gene expression with DNA methylation data, we identified regions that are candidates for DNA methylation-mediated gene silencing. Moreover, the gene expression data corroborate our cluster analysis by using a different method and independent data sets to demonstrate biological differences in the gene clusters we identified.

Spontaneous Loss of DNA Methylation at the Identified Genomic Regions Is Associated with Cell Death

DKO1 cells have highly impaired DNA methyltransferase machinery due to the absence of DNMT3B, very low protein levels of DNMT3A, and low levels of a truncated DNMT1 (Egger et al., 2006; Sharma et al., 2011). As a consequence of the impaired DNA methyltransferase machinery, the global DNA methylation level in this cell line is very low, with most of the genes that were methylated in the parental HCT116 cells losing this methylation in DKO1 cells. Therefore, we hypothesize that DKO1 cells would be under a constant selective pressure to maintain the residual DNA methylation at key regions necessary for this cancer cell to survive.

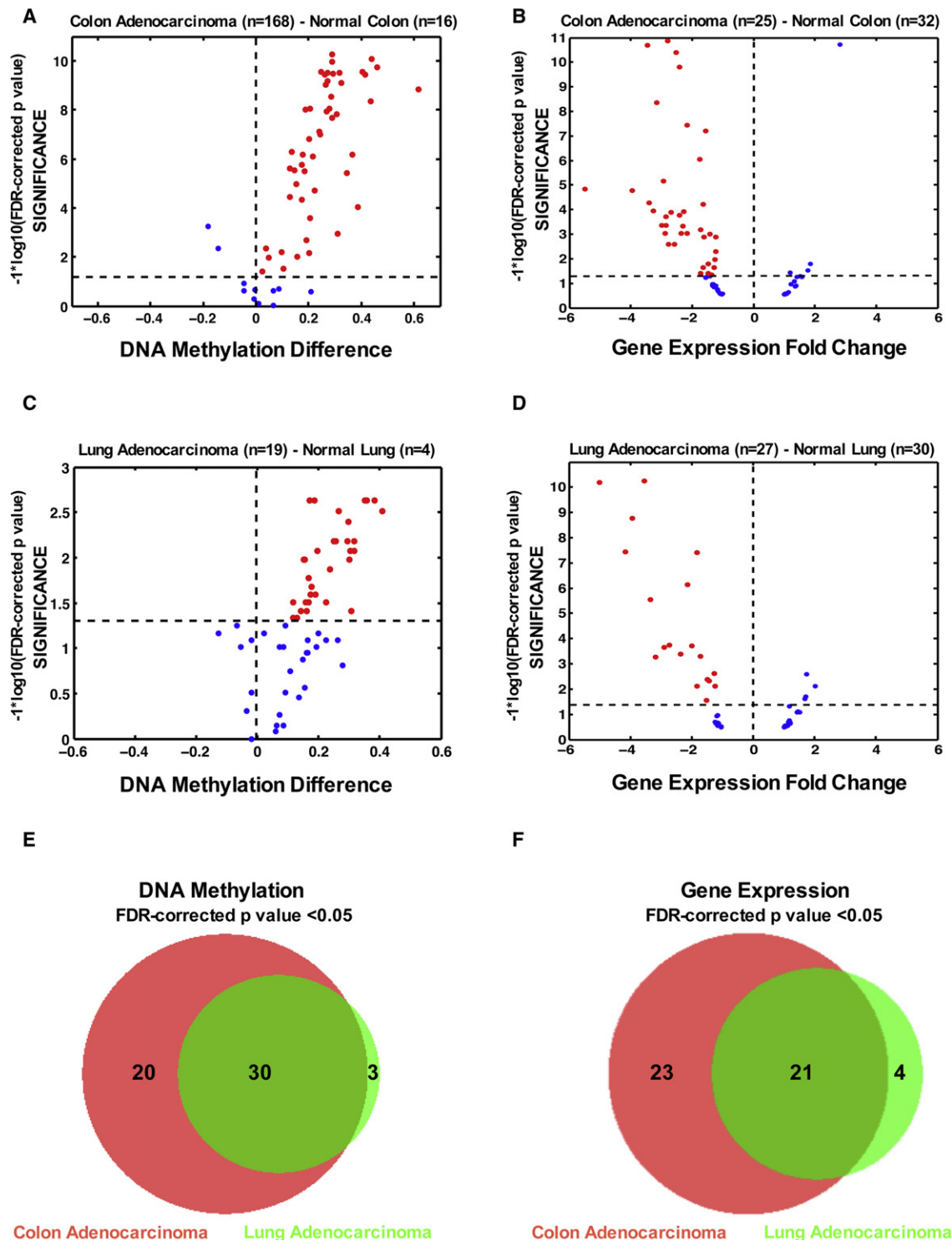


Figure 3. Validation of CpG Sites Identified with Cancer-Specific DNA Methylation Using Independent Data Sets and Association with Gene Repression

(A) Volcano plot of the CpG loci identified as cancer-specifically methylated in colon adenocarcinoma (normal n = 16, cancer n = 168) from TCGA Data Portal. The β value difference in DNA methylation between the tumor samples and the correspondent normal samples is plotted on the x axis, and the p value for a FDR-corrected Wilcoxon rank sum test of differences between the tumor and correspondent normal samples ($-1 \times \log_{10}$ scale) is plotted on the y axis. Probes that are significantly hypermethylated (FDR adjusted $p < 0.05$) in tumors are shown in red.

(B) Volcano plot gene expression data of cancer-specific DNA-methylated genes. Gene expression data were obtained from GEO (GSE 8671) from primary normal colon (n = 32) and primary colon cancer (n = 25). For the volcano plots, gene expression fold change between the normal tissues and the tumor tissues is

We next investigated whether DKO1 cells exhibit a higher basal level of cell death than HCT116 wild-type cells. When quantifying cell death by measuring the externalization of phosphatidylserine (PS) using annexin V by flow cytometry, we observed at least four times more spontaneous cell death in DKO1 than in the parental HCT116 cells (Figure 4A). This suggests that DKO1 cells are indeed under constant selective pressure, probably because during cell division, some daughter cells lose DNA methylation at key regions due to the impaired DNA methyltransferase activity in DKO1 cells (Egger et al., 2006; Spada et al., 2007), and consequently, they cannot survive.

We took advantage of the increased rates of spontaneous cell death in DKO1 cells to further test our hypothesis that cancer cells depend on constant DNA methylation of these regions in order to survive. Using cell sorting, we first separated DKO1 cells into two populations: annexin V positive (early spontaneous apoptosis), and annexin V negative (viable cells) (Figure 4A). These two populations have distinct morphologies, with annexin V-positive cells in the range of lower Forward Scatter (FSC) and higher Side Scatter (SSC), a characteristic feature of apoptotic cells (Darzynkiewicz et al., 1992), compared to annexin V-negative cells (Figure 4B).

We then compared the DNA methylation levels of *EYA4* and *IRAK3* gene promoter regions in early apoptotic and viable cells. We have previously defined these genes as harboring cancer-specific DNA methylation and differential expression in cancer versus normal cells. Furthermore, these genes were in the top tier for significantly hypermethylated genes, and for gene repression, in colon and lung adenocarcinoma. In addition we also compared the DNA methylation levels of *SYCP3* and *ADAM2* gene promoter regions between early apoptotic and viable cells. These genes were identified as having somatic cell-specific DNA methylation and differential gene expression between somatic and germ cells (data not shown). In agreement with our hypothesis that DNA methylation-induced silencing of these regions is required for survival, early apoptotic cells showed at least a 27% reduction in DNA methylation in all four regions analyzed, with some specific CpG sites having as much as 80% reduction in DNA methylation (Figures 4C and S2A). Because degradation of cellular mRNA is an early apoptosis-induced event (Del Prete et al., 2002), we could not reliably measure whether this demethylation was associated with re-expression of these genes in the dying cells. In contrast, DNA degradation is a late apoptotic event, which allowed us to study the DNA methylation status during the first steps of apoptosis.

An alternative hypothesis is that global demethylation in DKO1 cells, due to impaired DNA methyltransferase activity, leads to genomic instability and cell death. To test this hypothesis, we measured the global DNA methylation levels of the early spontaneous apoptotic and viable cells and did not find a global reduction in DNA methylation (Figure S2B), further suggesting that demethylation of these specific genes lead to cell death. In addition to test whether apoptosis itself could cause demethylation of these regions, we treated HCT116 cells with 0.2 μ M of Staurosporine (STS), a drug known to induce cell death by blocking protein kinases (Manns et al., 2011). Next, we sorted viable and STS-induced dead cells and did not observe any difference in DNA methylation of these candidate regions (Figure S2C). Altogether, this strongly suggests that demethylation of these regions is causing cell death rather than the other way around.

These data, together with our previous data showing that DKO1 cells have reduced cell viability when this low level of DNMT1, and consequently the DNA methylation level, is further reduced by RNAi (Egger et al., 2006; Spada et al., 2007), and that complete knockout of the maintenance *DNMT1* leads to massive cell death (Chen et al., 2007), demonstrate that these cells are under constant selective pressure to retain DNA methylation at these key regions that we identified here in order to survive.

Functional Validation

We sought to further demonstrate that re-expression of genes whose DNA methylation is critical for cancer cell survival leads to increased cell death. We cloned the cDNA of six genes from the cancer cluster (*IRAK3*, *P2RY14*, *CDO1*, *BCHE*, *ESX1*, and *ARMCX1*), two from the somatic cluster (*ADAM2* and *SYCP3*), and one from the cell line cluster (*STEAP4*) into the pLJM1 lentiviral vector to individually reexpress these genes in HCT116 and RKO colon carcinoma cell lines (Figures S3A and S3B). We observed that expression of each of these genes decreased cell viability in both HCT116 and RKO cells (Figures 5A and 5B). We also re-expressed *NOX4* as a control gene (Figures 5A and 5B). *NOX4* was heavily methylated in HCT116 (β value of 0.95) and completely demethylated in DKO1 (β value of 0.007), suggesting that DNA methylation-mediated repression of this gene is not necessary for DKO1 survival. It is important to note that these ten genes have a low relative expression in RKO (Figure S3B) and a very high basal DNA methylation level in this cell line (Figure S3E).

plotted on the x axis, and the p value for a FDR-corrected t test of differences between the normal and the tumor tissues ($-1 \times \log_{10}$ scale) is plotted on the y axis. Probes that are significantly ($p < 0.05$) downregulated in tumor tissues are shown in red.

(C) Volcano plot of the CpG loci identified as cancer-specifically methylated in lung adenocarcinoma (normal $n = 4$, cancer $n = 19$) from TCGA Data Portal. The β value difference in DNA methylation between the tumor samples and the correspondent normal samples is plotted on the x axis, and the p value for a FDR-corrected Wilcoxon rank sum test of differences between the tumor and correspondent normal samples ($-1 \times \log_{10}$ scale) is plotted on the y axis. Probes that are significantly hypermethylated (FDR adjusted $p < 0.05$) in tumors are shown in red.

(D) Volcano plot gene expression data of cancer-specific DNA-methylated genes. Gene expression data were obtained from GEO (GSE7670) from primary lung adenocarcinoma ($n = 27$) and primary lung ($n = 30$). For the volcano plots, gene expression fold change between the normal tissues and the tumor tissues is plotted on the x axis, and the p value for a FDR-corrected t test of differences between the normal and the tumor tissues ($-1 \times \log_{10}$ scale) is plotted on the y axis. Probes that are significantly ($p < 0.05$) downregulated in tumor tissues are shown in red.

(E) Venn diagram showing the overlap between the genes statistically hypermethylated in colon adenocarcinoma ($n = 50$; FDR adjusted $p < 0.05$) and lung adenocarcinoma ($n = 33$; FDR adjusted $p < 0.05$).

(F) Venn diagram showing the overlap between the genes statistically repressed in colon adenocarcinoma ($n = 44$; FDR adjusted $p < 0.05$) and lung adenocarcinoma ($n = 25$; FDR adjusted $p < 0.05$).

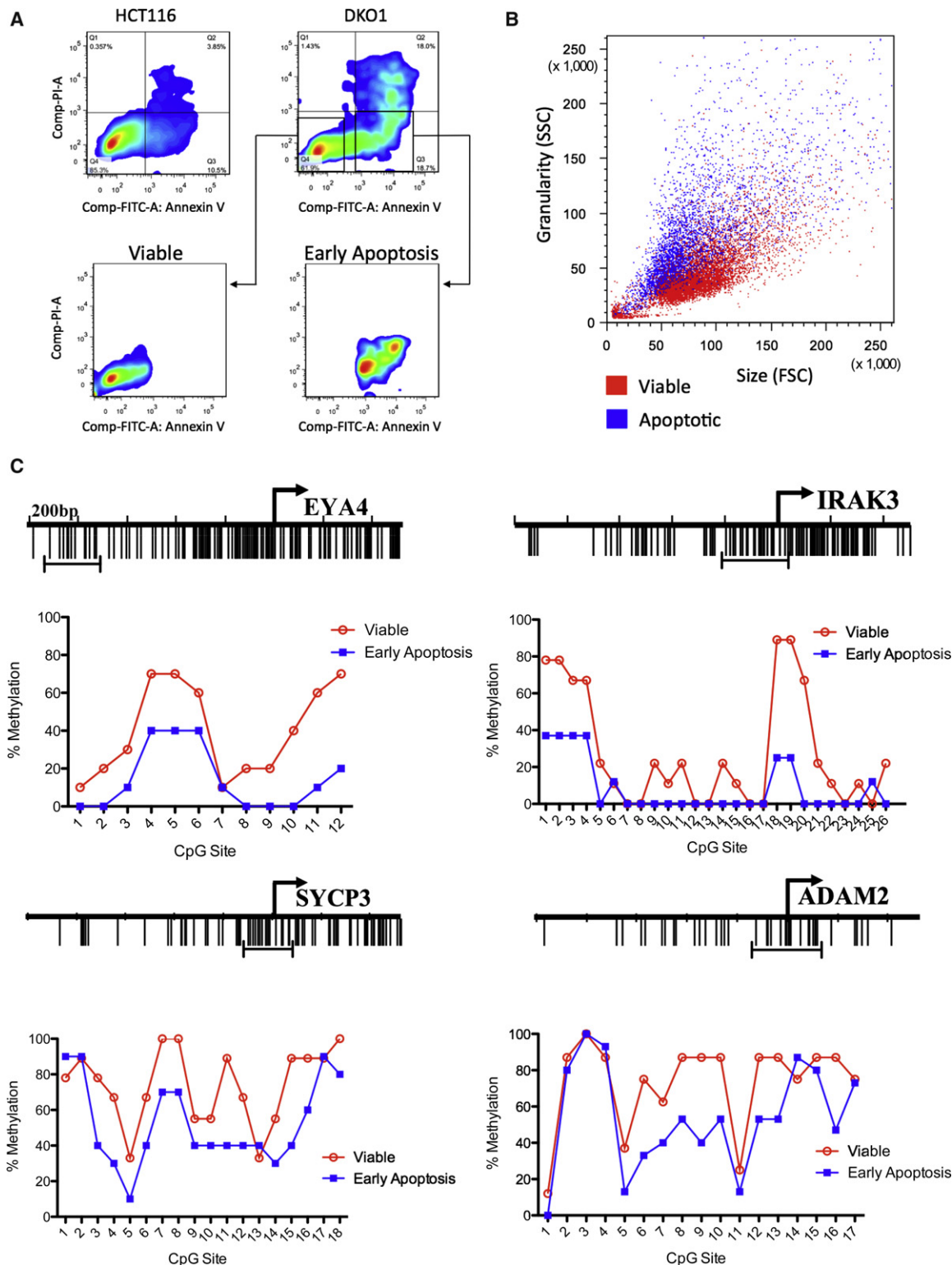


Figure 4. Apoptosis Analysis of HCT116 and DKO1 Cells

(A) HCT116 wild-type and HCT116 DKO1 cells were stained with annexin V-FITC and PI and analyzed by FACS, showing an increased level of basal apoptotic cell death in the HCT116 DKO1 cell line compared to HCT116 wild-type. HCT116 DKO1 cells were then sorted in viable (annexin V and PI negative) and early apoptosis (annexin V positive and PI negative).

(B) The morphology of viable DKO1 and early apoptosis is clearly distinct. The apoptotic cells (blue) show a characteristic phenotype of higher SSC and lower FSC than the viable cells (red).

To gain more detailed information of how cancer cells become dependent on DNA methylation of these genes, we investigated how the silencing of one candidate, interleukin-1 receptor-associated kinase 3 (*IRAK3*), affects cancer cell survival in more detail. *IRAK3* has a cancer-specific DNA methylation pattern, a reduced expression in colon adenocarcinoma compared to normal colon, and a decreased DNA methylation in spontaneously dying DKO1 cells when compared to viable DKO1 cells. In addition, *IRAK3* was a promising candidate because, through *IRAK1* (Kobayashi et al., 2002), it indirectly inhibits three essential pathways that cancer cells rely on to survive: STAT3, NFkB, and MAPK (Figure S3F) (Ngo et al., 2011; Su et al., 2009; Turnis et al., 2010). These pathways, in turn, regulate the expression of the antiapoptotic gene *SURVIVIN* (Jiang et al., 2011; Zhou et al., 2009). Consistent with our hypothesis, using the Oncomine platform (<http://www.oncomine.org>), we found reduced *IRAK3* expression in several types of cancer when compared to normal tissue (Figure 5C) including colon adenocarcinoma when compared to normal colon (Student's t test $p = 6.59\text{E-}4$, top 15% underexpressed gene rank) (Kaiser et al., 2007), in lung adenocarcinoma when compared to normal lung (Student's t test $p = 5.70\text{E-}7$, top 6% underexpressed gene rank) (Su et al., 2007), in prostate carcinoma when compared to normal prostate (Student's t test $p = 4.01\text{E-}5$, top 3% underexpressed gene rank) (Welsh et al., 2001), and in cutaneous melanoma when compared to normal skin (Student's t test $p = 3.74\text{E-}8$, top 3% underexpressed gene rank) (Talantov et al., 2005) (Figure 5C). The consistently reduced expression level of *IRAK3* in a variety of cancers suggests that its silencing plays a role in the tumorigenic process. In addition the downregulation of *IRAK3* was correlated with a statistically significant upregulation of *IRAK1* and *SURVIVIN* in the same studies (Figures S3C and S3D).

To formally test whether the decreased expression of *IRAK3* was directly responsible for the increased expression of *SURVIVIN* and, consequently, increased cell survival, we re-expressed *IRAK3* in HCT116 cells. Re-expression of *IRAK3* caused a striking reduction in Survivin protein levels (Figure 5D) and caused a significant increase in cell death (Student's t test $p = 0.0219$; Figure 5E) and decrease in cell viability ($p < 0.0001$ Figure 5E), confirming that cancer cells require DNA methylation-induced silencing of *IRAK3*, and thus become dependent on the aberrant DNA methylation. Moreover, we sought to determine whether the silencing of *IRAK3* has any effect in a nontransformed cell. We performed a colony formation assay in a nontumorigenic cell line, URO-TSA, infected with *IRAK3* shRNA or a scrambled shRNA (Figure 5F). We observed that *IRAK3* knockdown was sufficient to induce a striking increase in colony formation (Figure 5F), thus demonstrating that the criteria we used were successful to identify functionally relevant genes and demonstrate that cancer cells become addicted to their epigenetic silencing.

DISCUSSION

Several genome-wide studies have revealed that a large number of promoter regions become de novo methylated in cancer (Noushmehr et al., 2010; Portela and Esteller, 2010). However, defining the specific “driver” gene regions that cancer cells depend on for survival has proven extremely difficult (Kalari and Pfeifer, 2010). In this study we have defined the gene promoters whose DNA methylation is required for survival of somatic cancer cells in culture. This group of genes could be further subdivided into at least three subgroups: those necessary to be methylated for the survival of (1) somatic cells, (2) cancer cells, and (3) cells in culture. These sets of genes retain DNA hypermethylation even after strong depletion of DNA methyltransferase activity, suggesting that DNA methylation is the main epigenetic mechanism used to maintain silencing because these cells do not seem able to switch to other repression mechanisms such as histone modifications alone.

Genes with germline-specific expression need to be tightly regulated in somatic tissues because their aberrant expression could be lethal for somatic cells. For example the gene “*Stil*,” in *Drosophila*, is only expressed in germ cells and is necessary for germ cell survival. When “*Stil*” is transiently expressed in somatic tissues, it results in lethality (Sahut-Barnola and Pauli, 1999). The genes we identified in the somatic-specific DNA methylation group are mainly germ cell-specific genes, and their demethylation and resulting re-expression in somatic cells can trigger apoptosis, as we showed for *SYCP3* and *ADAM2*. This suggests a primary role for DNA methylation as a mechanism for repression of testes-specific genes in somatic cells (which includes cancer cells). It also lends confidence to our analysis because it is known that several CpG island genes are normally DNA methylated in somatic tissue and unmethylated in germ cells (Shen et al., 2007).

Intriguingly, none of the genes identified in the cancer-specific group, whose DNA methylation is necessary for the survival of cancer cells, is classically known TSGs. This suggests that the genes we identified here are previously unknown tumor suppressors whose silencing is necessary for cancer cell survival. Interestingly, this group encompasses several cell signaling molecules, such as those with nucleotide receptor activity and G protein-coupled receptors (GPCRs). GPCRs have recently been described to be significantly mutated in several kinds of cancer and were found as a top category in a systematic search for TSGs by exome and transcriptome sequencing (Kan et al., 2010; Zhao et al., 2010). Taken together, these results indicate a more significant role of GPCRs, as TSGs, in cancer than previously thought.

TSGs can be silenced in cancer cells by several epigenetic mechanisms including DNA methylation, histone modifications, and nucleosome positioning (Jones and Baylin, 2007). It is also known that cancer cells depend on the silencing of TSGs and, consequently, are hypersensitive to the re-expression of these

(C) Bisulfite-sequencing analysis of CpG methylation status of four regions, from cancer-specific methylated cluster (*EYA4* and *IRAK3*) and from somatic tissue-specific DNA methylation cluster (*SYCP3* and *ADAM2*). The mean percent methylation at each CpG site is derived from clones shown on Figure S2A. The capped line represents the region analyzed.

See also Figure S2.

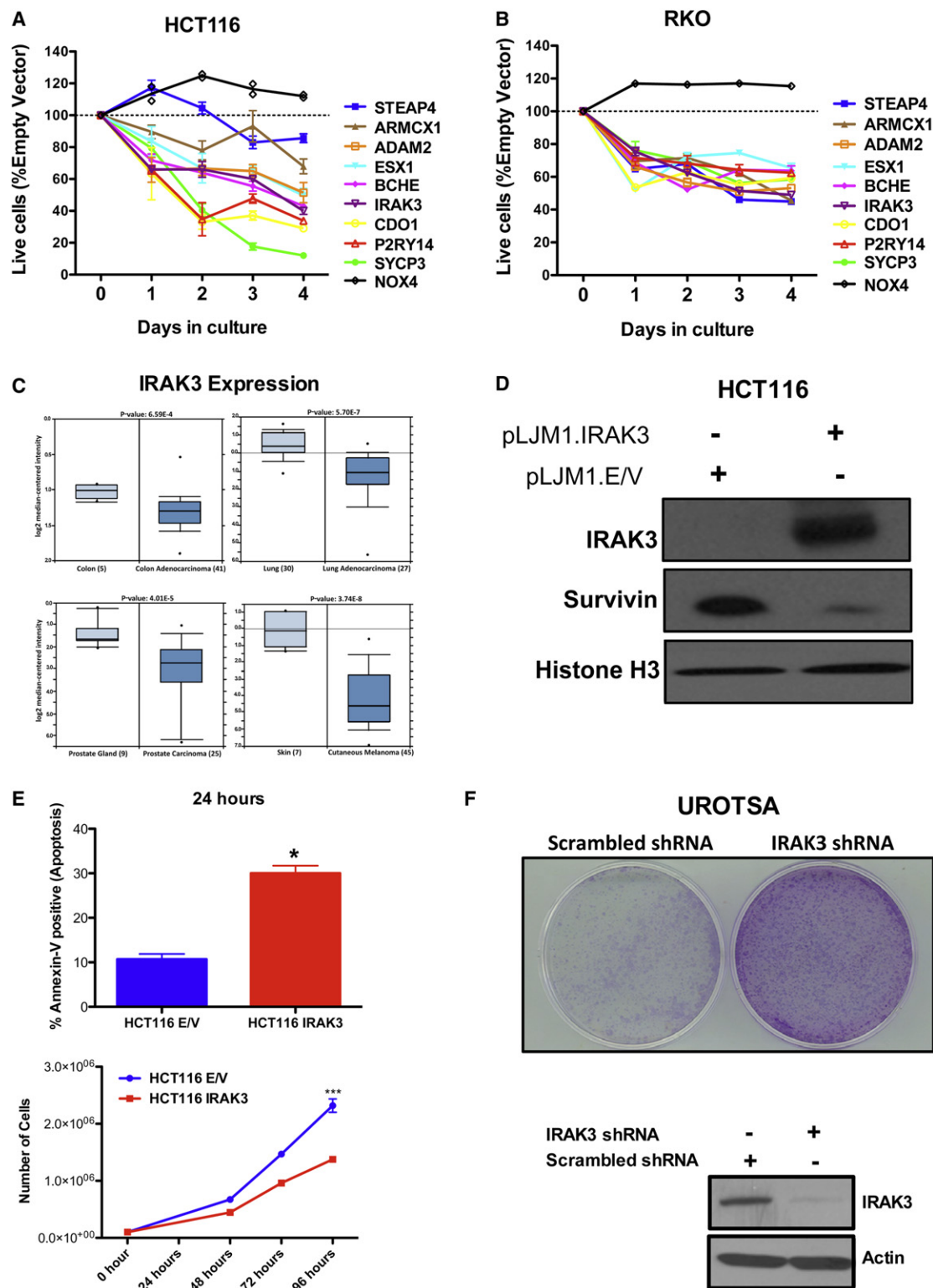


Figure 5. Functional Validations

(A) Overexpression of nine candidate genes from the cancer cluster (*P2RY14*, *IRAK3*, *CDO1*, *ESX1*, *ARMCX1*, *BCHE*), somatic cluster (*SYCP3* and *ADAM2*), and cell culture cluster (*STEAP4*). Shown is the fraction of Empty-Vector at the indicated times, normalized to the day 0 values. *NOX4* was used as a control gene because it is hypermethylated in HCT116 cells and completely demethylated in DKO1 cells. Data represent the mean \pm SEM.

(B) Overexpression of the same nine candidate genes reduces viability of RKO cancer cells. Shown is the fraction of Empty-Vector at the indicated times, normalized to the day 0 values. *NOX4* was used as a control gene. Data represent the mean \pm SEM.

genes (Luo et al., 2009; Martins et al., 2006; Ventura et al., 2007; Xue et al., 2007). We propose here that because of this TSG hypersensitivity, and because some of these key TSGs are silenced by epigenetic mechanisms, cancer cells become addicted to this aberrant epigenetic silencing.

Indeed, we demonstrated that re-expression of the genes we identified here decreases cell viability, highlighting the need for their constant repression. Furthermore, we showed that one of these genes, *IRAK3*, negatively regulates expression of the antiapoptotic gene *SURVIVIN*. It was recently shown that oncogenic activation of MYD88 led to IRAK1 phosphorylation and, consequently, NF κ B activation, promoting cell survival (Ngo et al., 2011). IRAK3 is a negative regulator of this signaling pathway, inhibiting IRAK1 phosphorylation (Janssens and Beyaert, 2003), thus supporting our findings and suggesting a tumor suppressor role for IRAK3. *IRAK3* was also previously identified, in an RNAi-based genetic screen, as able to suppress transformation of human mammary epithelial cells (Westbrook et al., 2005), consistent with our finding that *IRAK3* knockdown in nontumorigenic cells increased colony formation and suggesting that the genes found in this cancer group are excellent targets for therapy. In addition because these genes depend on DNA methylation-mediated gene silencing, these may be especially good targets for epigenetic therapy (Kelly et al., 2010).

It has been known for many years that de novo DNA methylation occurs during the cell-culturing process (Antequera et al., 1990; Jones et al., 1990; Wilson and Jones, 1983). Here, we identified a group of genes whose silencing by DNA methylation is required for cells to survive in culture. This group of genes was highly methylated in colon, bladder, and breast cell lines and unmethylated in primary-matched tissue analyzed, independent of the tumorigenic state (data not shown). Intriguingly, this group encompasses many nucleosome assembly genes, including several histone variants about which little is known. These results suggest that during the cell-culturing process, extensive changes in expression of nucleosome constituents are necessary for cell survival. It also highlights the importance of careful interpretation of epigenetic results obtained from cell culture experiments.

Taken together, by identifying the minimal DNA methylation profile necessary for the survival of cancer cells and comparing this profile in several primary normal tissues and cancer types, we were able to find, and experimentally validate, a group of genes whose de novo methylation in cancer is functionally relevant for the survival of cancer cells. We also found that, despite the complex nature of tumorigenesis, cancer cells

become dependent on the DNA methylation-mediated epigenetic silencing of these genes. These driver epigenetic events associated with cancer cell survival are potentially good candidates for the development of new, target-specific, therapies.

EXPERIMENTAL PROCEDURES

Cell Lines, DNA and RNA Preparations, Antibodies, and Primers

These are described in the Supplemental Experimental Procedures.

DNA Methylation Assay

Genomic DNA samples (1 μ g each) were bisulfite converted using the Zymo EZ DNA methylation kit (Zymo Research, Orange, CA, USA; catalog #D5002) according to the manufacturer's instructions. Bisulfite-converted DNA was eluted in an 18 μ l vol, and 3 μ l was removed for post-bisulfite quality control tests as described previously by Campan et al. (2009). All cell lines and clinical samples passed bisulfite conversion quality control and were subsequently processed for the Illumina Infinium DNA methylation platform (HumanMethylation27 BeadChip). A β value of 0–1.0 was reported for each CpG site (methylation from 0% to 100%, respectively). β Values were calculated as described previously by Wolff et al. (2010).

The Infinium methylation assays were performed by the USC Epigenome Center in accordance with the manufacturer's instructions. The assay information is available at <http://www.illumina.com>. Heat maps were generated for the β values. All the DNA methylation data from primary tissue was obtained from TCGA (<http://cancergenome.nih.gov/>).

To analyze the DNA methylation status of individual DNA molecules, we cloned bisulfite-converted PCR fragments into the pCR2.1 vector using the TOPO-TA cloning kit (Invitrogen, Carlsbad, CA, USA). Individual colonies were screened for the insert, and the region of interest was sequenced using M13 primers as previously described by Wolff et al. (2010).

H3K27me3 Status in ESCs as a Predictive Method for DNA Methylation in Cancer

H3K27me3 profile in H9 ESCs was obtained from previously published data by Lee et al. (2006). Next, we intersected the genomic position of the Infinium probes with the H3K27me3 status in H9 ESCs to define which probes are H3K27me3 positive and which are H3K27me3 negative in ESCs. From the approximately 24,000 probes used in Figure 1, we found approximately 7.7% as H3K27me3 positive in ESCs and 79.7% as H3K27me3 negative in ESCs, and we could not determine the H3K27me3 status in ESCs of 12.6% of the probes.

Genomic Architecture as a Predictive Method for DNA Methylation in Cancer

We used previously published data from Estéicio et al. (2010) that predict the inherent susceptibility to DNA methylation in cancer based on SINE and LINE retrotransposon density in a 20 kb window around the TSS of each gene. Briefly, they calculate the log odds ratio of SINE and LINE retrotransposons per 1 kb window, and the sum of log odds scores in the 20 kb region allowed the classification of each gene as methylation prone, methylation intermediate, and methylation resistant.

(C) Metaanalysis using the Oncomine (<http://www.oncomine.org>) for *IRAK3* expression. Box plots showing decreased expression of *IRAK3* during tumorigenesis on data sets performed in colon adenocarcinoma (Kaiser et al., 2007), lung adenocarcinoma (Su et al., 2007), prostate carcinoma (Welsh et al., 2001), and cutaneous melanoma (Talantov et al., 2005). The y axis represents log₂ median-centered intensity (normalized expression). Shaded boxes represent the interquartile range (25th–75th percentile). Whiskers represent the 10th–90th percentile. The bars denote the median.

(D) Overexpression of *IRAK3* in HCT116 cells induces a reduction in the Survivin levels. Western blot analyses of IRAK3 and Survivin after lentiviral infection with pLJM1 empty vector (EV) or pLJM1-IRAK3. Histone H3 was used as a loading control.

(E) *IRAK3* expression induces cell death of cancer cells. HCT116 infected with pLJM1 empty vector or pLJM1 *IRAK3* was stained with annexin V-FITC and PI and analyzed by FACS, showing an increased level of cell death in the cell overexpressing *IRAK3* (upper panel). Re-expression of *IRAK3* in HCT116 wild-type cells showed a reduced cell number in culture than HCT116 empty vector (lower panel). * $p < 0.05$, *** $p < 0.0001$. Data represent the mean \pm SEM.

(F) *IRAK3* knockdown induces colony formation in a nontumorigenic cell. UROTSa infected with a shRNA against *IRAK3* presented a higher colony formation activity than UROTSa infected with a scrambled shRNA. Western blot analysis of IRAK3 after lentiviral infection with shRNA against *IRAK3* or a scrambled shRNA was performed. Actin was used as a loading control.

See also Figure S3.

Apoptosis Assay

Cellular apoptosis was measured by annexin V and propidium iodide (PI) staining using annexin V-FITC Apoptosis Detection Kit (MBL), according to the manufacturer's protocol. Following staining the cells were analyzed and sorted by FACS analysis as described previously by De Carvalho et al. (2011).

Gene Expression Analysis

All gene expression data from primary tissue were obtained from GEO (GSE8671 and GSE7670). The data were median normalized and log2 transformed.

Ectopic Gene Expression

This is described in the [Supplemental Experimental Procedures](#).

Statistical Analysis

This is described in the [Supplemental Experimental Procedures](#).

ACCESSION NUMBERS

Infinium methylation data were deposited in NCBI's Gene Expression Omnibus: series accession number GSE36534.

SUPPLEMENTAL INFORMATION

Supplemental Information includes three figures, one table, and Supplemental Experimental Procedures and can be found with this article online at [doi:10.1016/j.ccr.2012.03.045](https://doi.org/10.1016/j.ccr.2012.03.045).

ACKNOWLEDGMENTS

This work was supported by R37CA082422 (to P.A.J.). We would like to thank Drs. Bert Vogelstein and Stephen B. Baylin for kindly providing DKO cells and also Lora Barsky from the Broad CIRM Center, Flow Cytometry Core Facility for technical assistance with FACS analysis. We thank the members of the P.A.J. laboratory and Daniel Weisenberger for helpful discussions and for careful reading of the manuscript. We thank Kimberly Siegmund for the helpful discussions about our statistical approaches. We also thank Peter Laird for useful discussions and The Cancer Genome Atlas.

Received: February 26, 2011

Revised: August 8, 2011

Accepted: March 27, 2012

Published: May 14, 2012

REFERENCES

- Antequera, F., Boyes, J., and Bird, A. (1990). High levels of de novo methylation and altered chromatin structure at CpG islands in cell lines. *Cell* 62, 503–514.
- Baylin, S.B., and Ohm, J.E. (2006). Epigenetic gene silencing in cancer—a mechanism for early oncogenic pathway addiction? *Nat. Rev. Cancer* 6, 107–116.
- Campan, M., Weisenberger, D.J., Trinh, B., and Laird, P.W. (2009). MethyLight. *Methods Mol. Biol.* 507, 325–337.
- Cedar, H., and Bergman, Y. (2009). Linking DNA methylation and histone modification: patterns and paradigms. *Nat. Rev. Genet.* 10, 295–304.
- Chen, T., Hevi, S., Gay, F., Tsujimoto, N., He, T., Zhang, B., Ueda, Y., and Li, E. (2007). Complete inactivation of DNMT1 leads to mitotic catastrophe in human cancer cells. *Nat. Genet.* 39, 391–396.
- Darzynkiewicz, Z., Bruno, S., Del Bino, G., Gorczyca, W., Hotz, M.A., Lassota, P., and Traganos, F. (1992). Features of apoptotic cells measured by flow cytometry. *Cytometry* 13, 795–808.
- De Carvalho, D.D., You, J.S., and Jones, P.A. (2010). DNA methylation and cellular reprogramming. *Trends Cell Biol.* 20, 609–617.
- De Carvalho, D.D., Binato, R., Pereira, W.O., Leroy, J.M., Colassanti, M.D., Proto-Siqueira, R., Bueno-Da-Silva, A.E., Zago, M.A., Zanichelli, M.A., Abdelhay, E., et al. (2011). BCR-ABL-mediated upregulation of PRAME is responsible for knocking down TRAIL in CML patients. *Oncogene* 30, 223–233.
- Del Prete, M.J., Robles, M.S., Guáo, A., Martínez-A, C., Izquierdo, M., and Garcia-Sanz, J.A. (2002). Degradation of cellular mRNA is a general early apoptosis-induced event. *FASEB J.* 16, 2003–2005.
- Egger, G., Jeong, S., Escobar, S.G., Cortez, C.C., Li, T.W., Saito, Y., Yoo, C.B., Jones, P.A., and Liang, G. (2006). Identification of DNMT1 (DNA methyltransferase 1) hypomorphs in somatic knockouts suggests an essential role for DNMT1 in cell survival. *Proc. Natl. Acad. Sci. USA* 103, 14080–14085.
- Estécio, M.R., Gallegos, J., Vallot, C., Castoro, R.J., Chung, W., Maegawa, S., Oki, Y., Kondo, Y., Jelinek, J., Shen, L., et al. (2010). Genome architecture marked by retrotransposons modulates predisposition to DNA methylation in cancer. *Genome Res.* 20, 1369–1382.
- Figuerola, M.E., Lugthart, S., Li, Y., Erpelinck-Verschueren, C., Deng, X., Christos, P.J., Schifano, E., Booth, J., van Putten, W., Skrabanek, L., et al. (2010). DNA methylation signatures identify biologically distinct subtypes in acute myeloid leukemia. *Cancer Cell* 17, 13–27.
- Gal-Yam, E.N., Egger, G., Iniguez, L., Holster, H., Einarsson, S., Zhang, X., Lin, J.C., Liang, G., Jones, P.A., and Tanay, A. (2008). Frequent switching of Polycomb repressive marks and DNA hypermethylation in the PC3 prostate cancer cell line. *Proc. Natl. Acad. Sci. USA* 105, 12979–12984.
- Hanahan, D., and Weinberg, R.A. (2000). The hallmarks of cancer. *Cell* 100, 57–70.
- Hanahan, D., and Weinberg, R.A. (2011). Hallmarks of cancer: the next generation. *Cell* 144, 646–674.
- Irizarry, R.A., Ladd-Acosta, C., Wen, B., Wu, Z., Montano, C., Onyango, P., Cui, H., Gabo, K., Rongione, M., Webster, M., et al. (2009). The human colon cancer methylome shows similar hypo- and hypermethylation at conserved tissue-specific CpG island shores. *Nat. Genet.* 41, 178–186.
- Janssens, S., and Beyaert, R. (2003). Functional diversity and regulation of different interleukin-1 receptor-associated kinase (IRAK) family members. *Mol. Cell* 11, 293–302.
- Jiang, Y.F., Sr., He, B., Li, N.P., Ma, J., Gong, G.Z., and Zhang, M. (2011). The oncogenic role of NS5A of hepatitis C virus is mediated by up-regulation of survivin gene expression in the hepatocellular cell through p53 and NF- κ B pathways. *Cell Biol. Int.* 35, 1225–1232.
- Jones, P.A., and Baylin, S.B. (2002). The fundamental role of epigenetic events in cancer. *Nat. Rev. Genet.* 3, 415–428.
- Jones, P.A., and Baylin, S.B. (2007). The epigenomics of cancer. *Cell* 128, 683–692.
- Jones, P.A., Wolkowicz, M.J., Rideout, W.M., 3rd, Gonzales, F.A., Marziasz, C.M., Coetzee, G.A., and Tapscott, S.J. (1990). De novo methylation of the MyoD1 CpG island during the establishment of immortal cell lines. *Proc. Natl. Acad. Sci. USA* 87, 6117–6121.
- Kaiser, S., Park, Y.K., Franklin, J.L., Halberg, R.B., Yu, M., Jessen, W.J., Freudenberg, J., Chen, X., Haigis, K., Jegga, A.G., et al. (2007). Transcriptional recapitulation and subversion of embryonic colon development by mouse colon tumor models and human colon cancer. *Genome Biol.* 8, R131.
- Kalari, S., and Pfeifer, G.P. (2010). Identification of driver and passenger DNA methylation in cancer by epigenomic analysis. *Adv. Genet.* 70, 277–308.
- Kan, Z., Jaiswal, B.S., Stinson, J., Janakiraman, V., Bhatt, D., Stern, H.M., Yue, P., Haverly, P.M., Bourgon, R., Zheng, J., et al. (2010). Diverse somatic mutation patterns and pathway alterations in human cancers. *Nature* 466, 869–873.
- Kelly, T.K., De Carvalho, D.D., and Jones, P.A. (2010). Epigenetic modifications as therapeutic targets. *Nat. Biotechnol.* 28, 1069–1078.
- Kobayashi, K., Hernandez, L.D., Galán, J.E., Janeway, C.A., Jr., Medzhitov, R., and Flavell, R.A. (2002). IRAK-M is a negative regulator of Toll-like receptor signaling. *Cell* 110, 191–202.
- Lee, T.I., Jenner, R.G., Boyer, L.A., Guenther, M.G., Levine, S.S., Kumar, R.M., Chevalier, B., Johnstone, S.E., Cole, M.F., Isono, K., et al. (2006). Control of developmental regulators by Polycomb in human embryonic stem cells. *Cell* 125, 301–313.

- Luo, J., Solimini, N.L., and Elledge, S.J. (2009). Principles of cancer therapy: oncogene and non-oncogene addiction. *Cell* 136, 823–837.
- Manns, J., Daubrawa, M., Driessen, S., Paasch, F., Hoffmann, N., Löffler, A., Lauber, K., Dieterle, A., Alers, S., Iftner, T., et al. (2011). Triggering of a novel intrinsic apoptosis pathway by the kinase inhibitor staurosporine: activation of caspase-9 in the absence of Apaf-1. *FASEB J.* 25, 3250–3261.
- Martins, C.P., Brown-Swigart, L., and Evan, G.I. (2006). Modeling the therapeutic efficacy of p53 restoration in tumors. *Cell* 127, 1323–1334.
- Meissner, A. (2010). Epigenetic modifications in pluripotent and differentiated cells. *Nat. Biotechnol.* 28, 1079–1088.
- Ngo, V.N., Young, R.M., Schmitz, R., Jhavar, S., Xiao, W., Lim, K.H., Kohlhammer, H., Xu, W., Yang, Y., Zhao, H., et al. (2011). Oncogenically active MYD88 mutations in human lymphoma. *Nature* 470, 115–119.
- Noushmehr, H., Weisenberger, D.J., Diefes, K., Phillips, H.S., Pujara, K., Berman, B.P., Pan, F., Pelloski, C.E., Sulman, E.P., Bhat, K.P., et al; Cancer Genome Atlas Research Network. (2010). Identification of a CpG island methylator phenotype that defines a distinct subgroup of glioma. *Cancer Cell* 17, 510–522.
- Ohm, J.E., McGarvey, K.M., Yu, X., Cheng, L., Schuebel, K.E., Cope, L., Mohammad, H.P., Chen, W., Daniel, V.C., Yu, W., et al. (2007). A stem cell-like chromatin pattern may predispose tumor suppressor genes to DNA hypermethylation and heritable silencing. *Nat. Genet.* 39, 237–242.
- Portela, A., and Esteller, M. (2010). Epigenetic modifications and human disease. *Nat. Biotechnol.* 28, 1057–1068.
- Rhee, I., Bachman, K.E., Park, B.H., Jair, K.W., Yen, R.W., Schuebel, K.E., Cui, H., Feinberg, A.P., Lengauer, C., Kinzler, K.W., et al. (2002). DNMT1 and DNMT3b cooperate to silence genes in human cancer cells. *Nature* 416, 552–556.
- Robertson, K.D. (2005). DNA methylation and human disease. *Nat. Rev. Genet.* 6, 597–610.
- Sabates-Bellver, J., Van der Flier, L.G., de Palo, M., Cattaneo, E., Maake, C., Rehrauer, H., Laczko, E., Kurowski, M.A., Bujnicki, J.M., Menigatti, M., et al. (2007). Transcriptome profile of human colorectal adenomas. *Mol. Cancer Res.* 5, 1263–1275.
- Sahut-Barnola, I., and Pauli, D. (1999). The *Drosophila* gene stand still encodes a germline chromatin-associated protein that controls the transcription of the ovarian tumor gene. *Development* 126, 1917–1926.
- Schlesinger, Y., Straussman, R., Keshet, I., Farkash, S., Hecht, M., Zimmerman, J., Eden, E., Yakhini, Z., Ben-Shushan, E., Reubinoff, B.E., et al. (2007). Polycomb-mediated methylation on Lys27 of histone H3 pre-marks genes for de novo methylation in cancer. *Nat. Genet.* 39, 232–236.
- Sharma, S., Kelly, T.K., and Jones, P.A. (2010). Epigenetics in cancer. *Carcinogenesis* 31, 27–36.
- Sharma, S., De Carvalho, D.D., Jeong, S., Jones, P.A., and Liang, G. (2011). Nucleosomes containing methylated DNA stabilize DNA methyltransferases 3A/3B and ensure faithful epigenetic inheritance. *PLoS Genet.* 7, e1001286.
- Shen, L., Kondo, Y., Guo, Y., Zhang, J., Zhang, L., Ahmed, S., Shu, J., Chen, X., Waterland, R.A., and Issa, J.P. (2007). Genome-wide profiling of DNA methylation reveals a class of normally methylated CpG island promoters. *PLoS Genet.* 3, 2023–2036.
- Solimini, N.L., Luo, J., and Elledge, S.J. (2007). Non-oncogene addiction and the stress phenotype of cancer cells. *Cell* 130, 986–988.
- Spada, F., Haemmer, A., Kuch, D., Rothbauer, U., Schermelleh, L., Kremmer, E., Carell, T., Längst, G., and Leonhardt, H. (2007). DNMT1 but not its interaction with the replication machinery is required for maintenance of DNA methylation in human cells. *J. Cell Biol.* 176, 565–571.
- Su, J., Zhang, T., Tyson, J., and Li, L. (2009). The interleukin-1 receptor-associated kinase M selectively inhibits the alternative, instead of the classical NF- κ B pathway. *J. Innate Immun.* 1, 164–174.
- Su, L.J., Chang, C.W., Wu, Y.C., Chen, K.C., Lin, C.J., Liang, S.C., Lin, C.H., Whang-Peng, J., Hsu, S.L., Chen, C.H., and Huang, C.Y. (2007). Selection of DDX5 as a novel internal control for Q-RT-PCR from microarray data using a block bootstrap re-sampling scheme. *BMC Genomics* 8, 140.
- Taberlay, P.C., and Jones, P.A. (2011). DNA methylation and cancer. *Prog. Drug Res.* 67, 1–23.
- Talantov, D., Mazumder, A., Yu, J.X., Briggs, T., Jiang, Y., Backus, J., Atkins, D., and Wang, Y. (2005). Novel genes associated with malignant melanoma but not benign melanocytic lesions. *Clin. Cancer Res.* 11, 7234–7242.
- Turnis, M.E., Song, X.T., Bear, A., Foster, A.E., Gottschalk, S., Brenner, M.K., Chen, S.Y., and Rooney, C.M. (2010). IRAK-M removal counteracts dendritic cell vaccine deficits in migration and longevity. *J. Immunol.* 185, 4223–4232.
- Ventura, A., Kirsch, D.G., McLaughlin, M.E., Tuveson, D.A., Grimm, J., Lintault, L., Newman, J., Reczek, E.E., Weissleder, R., and Jacks, T. (2007). Restoration of p53 function leads to tumour regression in vivo. *Nature* 445, 661–665.
- Weinstein, I.B. (2002). Cancer. Addiction to oncogenes—the Achilles heel of cancer. *Science* 297, 63–64.
- Welsh, J.B., Sapinoso, L.M., Su, A.I., Kern, S.G., Wang-Rodriguez, J., Moskaluk, C.A., Frierson, H.F., Jr., and Hampton, G.M. (2001). Analysis of gene expression identifies candidate markers and pharmacological targets in prostate cancer. *Cancer Res.* 61, 5974–5978.
- Westbrook, T.F., Martin, E.S., Schlabach, M.R., Leng, Y., Liang, A.C., Feng, B., Zhao, J.J., Roberts, T.M., Mandel, G., Hannon, G.J., et al. (2005). A genetic screen for candidate tumor suppressors identifies REST. *Cell* 121, 837–848.
- Widschwendter, M., Fiegl, H., Egle, D., Mueller-Holzner, E., Spizzo, G., Marth, C., Weisenberger, D.J., Campan, M., Young, J., Jacobs, I., and Laird, P.W. (2007). Epigenetic stem cell signature in cancer. *Nat. Genet.* 39, 157–158.
- Wilson, V.L., and Jones, P.A. (1983). DNA methylation decreases in aging but not in immortal cells. *Science* 220, 1055–1057.
- Wolff, E.M., Chihara, Y., Pan, F., Weisenberger, D.J., Siegmund, K.D., Sugano, K., Kawashima, K., Laird, P.W., Jones, P.A., and Liang, G. (2010). Unique DNA methylation patterns distinguish noninvasive and invasive urothelial cancers and establish an epigenetic field defect in premalignant tissue. *Cancer Res.* 70, 8169–8178.
- Xue, W., Zender, L., Miething, C., Dickins, R.A., Hernando, E., Krizhanovskiy, V., Cordon-Cardo, C., and Lowe, S.W. (2007). Senescence and tumour clearance is triggered by p53 restoration in murine liver carcinomas. *Nature* 445, 656–660.
- Zhao, Q., Kirkness, E.F., Caballero, O.L., Galante, P.A., Parmigiani, R.B., Edsall, L., Kuan, S., Ye, Z., Levy, S., Vasconcelos, A.T., et al. (2010). Systematic detection of putative tumor suppressor genes through the combined use of exome and transcriptome sequencing. *Genome Biol.* 11, R114.
- Zhou, J., Bi, C., Janakakumara, J.V., Liu, S.C., Chng, W.J., Tay, K.G., Poon, L.F., Xie, Z., Palaniyandi, S., Yu, H., et al. (2009). Enhanced activation of STAT pathways and overexpression of survivin confer resistance to FLT3 inhibitors and could be therapeutic targets in AML. *Blood* 113, 4052–4062.

ATM Phosphorylation of Mdm2 Ser394 Regulates the Amplitude and Duration of the DNA Damage Response in Mice

Hugh S. Gannon,¹ Bruce A. Woda,² and Stephen N. Jones^{1,3,*}

¹Department of Cell Biology

²Department of Pathology

³Department of Cancer Biology

University of Massachusetts Medical School, Worcester, MA 01655, USA

*Correspondence: stephen.jones@umassmed.edu

DOI 10.1016/j.ccr.2012.04.011

SUMMARY

DNA damage induced by ionizing radiation activates the ATM kinase, which subsequently stabilizes and activates the p53 tumor suppressor protein. Although phosphorylation of p53 by ATM was found previously to modulate p53 levels and transcriptional activities in vivo, it does not appear to be a major regulator of p53 stability. We have utilized mice bearing altered *Mdm2* alleles to demonstrate that ATM phosphorylation of Mdm2 serine 394 is required for robust p53 stabilization and activation after DNA damage. In addition, we demonstrate that dephosphorylation of Mdm2 Ser394 regulates attenuation of the p53-mediated response to DNA damage. Therefore, the phosphorylation status of Mdm2 Ser394 governs p53 protein levels and functions in cells undergoing DNA damage.

INTRODUCTION

The p53 tumor suppressor has been called the “guardian of the genome” due to its ability to prevent genotoxic insults from inducing heritable alterations in damaged cells (Lane, 1992). In response to cellular stresses such as DNA double-strand breaks, hypoxia, and inappropriate oncogene activation, the p53 transcription factor is stabilized within the cell and induces the expression of various p53 target genes involved in cell cycle arrest, apoptosis, and senescence (Vousden and Lu, 2002). These p53-dependent effector pathways regulate the proliferation and propagation of damaged cells to limit cellular transformation and tumorigenesis, and mice deleted for p53 rapidly develop thymic lymphomas, sarcomas and other tumor types (Donehower et al., 1992). Additionally, over 50% of all human tumors harbor p53 mutations (Soussi and Bérout, 2001; Hollstein et al., 1991). These findings clearly demonstrate the necessity of functional p53 signaling in suppressing tumorigenesis.

DNA damage induced by ionizing radiation (IR) is a well-established initiator of p53 activity. Wild-type (WT) mice that are treated with whole body IR undergo p53-dependent apoptosis in both radiosensitive tissues such as thymus, spleen, and small intestine, and in hematopoietic cells (Gudkov and Komarova, 2003). Mice exposed to 8 Grays (Gy) or more of IR will die within 3 weeks due to depletion of the hematopoietic compartment, a condition known as hematopoietic syndrome (Komarova et al., 2004). In contrast, p53 null mice are more tolerant of acute radiation, as their hematopoietic cells are less prone to IR-induced apoptosis. However, p53-deficient mice will display an increased rate of tumorigenesis following IR treatment (Kemp et al., 1994).

Because p53-dependent cell cycle arrest and apoptosis are deleterious to the growth and survival of nondamaged cells, p53 activity must be kept at minimal levels under normal, homeostatic conditions. Although p53 regulation by numerous cellular proteins has been observed under various experimental conditions, it has become increasingly apparent that the Mdm2

Significance

The p53-mediated DNA damage response pathway suppresses the oncogenic transformation of cells exposed to genotoxic insults. A better understanding of the mechanisms that govern p53 activation during the DNA damage response is crucial to developing new cancer therapies, because tumors that harbor wild-type p53 alleles have the potential for restoration of p53 activity, and because selectively regulating p53 functions might also ameliorate radiation therapy-induced pathologies. Our work determines that mouse Mdm2 Ser394 phosphorylation (human MDM2 Ser395) is required for DNA damage-induced p53 activation and also regulates the duration of the p53 response to DNA damage. Thus, devising means to alter the phosphorylation status of this residue should greatly facilitate our ability to regulate p53 activity in normal and neoplastic cells.

oncoprotein is the chief negative regulator of p53 in damaged and nondamaged cells (Bond et al., 2005). Mdm2 represses p53 activity by binding and sequestering p53 away from p53 target gene promoters (Momand et al., 1992; Chen et al., 1995). Furthermore, Mdm2 contains a RING domain with E3 ubiquitin ligase activity and can ubiquitinate p53, leading to p53 nuclear export and degradation in the 26S proteasome (Honda et al., 1997). Interestingly, Mdm2 is a transcriptional target of p53, and p53 transactivation of *Mdm2* expression is thought to form an autoregulatory feedback loop to limit p53 activity in the cell (Juven et al., 1993; Wu et al., 1993). The importance of Mdm2-mediated inhibition of p53 signaling has been demonstrated previously in vivo. *Mdm2*^{-/-} mice die at E5–E6 during development due to aberrant p53-mediated apoptosis (Jones et al., 1995; Montes de Oca Luna et al., 1995), whereas Mdm2 overexpression in mice inhibits p53 tumor suppression, resulting in the formation of lymphomas, soft tissue sarcomas, and osteosarcomas (Jones et al., 1998). Thus proper regulation of Mdm2 expression and activity is critical for normal p53 signaling and cellular function.

Activation of p53 in response to DNA damage necessitates a transient attenuation of Mdm2-dependent p53 inhibition. Post-translational modifications of the p53 protein by DNA damage-inducible kinases were initially thought to inhibit the interaction of p53 and Mdm2 (Shieh et al., 1997). The ATM (mutated in ataxia and telangiectasia) kinase is necessary for p53 stabilization in tissues such as mouse embryonic fibroblasts (MEFs) and murine thymus following IR (Jack et al., 2002; Gurley and Kemp, 2007), and ATM will directly and indirectly (via Chk2) phosphorylate p53 on Ser18 and Ser23 in irradiated mice (Ser15 and Ser20 on human p53) (Chao et al., 2000; Wu et al., 2002). These serine residues are located within or adjacent to the Mdm2 binding domain of p53, and initial in vitro studies demonstrated that phosphorylation of p53 decreased the p53-Mdm2 interaction in transfection and overexpression experiments (Shieh et al., 1997). Several groups, including our own, subsequently generated mouse models bearing modified *p53* alleles to examine the role of these posttranslational modifications in p53 regulation and function in vivo (Chao et al., 2003, 2006; Sluss et al., 2004). These studies revealed that phosphorylation of these ATM-target serines on p53 modulated the transcriptional activity of p53, but had only a moderate effect on DNA damage-induced stabilization of the p53 protein.

In addition to modifying p53, transfection-based assays have revealed that ATM can directly phosphorylate serine 395 of human MDM2 (Khosravi et al., 1999; Maya et al., 2001). One study utilized an *MDM2* expression construct with the serine residue 395 codon replaced by sequences encoding aspartic acid (S395D), thus mimicking a constitutively phosphorylated serine residue. The MDM2 S395D protein exhibited a decreased capacity to induce p53 degradation and nuclear export, suggesting that phosphorylation of MDM2 Ser395 altered p53 activation following DNA damage. Further in vitro work suggested that ATM phosphorylation of multiple amino acid residues on MDM2, including Ser395, inhibited both MDM2 RING domain oligomerization and E3 ligase activity (Cheng et al., 2009, 2011). Interestingly, recent work has indicated that ATM phosphorylation of MDM2 switches MDM2 from a negative to a positive regulator of p53, as phosphorylation of MDM2 Ser395

increased the interaction between MDM2 protein and *p53* mRNA and led to increased p53 translation (Gajjar et al., 2012). These transfection-based studies suggest that the ATM-dependent induction of the p53 protein is mediated by ATM phosphorylation of MDM2.

In keeping with a role for MDM2 Ser395 phosphorylation in the p53 DNA damage response, we have previously shown that the Wip1 oncoprotein can dephosphorylate MDM2 Ser395 in vitro (Lu et al., 2007). Wip1 antagonizes ATM function by dephosphorylating many known ATM target proteins, including ATM itself. Therefore, Wip1 has been proposed to reset DNA damage signaling to prestress levels following resolution of the DNA damage response (Lu et al., 2008). Like Mdm2, the Wip1 gene is a direct transcriptional target of p53, and p53 induction of *Wip1* expression might also limit the p53-dependent DNA damage response. Although the coincidental timing of MDM2 Ser395 phosphorylation and dephosphorylation suggests that this modification may coordinate the p53-dependent response to DNA damage, the in vivo functional significance MDM2 phosphorylation in Mdm2-p53 regulation, p53 activation, and in tumorigenesis remains unknown.

To determine the role of MDM2 Ser395 phosphorylation in p53 regulation under physiological settings, we have generated two knock-in mouse models bearing *Mdm2* Ser394 substitutions (the orthologous human Ser395 residue in the mouse) and analyzed the effects of these substitutions on p53-mediated DNA damage response and tumor suppression.

RESULTS

To investigate the role of Mdm2 Ser394 phosphorylation under physiological conditions, we generated a mouse model in which this serine residue is substituted with an alanine residue (S394A). This model produces a mutant Mdm2 protein with a conserved native structure that cannot be phosphorylated at position 394. Site-directed mutagenesis was performed to introduce missense mutations within the 394 codon of *Mdm2* exon 12, and a gene-replacement vector was constructed to replace the endogenous *Mdm2* exon 12 sequences with a mutated exon 12 (Figure 1A). The introduced mutations also inserted a novel *BclI* restriction digest site at codon 394, which allows direct detection of the mutated sequence by a PCR strategy. Gene targeting experiments in PC3 (129SV) embryonic stem (ES) cells (O'Gorman et al., 1997) yielded properly-targeted ES cell clones, as confirmed by Southern and PCR analyses (Figures S1A–S1C available online). Blastocyst injection experiments produced several high-degree male chimeras that passed the S394A allele through their germ line while simultaneously deleting the floxed neomycin cassette due to expression of the protamine-Cre transgene (present in the PC3 ES cells). The resultant F₁ and F₂ generation mice were identified by Southern blot of genomic DNA (Figure S1D). The presence of the S394A mutation in these mice was confirmed by utilizing the PCR-*BclI* digest strategy (Figure 1B). This corroborated the Southern genotyping results and demonstrated retention of the mutation in both heterozygous (A/+) and homozygous (A/A) mice. All genotyping techniques were reaffirmed by direct genomic sequencing of the exon 12 region in F₁ and F₂ mouse genomic DNA (Figure S1E).

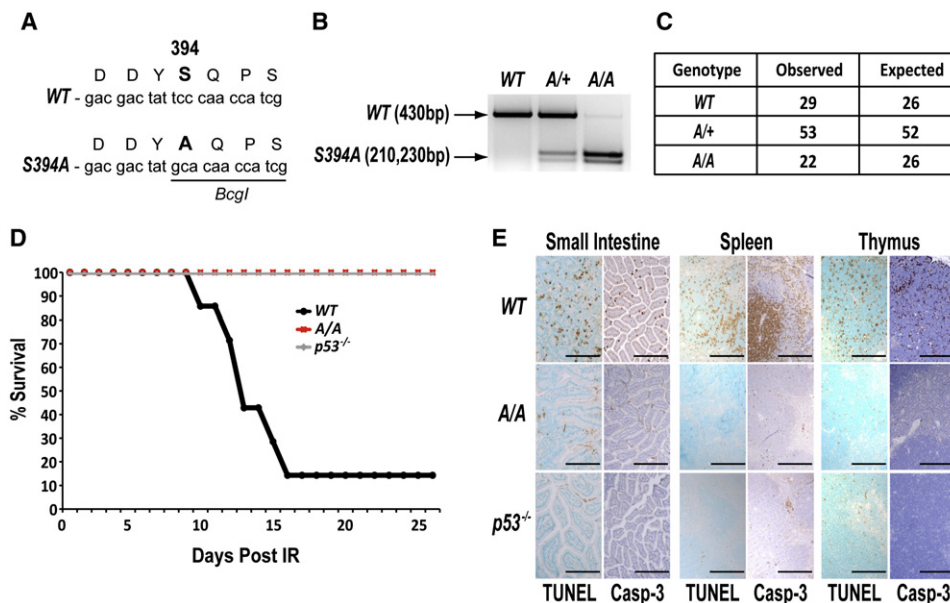


Figure 1. Phosphorylation of Mdm2 Ser394 Regulates Radiosensitivity in Mice

(A) DNA sequence of the WT and S394A alleles at *Mdm2* codon 394. The mutations in S394A also introduce a *BclI* restriction digest site.

(B) PCR-*BclI* analysis of F₂ generation mice. Primers flanking *Mdm2* codon 394 were used to amplify DNA samples from WT, A/+, and A/A F₂ generation mice, followed by *BclI* digestion.

(C) Mice that are either heterozygous and homozygous for the S394A allele are viable and were observed at Mendelian ratios after heterozygous intercrosses ($p = 0.322$).

(D) Cohorts of wild-type ($n = 14$), A/A ($n = 14$), and p53^{-/-} ($n = 8$) mice were irradiated with 8Gy and survival was observed over 26 days.

(E) WT, A/A, and p53^{-/-} mice were irradiated with 2Gy and were sacrificed 6 hr later. Small intestine, spleen, and thymus were harvested and stained for TUNEL or anti-cleaved caspase-3 (Casp-3). Scale bars represent 250 μ m.

See also Figure S1.

A/+ and A/A mice are viable and were recovered from heterozygous intercrosses at Mendelian ratios (Figure 1C). Because *Mdm2*^{-/-} mice are embryonic lethal (Jones et al., 1995; Montes de Oca Luna et al., 1995), total ablation of Mdm2 function during development must not be occurring in A/+ or A/A mice. We also did not detect any differences between WT and A/A mice in body weights at 8 weeks of age (WT 25.67 \pm 2.9 g and A/A 24.3 \pm 4.2 g), in male-to-female sex distribution (WT 1:0.82 and A/A 1:0.90), or in overall litter size (WT 8.5 \pm 1.8 and A/A 8.7 \pm 1.9). Because mice with decreased p53 function have decreased fecundity (Levine et al., 2011), our results suggest that basal p53 activity is not perturbed in A/A mice.

Because ATM phosphorylation of MDM2 Ser395 was previously observed in cell lines following IR treatment (Maya et al., 2001), we assessed the sensitivity of A/A mice to whole body γ -irradiation. We irradiated cohorts of WT, A/A, and p53^{-/-} mice with a threshold-lethal dose of IR (8Gy). As expected, 86% of wild-type mice died by 16 days post-IR (Figure 1D). However, like p53^{-/-} mice, A/A mice were completely radioreistant, indicating that Mdm2 Ser394 phosphorylation regulates p53 activity in vivo following DNA damage. Activation of p53 by IR damage in mice induces apoptosis in radiosensitive organs such as small intestine, spleen, and thymus (Gudkov and Komarova, 2003). To evaluate p53 apoptotic function in these tissues, we treated WT, A/A, and p53^{-/-} mice with 2Gy IR and 6 hr later assayed apoptosis by terminal deoxynucleotidyl transferase dUTP nick end labeling (TUNEL) and cleaved

caspase-3 immunohistochemistry (Figure 1E). Very few apoptotic cells were detected in the small intestine, spleen, or the thymus of A/A mice following DNA damage, whereas apoptosis was readily apparent in all of these tissues in irradiated wild-type mice. As expected, little or no apoptosis was observed in tissues of IR-treated p53^{-/-} control mice, and apoptosis was not detected in the untreated animals, regardless of genotype (Figure S1F). These studies indicate markedly reduced p53-dependent apoptotic function in A/A mice after IR treatment.

To more accurately quantitate this IR-dependent effect, we utilized Annexin V and propidium iodide (PI) staining to assay apoptosis in ex vivo thymocytes by flow cytometry (Figure S2A). Wild-type thymocytes are sensitive to apoptosis due to p53-induced activation of proapoptotic *Puma* expression (Jeffers et al., 2003). In agreement with the whole-body IR results, WT thymocytes treated with 2Gy IR displayed 3.1-fold more early apoptotic (Annexin V^{high} PI^{low}) cells at 12 hr compared to untreated WT cells, whereas A/A thymocytes displayed only a modest 1.5-fold increase in apoptotic cells and p53^{-/-} thymocytes showed no induction of apoptosis after DNA damage (Figure 2A).

To establish that the decreased apoptosis in DNA damaged A/A thymocytes is due to altered p53 function, we treated WT, A/A, and p53^{-/-} thymocytes with Nutlin-3a, a small-molecule inhibitor of Mdm2-p53 binding (Vassilev et al., 2004). WT and A/A thymocytes cotreated with Nutlin-3a and IR each stabilized p53 after IR damage (Figure 2B), and blocking the interaction of

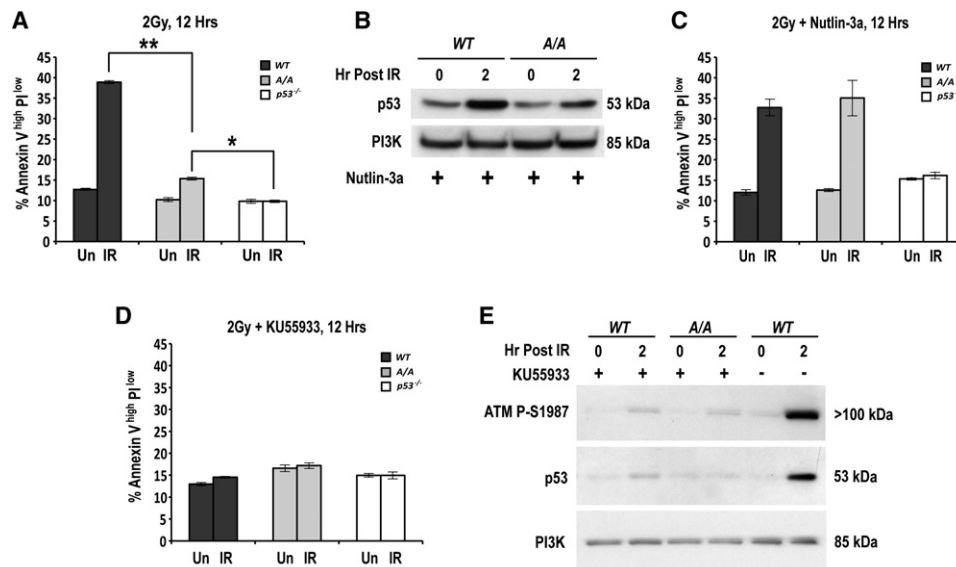


Figure 2. ATM Phosphorylation of Mdm2 Ser394 Promotes p53-Dependent Apoptosis after DNA Damage

(A) Ex vivo thymocytes were either left untreated or irradiated with 2Gy for 12 hr and apoptotic cells were quantified by flow cytometry (n = 3 per genotype). Standard deviation indicated by error bars. Asterisk (p = 0.0001) and double asterisk (p = 0.0001) indicate significant differences.

(B) Ex vivo thymocytes were either untreated or irradiated with 2Gy for 1 hr, and all cells were then incubated with 12 μ M Nutlin-3a for 1 hr. Protein levels were analyzed by western blot.

(C) Ex vivo thymocytes were either left completely untreated or irradiated with 2Gy for 12 hr and incubated with 12 μ M Nutlin-3a 3 hr after IR (9 hr total) (n = 3 per genotype). Apoptotic cells were quantified by flow cytometry. Standard deviation indicated by error bars.

(D) Ex vivo thymocytes were preincubated with 10 μ M KU55933 for 1 hr. Cells were then either left untreated or irradiated with 2Gy for 12 hr and apoptotic cells were quantified by flow cytometry (n = 3 per genotype). Standard deviation indicated by error bars.

(E) Ex vivo thymocytes were either left untreated or preincubated with 10 μ M KU55933 for 1 hr. Cells were then either untreated or irradiated with 2Gy for 2 hr, and protein levels were analyzed by western blot.

See also Figure S2.

p53 with Mdm2-S394A completely rescued the ability of p53 to induce apoptosis in A/A thymocytes following DNA damage (Figure 2C). To confirm that Nutlin-3a treatment restored IR-induced apoptosis in A/A cells by inhibiting Mdm2-p53 signaling, we performed FACS analysis on A/A thymocytes that were genetically deleted for p53. As expected, the addition of Nutlin-3a failed to restore IR-induced apoptosis in A/A cells lacking p53 (Figure S2B).

To verify that the effect of the Mdm2 S394A mutation on IR-apoptosis was truly ATM-dependent, we repeated the apoptosis assays using the ATM-specific inhibitor KU55933 (Hickson et al., 2004). Inhibition of ATM reduced apoptosis in irradiated thymocytes to levels observed in untreated cells in all genotypes (Figure 2D). Additionally, the ATM inhibitor blocked the robust ATM activation and p53 protein stabilization induced by IR damage (Figure 2E).

To further investigate the lack of IR-induced p53 function in A/A mice, we compared the stabilization and activity of p53 in WT and A/A radiosensitive tissues after DNA damage. We first harvested whole spleen protein extracts 4 hr after whole-body IR treatment. As expected, activation of the ATM kinase in wild-type mice by 4Gy IR was readily detected, as judged by the extent of autophosphorylated ATM Ser1987, the mouse ortholog of human ATM Ser1981 (Pellegrini et al., 2006), and this tissue displayed robust IR-stabilization of p53 (Figure 3A). However, A/A mice lack any detectable stabilization of the p53

protein, despite comparable activation of ATM by IR. This lack of p53 protein upregulation in IR-treated A/A spleen extracts was seen in multiple mice (Figure S3A), and corresponded with greatly decreased induction of the p53-target genes *Puma*, *p21*, *Bax*, and *Noxa*, as measured by quantitative real time PCR (qRT-PCR) (Figure 3B). However, IR-treated A/A spleens did show a low-level activation of p53, as expression of p53 target genes was slightly elevated relative to levels in IR-treated p53^{-/-} spleens.

Similar results were seen at multiple time points in thymus extracts following whole-body IR treatment of mice (Figures 3C and S3B). The level of p53 protein in wild-type thymus was upregulated by 6.4-fold (1 hr), 4.8-fold (2 hr), and 1.8-fold (4 hr) following 4Gy IR, whereas p53 levels in IR-treated A/A thymus were upregulated by only 2.1-fold, 1.3-fold, and 1.2-fold at these respective time points (Figure 3C). Again, these differences were seen despite similar activation of the ATM kinase. As observed in spleen, expression of the p53-target genes *Puma* and *p21* were significantly reduced in A/A thymus at all time points after IR treatment (Figure 3D). Because the p53 protein is phosphorylated by ATM on p53 Ser18 in the treated A/A thymus (Figure 3C), the reduced levels of p53 target gene expression in this tissue are likely due to decreased p53 protein stabilization in A/A mice after IR, and not due to failure of ATM to induce proper posttranslational modification of p53. Analysis of multiple p53 target genes in irradiated WT and A/A thymocytes using p53

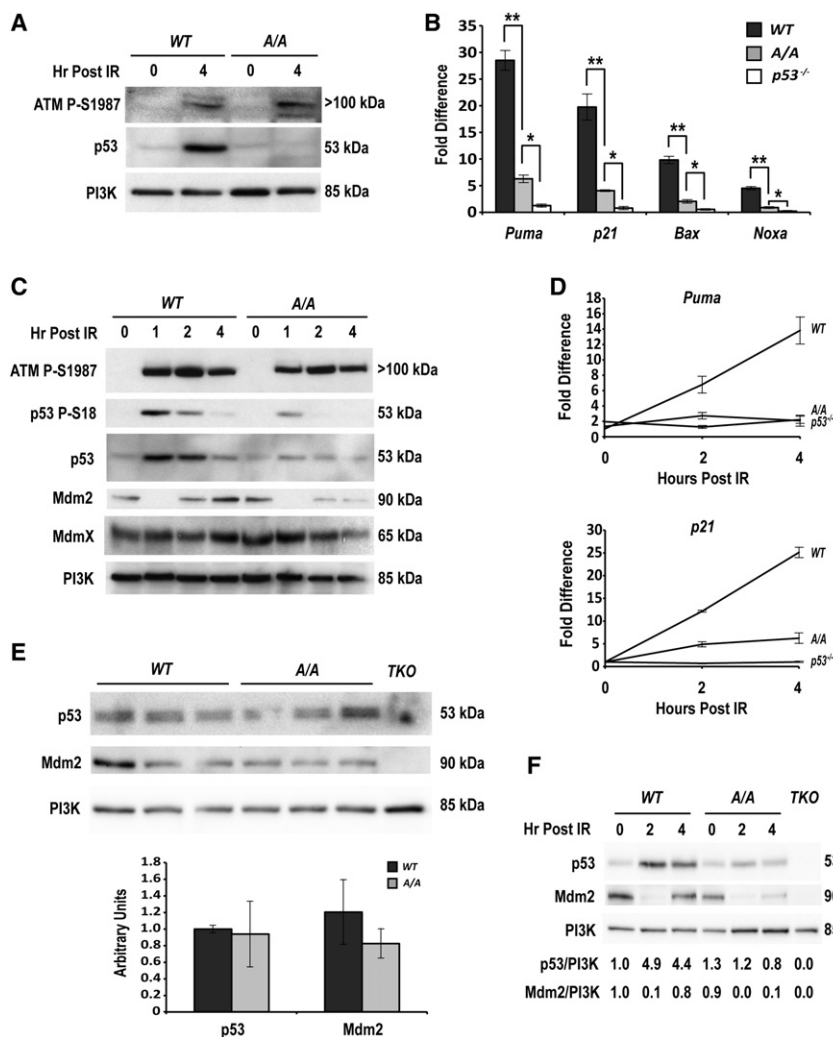


Figure 3. Mdm2 Ser394 Phosphorylation Is Necessary for p53 Stability and Activity after DNA Damage

(A) Mice were either untreated or irradiated with 4Gy and spleens were harvested 4 hr later. Protein levels were then analyzed by western blot.

(B) Mice were either untreated or irradiated with 4Gy and spleens were harvested 4 hr later (n = 3 per genotype). Relative expression levels of p53 target genes in irradiated spleen extracts were determined by qRT-PCR. Levels were normalized to untreated wild-type and are presented as the ratio of mRNA to *Gapdh* mRNA. Standard deviation indicated by error bars. Asterisks indicate a significant difference: double asterisk *Puma* p = 0.002, *p21* p = 0.01, *Bax* p = 0.003, *Noxa* p = 0.002; single asterisk *Puma* p = 0.01, *p21* p = 0.001, *Bax* p = 0.01, *Noxa* p = 0.008.

(C) Mice were either untreated or irradiated with 4Gy and thymi were harvested at the indicated times. Protein levels were then analyzed by western blot.

(D) Mice were either untreated or irradiated with 4Gy and thymi were harvested 2 or 4 hr later (n = 3 per genotype). Relative expression levels of p53 target genes were determined by qRT-PCR. Data are presented as the ratio of mRNA to *Gapdh* mRNA. Standard deviation indicated by error bars. Significant differences were seen between WT and A/A *Puma* at 2 (p = 0.035) and 4 (p = 0.002) hr and between WT and A/A *p21* at 2 (p = 0.0001) and 4 (p = 0.0001) hr.

(E) Protein levels from whole thymus extracts from untreated mice were analyzed by western blot (n = 3 per genotype). Quantified levels of p53 (p = 0.83) and Mdm2 (p = 0.11) relative to PI3K were normalized to wild-type.

(F) Mice were either untreated or irradiated with 4Gy and thymi were harvested at the indicated times. Protein levels were then analyzed by western blot. Quantified levels of p53 and Mdm2 relative to PI3K were normalized to untreated wild-type.

See also Figure S3.

signaling pathway PCR arrays confirmed reduced activation of multiple p53 target genes in treated A/A cells (Figure S3C). These results reveal that Mdm2 Ser394 phosphorylation is required in vivo for p53 stabilization and robust p53 activation after DNA damage.

Mdm2 destabilization in response to DNA damage has been shown previously (Stommel and Wahl, 2004), and we observed an initial decrease in Mdm2 protein in both WT and A/A tissues. Interestingly, these Mdm2 levels recovered at 2 and 4 hr in both genotypes, with more Mdm2 protein being present in WT at these times compared to A/A (Figure 3C). To determine if the initial decrease in Mdm2 levels was due to epitope masking by IR-induced phosphorylation, we treated these extracts with calf intestinal phosphatase (CIP); however, this treatment neither increased nor altered the pattern of Mdm2 levels after DNA damage (Figure S3D). Interestingly, the phosphorylation status of Mdm2 Ser394 had no effect on the levels of MdmX, an Mdm2-related p53 regulatory protein, in this tissue. The specificities of the Mdm2 and MdmX antibodies were validated using

Mdm2^{-/-}, *MdmX*^{-/-}, *p53*^{-/-} triple-knockout (TKO) thymus extracts (Figure S3E).

We next wanted to determine why differences in p53 and Mdm2 levels are observed in irradiated WT versus A/A cells. One possibility is that p53 and Mdm2 protein levels are initially lower in A/A cells than in WT cells, leading to an overall reduced DNA damage response in A/A mice. To test this, we carefully quantitated p53 and Mdm2 protein levels in untreated WT and A/A whole thymus extracts and found no significant difference in the levels of either p53 or Mdm2 proteins at baseline (Figure 3E). These data support the similar baseline levels of apoptosis and gene expression that we observed in WT and A/A tissues in the absence of DNA damage (Figures 2 and 3E). Furthermore, careful quantitation confirmed that there is less p53 protein and Mdm2 protein in A/A thymus than in WT thymus after IR (Figure 3F). Because baseline Mdm2 levels were equivalent in A/A and WT tissue, the reduced amount of Mdm2 and p53 in A/A versus WT tissues reflects a specific difference in the response of A/A cells to DNA damage.

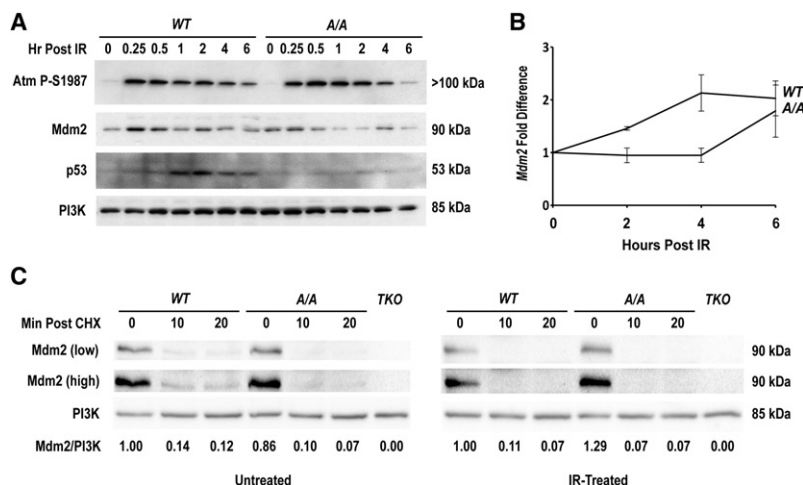


Figure 4. Phosphorylation of Mdm2 Ser394 Does Not Significantly Impact Mdm2 Destabilization after DNA Damage

(A) Ex vivo thymocytes were either untreated or irradiated with 2Gy for the indicated times. Protein levels were then analyzed by western blot.

(B) Ex vivo thymocytes were either untreated or irradiated with 2Gy for the indicated time points ($n = 3$ per genotype). Relative expression levels of *Mdm2* were determined by qRT-PCR. Data are presented as the ratio of mRNA to *Gapdh* mRNA. Standard deviation indicated by error bars.

(C) Ex vivo thymocytes were incubated with 50 μ g/ml of CHX and either left untreated or irradiated with 2Gy for the indicated times. Protein levels were then analyzed by western blot. Quantified levels of Mdm2 relative to PI3K were normalized to untreated wild-type.

See also Figure S4.

To further examine the effects of Mdm2 Ser394 phosphorylation on p53 and Mdm2 stability, we performed western blots using irradiated *WT* and *A/A* ex vivo thymocytes. Stabilization of p53 was detected in primary wild-type thymocytes at 1–2 hr post-IR, and p53 levels remained elevated in these cells 6 hr after IR damage (Figures 4A and S4). In contrast, p53 stabilization was not apparent in *A/A* thymocytes at these early time points after DNA damage, even though ATM was clearly activated by IR treatment. Similar to whole thymus extracts, Mdm2 levels also appear decreased in irradiated *A/A* thymocytes compared to IR-treated *WT* cells. The increased levels in wild-type Mdm2 protein may be due to increased p53-induced *Mdm2* transcription, and indeed, like other p53-dependent targets, *Mdm2* transcripts are lower in the irradiated *A/A* thymocytes (Figure 4B). Alternatively, the difference in Mdm2 protein levels after DNA damage may be due to decreased Mdm2 protein stability in *A/A* thymocytes compared to *WT* cells. To examine the effects of Mdm2 Ser394 phosphorylation on Mdm2 stability in vivo, we incubated untreated and irradiated *WT* and *A/A* thymocytes with the protein synthesis inhibitor cycloheximide (CHX). Although Mdm2 protein is relatively unstable in thymocytes, we found that IR treatment lead to further decreases in Mdm2 stability in both genotypes (Figure 4C). However, the stability of Mdm2 proteins in untreated and IR-treated *WT* and *A/A* thymocytes was comparatively indistinguishable. Therefore, our results indicate that the lower Mdm2 protein levels in *A/A* thymocytes after DNA damage reflects less p53 activation of *Mdm2* transcription in these cells and not reduced Mdm2-S394A protein stability.

The reduced p53 transactivation of *p21* observed in the spleen and thymus of IR-treated *A/A* mice (Figure 3) suggests that Mdm2 Ser394 phosphorylation may also impact p53 regulation of cell proliferation. To examine this further, we assayed p53 function in *WT* and *A/A* MEFs. No difference in the growth rate of *A/A* or *WT* cells was observed using a standard proliferation assay (Figure 5A). This result is in keeping with the equivalent low levels of p53 observed in nondamaged *WT* and *A/A* tissues (Figure 3). However, greater p53 protein stabilization was observed in *WT* MEFs than in *A/A* MEFs at 6 and 12 hr post-IR (Figure 5B). Likewise, transactivation of *p21* was greater in *WT* MEFs than in *A/A* cells, and induction of *Mdm2* transcripts was

delayed in *A/A* MEFs (Figure 5C). FACS analysis of *WT*, *A/A*, and *p53*^{-/-} MEFs at 18 and 45 hr post-IR revealed that *A/A* cells are compromised in their ability undergo growth arrest after DNA damage (Figure 5D). However, as compared to *p53*^{-/-} cells, the *A/A* MEFs do retain the ability to undergo a partial growth arrest after IR damage. Additionally, no differences were observed in the nuclear versus cytoplasmic fraction of Mdm2 protein in *A/A* and *WT* MEFs before or after DNA damage (Figure S5). These data reveal that phosphorylation of Mdm2 Ser394 also governs the ability of Mdm2 to regulate p53-mediated cell growth arrest after IR.

Because ATM phosphorylation of Mdm2 Ser394 is necessary for robust p53 activation after DNA damage, we wanted to test whether this posttranslational modification alone was sufficient to induce p53 activity in untreated tissues. To this end, we generated a different mouse model in which *Mdm2* Ser394 was mutated to aspartic acid (S394D), thus mimicking a constitutively phosphorylated serine residue (Figure 6A). We followed the same gene replacement strategy used to generate the S394A model (Figures S6A–S6D). We hypothesized that if phosphorylation of Mdm2 Ser394 is sufficient by itself to disrupt Mdm2 regulation of p53, then substitution of aspartic acid at codon 394 might lead to embryonic lethality in mice bearing functional *p53* alleles (as is seen in *Mdm2* null mice). However, both heterozygous (*D/+*) and homozygous (*D/D*) mice proved to be viable, and both genotypes were recovered from heterozygous intercrosses at Mendelian ratios (Figure S6E). The viability of this knock-in mutant suggests that baseline levels of p53 protein would be unchanged in this model compared to controls, and subsequent quantitation of p53 and Mdm2 protein levels in untreated thymus protein extracts revealed no significant differences between *WT* and *D/D* (Figure 6B).

The viability of *D/D* mice also suggests that either multiple DNA damage signals are needed to attenuate Mdm2 regulation and activate p53, or that the *Mdm2* S394D mutation poorly mimics a phosphoserine residue. The latter possibility would result in *D/D* mice presenting with phenotypes similar to our *A/A* model, because aspartic acid (like alanine) cannot be phosphorylated. To test this, we treated *WT* and *D/D* mice with 4Gy whole-body irradiation and examined p53 stabilization in thymus cells at various early time points after DNA damage. In contrast

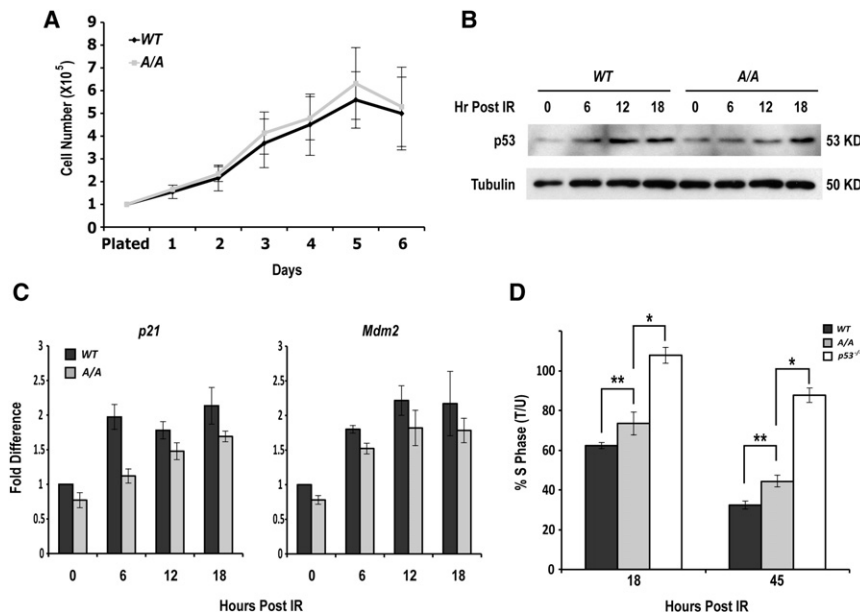


Figure 5. Mdm2 Ser394 Phosphorylation Is Necessary for Full p53 Stabilization and Function in MEFs

(A) Primary MEFs proliferation was counted each day ($n = 3$ per genotype). Standard deviation indicated by error bars.

(B) Primary MEFs were either untreated or irradiated with 4Gy for the indicated times, and protein levels were then analyzed by western blot.

(C) Primary MEFs were either untreated or irradiated with 4Gy for the indicated times ($n = 3$ per genotype). Relative expression levels of p53 target genes were determined by qRT-PCR. Data are presented as the ratio of mRNA to *Gapdh* mRNA. Standard deviation indicated by error bars.

(D) Primary MEFs were treated with 4Gy IR for the indicated time points and then incubated with bromodeoxyuridine (BrdU) for 3 hr ($n = 3$ per genotype). Cells were then analyzed by flow cytometry. Standard deviation indicated by error bars. Asterisks indicate a significant difference: double asterisk 18 hr $p = 0.0318$, 45 hr $p = 0.0126$; single asterisk 18 hr, $p = 0.0004$, 45 hr $p = 0.0001$. See also Figure S5.

to what we observed in *A/A* cells, p53 protein stabilization by IR damage in *D/D* thymus extracts was comparable to wild-type (Figure 6C). This was also observed in IR-treated ex vivo thymocytes (Figure S6F). Likewise, the pattern of Mdm2 protein destabilization followed by recovery was equivalent between the *WT* and *D/D* tissues (Figure 6C), which reflects the equal induction of *Mdm2* transcript levels seen in DNA damaged thymocytes (Figure 6D). *Puma* transcript levels were also similarly increased in the IR-treated *WT* and *D/D* cells (Figure 6D), and the levels of DNA damage-induced apoptosis were the same between *WT* and *D/D* thymocytes at 12 hr after IR treatment (Figure 6E). Similar results were obtained in thymocytes at 24 hr post-IR (Figure S5G), as well as in thymocytes isolated 48 hr after whole-body IR in *WT*, *D/D*, and *p53*^{-/-} mice (Figure S5H). Collectively, these findings demonstrate that *Mdm2* S394D mimics the effects of the phosphorylated Mdm2 Ser394 protein in wild-type mice after DNA damage. As baseline levels of p53 protein and apoptosis in nondamaged *WT* and *D/D* cells are the same in these assays, the mimicking of Mdm2 Ser394 phosphorylation in *D/D* thymocytes is not sufficient in the absence of other DNA damage-induced signals to induce p53 activation.

To confirm the effects of this Mdm2 Ser394 phospho-mimic in cell growth, *WT* and *D/D* MEFs were analyzed for cell proliferation (Figure 6F). As with *A/A* MEFs, the *D/D* MEFs proliferated at the same rate as wild-type MEFs in culture. However, IR-treatment of *D/D* MEFs induced p53 stabilization at levels similar to IR-treated *WT* MEFs (Figure 6G), and IR damage induced an equivalent p53-mediated reduction in S phase in both *WT* and *D/D* cells (Figure 6H).

Previous in vitro work has established that the Wip1 phosphatase can dephosphorylate multiple ATM targets, including human ATM Ser1981, p53 Ser15, and MDM2 Ser395 (Shreeram et al., 2006; Lu et al., 2005, 2007). This dephosphorylation has been proposed to return DNA damage signaling to basal levels once the DNA damage has been resolved. Because Wip1 cannot dephosphorylate the Mdm2-S394D residue, we hypothesized

that *D/D* and *WT* mice might have differences in the duration of Mdm2-p53 signaling after IR treatment. Therefore, we analyzed p53 stabilization and activity at later time points in the DNA damage response. Like *D/D* thymocytes (Figure S6F), *WT* and *D/D* spleen samples had equal levels of ATM activity and p53 levels at 4 hr post-IR. However, the level of p53 protein remained persistently elevated at 8 hr post-IR in *D/D* extracts, despite the reduction in ATM activity and similar levels of Mdm2 by this later time point (Figures 7A and S7A). A similar response pattern was seen in primary thymocytes. Although p53 was stabilized to a similar extent in *WT* and *D/D* mice at early time points after IR damage (see Figure 6C), p53 levels remain elevated in *D/D* thymocytes at 12 hr post-IR, whereas p53 stabilization is less obvious at this later time point in wild-type cells (Figure 7B). As in spleen, the elongated duration of p53 stabilization in *D/D* thymocytes was seen well after resolution of the DNA damage response, as indicated by the absence of phospho-ATM at 12 hr post-IR, and despite the presence of Mdm2. The elongated p53 response in *D/D* thymocytes was reflected by increased levels of *Puma*, *p21*, *Mdm2*, and *Wip1* expression found in these cells at 12 and 18 hr post-IR (Figure 7C), and p53 signaling pathway PCR array analysis of additional p53 target genes confirmed that p53 activation remained elevated in *D/D* thymocytes relative to wild-type levels at 12 hr following IR (Figure S7B).

Finally, to explore the importance of Mdm2 Ser394 phosphorylation in p53-mediated tumor suppression, we established cohorts of *WT*, *A/A*, and *D/D* mice and performed a tumor assay. In 24 months, 20 of 31 (65%) *A/A* mice developed spontaneous tumors, whereas only 1 of 24 (4%) *D/D* mice presented with a tumor of the salivary gland epithelium (Figure 8A). None of the wild-type mice presented with a tumor during this interval. Most of the *A/A* tumors arose between 18–24 months of age, which closely resembles previous *p53*^{+/-} tumor curves (Harvey et al., 1993; Jacks et al., 1994). Like other mouse models with diminished p53 activity, most of the tumors (13/20; 65%) were

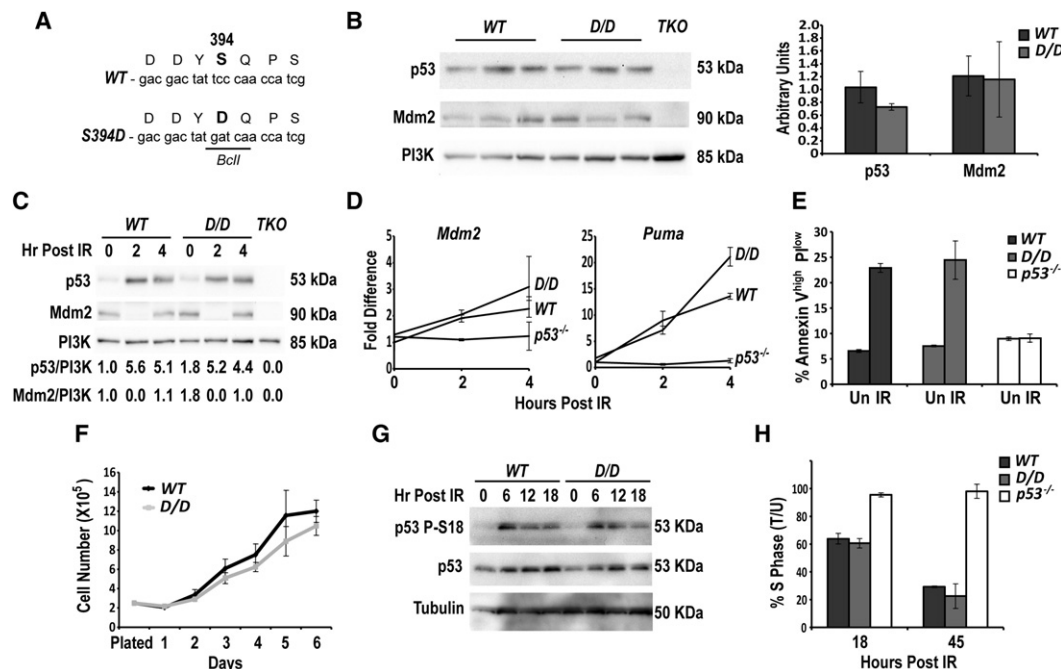


Figure 6. Phosphorylation of Mdm2 Ser394 Is Necessary But Not Sufficient to Stabilize and Activate p53

(A) DNA sequence of both the WT and S394D allele at *Mdm2* codon 394. The mutations in S394D also introduce a *BclI* restriction digest site.

(B) Protein levels from whole thymus extracts from untreated mice were analyzed by western blot ($n = 3$ per genotype). Quantified levels of p53 ($p = 0.10$) and Mdm2 ($p = 0.88$) relative to PI3K were normalized to wild-type.

(C) Mice were either untreated or irradiated with 4Gy and thymi were harvested at the indicated times. Protein levels were then analyzed by western blot. Quantified levels of p53 and Mdm2 relative to PI3K were normalized to untreated wild-type.

(D) Ex vivo thymocytes were either untreated or irradiated with 2Gy for 2 or 4 hr ($n = 3$ per genotype). Relative expression of *Mdm2* and *Puma* was determined by qRT-PCR. Data are presented as the ratio of mRNA to *Gapdh* mRNA. Standard deviation indicated by error bars.

(E) Ex vivo thymocytes were isolated and were either left untreated or irradiated with 2Gy for 12 hr ($n = 3$ per genotype). Apoptotic cells were quantified by flow cytometry. Standard deviation indicated by error bars.

(F) Primary MEF proliferation was counted each day ($n = 3$ per genotype). Standard deviation indicated by error bars.

(G) Primary MEFs were either untreated or irradiated with 4Gy for the indicated times, and protein levels were analyzed by western blot.

(H) Primary MEFs were treated with 4Gy IR for 18 hr or 8Gy IR for 45 hr and incubated with BrdU for 3 hr ($n = 3$ per genotype). Cells were then analyzed by flow cytometry. Standard deviation indicated by error bars.

See also Figure S6.

found to be T cell-derived lymphomas as determined by morphology, negative staining for the B cell marker B220, and positive staining for the T cell marker CD3 (Figure 8B, left panels). The remaining A/A tumors displayed severe splenomegaly and cellular infiltration in the liver and kidneys. One of these tumors stained positive for B220 and displayed expansion of the white pulp in the spleen, indicative of B cell lymphoma (Figure 8B, right panels). Sequencing of *p53* transcripts isolated from four randomly selected tumors indicated wild-type *p53* expression levels and no *p53* mutations in these A/A samples. These results reveal that posttranslational modification of Mdm2 Ser394 impacts p53-mediated tumor suppression as well as the p53 DNA damage response in vivo.

DISCUSSION

In our present study utilizing mouse models of Mdm2 Ser394 phosphorylation, we provide direct evidence that ATM phosphorylation of Mdm2 Ser394 regulates the ability of Mdm2 to destabilize p53 in vivo, and that this signaling impacts p53-mediated apoptosis and tumor suppression. S394A mice lack

p53-dependent physiological responses in radiosensitive organs after IR treatment resulting in phenotypes that nearly match those seen in IR treated *p53*^{-/-} mice: radioresistance, greatly reduced p53 target gene induction, and greatly reduced apoptosis. Importantly, the differences between A/A and WT mice were seen only in irradiated mice and tissues, as baseline levels were similar in all assays. This owes to the conservation of Mdm2 structure and function in the S394A protein, and indicates that the only difference between the wild-type and mutant Mdm2 protein is the phosphorylation status of Ser394 after cellular stress. It is likely that the compromised p53 transactivation and the reduced number of cells undergoing apoptosis and cell cycle arrest are due to the lack of p53 protein accumulation in DNA damaged A/A cells. Thus, phosphorylation of Mdm2 Ser394 by the ATM kinase is a major regulator of p53 stability and the subsequent p53-mediated DNA damage response in multiple tissue types.

Although loss of Mdm2 Ser394 phosphorylation greatly reduced p53-mediated apoptosis in lymphocytes and growth arrest in MEFs, it did not completely abrogate these responses (as seen in *p53*^{-/-} mice). As anticipated by the literature, other

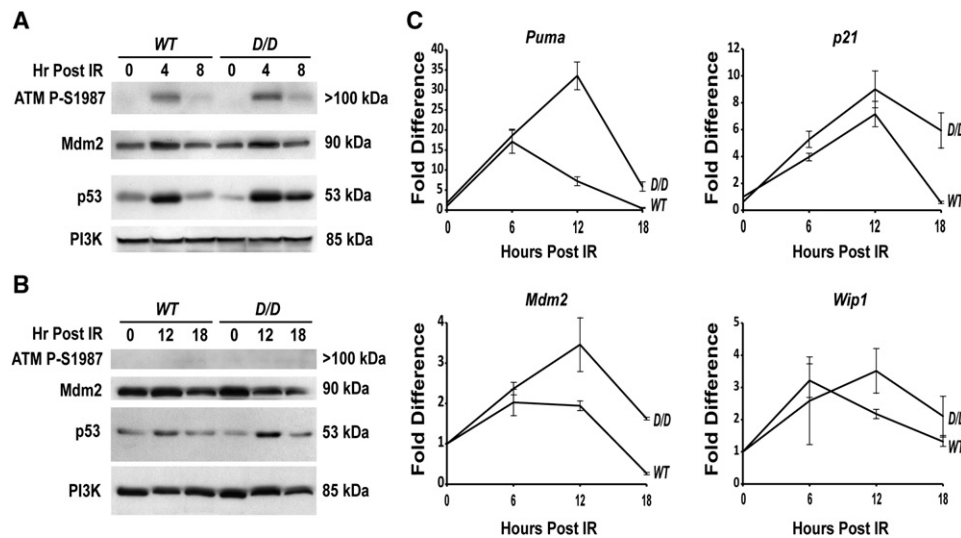


Figure 7. Mdm2 Ser394 Phosphorylation Regulates the Attenuation of the p53 Response to DNA Damage

(A) Mice were either untreated or irradiated with 4Gy and spleens were harvested either 4 or 8 hr later. Protein levels were then analyzed by western blot.

(B) Ex vivo thymocytes were either untreated or irradiated with 2Gy for either 12 or 18 hr. Protein levels were then analyzed by western blot.

(C) Ex vivo thymocytes were either untreated or irradiated with 2Gy for the indicated times ($n = 3$ per genotype). Relative expression levels of p53 target genes were determined by qRT-PCR. Data are presented as the ratio of mRNA to *Gapdh* mRNA. Standard deviation indicated by error bars.

See also Figure S7.

modifications to Mdm2, MdmX, and p53 must also assist in regulating p53 functions after DNA damage (Chao et al., 2003, 2006; Sluss et al., 2004; Wang et al., 2009). In agreement with this hypothesis, it is interesting to note the lack of p53 stabilization or p53 target gene activation in *D/D* mice and cells in the absence of IR treatment (Figures 6B–6D). Although the absence of a p53 response in undamaged *D/D* cells may reflect the inability of the substituted aspartate residue to perfectly mimic a phosphorylated serine residue (due to differences in the size and overall negative charge of these residues), equivalent levels of p53-mediated apoptosis and growth arrest are seen in *WT* and *D/D* cells after DNA damage. Therefore, other DNA-damage induced signals in addition to Mdm2-S394 phosphorylation are required to fully activate the DNA damage response. This interpretation also accounts for the viability of the S394D model, and the similar growth characteristics of nondamaged *WT*, *A/A*, and *D/D* MEFs. Collectively, our results indicate that ATM phosphorylation of Mdm2 Ser394 is necessary but not sufficient to induce a robust p53 response to IR.

Although the levels of p53 induction and activation are equivalent at early time points after IR in *WT* and *D/D* cells, p53 protein levels and activities remain elevated in *D/D* cells at later time points after IR treatment (Figures 7 and S7). In contrast, the DNA damage response in wild-type cells begins to wane after 6 hr post-IR, coincident with the induction of *Wip1* expression (Figures 7B and 7C). Because *Wip1* is unable to dephosphorylate the Mdm2 S394D residue, elevation of p53 functions in *D/D* cells at later time points after IR indicates that Mdm2-S394 phosphorylation also regulates the duration of the p53 response. However, p53 levels and activities eventually return to baseline in the *D/D* cells, possibly due to the eventual loss of other secondary modifications to Mdm2 or p53. These findings are in keeping with a proposed role for

Wip1 as gatekeeper of the Mdm2-p53 autoregulatory loop (Lu et al., 2007).

Interestingly, p53 tumor suppressor function is deficient in untreated *A/A* mice, as 65% of these mice developed spontaneous lymphomagenesis in the absence of exogenous IR treatment. Because our data indicate that p53 levels and activities are identical between *WT* and *A/A* cells in the absence of DNA damage, the stochastic nature of endogenous DNA damage signaling arising from inappropriate oncogene activation or DNA replication errors may account for this rather long latency period. Tumor formation in our *A/A* model is in keeping with previous reports of a role for ATM-p53 signaling and p53 activation of the proapoptotic gene *Puma* in p53-mediated suppression of lymphoma formation (Jeffers et al., 2003; Sluss et al., 2010). Likewise, the reduced capacity of p53 to suppress growth after DNA damage in *A/A* cells may also contribute to the spontaneous tumorigenic phenotype of *A/A* mice. It remains to be seen if phosphorylation of Mdm2 Ser394 by ATM also regulates p53-mediated suppression of tumors induced by sublethal doses of radiation or the forced expression of activated oncogenes.

Transfection-based experiments have determined that mutation of six separate ATM phosphorylation sites in the carboxy-terminus of MDM2, including Ser395, alters MDM2 protein oligomerization, E3-ligase activity, and the interaction of MDM2 with p53 (Cheng et al., 2009, 2011). Because p53 activity is not totally ablated in the *A/A* model, these additional ATM targets on Mdm2 may contribute to full p53 activation after DNA damage. Furthermore, a recent study found that ATM phosphorylation of MDM2 Ser395 led to increased p53 mRNA translation, which suggests that MDM2 may be necessary for p53 protein upregulation after DNA damage (Gajjar et al., 2012). Diminished Mdm2 E3 ligase activity and phospho-Mdm2-dependent upregulation of p53 would each explain the

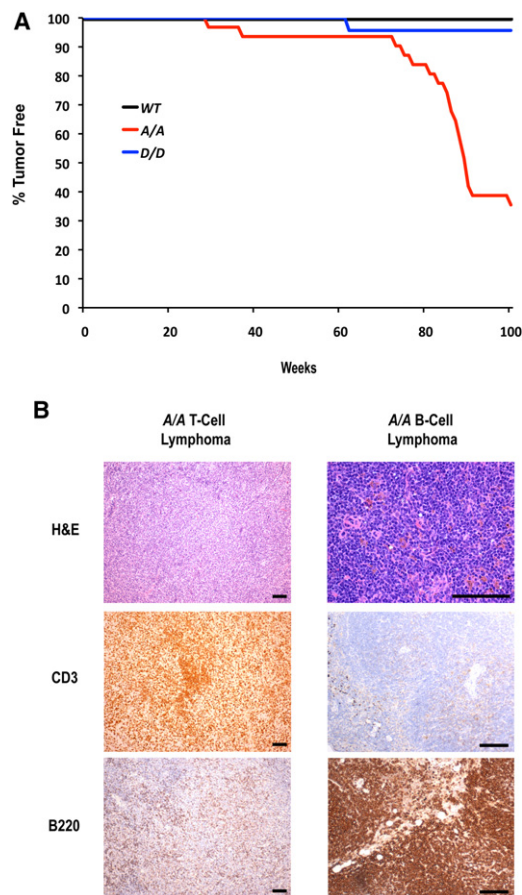


Figure 8. Phosphorylation of Mdm2 Ser394 Impacts p53 Tumor Suppression in Mice

(A) Spontaneous tumorigenesis in wild-type ($n = 50$), A/A ($n = 31$), and D/D ($n = 24$) mice.

(B) Representative tumor sections from an A/A T cell lymphoma (mesenteric lymph node, *left*) and an A/A B cell lymphoma (spleen, *right*). Tissue sections were stained with hematoxylin and eosin (H&E), anti-CD3, or anti-B220. Scale bars represent 100 μm .

seemingly paradoxical results of having decreased p53 levels and activities in the absence of increased Mdm2 protein in IR-treated A/A thymus extracts. These mechanisms would also explain the increased p53 activation at later times of the DNA damage response in D/D cells despite nearly equivalent levels of Mdm2 compared to wild-type. Our in vivo data are in keeping with both of these proposed models and confirm a significant role for Mdm2 S394 phosphorylation in the p53 DNA damage response.

In conclusion, our study reveals that ATM phosphorylation of Mdm2 at serine residue 394 is a critical regulator of Mdm2-p53 signaling. Phosphorylation of this Mdm2 residue by ATM following DNA damage is necessary for p53 stabilization, thereby upregulating p53 activity and activating p53 downstream functions in primary cells and tissues. Furthermore, the phosphorylation status of Mdm2 Ser394 governs the duration of the p53 response, underscoring the importance of this single phosphorylation target in regulating Mdm2-p53 signaling and p53-mediated tumor suppression. Full understanding of the

multiple posttranslational modifications that influence p53 signaling will likely assist in developing better molecular diagnostics and therapeutics for human cancer patients.

EXPERIMENTAL PROCEDURES

Generation of S394A and S394D Mice

The targeting constructs contain a subcloned fragment of the *Mdm2* genomic sequence (129Sv strain). Site-directed mutagenesis was performed (Stratagene #200523). The targeting vectors were sequenced to ensure that no unwanted mutations were introduced. PC3 ES cells were electroporated with each targeting vector. Homologous recombination was detected by Southern blot using 5' and 3' external probes after *SpeI* and *BamHI* restriction digests, respectively. Targeted cells were microinjected into E3.5 blastocysts (C57BL/6 strain), and the embryos were surgically implanted into pseudopregnant foster mice by standard procedures. Transmission of the knock-in allele and excision of the neo cassette in F_1 offspring of male chimeric mice was confirmed by digestion with *EcoRI* followed by Southern analysis using a 3' internal probe described previously (Steinman and Jones, 2002).

Mice

All mice used in this study were on a mixed 129Sv \times C57BL/6 background. Genomic PCR followed by either *BcgI* (S394A) or *BclI* (S394D) digestion was used to identify inheritance of the mutant alleles. Sequencing of DNA samples was performed by Sequegen. All mice and cells were irradiated with a cesium-137 source (Gammacell 40). Animals in the spontaneous tumor cohorts or IR-treated cohorts were killed if tumor burden was apparent or when moribund. Animals were maintained and used in accordance with federal guidelines and those established by the Institutional Animal Care and Use Committee at the University of Massachusetts Medical School.

Histology

Tissues were fixed in 10% formalin. Irradiated tissue sections (5 μm) were stained with anti-cleaved caspase-3 antibody (Cell Signaling #9661) or stained for TUNEL using the In Situ Cell Death Detection Kit, POD (Roche 11684817910). Tumor samples were stained with anti-CD3 (Abcam ab16044) or anti-CD45R/B220 (BD Pharmingen). All staining was performed by the UMMS Diabetes and Endocrinology Research Center Morphology Core.

Western Blotting and Reagents

Tissues and cells were lysed in NP-40 lysis buffer (50 mM Tris-HCl, pH 7.5; 150 mM NaCl; 0.5% NP-40; 20% glycerol) supplemented with 1 \times protease inhibitor cocktail (Roche). Protein extracts were analyzed by standard western blotting with the following antibodies: p53 (1C12), phospho-Atm Ser1987 (10H11.E12), and phospho-p53 Ser18 (#9284) from Cell Signaling; Mdm2 (mix of sc-812 and sc-1022) and lamin A/C (sc-6215) from Santa Cruz; MdmX (MDMX-82) and tubulin (T5168) from Sigma; PI3K (#06-496) from Upstate; actin (ab8229) from Abcam. Nutlin-3a (N6287) and cycloheximide (C4859) were from Sigma. PI3K and tubulin were used as loading controls. KU55933 (118502) was from Calbiochem. The CIP (M0290) and phosphatase treatment protocol were from NEB. Cellular fractionation was performed according to the manufacturer's protocol from the NE-PER Nuclear and Cytoplasmic Extraction Kit (78833) from Thermo Scientific. Protein levels in Figure 3C were quantified by densitometry using the ImageJ software. All other protein quantification was performed using the Chemidoc XRS+ Molecular Imaging System from BioRad.

Quantitative Real Time PCR

Total mRNA was isolated according to the Trizol Reagent protocol (Invitrogen) and cDNA was generated using the SuperScript II First Strand Synthesis Kit (Invitrogen). The following primers were used in qRT-PCR:

p21: 5'-TGAGGAGGAGCATGAATGGAGACA-3'
5'-AACAGGTGCGACATCACCAGGATT-3',
Puma: 5'-CCTGGAGGGTCATGTACAATCT-3'
5'-TGCTACATGGTGCAGAAAAAGT-3',

Bax: 5'-CTGAGCTGACCTTGGAGC-3'
 5'-GACTCCAGCCACAAAGATG-3',
Noxa: 5'-CCACCTGAGTTCGCAGCTCAA-3'
 5'-GTTGAGCACACTCGTCCTTCA-3',
Mdm2: 5'-GCATTCTGGTGATTGCCTGGATCA-3'
 5'-AGACTGTGACCCGATAGACCTCAT-3'
Gapdh: 5'-TGGCAAAGTGGAGATTGTTGCC-3'
 5'-AAGATGGTGATGGGCTTCCCG-3'.

All data are presented as the ratio of mRNA to *Gapdh* mRNA.

For the QIAGEN p53 PCR Array experiments, mRNA was isolated using the RNeasy kit (74104) with DNase (79254) from QIAGEN. cDNA was synthesized using the RT2 First Strand Kit (330401) from QIAGEN. p53 PCR Arrays (PAMM-027C) were run according to manufacturer's protocol using the RT2 SYBR Green ROX qPCR Mastermix (330520) from QIAGEN.

Flow Cytometry

For apoptosis, samples were treated according to the Annexin V-FITC Apoptosis Detection Kit I protocol (BD Pharmingen #556547). Early apoptotic cells (Annexin V^{high} PI^{low}) were quantitated and presented. For cell cycle arrest, treated MEFs were pulsed labeled with 60 μ M bromodeoxyuridine (BrdU) for 3 hr. Cells were then trypsinized, fixed in 70% ethanol overnight, incubated with anti-BrdU antibody (Becton Dickinson #347583) and PI, and analyzed by flow cytometry. Data are presented as the percentage of cells in S phase in the treated samples compared to the untreated samples. Flow cytometry was performed by the UMASS Medical School Flow Cytometry Core Lab.

SUPPLEMENTAL INFORMATION

Supplemental Information includes seven figures and can be found with this article online at doi:10.1016/j.ccr.2012.04.011.

ACKNOWLEDGMENTS

We thank Marilyn Keeler and Judith Gallant for help with the ES cell and blastocyst injection experiments, and Lawrence Donehower for comments on the manuscript. Core facilities were partly supported by grant DK32520 from the NIDDK. This research was supported by grant CA077735 from the National Cancer Institute (S.N.J.).

Received: August 18, 2011

Revised: December 13, 2011

Accepted: April 3, 2012

Published: May 14, 2012

REFERENCES

- Bond, G.L., Hu, W., and Levine, A.J. (2005). MDM2 is a central node in the p53 pathway: 12 years and counting. *Curr. Cancer Drug Targets* 5, 3–8.
- Chao, C., Saito, S., Anderson, C.W., Appella, E., and Xu, Y. (2000). Phosphorylation of murine p53 at ser-18 regulates the p53 responses to DNA damage. *Proc. Natl. Acad. Sci. USA* 97, 11936–11941.
- Chao, C., Hergenhausen, M., Kaeser, M.D., Wu, Z., Saito, S., Iggo, R., Hollstein, M., Appella, E., and Xu, Y. (2003). Cell type- and promoter-specific roles of Ser18 phosphorylation in regulating p53 responses. *J. Biol. Chem.* 278, 41028–41033.
- Chao, C., Herr, D., Chun, J., and Xu, Y. (2006). Ser18 and 23 phosphorylation is required for p53-dependent apoptosis and tumor suppression. *EMBO J.* 25, 2615–2622.
- Chen, J., Lin, J., and Levine, A.J. (1995). Regulation of transcription functions of the p53 tumor suppressor by the mdm-2 oncogene. *Mol. Med.* 1, 142–152.
- Cheng, Q., Chen, L., Li, Z., Lane, W.S., and Chen, J. (2009). ATM activates p53 by regulating MDM2 oligomerization and E3 processivity. *EMBO J.* 28, 3857–3867.
- Cheng, Q., Cross, B., Li, B., Chen, L., Li, Z., and Chen, J. (2011). Regulation of MDM2 E3 ligase activity by phosphorylation after DNA damage. *Mol. Cell. Biol.* 31, 4951–4963.
- Donehower, L.A., Harvey, M., Slagle, B.L., McArthur, M.J., Montgomery, C.A., Jr., Butel, J.S., and Bradley, A. (1992). Mice deficient for p53 are developmentally normal but susceptible to spontaneous tumours. *Nature* 356, 215–221.
- Gajjar, M., Candeias, M.M., Malbert-Colas, L., Mazars, A., Fujita, J., Olivares-Illana, V., and Fähræus, R. (2012). The p53 mRNA-Mdm2 interaction controls Mdm2 nuclear trafficking and is required for p53 activation following DNA damage. *Cancer Cell* 21, 25–35.
- Gudkov, A.V., and Komarova, E.A. (2003). The role of p53 in determining sensitivity to radiotherapy. *Nat. Rev. Cancer* 3, 117–129.
- Gurley, K.E., and Kemp, C.J. (2007). Ataxia-telangiectasia mutated is not required for p53 induction and apoptosis in irradiated epithelial tissues. *Mol. Cancer Res.* 5, 1312–1318.
- Harvey, M., McArthur, M.J., Montgomery, C.A., Jr., Butel, J.S., Bradley, A., and Donehower, L.A. (1993). Spontaneous and carcinogen-induced tumorigenesis in p53-deficient mice. *Nat. Genet.* 5, 225–229.
- Hickson, I., Zhao, Y., Richardson, C.J., Green, S.J., Martin, N.M., Orr, A.I., Reaper, P.M., Jackson, S.P., Curtin, N.J., and Smith, G.C. (2004). Identification and characterization of a novel and specific inhibitor of the ataxia-telangiectasia mutated kinase ATM. *Cancer Res.* 64, 9152–9159.
- Hollstein, M., Sidransky, D., Vogelstein, B., and Harris, C.C. (1991). p53 mutations in human cancers. *Science* 253, 49–53.
- Honda, R., Tanaka, H., and Yasuda, H. (1997). Oncoprotein MDM2 is a ubiquitin ligase E3 for tumor suppressor p53. *FEBS Lett.* 420, 25–27.
- Jack, M.T., Woo, R.A., Hirao, A., Cheung, A., Mak, T.W., and Lee, P.W. (2002). Chk2 is dispensable for p53-mediated G1 arrest but is required for a latent p53-mediated apoptotic response. *Proc. Natl. Acad. Sci. USA* 99, 9825–9829.
- Jacks, T., Remington, L., Williams, B.O., Schmitt, E.M., Halachmi, S., Bronson, R.T., and Weinberg, R.A. (1994). Tumor spectrum analysis in p53-mutant mice. *Curr. Biol.* 4, 1–7.
- Jeffers, J.R., Parganas, E., Lee, Y., Yang, C., Wang, J., Brennan, J., MacLean, K.H., Han, J., Chittenden, T., Ihle, J.N., et al. (2003). Puma is an essential mediator of p53-dependent and -independent apoptotic pathways. *Cancer Cell* 4, 321–328.
- Jones, S.N., Hancock, A.R., Vogel, H., Donehower, L.A., and Bradley, A. (1998). Overexpression of Mdm2 in mice reveals a p53-independent role for Mdm2 in tumorigenesis. *Proc. Natl. Acad. Sci. USA* 95, 15608–15612.
- Jones, S.N., Roe, A.E., Donehower, L.A., and Bradley, A. (1995). Rescue of embryonic lethality in Mdm2-deficient mice by absence of p53. *Nature* 378, 206–208.
- Juven, T., Barak, Y., Zauberman, A., George, D.L., and Oren, M. (1993). Wild type p53 can mediate sequence-specific transactivation of an internal promoter within the mdm2 gene. *Oncogene* 8, 3411–3416.
- Kemp, C.J., Wheldon, T., and Balmain, A. (1994). p53-deficient mice are extremely susceptible to radiation-induced tumorigenesis. *Nat. Genet.* 8, 66–69.
- Khosravi, R., Maya, R., Gottlieb, T., Oren, M., Shiloh, Y., and Shkedy, D. (1999). Rapid ATM-dependent phosphorylation of MDM2 precedes p53 accumulation in response to DNA damage. *Proc. Natl. Acad. Sci. USA* 96, 14973–14977.
- Komarova, E.A., Kondratov, R.V., Wang, K., Christov, K., Golovkina, T.V., Goldblum, J.R., and Gudkov, A.V. (2004). Dual effect of p53 on radiation sensitivity in vivo: p53 promotes hematopoietic injury, but protects from gastro-intestinal syndrome in mice. *Oncogene* 23, 3265–3271.
- Lane, D.P. (1992). Cancer. p53, guardian of the genome. *Nature* 358, 15–16.
- Levine, A.J., Tomasini, R., McKeon, F.D., Mak, T.W., and Melino, G. (2011). The p53 family: guardians of maternal reproduction. *Nat. Rev. Mol. Cell Biol.* 12, 259–265.
- Lu, X., Nannenga, B., and Donehower, L.A. (2005). PPM1D dephosphorylates Chk1 and p53 and abrogates cell cycle checkpoints. *Genes Dev.* 19, 1162–1174.
- Lu, X., Ma, O., Nguyen, T.A., Jones, S.N., Oren, M., and Donehower, L.A. (2007). The Wip1 Phosphatase acts as a gatekeeper in the p53-Mdm2 autoregulatory loop. *Cancer Cell* 12, 342–354.

- Lu, X., Nguyen, T.A., Moon, S.H., Darlington, Y., Sommer, M., and Donehower, L.A. (2008). The type 2C phosphatase Wip1: an oncogenic regulator of tumor suppressor and DNA damage response pathways. *Cancer Metastasis Rev.* 27, 123–135.
- Maya, R., Balass, M., Kim, S.T., Shkedy, D., Leal, J.F., Shifman, O., Moas, M., Buschmann, T., Ronai, Z., Shiloh, Y., et al. (2001). ATM-dependent phosphorylation of Mdm2 on serine 395: role in p53 activation by DNA damage. *Genes Dev.* 15, 1067–1077.
- Momand, J., Zambetti, G.P., Olson, D.C., George, D., and Levine, A.J. (1992). The mdm-2 oncogene product forms a complex with the p53 protein and inhibits p53-mediated transactivation. *Cell* 69, 1237–1245.
- Montes de Oca Luna, R., Wagner, D.S., and Lozano, G. (1995). Rescue of early embryonic lethality in mdm2-deficient mice by deletion of p53. *Nature* 378, 203–206.
- O’Gorman, S., Dagenais, N.A., Qian, M., and Marchuk, Y. (1997). Protamine-Cre recombinase transgenes efficiently recombine target sequences in the male germ line of mice, but not in embryonic stem cells. *Proc. Natl. Acad. Sci. USA* 94, 14602–14607.
- Pellegrini, M., Celeste, A., Difilippantonio, S., Guo, R., Wang, W., Feigenbaum, L., and Nussenzweig, A. (2006). Autophosphorylation at serine 1987 is dispensable for murine Atm activation in vivo. *Nature* 443, 222–225.
- Shieh, S.Y., Ikeda, M., Taya, Y., and Prives, C. (1997). DNA damage-induced phosphorylation of p53 alleviates inhibition by MDM2. *Cell* 91, 325–334.
- Shreeram, S., Demidov, O.N., Hee, W.K., Yamaguchi, H., Onishi, N., Kek, C., Timofeev, O.N., Dudgeon, C., Fornace, A.J., Anderson, C.W., et al. (2006). Wip1 phosphatase modulates ATM-dependent signaling pathways. *Mol. Cell* 23, 757–764.
- Sluss, H.K., Armata, H., Gallant, J., and Jones, S.N. (2004). Phosphorylation of serine 18 regulates distinct p53 functions in mice. *Mol. Cell. Biol.* 24, 976–984.
- Sluss, H.K., Gannon, H., Coles, A.H., Shen, Q., Eischen, C.M., and Jones, S.N. (2010). Phosphorylation of p53 serine 18 upregulates apoptosis to suppress Myc-induced tumorigenesis. *Mol. Cancer Res.* 8, 216–222.
- Soussi, T., and Bérout, C. (2001). Assessing TP53 status in human tumours to evaluate clinical outcome. *Nat. Rev. Cancer* 1, 233–240.
- Steinman, H.A., and Jones, S.N. (2002). Generation of an Mdm2 conditional allele in mice. *Genesis* 32, 142–144.
- Stommel, J.M., and Wahl, G.M. (2004). Accelerated MDM2 auto-degradation induced by DNA-damage kinases is required for p53 activation. *EMBO J.* 23, 1547–1556.
- Vassilev, L.T., Vu, B.T., Graves, B., Carvajal, D., Podlaski, F., Filipovic, Z., Kong, N., Kammlott, U., Lukacs, C., Klein, C., et al. (2004). In vivo activation of the p53 pathway by small-molecule antagonists of MDM2. *Science* 303, 844–848.
- Vousden, K.H., and Lu, X. (2002). Live or let die: the cell’s response to p53. *Nat. Rev. Cancer* 2, 594–604.
- Wang, Y.V., Leblanc, M., Wade, M., Jochemsen, A.G., and Wahl, G.M. (2009). Increased radioresistance and accelerated B cell lymphomas in mice with Mdmx mutations that prevent modifications by DNA-damage-activated kinases. *Cancer Cell* 16, 33–43.
- Wu, X., Bayle, J.H., Olson, D., and Levine, A.J. (1993). The p53-mdm-2 autoregulatory feedback loop. *Genes Dev.* 7 (7A), 1126–1132.
- Wu, Z., Earle, J., Saito, S., Anderson, C.W., Appella, E., and Xu, Y. (2002). Mutation of mouse p53 Ser23 and the response to DNA damage. *Mol. Cell. Biol.* 22, 2441–2449.

In Vivo Imaging of Tumor-Propagating Cells, Regional Tumor Heterogeneity, and Dynamic Cell Movements in Embryonal Rhabdomyosarcoma

Myron S. Ignatius,^{1,3} Eleanor Chen,^{1,3,4} Natalie M. Elpek,² Adam Z. Fuller,^{1,3} Inês M. Tenente,^{1,3,5} Ryan Clagg,^{1,3} Sali Liu,^{1,3} Jessica S. Blackburn,^{1,3} Corinne M. Linardic,⁶ Andrew E. Rosenberg,¹ Petur G. Nielsen,¹ Thorsten R. Mempel,² and David M. Langenau^{1,3,*}

¹Department of Pathology and Center for Cancer Research

²Center for Immunology and Inflammatory Diseases

Massachusetts General Hospital, Charlestown, MA 02129, USA

³Harvard Stem Cell Institute, Boston, MA 02114, USA

⁴Department of Pathology, Brigham and Women's Hospital, Boston, MA 02115, USA

⁵Instituto de Ciências Biomédicas Abel Salazar, 4099-003 Porto, Portugal

⁶Departments of Pediatrics, Pharmacology, and Cancer Biology, Duke University Medical Center, Durham, NC 27710, USA

*Correspondence: dlangenau@partners.org

DOI 10.1016/j.ccr.2012.03.043

SUMMARY

Embryonal rhabdomyosarcoma (ERMS) is an aggressive pediatric sarcoma of muscle. Here, we show that ERMS-propagating potential is confined to *myf5*⁺ cells and can be visualized in live, fluorescent transgenic zebrafish. During early tumor growth, *myf5*⁺ ERMS cells reside adjacent normal muscle fibers. By late-stage ERMS, *myf5*⁺ cells are reorganized into distinct regions separated from differentiated tumor cells. Time-lapse imaging of late-stage ERMS revealed that *myf5*⁺ cells populate newly formed tumor only after seeding by highly migratory *myogenin*⁺ ERMS cells. Moreover, *myogenin*⁺ ERMS cells can enter the vasculature, whereas *myf5*⁺ ERMS-propagating cells do not. Our data suggest that non-tumor-propagating cells likely have important supportive roles in cancer progression and facilitate metastasis.

INTRODUCTION

Rhabdomyosarcoma (RMS) is a pediatric malignancy that shares common features with skeletal muscle arrested in embryonic development (Xia et al., 2002). The two main subtypes of pediatric rhabdomyosarcoma, embryonal RMS (ERMS) and alveolar RMS (ARMS), differ in their clinical, biological, and molecular characteristics. For example, ERMS and ARMS can be distinguished based on histology and have different long-term prognoses, with ERMS patients having better overall outcome than ARMS patients. These divergent clinical features likely reflect the use of different molecular programs that lead to transformation. For example, we have identified that the RAS pathway is active in a majority of human ERMS (Hettmer

et al., 2011; Langenau et al., 2007). By contrast, 85% of ARMS cells have recurrent chromosomal translocations that juxtapose PAX3 or PAX7 with the forkhead transcription factor (FKHR) (Xia et al., 2002). Finally, it is likely that ERMS and translocation-positive ARMS arise in different cell types that eventually undergo transformation. Keller et al. (2004) found that PAX3-FKHR+ ARMS can arise from Myf6-expressing myoblast cells but not dermamyotome or satellite cells that express Pax7. By contrast, ERMS can arise from either satellite cells or myoblasts that eventually reinstate molecular programs found in satellite cells (Rubin et al., 2011). Despite elegant studies defining possible cells of origin in RMS, identification of an ERMS-propagating cell that is required for continued tumor growth in vivo has not been described in mice or humans.

Significance

Tumor-propagating potential is not found in all malignant cells, and, in most cancers, cells with more differentiated features are largely incapable of remaking tumor and yet constitute a majority of the tumor mass. A role for differentiated malignant cells in tumor growth, including dissemination and metastasis, has not been fully explored. We find that mid-differentiated *myogenin*-positive ERMS cells lack tumor-propagating potential yet are responsible for local invasion and can enter the vasculature. Slow-moving *myf5*⁺ ERMS-propagating cells are recruited to new sites of tumor growth after seeding by differentiated ERMS cells. This finding may explain the clinical observation that *Myogenin* positivity correlates with poor clinical outcome in human ERMS and suggests that differentiated tumor cells play critical roles in metastasis.

Tumor-propagating cells have been characterized in many malignancies, and in some tumors, this potential is confined to a molecularly definable cell population that can be enriched by cell surface markers. For example, in acute myeloid leukemia, a rare CD34⁺CD38[−] cell enriches for leukemia-propagating potential while in breast cancer CD44⁺CD24^{low/−} expression is associated with tumor-propagating potential (reviewed in [Dalerba et al., 2007](#)). Molecularly defined, rare CD133⁺ tumor-propagating cells have also been identified in a subset of gliomas and exhibit striking differences in response to nitric oxide and hypoxia inducible factor signaling when compared to more differentiated tumor cells ([Eyler et al., 2011](#); [Li et al., 2009](#)). Thus, it is likely that many tumors contain hierarchically organized cell subpopulations that retain the capacity to remake tumor and yet give rise to differentiated tumor cell progeny. One might expect that selection would favor the evolution of tumors with high numbers of tumor-propagating cells at a cost of differentiated cell types. Paradoxically, however, in most malignancies, tumor-propagating cells are far less abundant than differentiated tumor cells that are incapable of remaking tumor. These data suggest that differentiated tumor cells may provide important supportive roles in overall growth and maintenance. To date, a role for differentiated, non-tumor-propagating ERMS cells has yet to be fully explored.

Stem cells often reside in distinct niches in normal tissue, and their functions are exquisitely controlled by local factors secreted by supporting cells. For example, hematopoietic stem cells (HSCs) have been shown to home to niches within the calvarium that are tightly associated with osteoblasts ([Lo Celso et al., 2009](#)). These and other niche-associated cells presumably provide paracrine-signaling factors to recruit and maintain these cells in a specific niche. Unlike other tissues, the muscle stem cell niche is defined by juxtaposition of satellite cells next to differentiated muscle fibers, and their numbers and differentiation capacity are controlled by complex signaling pathways regulated by mature muscle cells (reviewed in [Bentzinger et al., 2012](#)). Despite a large body of data defining stem cell niches in normal tissue, few studies have identified tumor-specific niches and/or regions of compartmentalized tumor cell function and fewer still have used microscopic imaging to directly visualize tumor-propagating cells within live animals. In one example, [Sipkins et al. \(2005\)](#) used a combination of multiphoton and confocal microscopy to image the HSC niche in the calvarium of mice and demonstrated that these sites can attract multiple tumor cell types; however, it is unknown if these malignant cells are capable of reinitiating tumors. In ERMS, as with most solid tumors, it is unknown whether tumor-propagating cells reside in distinct regions within the tumor mass and whether the more differentiated cells play a role in promoting tumor progression.

Here, we utilize a transgenic zebrafish model of ERMS to identify the tumor-propagating cell in this disease and to define the functional consequences of tumor cell heterogeneity within live animals. Because ERMS cell subpopulations can be fluorescently labeled based on myogenic factor expression, ERMS cell subtypes can be visualized in live animals and the processes of cell growth, division, and local dissemination can be visualized as dynamic processes in live animals. Our data provide an explanation for the large number of non-tumor-propagating cells in

established cancers and reveal an important supportive role for differentiated tumor cell types in local dissemination and metastasis.

RESULTS

Imaging Distinct Stages of ERMS Growth

Externally visible ERMS can develop as early as 10 days of life in zebrafish injected with *rag2-KRASG12D* ([Langenau et al., 2007](#)), and >80% of ERMS develop in the tail musculature ($n > 50$). To assess how tumors initiate and evolve in zebrafish ERMS, we injected α -actin-GFP transgenic zebrafish at the one-cell stage of development with *rag2-dsREDexpress* and *rag2-KRASG12D* (Figures 1A–1F), facilitating imaging of ERMS cells in relation to normal muscle. Microinjection of multiple transgenes into one-cell-stage animals leads to cointegration and coexpression in animals that develop ERMS ([Langenau et al., 2008](#)). This approach provides a robust method to create mosaic transgenic animals with fluorescently labeled ERMS cell subpopulations ([Langenau et al., 2007](#)).

Sequential confocal imaging over several days showed that ERMS forms in a choreographed and stereotypical manner (Figures 1A–1F and 1J–1M). Specifically, dsRed⁺ ERMS mononuclear cells arise at the extreme outer borders of the myotome segments and move toward the midline where they are initially unable to bypass the horizontal myosepta—a single cell layer that separates myotome segments (Figure 1A; stage 1, $n = 7$). After several days, a subset of cells cross the horizontal myosepta and take up residence between normal muscle fibers within the newly colonized myotome segment (stage 2; Figures 1B and 1C; $n = 5$). Differentiated ERMS cells that express both *rag2-dsREDexpress* and α -actin-GFP can move laterally into neighboring muscle segments by transiting through the collagen matrix of the myoseptum ($n = 6$; Figures 1D–1F; [Movie S1](#) available online) or stream into new myotome segments by growing past the edge of myoseptum ($n = 3$, early stage 3). The collagen matrix of the muscle myoseptum is a cell-impermeable barrier that is the site of muscle attachment in teleost fish and is similar in function to tendons in mouse and humans. Late-stage ERMS cells undergo rapid loss of fibers, breakdown of normal muscle architecture including collagen remodeling, and development of mononuclear tumor cells, reminiscent of the spindle variant of human ERMS.

Neovascularization is a hallmark of cancer and an ideal surrogate for assessing tumorigenicity. To assess when KRASG12D-expressing cells are transformed, we monitored neovascularization in *flil1-GFP* transgenic animals that were injected at the one-cell stage of life with *rag2-KRASG12D* and *rag2-dsREDexpress*. Animals were monitored for tumor growth by confocal microscopy beginning at 10 days of life ($n = 22$; Figures 1G–1I). ERMS at stage 1 failed to recruit new vasculature ($n = 0$ of 3), but stage 2 and early stage 3 ERMS had begun to recruit new vasculature ($n = 8$ of 8; Figure 1H) with new branches arising from both the intersegmental vessels and vertebral artery. By late stage 3, ERMS developed intricate networks of new vessels ($n = 11$ of 11; Figure 1I). Our imaging studies define distinct stages of ERMS growth and suggest that RAS-expressing cells become fully transformed by stage 2 of tumor development (Figures 1J–1M).

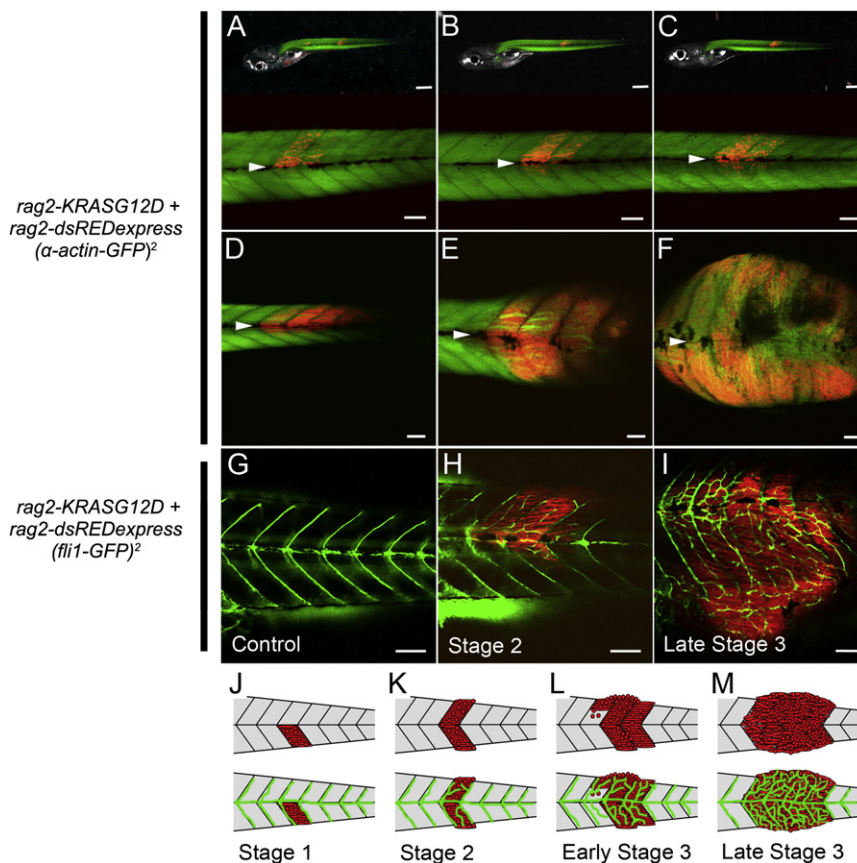


Figure 1. Visualizing Distinct Stages of Embryonal RMS Growth

(A–F) *rag2-dsRED*-labeled ERMS arising in *α-actin-GFP* transgenic zebrafish. The same animal imaged at 6, 9, and 12 days postfertilization (dpf) is shown in (A), (B), and (C), respectively. A representative zebrafish where *dsRED*⁺ ERMS cells have already bypassed the horizontal myoseptum and migrated into new segments that were previously free of tumor (F, stage 3) at 13, 18, and 24 dpf is shown in (D), (E), and (F), respectively. The horizontal myoseptum is denoted by white arrows.

(G–I) *fli1-GFP* transgenic control animal (G) compared with a *rag2-dsRED*-labeled ERMS arising in *fli1-GFP* transgenic zebrafish at early stage 2 (H) or a late stage 3 (I).

(J–M) Schematic of stages of ERMS growth.

Scale bars in the upper panels of (A) through (C), 500 μ m. Scale bars in the lower panels of (A) through (C) and in (D) through (I), 100 μ m.

See also Movie S1.

Identification of Molecularly Distinct Fluorescent-Labeled ERMS Cell Subpopulations

Previous experiments in zebrafish have identified an ERMS cell subpopulation that had superior tumor-propagating potential when compared to other tumor-derived cells. This ERMS-propagating cell was *rag2-dsRED*^{express}/*α-actin*^{-negative} and expressed high levels of *myf5*, *c-met*, and *m-cadherin*—markers of satellite and early muscle progenitor cells (Langenau et al., 2007). *MYF5* is highly upregulated in human ERMS compared to both translocation positive ARMS and normal muscle (Zibat et al., 2010) and in comparing zebrafish ERMS to normal muscle (Langenau et al., 2007). To directly assess whether *myf5* labels distinct ERMS cell subpopulations, *myf5-GFP/myosin light chain 2-mCherry* (*myl2*) syngeneic animals were created by four rounds of outcrossing to CG1 syngeneic animals (Smith et al., 2010) and injected at the one-cell stage with *rag2-KRASG12D*. *myf5-GFP* transgenic animals exhibit green fluorescent protein (GFP) expression in early somitogenesis and later in satellite cells and early muscle progenitor cells (Chen et al., 2007; Seger et al., 2011) while the *myl2* promoter drives expression in differentiated muscle cells (Ju et al., 2003; Smith et al., 2010). Fluorescent-labeled ERMS cell subpopulations were isolated from double transgenic animals by fluorescence-activated cell sorting (FACS). Reanalysis of sorted cells by FACS confirmed that ERMS contained four distinct populations of cells (purity > 87% and viability > 97%).

To verify that discrete fluorescent-labeled ERMS cell subpopulations were molecularly distinct, sorted cell populations were

assessed for gene expression differences based on microarray (Figure 2A; Table S1) and real-time PCR (Figures 2B and S1). Gene expression analysis was completed on FACS-sorted ERMS cells derived from serially passaged tumors, ensuring that fluorescent-labeled cells were tumor derived. Microarray analysis confirmed that each cell subpopulation exhibited wide differences in gene expression. Subsequent real-time PCR analysis established that the *myf5-GFP+/myl2-mCherry-negative* cells expressed high levels of *myf5*, *c-met*, and *m-cadherin* but not *pax7a*, *pax7b*, or differentiated markers (Figures 2B and S1). By contrast, *myl2-mCherry+* ERMS cells expressed high levels of mature muscle markers including *myod*, *myogenin*, *troponin I fast-twitch isoform 2* (*tnni2a*), *α-actin 1b* (*acta1b*), *ventricular myosin heavy chain-like* (*vmhcl*), *actin-related protein 2/3 complex subunit 5B* (*arpc5b*), *carboxypeptidase vitellogenin-like* (*cpvl*), and *chemokine (C-X-C motif) receptor 4b* (*cxcr4b*). Finally, the double-negative cell population comprised predominantly blood cells that express *myeloid-specific peroxidase* (*mpx*) and *lymphocyte-specific protein tyrosine kinase* (*lck*). Our data confirm that fluorescent-labeled ERMS cell subpopulations can be prospectively isolated to relative purity following FACS and are molecularly distinct.

Given that FACS could identify unique ERMS cell subpopulations that exhibited wide differences in gene expression, we questioned whether these cells also differ in rates of proliferation and cellular turnover. Proliferation was assessed at 6 hr following intraperitoneal injection of EDU into ERMS-affected animals (Figures 2C–2E and S1). *myf5-GFP+/myl2-mCherry-negative* cells (24.1% \pm 4.8%) incorporated EDU over a 6 hr pulse, whereas differentiated ERMS cells that express *myl2-mCherry* were far less proliferative (8.9% \pm 5.0%; $p < 0.00001$). By contrast, following 3-day administration of EDU, all fluorescent-labeled ERMS cell subfractions exhibited equal proliferative capacity, suggesting that *myf5-GFP+/myl2-mCherry-negative*

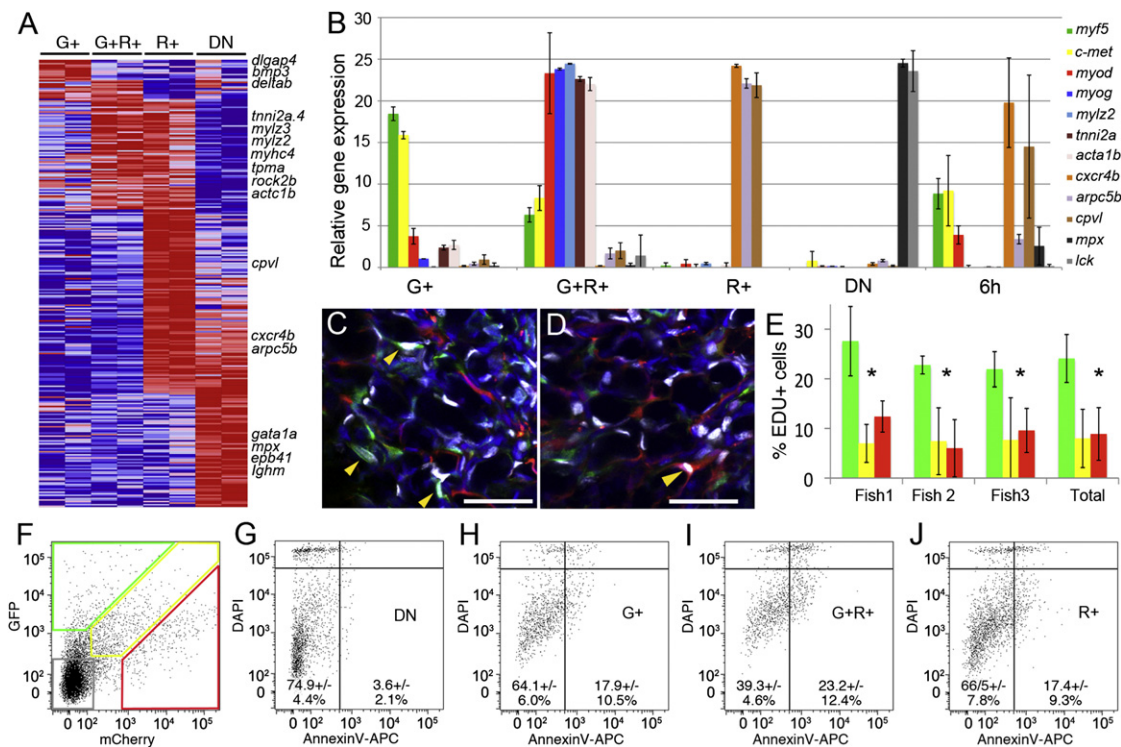


Figure 2. Fluorescent Transgenic Approaches Identify Discrete and Molecularly Definable ERMS Cell Subpopulations in *myf5-GFP/myl2-mCherry* Transgenic Fish

(A) Heat map showing differential gene expression between FACS-sorted ERMS cell subpopulations isolated from serially passaged *myf5-GFP/myl2-mCherry* ERMS (microarray log fold-change > 1.5). *myf5-GFP+/myl2-mCherry-negative* (G+), *myf5-GFP+/myl2-mCherry+* (G+R+), *myf5-GFP-negative/myl2-mCherry+* (R+), and double negative (DN).

(B) Quantitative real-time PCR of sorted ERMS cell subpopulations. Expression values, ± 1 SD.

(C and D) Confocal images of EDU-stained sections from serially passaged *myf5-GFP+/myl2-mCherry+* ERMS. Tumor regions with large numbers of either *myf5-GFP+* (C) or *myl2-mCherry+* ERMS cells (D). Blue denotes DAPI+ nuclei, and white denotes EDU+ nuclei. Yellow arrows indicate EDU-labeled cells. Scale bar, 25 μ m.

(E) Quantification of EDU incorporation over a 6 hr EDU pulse. Data for *myf5-GFP+/myl2-mCherry-negative* ERMS cells are denoted by green bars, data for *myf5-GFP+/myl2-mCherry+* cells are indicated by yellow bars, and data for *myf5-GFP-negative/myl2-mCherry+* cells are indicated by red bars. Three individual tumors shown as well as cumulative data across all tumors (Total). * $p < 0.00001$. Error bars, ± 1 SD.

(F) FACS plot of serially passaged *myf5-GFP/myl2-mCherry* ERMS.

(G–J) Gated ERMS cells assessed for DAPI and AnnexinV-APC staining (double negative, DN) (G); *myf5-GFP+/myl2-mCherry-negative* (G+) (H); *myf5-GFP+/myl2-mCherry+* (G+R+) (I); and *myf5-GFP-negative/myl2-mCherry+* (R+) (J). Live cells are shown within the DAPI-negative/AnnexinV-negative gates.

See also Figure S1 and Table S1.

cells divided and differentiated over this time (data not shown). In addition to striking differences in cell proliferation between ERMS cell subpopulations, *myf5-GFP+/myl2-mCherry+* cells had higher levels of apoptotic cellular turnover when compared with *myf5-GFP+/myl2-mCherry-negative* and *myf5-GFP-negative/myl2-mCherry+* cells ($p < 0.01$, Fisher's exact test; Figures 2F–2J). Taken together, our fluorescent transgenic approach identifies unique ERMS cell subpopulations that have different fluorescent reporter expression, divergent gene expression profiles, and varied capacities for proliferation and apoptosis.

***myf5-GFP+* Cells Are the ERMS-Propagating Cell Population**

To assess if *myf5-GFP* transgene expression enriches for ERMS-propagating potential, cells were isolated from transplant animals that developed *myf5-GFP+/myl2-mCherry+* ERMS (Figures 3A–3G) and subjected to two rounds of FACS in the

presence of propidium iodide or DAPI to isolate highly purified and viable cells (Figures 3H–3K; 87.7%–99.7% purity and >98% viability). ERMS cell subpopulations were introduced into CG1 syngeneic recipient animals at limiting dilution (Figure 3L–3R), and animals were assessed for engraftment from 10 to 120 days posttransplantation (Table 1). All animals developed ERMS before 45 days posttransplantation, confirming that slower cycling ERMS-propagating cell types would not be missed in our analysis. In three ERMS tumors tested, the tumor-propagating activity was confined to the *myf5-GFP+/myl2-mCherry-negative* cell subpopulation (Table 1), with an average frequency of 1 in 146 cells capable of reinitiating tumors in recipient animals (range 1 in 87–245, 95% confidence interval). By contrast, only 1 in 4,206 *myf5-GFP+/myl2-mCherry+* cells were capable of inducing tumors (range 1 in 1,550 to 11,409, 95% confidence interval, $p = 3.38 \times 10^{-15}$ when compared to ERMS-propagating activity in *myf5-GFP+/myl2-mCherry-negative* cells). Of 61 animals, none

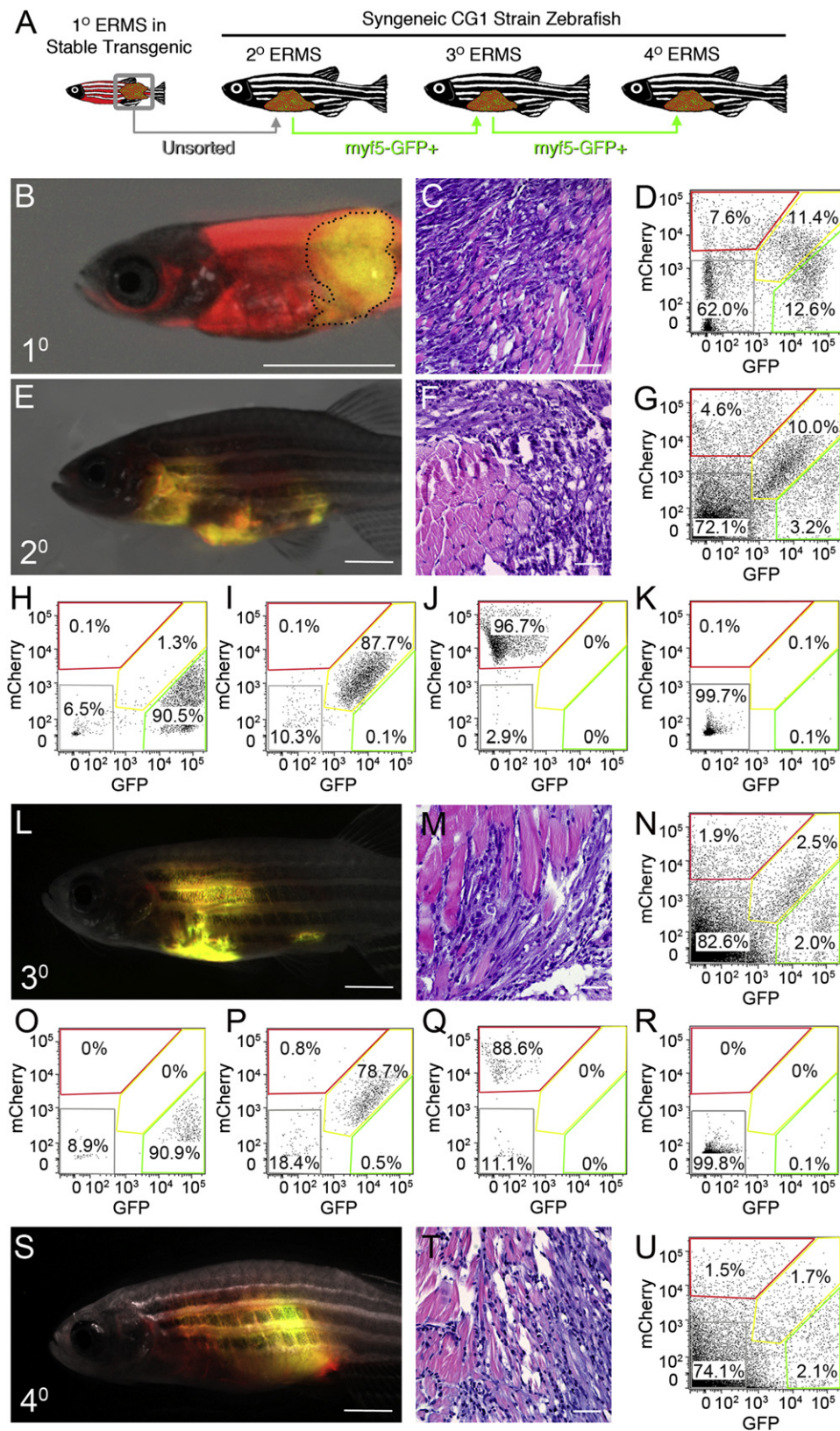


Figure 3. ERMS-Propagating Cells Express *myf5*-GFP but Not the *myl2*-mCherry Differentiated Muscle Marker

(A) Schematic of experimental design.

(B–D) A primary ERMS arising in syngeneic *myf5*-GFP/*myl2*-mCherry transgenic zebrafish (35 dpf). Broken black line denotes tumor area.

Table 1. Limiting Dilution Cell Transplantation Identifies that *myf5-GFP+/myl2-mCherry-negative* Cells Are the ERMS-Propagating Cells

ERMS #1 2° Transplants						3° Transplants
Cell #	G+	G+R+	R+	Neg		G+
1,000	6 of 6	2 of 7	0 of 6	0 of 7		6 of 6
10	5 of 9	0 of 9	0 of 8	0 of 10		7 of 8
10	0 of 8	0 of 8	0 of 9	0 of 7		0 of 10
TPC #	1 in 140**	1 in 3,461	NA	NA		1 in 67
95% CI	59–329	872–13,740	NA	NA		31–143
ERMS #2 2° Transplants						
Cell #	G+	G+R+	R+	Neg		
1,000	6 of 6	0 of 6	0 of 6	0 of 6		
10	4 of 7	2 of 10	0 of 10	0 of 10		
10	1 of 8	0 of 9	0 of 10	0 of 8		
TPC #	1 in 109**	1 in 3,495	NA	NA		
95% CI	44–270	808–15,120	NA	NA		
ERMS #3 2° Transplants						
Cell #	G+	G+R+	R+	Neg		
1,000	2 of 3	0 of 2	0 of 3	0 of 4		
10	8 of 9	0 of 8	0 of 8	1 of 8		
10	1 of 8	0 of 9	0 of 9	0 of 9		
TPC #	1 in 159**	NA	NA	1 in 4,840		
95% CI	63–401	NA	NA	632–37,094		

Asterisks denote significant differences in tumor-propagating cell number (TPC #) between *myf5-GFP+/myl2-mCherry-negative* and double-positive ERMS cells (***p* < 0.00001). Neg, negative; NA, not applicable; 95% CI, 95% confidence interval.

engrafted disease from terminally differentiated *myf5-GFP-negative/myl2-Cherry+* cells (lower bound for ERMS-propagating potential was 1 in >5,969 cells). In total, we observed a remarkable 28- to >40-fold enrichment of tumor-propagating potential within our *myf5-GFP+/myl2-mCherry-negative* cell type when compared with other sorted ERMS cell subpopulations. Similar results were also observed in primary ERMS. Specifically, three primary ERMS tumors were isolated from 20- to 30-day-old larval zebrafish, pooled, and fluorescent-labeled ERMS cell subpopulations were isolated by FACS. Of eight animals, three engrafted disease from 10² *myf5-GFP+/myl2-mCherry-negative* cells, whereas the remaining ERMS cell subpopulations could not transfer disease at this cell dose (0 of 23, purity 83%–98% and viability > 98.6%, *p* = 0.012, Fisher's exact test). These results further support our finding that the *myf5-GFP+/myl2-mCherry-negative* population is highly enriched for ERMS-propagating activity.

To assess the long-term tumor-propagating potential of the *myf5-GFP+/myl2-mCherry-negative* ERMS cells, cells were re-isolated from transplant recipient animals (Figure 3N) and introduced into CG1, syngeneic recipient animals (>78.9% purity and 96% viable; Figures 3O–3R). Again, the *myf5-GFP+/myl2-mCherry-negative* cell subpopulation was capable of remaking ERMS (Figure 3S–3U; Table 1). Histological analysis showed that primary and serially transplanted ERMS arising from *myf5-GFP+/myl2-mCherry-negative* cell populations have similar morphology and overall proportions of fluorescent-labeled ERMS cell subpopulations (Figures 3C, 3D, 3F, 3G, 3M, 3N, 3T, and 3U).

Visualizing *myf5-GFP+* ERMS-Propagating Cells In Vivo

To assess whether *myf5-GFP+* ERMS cells could be directly visualized in live animals, *rag2-dsREDexpress* and *rag2-KRASG12D* were coinjected into one-cell-stage *myf5-GFP* transgenic animals and assessed by confocal microscopy. Discrete *myf5-GFP+* tumor cells could be readily identified by confocal imaging with a majority of *myf5-GFP+* ERMS cells coexpressing both GFP and dsREDexpress (97.5 ± 2.9%; *n* = 568 cells counted in three animals). Moreover, *myf5-GFP+* early muscle progenitor cells from control animals were relatively rare (*n* = 3 [animals]; 2.3 ± 2.3 cells per imaging field), whereas *myf5-GFP+* cells were abundant in ERMS (*n* = 3; 194.2 ± 23.7 cells per field, *t* test, *p* = 0.0002). Taken together, our data suggest that a vast majority of *myf5-GFP+* cells contained within the boundaries of the ERMS mass are tumor derived.

To further refine the ERMS cell subpopulations for imaging studies, triple fluorescent transgenic ERMS animals were created by microinjecting *myogenin-H2B-RFP*, *myl2-lyn-cyan*, and *rag2-KRASG12D* into one-cell-stage *myf5-GFP* transgenic animals (Figures 4A–4C). Histone fusion proteins are long lived and confined to the nucleus, whereas *lyn-cyan* encodes for membrane localized blue fluorescent protein. Because transgenes cointegrate as concatamers (Langenau et al., 2008), ERMS cells coexpress all three transgenes and label distinct tumor cell compartments associated with stages of muscle development (Figure S2). In normal development, *myf5* is expressed in satellite cells and early muscle progenitor cells, *myogenin* is expressed in committed, mid-differentiated muscle myoblasts, and *myl2* is expressed in differentiated myoblasts. Transgenic reporters have been described for all three of these promoters, and each drives expression within the correct cellular compartments during normal muscle development (Chen et al., 2007; Du et al., 2003; Ju et al., 2003). Moreover, gene expression studies confirm that these promoters drive correct tissue-specific gene expression in ERMS (Figure S2), and additional cell transplantation experiments establish that *myf5-GFP+/myogenin-negative* cell types exclusively retain ERMS-propagating potential (Figure S2). For example, 4 of 18 animals engrafted ERMS from 10² *myf5-GFP+/myogenin-H2B-RFP-negative* sorted ERMS cells

(E–G) Fluorescent-labeled ERMS engraft into syngeneic secondary recipient animals when transplanted with unsorted primary ERMS cells.

(H–K) FACS plots of fluorescent-labeled ERMS cells isolated from secondary recipient fish following two rounds of FACS.

(L–R) Transplantation of *myf5-GFP+/myl2-mCherry-negative* FACs sorted cells induced ERMS in tertiary transplant animals (L–R) and quaternary recipients (S–U).

Hematoxylin- and eosin-stained sections (C, F, M, and T) and FACS (D, G, N, and U) of primary and serially passaged ERMS. Scale bars, 2 mm (for B, E, L, and S) and 100 μm (for C, F, M, and T).

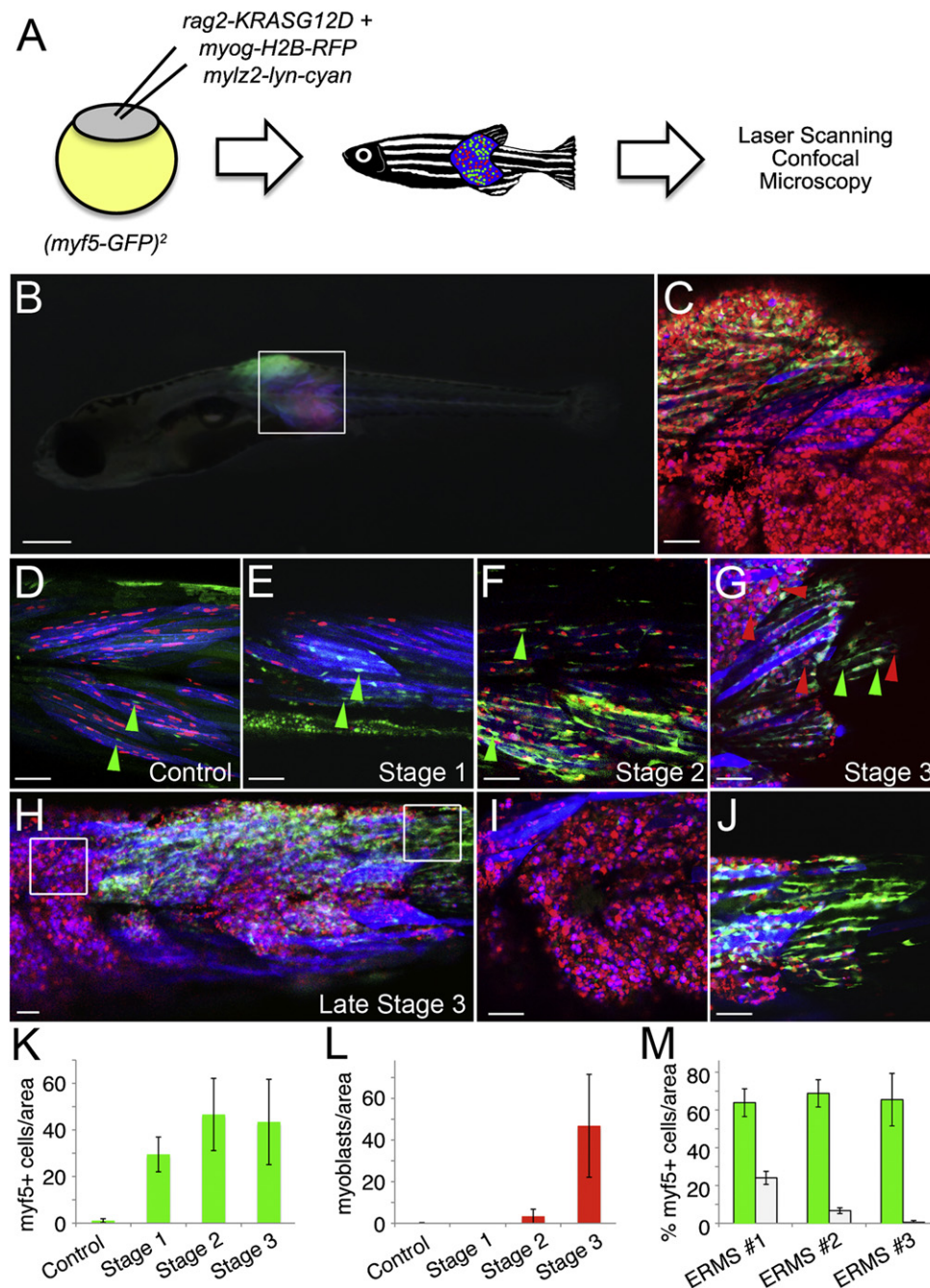


Figure 4. *myf5-GFP*⁺ ERMS-Propagating Cells Are Dynamically Reorganized during Tumor Growth

(A) Schematic of the experimental design.

(B) A *myf5-GFP* transgenic animal injected at the one-cell stage of life with *rag2-KRASG12D*, *myogenin-H2B-RFP*, and *mylz2-lyn-cyan* with triple fluorescent-labeled ERMS at 16 days of life.

(C) A merged confocal image of the boxed region shown in (B).

(D) Control *myf5-GFP* transgenic animal injected with *myogenin-H2B-RFP* and *mylz2-lyn-cyan*. *myf5-GFP*⁺ muscle precursor cells are denoted by green arrowheads.

(E–G) Representative image of an ERMS-affected zebrafish labeled with *myf5-GFP*, *myogenin-H2B-RFP*, and *mylz2-lyn-cyan* at stages 1, 2, and 3, respectively. Green arrowheads denote *myf5-GFP*⁺ cells, whereas red arrowheads denote mononuclear *myogenin-H2B-RFP*⁺ ERMS cells.

(H) Late stage 3 ERMS from a triple fluorescent-labeled animal.

(I and J) Boxed regions in (H) imaged at higher magnification show regional partitioning of differentiated cells (I) compared with *myf5-GFP*⁺ ERMS-propagating cells (J).

(K) Quantification of *myf5-GFP*⁺ cells during stages of ERMS growth when compared to control animals.

(L) Quantification of mononuclear *myogenin-H2B-RFP*⁺ cells during stages of ERMS growth when compared to control animals.

(68.5% purity, 99.8% viable), whereas *myogenin-H2B-RFP*+ cell types could not induce tumors, regardless of whether they expressed *myf5-GFP* ($n = 0$ of 32, $p = 0.013$, Fisher's exact test).

Confocal imaging of fluorescent-transgenic ERMS fish that express *myf5-GFP/myogenin-H2B-RFP/myl2-lyn-cyan* easily identified *myf5-GFP*+ cells, of which a small subset coexpress *myogenin-H2B-RFP* (Figure 4C). Some *myogenin-H2B-RFP*+ cells with nuclear fluorescent protein expression fail to express either *myf5-GFP* or *myl2-lyn-cyan*, indicating that these cells are most similar to midmyoblast stages. Gene expression studies confirm that *myogenin*-promoter expression drives H2B-fluorescent protein expression in a subset of myosin-heavy-chain-expressing muscle cell populations, implying that these represent differentiated cell types (Figure S2). Nearly all *myl2-lyn-cyan*+ cells coexpress *myogenin-H2B-RFP* ($99.5\% \pm 1\%$; $n = 8$ ERMS, $n > 1,700$ cells counted), reflecting that H2B-fluorescent protein expression persists in more differentiated ERMS cells.

***myf5-GFP*+ cells Are Reorganized into Discrete Compartments during Late-Stage Tumor Growth**

We next wanted to define the location of ERMS cell subpopulations during various stages of tumor growth. *myf5-GFP* transgenic animals were injected with *rag2-KRASG12D*, *myogenin-H2B-RFP*, and *myl2-lyn-cyan* and imaged by confocal microscopy starting at 10 days of life. Stage 1 ERMS exhibited greatly expanded numbers of *myf5-GFP*+ cells when compared to control animals and were confined to regions immediately adjacent to muscle fibers (Figures 4D–4G and 4K). Mononuclear *myogenin-H2B-RFP*+ and double-positive *myogenin-H2B-RFP*+/*myl2-lyn-cyan*+ ERMS cells were not observed in stage 1 ERMS; however, they were detected by stage 2 and increased in number as tumors progressed to stage 3 (Figures 4F–4I and 4L). By late stage 3 ERMS, *myf5-GFP*+ cells lost fiber contacts and began to populate discrete portions of the tumor that were physically separated from more differentiated *myogenin-H2B-RFP*- and *myl2-lyn-cyan*-expressing ERMS cells (Figures 4H–4J and 4M). The *myf5-GFP*+ cells were often located within different myotome segments compared to differentiated ERMS cell subpopulations; however, regional partitioning of cells based on differentiation status was also observed within a single myotome segment and in transplanted animals (Figure S2), confirming that compartmentalization did not result from physiological constraints imposed during development but rather was an intrinsic property of ERMS growth.

Human ERMS Cells Are Also Compartmentalized Based on Myogenic Factor Expression

To assess whether human RMS cells also contain distinct regions of tumor cells based on myogenic factor expression, primary human ERMS and xenografted human ERMS derived from RD and SMS-CTR cell lines (Linardic et al., 2005) were assessed for myogenic marker expression, including Myogenin,

PAX7, and MYOD. Distinct regions of high and low Myogenin-expressing cells were seen in a vast majority of primary tumor samples ($n = 12$ of 14, $p < 0.03$, Student's *t* test) and were present in all xenograft tumors ($n = 7$, six regions per tumor, $p < 0.02$, Student's *t* test; Figure 5 and Figure S3; Table S2). By contrast, most ARMS cells expressed Myogenin, and its expression was not confined to specific areas within the tumor mass ($n = 10$; range = 79%–99%), suggesting that regional partitioning of tumor cells based on Myogenin expression is specific to ERMS. We also stained four primary human ERMS tumors for PAX7 and identified regions of high and low expression in two of the four tumors. In one ERMS sample, expression was diffuse while the other tumor was PAX7 negative, indicating that not all primary ERMS cells express PAX7. Unfortunately, MYF5 antibodies have not been developed to detect human protein within paraffin-embedded sections, precluding analysis of less differentiated regions contained within the tumors.

***myogenin*+ ERMS Cells Are Highly Migratory and Precede the Recruitment of *myf5*+ ERMS-Propagating Cells into Newly Colonized Areas of Growth**

Having established that the *myf5-GFP*-expressing ERMS cell population contains tumor-propagating activity, we wanted to assess if these cells also promote invasive tumor growth. Multiphoton intravital microscopy recordings from *myf5-GFP/myogenin-H2B-RFP* or *myf5-GFP/myogenin-H2B-Amcyan* transgenic tumor zebrafish revealed that *myf5-GFP*+ single-positive ERMS cells were largely stationary and displayed only confined crawling movements (Figures 6A–6F and S4; Movies S2, S3, S4, and S5). In contrast, *myogenin*+ ERMS cells were robustly migratory and had the ability to invade across myotome segments through a normally impenetrable collagen matrix. Cells that expressed lower amounts of the H2B-fluorescent fusion protein were orderly arranged along the direction of muscle fibers, had uniform nuclear shape, and did not show any motility (Movies S2 and S3), suggesting that these were differentiated tumor cells of which a subset had undergone fusion (Figure 6F, right).

ERMS cell subpopulations also differ in their proliferative capacity. Primary ERMS cells from *myf5-GFP+/myogenin-H2B-RFP*+ animals were pulsed with EDU for 6 hr and then sectioned and assessed for EDU incorporation (Figures 6G–6I). *myf5-GFP*+ ERMS cells were highly proliferative ($39.4\% \pm 9.4\%$; $n = 3$), whereas *myf5-GFP-negative/myogenin-H2B-RFP*+ cells rarely proliferated ($2.6\% \pm 3.8\%$; $n = 3$, $p = 0.0001$). In vivo multiphoton imaging of transplant and primary ERMS confirmed that *myf5-GFP+/myl2-negative* ERMS-propagating cells are highly proliferative, with 27 of 90 GFP+ cells dividing into two daughter cells ($n = 3$ tumors). Multiphoton imaging revealed that resting *myf5-GFP*+ ERMS cells are elongated (Figure 6J) and then round up in shape just prior to cell division (Figure 6K). Following this dynamic shape change, *myf5-GFP*+ ERMS cells quickly divide

(M) Quantification of regional compartmentalization of ERMS cells based on differentiation status in late stage 3 tumors ($n = 3$). Green bars denote regions that contain higher percentages of *myf5-GFP*+ ERMS-propagating cells compared to white bars where *myf5-GFP*+ cells are less abundant and conversely more differentiated.

Error bars in (K–M), ± 1 SD. Scale bar, 500 μm for (B) and 50 μm for (C–J).

See also Figure S2.

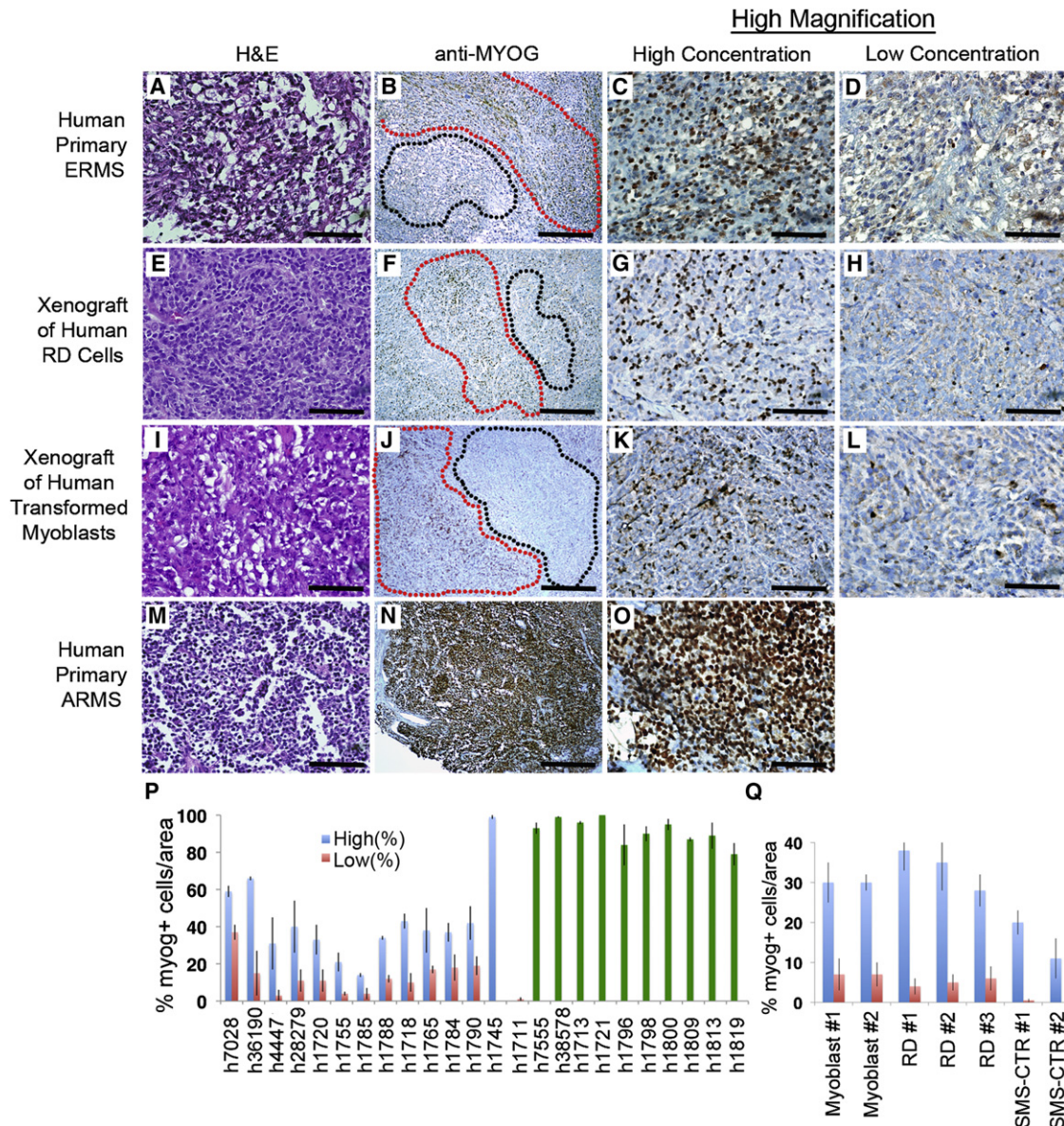


Figure 5. Human Embryonal RMS Exhibit Regional Portioning of Cells Based on Myogenic Factor Expression

(A–D) Primary human ERMS.

(E–L) RD human cell lines (E–H) or human RAS-transformed myoblasts (I–L) introduced into SCID/*beige* mice.

(M–O) Primary human ARMS. Hematoxylin/Eosin-stained sections (A, E, I, and M) and anti-Myogenin immunohistochemistry performed on adjacent sections (B, F, J, and N). Regions containing high numbers of Myogenin+ cells are denoted by red outline, while regions with low numbers of Myogenin+ cells are denoted by black outline (B, F, and J). ARMS did not show regional portioning based on Myogenin staining (N). Magnified views of areas with high concentrations of Myogenin+ cells (C, G, K, and O) or areas with low or absent expression (D, H, and L).

(P–Q) Quantification of regional compartments in primary and metastatic human RMS (P) and in mice xenografted with human RD and SMS-CTR ERMS cells and human RAS-transformed myoblasts (myoblasts, in Q). Numbers in (Q) denote tumors arising in separate animals. Blue bars denote areas with high percentages of Myogenin+ cells compared to areas with low numbers of cells (red bars). Green bars denote diffuse and ubiquitous expression of Myogenin within ARMS. Error bars, ± 1 SD. Scale bars, 50 μ m (for A, C–E, G–I, K–M, and O) and 200 μ m (for B, F, J, and N).

See also Figure S3 and Table S2.

into two GFP-labeled daughter cells (Figures 6L–6M). Subsequently, these daughter cells begin to reacquire parental morphology (Movie S6), reminiscent of normal *myf5-GFP*+ muscle precursors. By contrast, 0 of 90 *myf5-GFP*+ cells proliferated over this time, regardless of whether they expressed *myf5-GFP*.

To further visualize the dynamic movements of ERMS cells in vivo, late stage 3 triple transgenic ERMS affected animals were serially imaged over 16 hr to capture cell movements (Figures 7A–7H; Movie S7). As was seen in our multiphoton imaging, *myf5-GFP*+ cells that lack differentiated marker

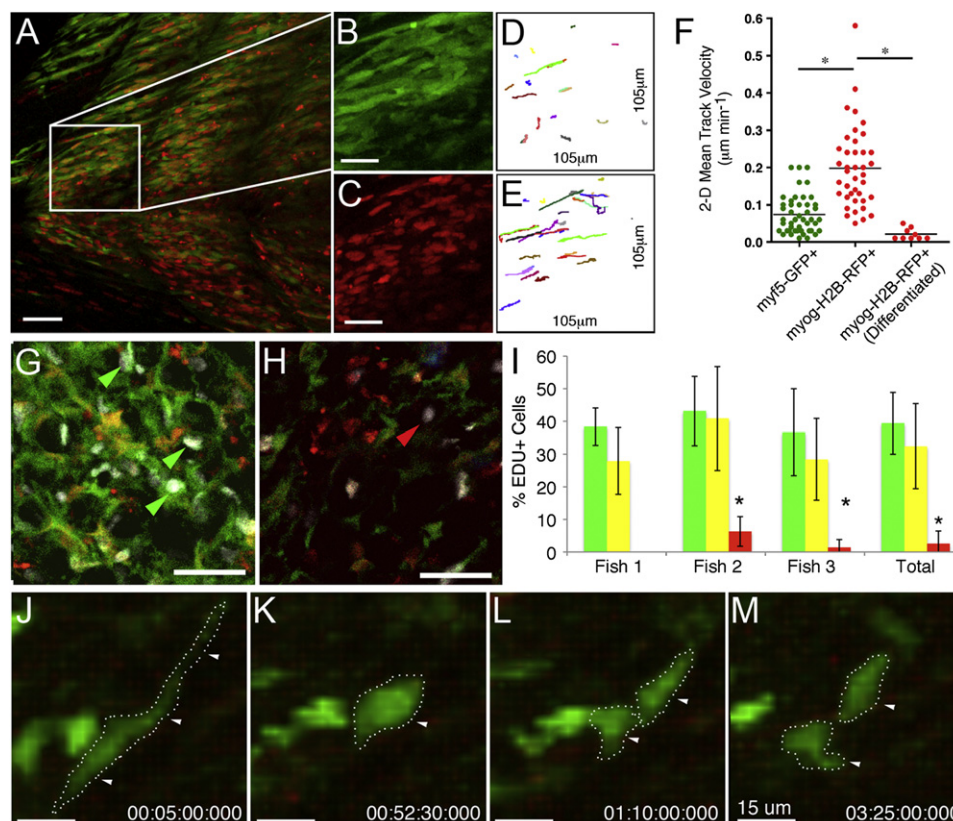


Figure 6. *myf5-GFP*⁺ ERMS-Propagating Cells Are Slow Moving but Highly Proliferative while *myogenin-H2B-RFP*⁺ Cells Do Not Divide but Are Highly Migratory

(A–E) Multiphoton recording of a stage 3 ERMS arising in *myf5-GFP*/*myogenin-H2B-RFP* transgenic zebrafish (B and C) Magnified view of the boxed region in (A) showing *myf5-GFP*⁺ (B) or *myogenin-H2B-RFP*⁺ ERMS cells (C).

(D and E) Tracks of cell movement over the 6.7-hr observation period. The same areas are shown as in (B) and (C), respectively.

(F) Mean track velocities of representative cell types contained within the tumor mass. **p* < 0.001.

(G and H) EDU staining of double transgenic *myf5-GFP*⁺/*myogenin-H2B-RFP*⁺ primary zebrafish ERMS (35 dpf). Confocal image of a tumor section with high numbers of *myf5-GFP*⁺ ERMS cells (G) compared to a section with high numbers of *myogenin-H2B-RFP*⁺ cells (H). White denotes nuclei that have incorporated EDU. EDU incorporation into *myf5-GFP*⁺ or *myogenin-H2B-RFP*⁺ ERMS cells denoted by green or red arrows, respectively.

(I) Quantification of proliferation over the 6 hr EDU pulse. *myf5-GFP*⁺/*myogenin-H2B-RFP*⁻ (green bars), double positive (yellow bars), and *myf5-GFP*⁻/*myogenin-H2B-RFP*⁺ (red bars). Error bars, ± 1 SD. Asterisk denotes significant differences, **p* = 0.0001.

(J–M) Static images of a *myf5-GFP*⁺ ERMS cells dividing. Scale bars, 50 μ m (for A, G, and H), 25 μ m (for B–E), and 15 μ m (for J–M).

See also Figure S4 and Movies S2, S3, S4, S5, and S6.

expression move only locally within the tumor and exhibit regional crawling movements, whereas *myogenin-H2B-RFP*⁺/*myl2-lyn-cyan*⁻ cells are highly motile and could be easily visualized migrating into adjacent nonaffected normal tissue (Figures 7A–7D; Movie S7). By contrast, differentiated ERMS cells that express *myogenin-H2B-RFP* and *myl2-lyn-cyan* are largely stationary.

To investigate which ERMS cells were the first to migrate into unaffected tissue, we conducted serial imaging experiments over longer observation intervals, focusing on regions that were adjacent to expanding tumor. Serial confocal imaging of fluorescent ERMS fish over several days revealed that *myogenin-H2B*⁺ ERMS cells precede the recruitment of *myf5-GFP*⁺ cells into newly colonized areas of tumor growth (*n* = 7; Figures 7I, 7J, and S4). Not only do fluorescent-labeled *myogenin-H2B*⁺ ERMS cells move locally within the tumor, but they also

enter the vasculature (Movie S8). A small portion of *myogenin-H2B-RFP*⁺/*myf5-GFP*⁻ cells were associated with vasculature and could invade neovascular beds in *fli1-GFP* transgenic animals (Figures 7K and 7L). To verify the fidelity of H2B-fluorescent labeling of ERMS cell subfractions and to directly visualize if *myf5-GFP*⁺ ERMS cells can enter the vasculature, we induced ERMS in stable transgenic animals that express *myf5-GFP/flk1-mCherry* by coinjecting both *rag2-KRASG12D* and *myogenin-H2B-Amcyan*. As was seen using the H2B-RFP transgenic reporter, we found that *myogenin-H2B-Amcyan*⁺ cells are highly migratory (Movies S4 and S5), were the first cell type to colonize new areas of tumor growth, and could be observed transiting the vasculature (Figures 7M and 7N; Movies S5 and S9). By contrast, *myf5-GFP*⁺ ERMS cells exhibited reduced motility when compared with *myogenin*⁺ ERMS cells and were never observed entering the vasculature

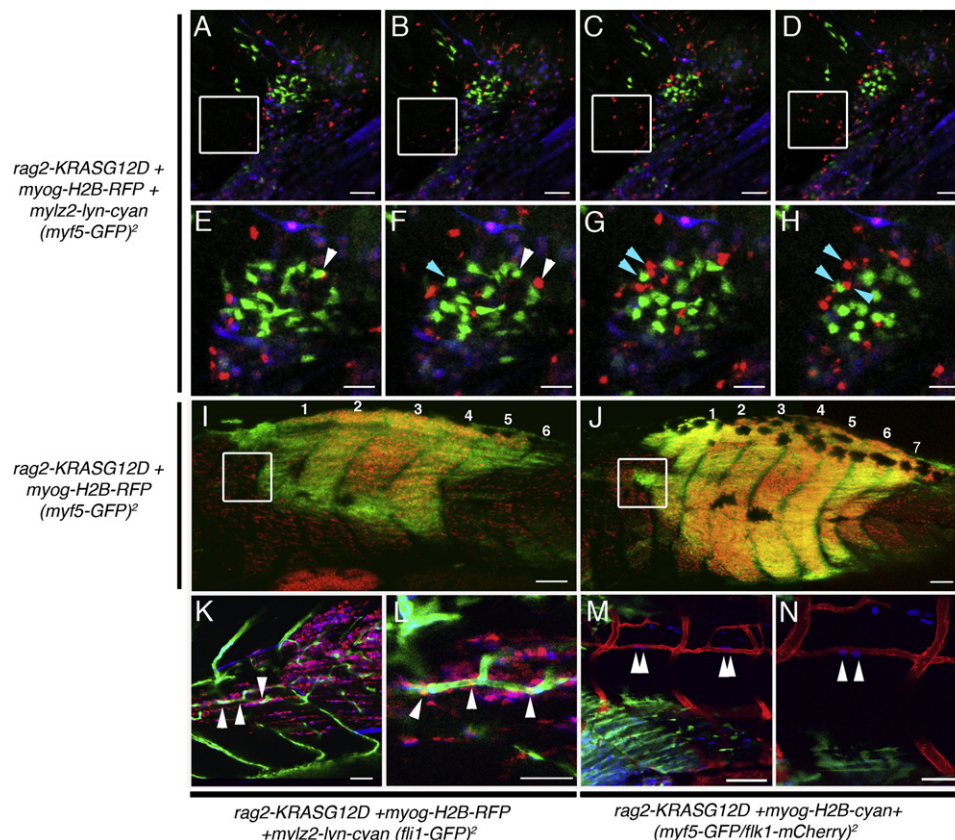


Figure 7. *myf5-GFP*+ ERMS-Propagating Cells Are Recruited to New Areas of Tumor Growth Only after Seeding by *myogenin*+ ERMS Cells

(A–H) Time-lapse images of *myf5-GFP* transgenic animal injected with *rag2-KRASG12D*, *myogenin-H2B-RFP* and *mylz2-lyn-cyan*. Panels are merged image planes taken every hour. *myogenin-H2B-RFP*+ cells migrate into normal tissues over time (white boxed region). Magnified views of time-lapse images documenting that *myf5-GFP*+ cells are largely stationary while *myogenin-H2B-RFP*+ cells are highly migratory and migrate away from GFP+ cells (denoted by arrows in E–H).

(I and J) Serial imaging of a *myf5-GFP* transgenic animal injected with *rag2-KRASG12D* and *myogenin-H2B-RFP* shown at 14 and 17 dpf, respectively. White boxes denote a region that initially contained only *myogenin-H2B-RFP*+ cells (I) but was later colonized by *myf5-GFP*+ cells (J).

(K and L) ERMS developing in a *fli1-GFP* transgenic animal injected with *rag2-KRASG12D*, *myogenin-H2B-RFP*, and *mylz2-lyn-cyan*. (K) Merged z-stacks showing three *myogenin-H2B-RFP*+ cells associated with and inside *fli1-GFP*+ vessels, which was confirmed by imaging a single image plane at higher magnification (L, white arrowhead).

(M and N) ERMS developing in a *flk1-mCherry* transgenic animal injected with *rag2-KRASG12D* and *myogenin-H2B-cyan* showing four cells entering the vasculature (white arrowheads in M) and a single plane image showing two cells transiting into the vasculature at higher magnification (white arrowheads in N).

Scale bar, 50 μ m (for A–H, K, L, and N) and 100 μ m (for I, J, M).

See also Figure S4 and Movies S7, S8, and S9.

(n = 10 animals). Again, slow-moving *myf5-GFP*+ cells were found in newly colonized regions only after initial invasion by *myogenin*+ ERMS cells.

DISCUSSION

Myf5 as a Marker of ERMS-Propagating Cells

The limiting dilution cell transplantation studies outlined here confirm the existence of a highly purified and molecularly definable ERMS-propagating cell that expresses *myf5*, *m-cadherin*, and *c-met* but not differentiated muscle markers. The *myf5-GFP*+ ERMS-propagating cell gives rise to all the other differentiated ERMS cells contained within the tumor mass and exhibits enhanced proliferative capacity as assessed by EDU incorporation and direct in vivo cell imaging. These results are in keeping

with our previous work showing that ERMS-propagating activity was largely confined to the *rag2-dsRED*+/ α -actin-negative ERMS cell population that preferentially expressed *myf5* and other activated satellite cell markers (Langenau et al., 2007). However, *rag2-dsRED*+/ α -actin-negative ERMS cells exhibited only a modest 3-fold enrichment for tumor-propagating potential when compared to *rag2-dsRED*+/ α -actin+ ERMS cells (Langenau et al., 2007). By contrast, experiments outlined here using new fluorescent transgenic reporter lines and syngeneic zebrafish show that the *myf5-GFP*+/*mylz2-negative* ERMS cells exhibit a remarkable 28- to >40-fold enrichment of tumor-propagating potential when compared to other ERMS-derived cell populations.

Myf5 is a myogenic regulatory factor related to MyoD and has important roles in muscle development. For example,

MyoD/Myf5-deficient mice lack muscle, while deficiencies in only one of these genes does not affect muscle specification (Rudnicki et al., 1993), suggesting important and yet redundant functions of these genes in development. It has also been shown that *Myf5* is highly expressed in activated satellite cells and has important roles in postnatal muscle regeneration in response to injury (Cooper et al., 1999; Gayraud-Morel et al., 2009; Ustanina et al., 2007), suggesting that *Myf5* may regulate self-renewal in normal muscle satellite cells. Microarray analysis and cross-species comparisons have shown that *MYF5* is upregulated in both zebrafish and human ERMS but not translocation-positive ARMS (Langenau et al., 2007; Zibat et al., 2010), and recent work from Rubin et al. (2011) has shown that *Myf5* is differentially expressed in murine ERMS regardless of which muscle cell subpopulation is initially targeted for transformation. These results suggest that *Myf5* gene programs are likely reinitiated in transformed cells and may have important roles in driving ERMS growth. By contrast, translocation-positive ARMS fail to express *MYF5*, precluding *MYF5* marker expression as an identifying characteristic of ARMS-propagating cells and raising the interesting possibility that the molecular mechanisms regulating tumor-propagating potential differ between molecular subtypes of RMS. Given the critical roles of the *Myf5* transcription factor in muscle development and regeneration in mice, it will be important to assess if *myf5* is a marker of ERMS-propagating cells or if it plays a regulatory role in ERMS self-renewal and growth.

Regional Partitioning of ERMS Cells Based on Differentiation Status

Evidence in solid tumors to support a discrete, specialized microenvironment that augments tumor growth and proliferation is now just beginning to emerge. For example, tumor-propagating cells, including those of glioblastomas, have been shown to reside in a vascular niche that promotes both their maintenance and their ability to divide and produce daughter cells capable of inducing tumors (reviewed by Gilbertson and Rich, 2007). In other solid tumors arising in skin, prostate, and breast, tumor stromal fibroblasts also serve an essential role in maintaining a favorable microenvironment for tumor growth and expansion. For example, work by Orimo et al. (2005) has shown that stromal fibroblasts associated with invasive breast carcinoma cells can promote tumor growth and angiogenesis through secretion of SDF-1. In normal muscle, stem cell numbers are exquisitely regulated by paracrine factors like Wnt5a (Poleskaya et al., 2003), Myostatin (McCroskery et al., 2003), and Notch ligands (Conboy et al., 2003). Many of these factors are secreted by normal fibers that can sense injury and elicit recruitment and expansion of muscle progenitors that are required for regeneration. Thus, mature muscle provides a supportive microenvironment that facilitates homeostatic regulation of muscle stem cells. In our zebrafish ERMS model, we document that *myf5-GFP+* ERMS-propagating cells are initially juxtaposed to muscle fibers in an expanded muscle satellite/progenitor cell niche, suggesting that early stage ERMS cells cannot escape the constraints of muscle architecture or are held in check by local secreted factors emanating from normal muscle. By the late stages of ERMS growth, ERMS-propagating cells are reorganized and take up residence in defined regions within the tumor mass. Following this regional partitioning of ERMS cells,

mid-differentiated *myogenin+* ERMS cells show enhanced migratory capability and move away from the ERMS-propagating cells from which they had arisen. These mid-differentiated *myogenin+* ERMS cells are highly migratory, seed new areas of tumor growth, and cease to move once they turn on differentiated muscle markers including muscle myosin light chain. Such biologically constrained characteristics of ERMS cells would ensure that tumor-propagating cells remain confined to regionally defined areas and do not compete with differentiated ERMS cells for local resources including growth factors and oxygen. The extent to which regional partitioning of tumor cells occurs in other solid tumors is unknown; however, assuming this phenomenon is found in diverse cancer types, it will be important to determine if regional partitioning of tumor cells provides protective advantages to tumor-propagating cells, facilitating the retention of a small number of cancer cells that evade treatment and eventually give rise to disease relapse.

A Role for Differentiated, Non-Tumor-Propagating Cells in Facilitating Tumor Growth and Metastasis

Myogenin immunohistochemical reactivity found in >80% of RMS cells distinguishes patients with poor clinical outcome (Heerema-McKenney et al., 2008), suggesting that *Myogenin+* cells have a unique role in RMS progression and metastasis. In our model, *myogenin-H2B+* cells arise from *myf5-GFP+* ERMS-propagating cells, lack tumor-propagating potential, and are the first cell type to migrate into new areas of tumor growth. A subset of *myogenin+* ERMS cells infiltrate blood vessels—a first step toward metastasis—and are also the first to colonize new areas of tumor growth, only to be infiltrated later by slow-migrating *myf5+* ERMS-propagating cells. Our work raises the interesting possibility that differentiated, non-ERMS-propagating cells may create a supportive environment that augments growth and is responsible for local tumor invasion. For example, it is possible that once mid-differentiated *myogenin+* cells infiltrate new areas of growth, that they secrete factors that recruit slow-moving *myf5+* ERMS-propagating cells, facilitating tumor spread. Alternatively, it is possible that *myogenin+* cells break down collagen and cell-cell contacts, acting as trailblazers to establish migratory tracks that allow slow-moving *myf5+* ERMS-propagating cells to transit into newly forming tumor. Our work also highlights that metastatic capacity and tumor-propagating potential need not be confined to the same tumor cell subpopulations, but rather that local infiltration and metastasis may be facilitated by differentiated, non-tumor-propagating cells. We expect that these same principles may be more broadly applicable to a diversity of cancers, accounting for why tumors retain large numbers of differentiated cell types that themselves are incapable of reconstituting tumor.

Our findings of a *myf5+* ERMS-propagating cell population and a *myogenin+* migratory population both contributing to tumorigenesis may have profound therapeutic implications. Instead of targeting only tumor-propagating cells for destruction, drug design should also take into account the mechanisms regulating the homeostasis of more differentiated tumor cells and their nonproliferative roles in regulating growth. Moreover, therapies that focus on modulating the differentiation status of ERMS cells should attempt to force the conversion of tumor-propagating cells into cells with terminally differentiated

myoblast characteristics that are incapable of recreating tumor, cannot migrate, and fail to enter into the vasculature.

EXPERIMENTAL PROCEDURES

Study Approval

These studies were approved by the Massachusetts General Hospital Subcommittee on Research Animal Care under protocol #2011N000127 (zebrafish), the Duke University Institutional Animal Care & Use Committee under protocol A 036-03-02 (mouse), and the Partners Human Research Committee under protocol #2009-P-002756 (human). Samples were obtained from the Pathology Department of Massachusetts General Hospital. Use of de-coded, paraffin-embedded human tissue samples does not require informed consent.

Animals

CG1-strain (Smith et al., 2010), α -actin-GFP (Higashijima et al., 1997), *myf5-GFP* (Chen et al., 2007), *flk1-GFP* (Lawson and Weinstein, 2002), *flk1-mCherry* (Wang et al., 2010), and *myl2-mCherry* transgenic zebrafish (Smith et al., 2010) have been reported previously.

The *rag2-KRASG12D*, *rag2-dsREDexpress*, *myogenin-H2B-RFP*, *myogenin-H2B-Amcyan*, and *myl2-lyn-cyan* constructs were microinjected into one-cell-stage zebrafish singly (*rag2-KRASG12D* injected into *myf5-GFP*/*myl2-mCherry* syngenic zebrafish, 60 ng/ μ l) or as combinations with linearized DNA at a final combined concentration of 120 ng/ μ l essentially as described (Langenau et al., 2008).

FACS and ERMS Cell Transplantation

FACS analysis and ERMS cell transplantation were completed essentially as described elsewhere (Smith et al., 2010; Langenau et al., 2007). Sort gates were placed based on wild-type control fish and *myf5-GFP*+, *myl2-mCherry*+, or *myl2-lyn-cyan*+ ERMS. DAPI, propidium iodide, or TOPRO3 was used to isolate viable cells. ERMS tumors were double sorted to obtain pure, viable cell populations. Sort purity was assessed after two rounds of sorting when possible. Following limiting dilution cell transplantation into nonirradiated syngeneic CG1-recipient animals, fish were analyzed for fluorescent tumor engraftment from 10 to 120 days posttransplantation. Tumor-propagating potential was quantified using the Extreme Limiting Dilution Analysis software (<http://bioinf.wehi.edu.au/software/elda/>). A subset of transplanted fish was sectioned and stained with hematoxylin and eosin to confirm the presence or absence of ERMS.

Immunohistochemistry, EDU Staining, and Annexin V Staining

Paraffin embedding and sectioning, cryostat sectioning, and immunohistochemical analysis were performed essentially as described elsewhere (Langenau et al., 2007; see also Supplemental Experimental Procedures). EDU staining was performed using the Click-IT Alexa Fluor 647 imaging kit (Invitrogen). Annexin analysis for apoptotic cells was performed via FACS using annexin V conjugated to Alexa Fluor 647 (Invitrogen).

Gene Expression Analysis

Total RNA was isolated from AB-strain embryos 6 and 24 hr postfertilization and FAC-sorted ERMS cell subpopulations (TRIzol, GIBCO/BRL) in the presence of glycol blue. Quantitative real-time PCR utilized gene-specific PCR primers (Supplemental Experimental Procedures), and expression was normalized to 18 s and β -actin controls to obtain relative transcript levels using the $2^{-\Delta\Delta CT}$ method. Relative gene expression was normalized within individual samples, and cumulative transcript expression across the four ERMS cell subpopulations was set to 25. Samples were assessed in relation to embryos 6 and 24 hr postfertilization to ensure that results for $2^{-\Delta\Delta CT}$ results for any given gene were not lower than 10-fold expression found in normal development. Microarray experiments were completed essentially as described (fold change cutoff > 1.5-fold log scale; Langenau et al., 2007). Microarray data have been deposited into the GEO database (GSE32425).

Laser Scanning Confocal Microscopy and Dual Photon Imaging

Larval zebrafish were anesthetized in Tricaine and embedded in a single drop of low melt 1% agarose on a glass bottom petri dish (No 1.5, Mat Tek Corpo-

ration). Each petri dish was supplemented with fish water and imaged using an inverted Pascal or LSM510 Zeiss laser scanning confocal microscope or an upright Ultima IV multiphoton microscope (Prairie Technologies). Quantification was completed by counting the total numbers of fluorescent-labeled ERMS cell subpopulations contained in two 250 \times 150 μ m areas per animal (Figures 4K and 4L; control, $n = 7$; stage 1, $n = 3$; stage 2, $n = 4$; stage 3, $n = 7$). Because regional niches can be compartmentalized within a single myotome segment, a smaller area was assessed for total numbers of *myf5-GFP*+ and *myogenin-H2B-RFP*+ ERMS cells (50 \times 50 μ m² area, six areas per tumor; Figure 4M).

For cell tracking, sequences of image stacks were transformed into maximum intensity-projected movies using Imaris 7.1 software (Bitplane) and exported as Quicktime movies. Manual two- or three-dimensional tracking was performed using the manual tracking plugin in ImageJ or using Imaris 7.1. Annotation and further processing of movies was completed using ImageJ and Quicktime 7.

SUPPLEMENTAL INFORMATION

Supplemental Information includes nine movies, two tables, four figures, and Supplemental Experimental Procedures and can be found with this article online at doi:10.1016/j.ccr.2012.03.043.

ACKNOWLEDGMENTS

E.C. and J.S.B. are supported by the National Institutes of Health (NIH) Training Grants T32 HL007627 and 5T32CA09216-26, respectively. C.M.L. is supported by R01 CA122706 and K12 HD043494. D.M.L. is supported by NIH Grants K01 AR055619, 1R01CA154923, and 1R21CA156056; the Alex's Lemonade Stand Foundation; the Sarcoma Foundation of America; the American Cancer Society; and the Harvard Stem Cell Institute. I.M.T. is supported by Fundação para a Ciência e Tecnologia (the Portuguese Foundation for Science and Technology) through Fellowship SFRH/BD/51288/2010. We thank Huai-Jen Tsai for *myf5-GFP* transgenic animals and Clarrisa Henry for critical review of our manuscript.

Received: September 20, 2011

Revised: February 6, 2012

Accepted: March 12, 2012

Published: May 14, 2012

REFERENCES

- Bentzinger, C.F., Wang, Y.X., and Rudnicki, M.A. (2012). Building muscle: molecular regulation of myogenesis. *Cold Spring Harb. Perspect. Biol.* 4, 4.
- Chen, Y.H., Wang, Y.H., Chang, M.Y., Lin, C.Y., Weng, C.W., Westerfield, M., and Tsai, H.J. (2007). Multiple upstream modules regulate zebrafish *myf5* expression. *BMC Dev. Biol.* 7, 1.
- Conboy, I.M., Conboy, M.J., Smythe, G.M., and Rando, T.A. (2003). Notch-mediated restoration of regenerative potential to aged muscle. *Science* 302, 1575–1577.
- Cooper, R.N., Tajbakhsh, S., Mouly, V., Cossu, G., Buckingham, M., and Butler-Browne, G.S. (1999). In vivo satellite cell activation via *Myf5* and *MyoD* in regenerating mouse skeletal muscle. *J. Cell Sci.* 112, 2895–2901.
- Dalerba, P., Cho, R.W., and Clarke, M.F. (2007). Cancer stem cells: models and concepts. *Annu. Rev. Med.* 58, 267–284.
- Du, S.J., Gao, J., and Anyangwe, V. (2003). Muscle-specific expression of *myogenin* in zebrafish embryos is controlled by multiple regulatory elements in the promoter. *Comp. Biochem. Physiol. B Biochem. Mol. Biol.* 134, 123–134.
- Eyler, C.E., Wu, Q., Yan, K., MacSwords, J.M., Chandler-Militello, D., Misuraca, K.L., Lathia, J.D., Forrester, M.T., Lee, J., Stamler, J.S., et al. (2011). Glioma stem cell proliferation and tumor growth are promoted by nitric oxide synthase-2. *Cell* 146, 53–66.
- Gayraud-Morel, B., Chrétien, F., and Tajbakhsh, S. (2009). Skeletal muscle as a paradigm for regenerative biology and medicine. *Regen. Med.* 4, 293–319.

- Gilbertson, R.J., and Rich, J.N. (2007). Making a tumour's bed: glioblastoma stem cells and the vascular niche. *Nat. Rev. Cancer* 7, 733–736.
- Heerema-McKenney, A., Wijnaendts, L.C., Pulliam, J.F., Lopez-Terrada, D., McKenney, J.K., Zhu, S., Montgomery, K., Mitchell, J., Marinelli, R.J., Hart, A.A., et al. (2008). Diffuse myogenin expression by immunohistochemistry is an independent marker of poor survival in pediatric rhabdomyosarcoma: a tissue microarray study of 71 primary tumors including correlation with molecular phenotype. *Am. J. Surg. Pathol.* 32, 1513–1522.
- Hettmer, S., Liu, J., Miller, C.M., Lindsay, M.C., Sparks, C.A., Guertin, D.A., Bronson, R.T., Langenau, D.M., and Wagers, A.J. (2011). Sarcomas induced in discrete subsets of prospectively isolated skeletal muscle cells. *Proc. Natl. Acad. Sci. USA* 108, 20002–20007.
- Higashijima, S., Okamoto, H., Ueno, N., Hotta, Y., and Eguchi, G. (1997). High-frequency generation of transgenic zebrafish which reliably express GFP in whole muscles or the whole body by using promoters of zebrafish origin. *Dev. Biol.* 192, 289–299.
- Ju, B., Chong, S.W., He, J., Wang, X., Xu, Y., Wan, H., Tong, Y., Yan, T., Korzh, V., and Gong, Z. (2003). Recapitulation of fast skeletal muscle development in zebrafish by transgenic expression of GFP under the myl2 promoter. *Dev. Dyn.* 227, 14–26.
- Keller, C., Arenkiel, B.R., Coffin, C.M., El-Bardeesy, N., DePinho, R.A., and Capecchi, M.R. (2004). Alveolar rhabdomyosarcomas in conditional Pax3:Fkhr mice: cooperativity of Ink4a/ARF and Trp53 loss of function. *Genes Dev.* 18, 2614–2626.
- Langenau, D.M., Keefe, M.D., Storer, N.Y., Guyon, J.R., Kutok, J.L., Le, X., Goessling, W., Neuberg, D.S., Kunkel, L.M., and Zon, L.I. (2007). Effects of RAS on the genesis of embryonal rhabdomyosarcoma. *Genes Dev.* 21, 1382–1395.
- Langenau, D.M., Keefe, M.D., Storer, N.Y., Jette, C.A., Smith, A.C., Ceol, C.J., Bourque, C., Look, A.T., and Zon, L.I. (2008). Co-injection strategies to modify radiation sensitivity and tumor initiation in transgenic Zebrafish. *Oncogene* 27, 4242–4248.
- Lawson, N.D., and Weinstein, B.M. (2002). In vivo imaging of embryonic vascular development using transgenic zebrafish. *Dev. Biol.* 248, 307–318.
- Li, Z., Bao, S., Wu, Q., Wang, H., Eyler, C., Sathornsumetee, S., Shi, Q., Cao, Y., Lathia, J., McLendon, R.E., et al. (2009). Hypoxia-inducible factors regulate tumorigenic capacity of glioma stem cells. *Cancer Cell* 15, 501–513.
- Linardic, C.M., Downie, D.L., Qualman, S., Bentley, R.C., and Counter, C.M. (2005). Genetic modeling of human rhabdomyosarcoma. *Cancer Res.* 65, 4490–4495.
- Lo Celso, C., Fleming, H.E., Wu, J.W., Zhao, C.X., Miake-Lye, S., Fujisaki, J., Côté, D., Rowe, D.W., Lin, C.P., and Scadden, D.T. (2009). Live-animal tracking of individual haematopoietic stem/progenitor cells in their niche. *Nature* 457, 92–96.
- McCroskery, S., Thomas, M., Maxwell, L., Sharma, M., and Kambadur, R. (2003). Myostatin negatively regulates satellite cell activation and self-renewal. *J. Cell Biol.* 162, 1135–1147.
- Orimo, A., Gupta, P.B., Sgroi, D.C., Arenzana-Seisdedos, F., Delaunay, T., Naeem, R., Carey, V.J., Richardson, A.L., and Weinberg, R.A. (2005). Stromal fibroblasts present in invasive human breast carcinomas promote tumor growth and angiogenesis through elevated SDF-1/CXCL12 secretion. *Cell* 121, 335–348.
- Polesskaya, A., Seale, P., and Rudnicki, M.A. (2003). Wnt signaling induces the myogenic specification of resident CD45+ adult stem cells during muscle regeneration. *Cell* 113, 841–852.
- Rubin, B.P., Nishijo, K., Chen, H.I., Yi, X., Schuetze, D.P., Pal, R., Prajapati, S.I., Abraham, J., Arenkiel, B.R., Chen, Q.R., et al. (2011). Evidence for an unanticipated relationship between undifferentiated pleomorphic sarcoma and embryonal rhabdomyosarcoma. *Cancer Cell* 19, 177–191.
- Rudnicki, M.A., Schnegelsberg, P.N., Stead, R.H., Braun, T., Arnold, H.H., and Jaenisch, R. (1993). MyoD or Myf-5 is required for the formation of skeletal muscle. *Cell* 75, 1351–1359.
- Seeger, C., Hargrave, M., Wang, X., Chai, R.J., Elworthy, S., and Ingham, P.W. (2011). Analysis of Pax7 expressing myogenic cells in zebrafish muscle development, injury, and models of disease. *Dev. Dyn.* 240, 2440–2451.
- Sipkins, D.A., Wei, X., Wu, J.W., Runnels, J.M., Côté, D., Means, T.K., Luster, A.D., Scadden, D.T., and Lin, C.P. (2005). In vivo imaging of specialized bone marrow endothelial microdomains for tumour engraftment. *Nature* 435, 969–973.
- Smith, A.C., Raimondi, A.R., Salthouse, C.D., Ignatius, M.S., Blackburn, J.S., Mizgirev, I.V., Storer, N.Y., de Jong, J.L., Chen, A.T., Zhou, Y., et al. (2010). High-throughput cell transplantation establishes that tumor-initiating cells are abundant in zebrafish T-cell acute lymphoblastic leukemia. *Blood* 115, 3296–3303.
- Ustanina, S., Carvajal, J., Rigby, P., and Braun, T. (2007). The myogenic factor Myf5 supports efficient skeletal muscle regeneration by enabling transient myoblast amplification. *Stem Cells* 25, 2006–2016.
- Wang, Y., Kaiser, M.S., Larson, J.D., Nasevicius, A., Clark, K.J., Wadman, S.A., Roberg-Perez, S.E., Ekker, S.C., Hackett, P.B., McGrail, M., and Essner, J.J. (2010). Moesin1 and Ve-cadherin are required in endothelial cells during in vivo tubulogenesis. *Development* 137, 3119–3128.
- Xia, S.J., Pressey, J.G., and Barr, F.G. (2002). Molecular pathogenesis of rhabdomyosarcoma. *Cancer Biol. Ther.* 1, 97–104.
- Zibat, A., Missiaglia, E., Rosenberger, A., Pritchard-Jones, K., Shipley, J., Hahn, H., and Fulda, S. (2010). Activation of the hedgehog pathway confers a poor prognosis in embryonal and fusion gene-negative alveolar rhabdomyosarcoma. *Oncogene* 29, 6323–6330.

Tetraspanin CD37 Directly Mediates Transduction of Survival and Apoptotic Signals

Rosa Lapalombella,¹ Yuh-Ying Yeh,¹ Liwen Wang,² Asha Ramanunni,¹ Sarwish Rafiq,^{1,3} Shruti Jha,¹ Justin Staubli,^{1,3} David M. Lucas,^{1,5} Rajeswaran Mani,^{1,4} Sarah E.M. Herman,^{1,3} Amy J. Johnson,^{1,5} Arletta Lozanski,¹ Leslie Andritsos,¹ Jeffrey Jones,¹ Joseph M. Flynn,¹ Brian Lannutti,¹⁰ Peter Thompson,¹¹ Paul Algate,¹² Scott Stromatt,¹² David Jarjoura,⁶ Xiaokui Mo,⁶ Dasheng Wang,⁵ Ching-Shih Chen,^{1,5} Gerard Lozanski,⁷ Nyla A. Heerema,⁷ Susheela Tridandapani,⁸ Michael A. Freitas,^{9,13} Natarajan Muthusamy,^{1,4,9,13,*} and John C. Byrd^{1,4,5,13,*}

¹Division of Hematology, Department of Internal Medicine

²Department of Chemistry

³The Integrated Biomedical Research Graduate Program

⁴Department of Veterinary Biosciences

⁵Division of Medicinal Chemistry and Pharmacognosy, College of Pharmacy

⁶Center for Biostatistics

⁷Department of Pathology

⁸Division of Pulmonary Medicine, Department of Internal Medicine

⁹Department of Molecular Virology, Immunology and Medical Genetics

The Ohio State University, Columbus, OH 43210, USA

¹⁰Gilead Pharmaceuticals Inc, Seattle, WA 98102, USA

¹¹OrbiMed Advisors, LLC, New York, NY 10017, USA

¹²Emergent BioSolutions, Seattle, WA 98121-3460, USA

¹³These authors contributed equally to this work

*Correspondence: raj.muthusamy@osumc.edu (N.M.), john.byrd@osumc.edu (J.C.B.)

DOI 10.1016/j.ccr.2012.03.040

SUMMARY

Tetraspanins are commonly believed to act only as “molecular facilitators,” with no direct role in signal transduction. We herein demonstrate that upon ligation, CD37, a tetraspanin molecule expressed on mature normal and transformed B cells, becomes tyrosine phosphorylated, associates with proximal signaling molecules, and initiates a cascade of events leading to apoptosis. Moreover, we have identified two tyrosine residues with opposing regulatory functions: one lies in the N-terminal domain of CD37 in a predicted “ITIM-like” motif and mediates SHP1-dependent death, whereas the second lies in a predicted “ITAM motif” in the C-terminal domain of CD37 and counteracts death signals by mediating phosphatidylinositol 3-kinase-dependent survival.

INTRODUCTION

It is generally assumed that tetraspanins are not directly involved in signal transduction, because of the lack of embedded signaling motifs, and that they instead serve as “molecular facilitators” of signal transduction (Maecker et al., 1997). For instance, tetraspanins such as CD53 and CD63 associate with a protein tyrosine phosphatase in rat lymph node cells and a rat mast cell line, respectively (Carmo and Wright, 1995), whereas CD9-mediated signaling in platelets involves activation of the protein tyrosine

kinase p72^{SYK} (Ozaki et al., 1995). Tetraspanins can also associate noncovalently with other immune molecules—for example, CD9 and CD63 with integrins (Berdichevski et al., 1995; Rubinstein et al., 1994), CD81 with CD19/CD21 on B cells (Matsumoto et al., 1993), and with CD4 or CD8 on T cells (Imai and Yoshie, 1993)—suggesting that signaling through tetraspanins, possibly following binding to a yet-unidentified ligand, may regulate the functions of key players in immune recognition.

CD37 is a member of the transmembrane 4 superfamily (TM4SF) of tetraspanin proteins, which have four potential

Significance

The signaling role of CD37 in normal and transformed B cells has not been characterized. Our extensive studies have identified a unique function of CD37 as a death receptor in B cells. We have demonstrated that CD37 is a tetraspanin that can directly mediate dual signal transduction through the C- and N-terminal domain. The finding that two independent regions of CD37 exert completely different functions by concurrently activating cell death and survival pathways opens up opportunities for immunotherapy directed at CD37 cell death-mediated signaling in combination with development of small inhibitory peptides or kinase inhibitors that target the C-terminal activation domain to maximize cell death.

membrane-spanning regions (Horejsí and Vitek, 1991; Wright and Tomlinson, 1994). CD37 is expressed in developing B cells from pre-B to peripheral mature B cell stages, but not plasma cells. T cells, monocytes, and natural killer (NK) cells express very low levels of CD37 (Schwartz-Albiez et al., 1988), and it is absent on platelets and erythrocytes (van Spriel et al., 2004). CD37 forms protein complexes with CD53, CD81, CD82, and class II glycoprotein on the B cell surface that may represent an ion channel or a transporter (Angelisová et al., 1994). Moreover, CD37 is expressed in B cell endosomes and exosomes, reflecting possible involvement in intracellular trafficking or antigen presentation. Targeted inactivation of CD37 in mice revealed no changes in the development of lymphoid organs, but reduced IgG1 levels and alteration of response to T cell-dependent antigens, indicating a possible role for CD37 in T cell-B cell interaction (Knobeloch et al., 2000). Although the precise function of CD37 and its ligand remains unknown, it has been proposed to have a role in signal transduction pathways that affects cell development, activation, and motility (Wright and Tomlinson, 1994). The direct involvement of CD37 in signaling seems unlikely because of short cytoplasmic tails (8 to ~14 amino acids) that lack canonic signaling motifs.

Given its B cell-selective expression, CD37 represents a candidate therapeutic target for B cell malignancies, such as chronic lymphocytic leukemia (CLL). Several peptides, including anti-CD37 SMIP[™] (monospecific protein therapeutic, also referred to as SMIP-016), have been shown to induce rapid and potent *in vitro* direct tumoricidal activity in lymphoma/leukemia cells (Zhao et al., 2007). TRU-016, a humanized SMIP-016, is currently in a phase 1 clinical trial for relapsed CLL and small lymphocytic lymphoma (SLL) (<http://www.clinicaltrials.gov/>). Other CD37 targeted antibodies are currently in early clinical development (Hal-lek et al., 2008; Heider et al., 2011). However, the molecular basis of CD37-mediated cell death is unknown.

RESULTS

Identification of Tyrosine-Phosphorylated Proteins following CD37 Ligation Using Nano-LC-MS/MS

Expression of CD37 on CLL cells is variable, with significantly higher expression on IgVH-mutated versus IgVH-unmutated cells (see Figure S1A available online). Death induced by SMIP-016 is dose and time dependent (Zhao et al., 2007) and correlates with CD37 antigen density (Figure S1B), but not prognostic factors associated with poor outcome in CLL (Figures S1C–S1E). How CD37 ligation induces apoptosis is unknown. Treatment of CLL cells with SMIP-016 induces tyrosine phosphorylation of multiple proteins (Figure 1A), as indicated by immunoblot using anti-phosphotyrosine antibody 4G10 (Zhao et al., 2007). To identify these tyrosine-phosphorylated proteins, we undertook a proteomic approach. CLL cells were treated with SMIP-016 or trastuzumab, which does not bind CLL cells because these cells do not express HER2. Trastuzumab therefore is a good negative control to rule out potential Fcγ receptor-mediated signaling. The lysates were separated by SDS-PAGE following immunoprecipitation with 4G10, and the immunoprecipitated proteins were recovered by in-gel digestion. Following a phosphopeptide enrichment step, peptides were analyzed by LC-MS/MS.

Independent experiments from five patients reproducibly identified several tyrosine-phosphorylated proteins, including protein phosphatase non-receptor-type 6 (PTPN6/SHP1) and the SRC family kinase LYN. SMIP-016-induced tyrosine phosphorylation of SHP1 and LYN was confirmed by immunoprecipitation using 4G10, followed by anti-SHP1 or anti-LYN immunoblot analysis, and vice versa (Figure S1F and data not shown). Tyrosine phosphorylation of SHP1 (Yi et al., 1992) has been implicated in cell growth regulation, and loss of SHP1 in leukemia and other malignancies suggest it to be a tumor suppressor (Wu et al., 2003). We first assessed SHP1, SHP2, and PP2A protein levels in CLL (Figure S1G) and found variable expression of these proteins. To determine whether phosphorylation of SHP1 alters its phosphatase activity, we immunoprecipitated SHP1 from CLL patient cells treated with either trastuzumab or SMIP-016 and assessed its tyrosine phosphatase activity. SHP1 purified from SMIP-016-treated cells exhibited increased enzymatic activity relative to trastuzumab control (Figure 1B). SHP1 downregulation by siRNA resulted in almost complete loss of SMIP-016-induced cytotoxicity compared to nonsense siRNA (Figure 1C), supporting that SHP1 is involved in CD37-mediated cell death, which contrasts with SHP1-independent death induced by CD20 ligation (Kheirallah et al., 2010).

We also identified CD37, SHIP-1, and SYK in the LC-MS/MS analysis. CD37 has three tyrosine residues in its cytoplasmic tail. Detailed sequence analysis shows one of them at the N-terminal (N-t) domain within a predicted weak immune tyrosine-based inhibitory motif (ITIM) and the other two at the C-terminal (C-t) domain, with one located in an YxxL context within a single immune tyrosine-based activation motif (ITAM) (Figure 1D). An ITIM is a conserved sequence of amino acids (S/I/V/LxYxxI/V/L) that is found in the cytoplasmic tails of many inhibitory receptors of the immune system. Interaction of ITIM-bearing receptors with their ligands results in SRC family kinase-mediated tyrosine phosphorylation of the ITIM motif and recruitment of other enzymes, such as SHP1 and SHP2, or SHIP-1, an inositol phosphatase, that decrease the activation of cell signaling molecules. Similarly, the two tyrosine residues contained within the ITAM motif (defined by a consensus sequence: YxxI/Lx(6–12)YxxI/L, where x represents any amino acid) are typically phosphorylated by the SRC family of tyrosine kinases. This results in recruitment of SYK, and initiation of downstream cell activation signals leading to proliferation. The observations that (1) LYN and SHP1 are phosphorylated upon CD37 ligation, (2) SHP1 is directly involved in CD37-mediated cell death, and (3) SHP1 is known to bind to weak ITIM suggested that the ITIM-like motif in CD37 N-t might be functional. We confirmed that, in CLL cells stimulated with SMIP-016, CD37 was tyrosine phosphorylated and associated with both SHP1 and LYN (Figures 1E and 1F). Thus, CD37 engages the negative signaling effectors SHP1 and LYN when tyrosine phosphorylated, consistent with the presence of an ITIM.

SMIP-016-Induced Apoptosis Requires Translocation of CD37 into the Lipid Rafts

Lipid rafts are plasma membrane microdomains enriched in gangliosides (glycosphingolipids) and cholesterol that are involved in many signal transduction processes. For instance,

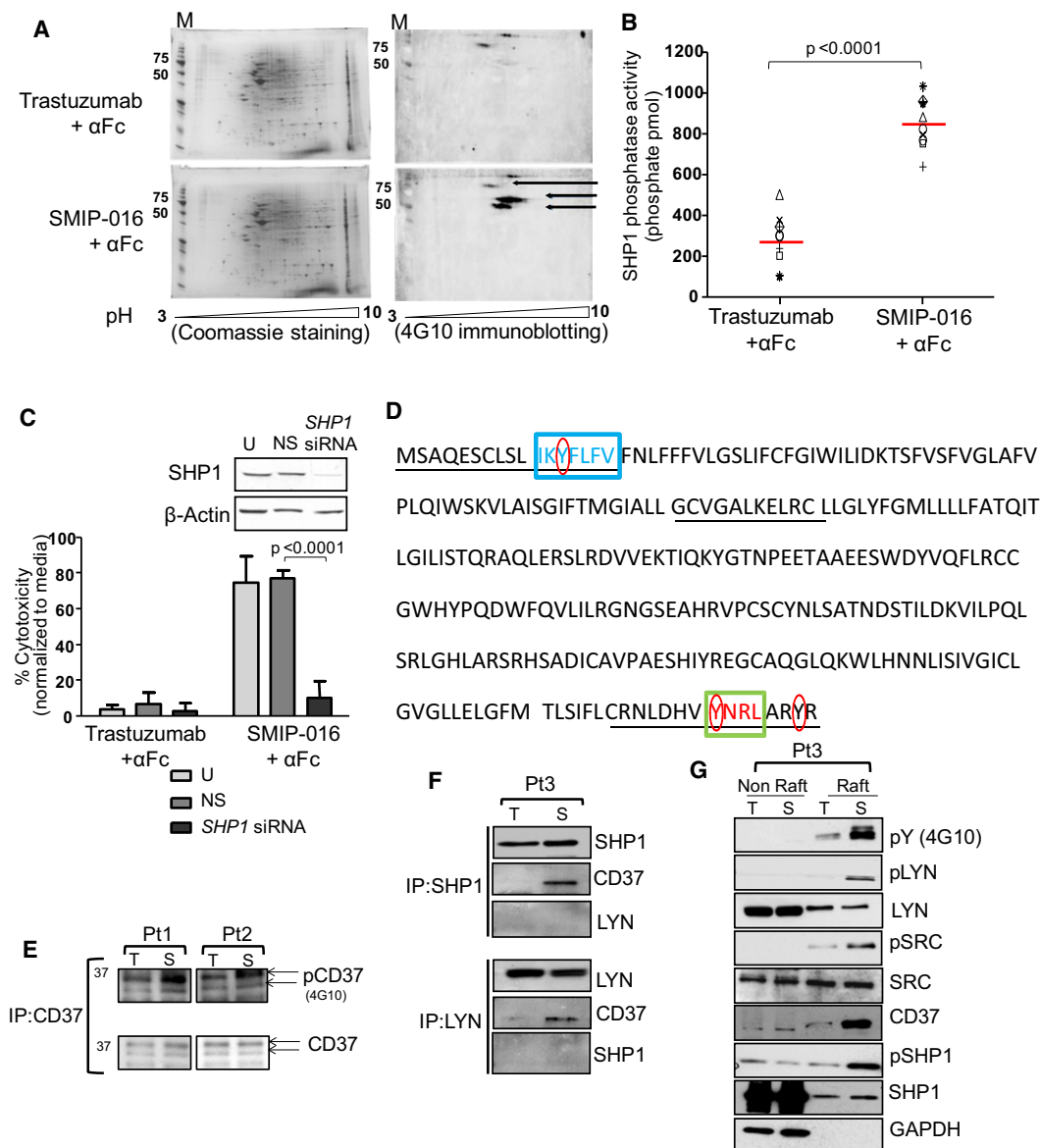


Figure 1. CD37 Ligation Induces Tyrosine Phosphorylation of SHP1, LYN, and CD37

(A) Lysates from trastuzumab+αFc- or SMIP-016+αFc-treated (15 min) CLL cells were analyzed by 2-D electrophoresis. A representative experiment is shown. M, molecular weight marker.

(B and C) SHP1 phosphatase activity of trastuzumab+αFc- or SMIP-016+αFc-treated cells (15 min) (B). Each symbol represents a different CLL patient sample, and red line represents the average (C) SMIP-016-induced cytotoxicity (24 hr) of untransfected CLL cells (U) or CLL cells transfected with *SHP1* siRNA or a nonsense siRNA (NS), as measured by annexin-V/PI staining (mean ± SD, n = 6). The immunoblot shows protein knockdown by siRNA in a representative sample.

(D) Amino acid sequence of human CD37 protein. Underscored text, intracellular regions; blue box, ITIM-like motif; green box, ITAM motif; red circles, cytosolic tyrosine residues.

(E) Lysates from trastuzumab+αFc-treated (T) or SMIP-016+αFc-treated (S) CLL cells (15 min) were immunoprecipitated with anti-CD37 followed by CD37 or 4G10 immunoblot. Two representative samples out of a total of three are shown.

(F) Lysates from trastuzumab+αFc-treated (T) or SMIP-016+αFc-treated (S) CLL cells (15 min) were immunoprecipitated using anti-SHP1 or anti-LYN followed by SHP1, LYN, or CD37 immunoblot. Representative of four patient samples is shown.

(G) Distributions of CD37, pLYN, pSHP1, and pSRC in the non-raft (NR) and lipid raft (R) fractions prepared from CLL cells treated with trastuzumab+αFc (T) or SMIP-016+αFc (S) (15 min). A representative experiment is shown.

See also Figure S1.

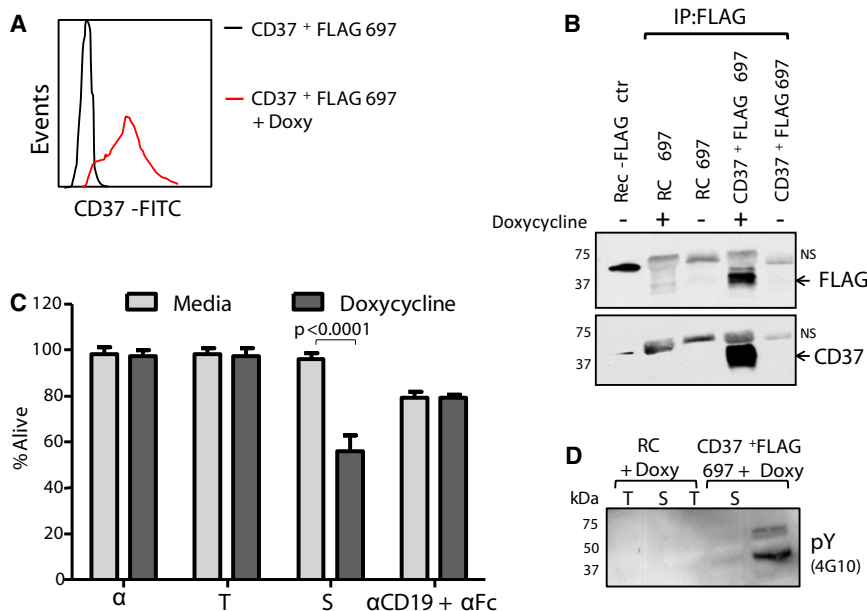


Figure 2. Generation of CD37⁺FLAG 697 Cell Line

(A and B) Expression of CD37 in CD37⁺FLAG 697 cells measured by flow cytometry (A) and immunoblot (B) with or without doxycycline (Doxy) stimulation (24 hr); 697 cells expressing a reverse complement sequence (RC) of CD37 were used as a negative control. NS, nonspecific bands.

(C) CD37⁺FLAG 697 cells were treated for 24 hr with αFc, trastuzumab+αFc (T), SMIP-016+αFc (S), or anti-CD19+αFc, and cytotoxicity was measured by annexin-V/PI (mean ± SD, n = 8).

(D) Lysates derived from trastuzumab+αFc-treated (T) or SMIP-016+αFc-treated (S) CD37⁺FLAG 697 cells (15 min) were analyzed by immunoblot using 4G10 antibody. Representative of three experiments is shown.

apoptosis induced by rituximab (anti-CD20) requires translocation of CD20 into lipid rafts where it interacts and activates protein tyrosine kinases LYN, FYN, and LCK (Janas et al., 2005; Semac et al., 2003). Upon cross-ligation with SMIP-016, but not trastuzumab, CD37 became associated within membrane lipid rafts along with pSHP1, pLYN, and pSRC (Figure 1G). GAPDH serves as a negative control for the isolation of detergent insoluble membranes, whereas total LYN, SHP1, and SRC serve as a positive control because they have been shown to normally reside in lipid rafts (Mone et al., 2004). The purity of the fractions was confirmed using cholera toxin B subunit-HRP (CT-B) that binds to GM-1, a specific marker of membrane lipid raft (Figure S1I). Cytochalasins inhibit F-actin polymerization, interfere with lipid raft aggregation, and inhibit anti-HLA-DR and anti-CD47 antibody-induced lymphocyte cell death (Truman et al., 1994). Similarly, cytochalasin D (CytD) or latrunculin B (LatB) pretreatment of CLL cells reduced SMIP-016-induced cell death (Figure S1J) and aggregation (Figure S1K).

Generation of CD37⁺FLAG 697 pTet-on Cell Lines

To study in more detail the biology of CD37, we created an inducible CD37⁺FLAG 697 cell line, a derivative of the CD37-negative 697 human acute lymphoblastic leukemia (ALL) cell line, that expresses CD37 upon induction with doxycycline (Figures 2A and 2B). Consistent with the signaling competence of the transfected CD37, treatment of CD37⁺FLAG 697 cells with SMIP-016 significantly induced cytotoxicity (Figure 2C) as well as tyrosine phosphorylation of multiple proteins (Figure 2D). Anti-CD19 was used as a control, because CD19 levels are not affected by doxycycline treatment.

CD37 Is Tyrosine Phosphorylated upon Ligation by SMIP-016

To study phosphorylation events, protein lysates from SMIP-016-treated CD37⁺FLAG 697 cells were immunoprecipitated with 4G10 followed by immunoblot analysis using antibodies

specific to proximal signaling targets. These studies identified tyrosine phosphorylation of CD37 (as detected with anti-FLAG), LYN, SHP1, and SYK, following SMIP-016 treatment (Figure 3A).

Next, 4G10 immunoprecipitates from SMIP-016-treated CD37⁺FLAG 697 cells were separated by SDS-PAGE and were subjected to in-gel trypsin digestion followed by a phosphopeptide enrichment step. Proteomics analysis was then performed by neutral loss tandem mass spectrometry on a Thermo Scientific LTQ Orbitrap XL. Five unique peptides of CD37 isoforms A and B were found in SMIP-016-treated but not trastuzumab-treated samples (Figure 3B), with 30% of the sequence covered including phosphorylation at Tyr²⁷⁴ (C-terminal region). No alternative proteins were identified from the 37 kDa region of the gel. The presence of CD37 in these immunoprecipitates was independently verified by anti-FLAG immunoblot (data not shown). Furthermore, lysates from SMIP-016 or trastuzumab-treated cells were immunoprecipitated with anti-FLAG antibody and analyzed by 4G10 immunoblot showing the presence of a band of approximately 37 kDa (Figures 3C and 3D), in the SMIP-016 treated lysates, that was abolished by treatment with λ-protein phosphatase (Figure 3D). Coimmunoprecipitation studies using CD37⁺FLAG 697 cells were conducted to confirm that CD37 associates with LYN, SHP1, and SYK upon ligation with SMIP-016 (Figure 3E) and that LYN and SYK were also phosphorylated (Figure 3F), similar to CLL cells. Initial attempts to downmodulate SHP1 in this cell line model using siRNA were unsuccessful, prompting creation of a 697 cell line with stable expression of CD37 and doxycycline-inducible expression of a short hairpin (sh) RNA for SHP1 (shSHP1). In these cells, downmodulation of SHP1 (by 120 hr) resulted in a reduction of SMIP-016-mediated cell death, consistent with the data in primary CLL cells (Figure 3G).

CD37 Possesses Dual Inhibitory and Activation Signaling Functions

To study the relevance of tyrosine phosphorylation in CD37-mediated killing, 697 cell lines carrying mutations or deletions of tyrosine residues in the cytosolic regions of the CD37 molecule were generated (Figure 4A). The deletion of Tyr²⁷⁴ or its

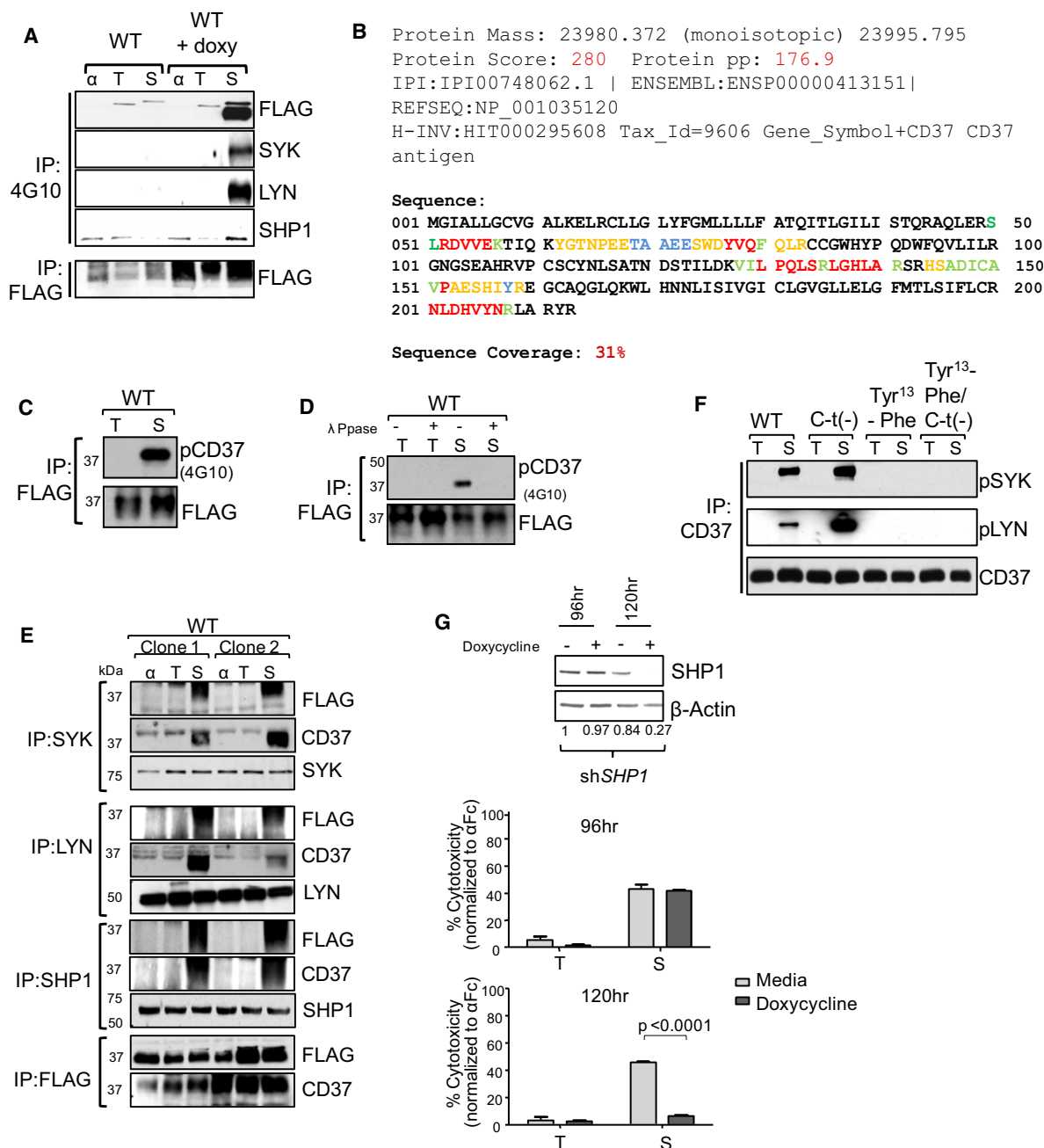


Figure 3. CD37 Is Tyrosine Phosphorylated upon Ligation by SMIP-016

(A) Lysates derived from CD37⁺FLAG 697 cells (with or without doxycycline) treated with α Fc (α), trastuzumab + α Fc (T), or SMIP-016 + α Fc (S) (15 min) were immunoprecipitated with 4G10, followed by immunoblot analysis using antibodies specific to SHP1, SYK, LYN, and CD37. Representative of three experiments is shown. Doxycycline-induced expression of CD37 was verified by anti-FLAG immunoblot (bottom panel).

(B) Sequence coverage of CD37 by phosphoproteomic analysis in SMIP-016-treated CD37⁺FLAG 697 cells as identified by the MassMatrix software.

(C) Lysates derived from trastuzumab + α Fc-treated (T) or SMIP-016 + α Fc-treated (S) CD37⁺FLAG 697 cells (15 min) were immunoprecipitated with anti-FLAG, followed by 4G10 immunoblot.

(D) Anti-FLAG-immunoprecipitated lysates from C were treated with λ -protein phosphatase (λ -ppase) followed by 4G10 immunoblot.

(E) Lysates derived from trastuzumab + α Fc-treated (T) or SMIP-016 + α Fc-treated (S) CD37⁺FLAG 697 cells (15 min) were immunoprecipitated with anti-FLAG, -SHP1, -SYK, or -LYN antibody followed by immunoblot with the indicated antibodies. Results from two different WT cell lines are shown.

(F) Lysates from trastuzumab + α Fc-treated (T) or SMIP-016 + α Fc-treated (S) (15 min) WT, C-t(-), Tyr¹³-Phe, or Tyr¹³-Phe/C-t(-) cell lines were immunoprecipitated using anti-CD37, followed by pSYK and pLYN immunoblot.

(G) SMIP-016-induced cytotoxicity of cells with doxycycline-induced downregulation of SHP1 measured by annexin-V/PI staining. Mean \pm SD, n = 3. T, trastuzumab + α Fc; S, SMIP-016 + α Fc. The SHP1 protein level is determined using immunoblot. A representative immunoblot is shown.

mutation to phenylalanine (Phe) did not affect surface expression of CD37 but significantly increased the cytotoxic effect of SMIP-016 (Figure 4B). Deletion of the entire C-t cytosolic portion of CD37, which includes Tyr²⁷⁴ and Tyr²⁸⁰ (Figure 4A), also did not affect surface expression of CD37 but again significantly enhanced the cytotoxic effect of SMIP-016 (Figure 4C) consistent with a regulatory function of this region in CD37-mediated cell death. To test the relevance of Tyr¹³ in the putative N-t ITIM domain, 697 cell lines expressing an N-t truncated CD37 [N-t(-)], a single deletion mutant [Tyr¹³(-)], or a Tyr¹³-Phe mutant were generated (Figure 4A). In the N-t(-) and Tyr¹³(-) cells, no surface CD37 was observed, although CD37 mRNA was still produced and translated (data not shown). The lack of surface expression of CD37 therefore could be attributed to the presence of a membrane localization signal in the deleted portions of the molecule. In contrast, the substitution of Tyr¹³ to Phe did not affect surface expression of CD37 but significantly reduced the cytotoxic effect of SMIP-016 (Figure 4D), indicating that this region positively regulates CD37-mediated cell death, consistent with an ITIM function for this domain. A similar death pattern among the cell lines was also observed for NK cell-mediated antibody-dependent cellular cytotoxicity (ADCC) (Figure S2A), further demonstrating the physiologic relevance of CD37 phosphorylation at the ITIM and ITAM sites.

The effects of N-t and C-t tyrosine deletions on protein-protein interactions and tyrosine phosphorylation were also studied. SMIP-016 treatment of cells induced phosphorylation of both the C-t-deleted and the wild-type (WT) CD37 (Figure 4E) that was sensitive to λ -protein phosphatase treatment (Figure 4F), but the amount of phosphorylation was visibly higher for the C-t-deleted CD37, suggesting that the C-t domain interferes with phosphorylation of the N-t. Furthermore, the lack of the C-t region did not prevent CD37 association with SHP1, LYN, and SYK (Figure 4G) or coassociation of LYN and SHP1 (Figure S2B). In contrast, the replacement of Tyr¹³ with Phe notably reduced SMIP-016-induced CD37 phosphorylation (Figure 4H) and prevented association of SHP1 and LYN with CD37 (Figure 4I) as well as each other (Figure S2B). Together, these data suggest that Tyr¹³ acts in the context of an ITIM motif, phosphorylation of which mediates apoptosis through recruitment and activation of LYN and SHP1. Importantly, the Tyr¹³-Phe/C-t(-) double mutant CD37 was not phosphorylated when cells were treated with SMIP-016 (Figure 4H). Furthermore, consistent with our previous report (Zhao et al., 2007), herbimycin treatment of the WT and the C-t(-) cell lines prevented cell death (data not shown) and SHP1-CD37 association in both cell lines (Figure 4J). To further demonstrate the phosphorylation and ITIM function of CD37 at the N-t region, we performed a GST pull-down experiment based on the assumption that SH2 domains of SHP1 can bind only to phosphorylated ITIM domains. Lysates derived from 697 cells expressing various forms of CD37 and treated with trastuzumab or SMIP-016 were incubated with GST-SHP1(SH2)N-t, GST-SHP1(SH2)C-t, or GST-SHIP(SH2) fusion proteins, and protein-protein complexes were then purified using glutathione agarose beads (GSH beads). The results show that both GST-SHP1(SH2)N-t and GST-SHP1(SH2)C-t pulled down the WT and the C-t(-)-deleted CD37, but not the Tyr¹³-Phe or the Tyr¹³-Phe/C-t(-) CD37. GST and GST-SHIP(SH2) served as negative controls (Figure S2C). The p85

regulatory and the p110 catalytic subunits of phosphatidylinositol 3-kinase (PI3K) have been shown to bind to phosphorylated tyrosines within the ITAM (YxxL) motif of the Fc γ R1a in macrophages (Cooney et al., 2001). However, it is not known whether this association is ITAM-mediated and direct, or indirect via an adaptor molecule. We hypothesized that the C-t portion of CD37 negatively regulates cell death by activating a PI3K-dependent survival signaling. Interestingly, WT but not C-t(-) CD37 recruit p85 and p110 δ upon stimulation with SMIP-016, indicating that these proteins bind to the C-t portion of CD37 (Figure 4K), consistent with an ITAM function for this domain. The targets of PI3K family kinases include AKT, which is known to mediate B cell proliferation and survival in response to B cell receptor cross-ligation through phosphorylation and inactivation of its downstream target GSK3 β . Upon CD37 ligation with SMIP-016, AKT and GSK3 β become phosphorylated in WT but not C-t(-) cell lines (Figure 4L). Moreover, treatment of the WT cell line with the PI3K inhibitor LY294002, using a concentration (10 μ M) that inhibits PI3K, resulted in increased SMIP-016-mediated cell death up to the level of the C-t(-) cell line (Figure 4M). A similar effect is also seen in primary CLL cells, where the combination of suboptimal doses of SMIP-016 (0.1 μ g/ml) with LY294002 or with the PI3K δ inhibitor CAL-101 is more cytotoxic than any agent alone (Figures S2D and S2E). Surprisingly, PI3K γ was also recruited upon CD37 cross-ligation. However, its binding was specific to the N-t portion, because it was found to be associated to CD37 even in the absence of the C-t domain (Figure 4N). A functional interaction between PI3K p85/p55 and SHP1 has been shown in T lymphocytes (Cuevas et al., 1999). This interaction was also associated with a reduction in PI3K-mediated phosphorylation of AKT, suggesting that PI3K signaling can be regulated by SHP1. Together, these results suggest that, upon ligation of CD37, two opposing stimuli act simultaneously on AKT and that the outcome for the cell represents a balance between these two counteracting pathways.

CD37 Ligation Mediates Mitochondrial Membrane Depolarization in CLL Cells

We have previously shown that cross-ligation of CD37 by SMIP-016 induces apoptosis of CLL cells (Zhao et al., 2007) as early as 4 hr (data not shown) and peaked at 18 hr. Apoptosis is induced via two main routes involving either the mitochondria (the intrinsic pathway) or the activation of death receptors (the extrinsic pathway). Both pathways converge to induce the activation of caspases, although in the past years, mitochondrial-mediated caspase-independent forms of apoptosis have been reported (Loeffler et al., 2001). We therefore measured mitochondrial membrane depolarization (MMD) of CLL cells in response to SMIP-016 using JC-1 staining. Although no MMD was observed in trastuzumab-treated samples, (Figures 5A and 5B), CD37 ligation resulted in 50% MMD. BIM is a critical BH3 only domain BCL-2 family member protein responsible for mitochondrial-induced apoptosis. Interestingly, CD37 ligation of CLL cells resulted in consistent upregulation of BIM at both the protein (Figure 5C) and mRNA level (Figure 5D), while the protein level of other pro- and antiapoptotic proteins, such as BAX, BCL2, and MCL1, remained unchanged (Figure 5C and Figure S3).

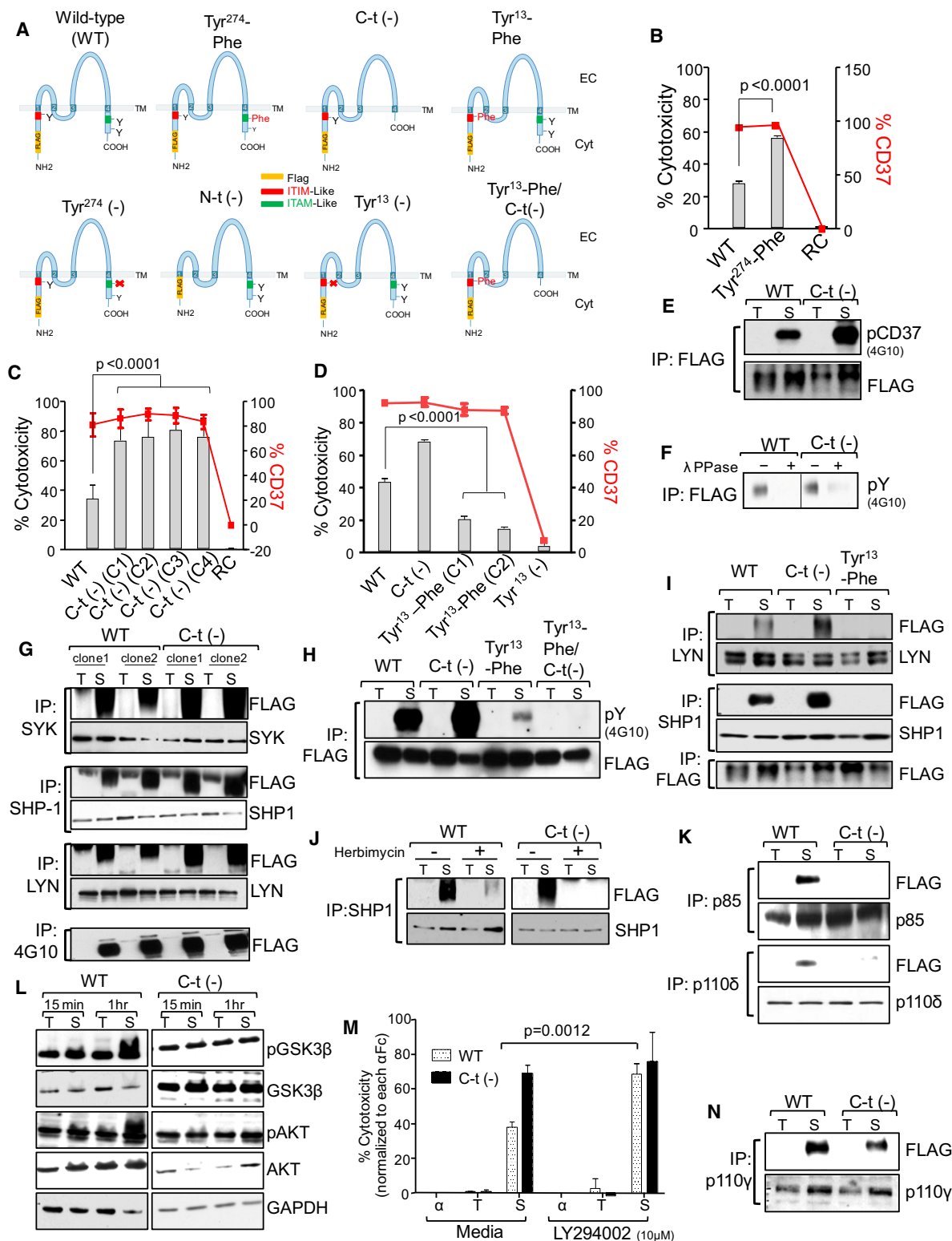


Figure 4. CD37 Possesses Dual Inhibitory and Activation Signaling Function

(A) Schematic representation of the human CD37 protein showing the mutations introduced in the cytosolic regions.

(B–D) CD37*FLAG 697 WT or mutant cell lines were treated with SMIP-016+αFc. Cell death was assessed at 24 hr by annexin-V/PI assay (gray bars). Data shown were normalized to αFc alone (B and C, n = 10; D, n = 16). Expression of CD37 was assessed by flow cytometry (red lines). RC, cells expressing a reverse complement sequence of CD37.

CD37 Cross-Ligation Increases FoxO3a-Dependent Transcription of *BIM*

CLL and a variety of other B cell lymphomas show aberrant expression of TCL1, an oncoprotein with multiple roles in B cell transformation, including active translocation of pAKT to the nucleus (Figure S4A). Cytoplasmic pAKT is modest in nonstimulated CLL cells, whereas nuclear pAKT is dramatically increased (Herman et al., 2010). CD37 ligation by SMIP-016 resulted in a decrease of CD40L-induced PI3K activity (Figure S4B). More importantly, ligation of CD37 in CLL cells decreased basal nuclear pAKT (Figure 6A) and CD40L-induced cytosolic pAKT (Figure S4C). Given the observation that increased pAKT is present in CLL cell nuclei, we hypothesized that this kinase might be influencing FoxO3a, a downstream targets of pAKT and a major transcription factor regulating the expression of *BIM*. As shown in Figure 6B, cross-ligation of CD37 significantly increases the nuclear FoxO3a level. To determine whether SMIP-016 upregulates *BIM* transcriptionally, a region of the *BIM* promoter containing the FoxO-binding site (FHRE) was cloned into a luciferase reporter construct (Figure 6C) and was transiently transfected into CLL cells. As shown in Figure 6D, *BIM* promoter activity was significantly induced by SMIP-016 treatment of the transfected cells. Furthermore, electrophoretic mobility shift assay (EMSA) using an oligonucleotide sequence derived from the *BIM* promoter region containing FHRE showed increased protein binding in nuclear extract derived from CLL cells treated with SMIP-016, but not the trastuzumab control (Figure 6E). This binding was specific for WT but not mutant FHRE and was prevented by using an excess of cold WT, but not mutant, oligonucleotide probe (Figure 6F). The physical interaction of FoxO3a with the *BIM* promoter in response to SMIP-016 was further confirmed by oligonucleotide pulldown assay (Figure 6G) showing that SMIP-016 treatment increase the binding of FoxO3a to the oligos containing a WT but not mutant FHRE. Next, ChIP assay showed an increased binding of FoxO3a to the endogenous *BIM* promoter in SMIP-016-treated CLL cells (Figure 6H) but not in cells treated with irrelevant antibody (IgG; data not shown). Thus, the increased transcriptional upregulation of *BIM* via FoxO3a following CD37 ligation by

SMIP-016 correlates with the increased *BIM* protein expression described above.

BIM Upregulation Contributes to CD37 Ligation-Mediated Apoptosis

BIM mRNA and protein upregulation was concurrent with its translocation to the mitochondria as well as the cleavage of mitochondrial BAX into p21 and p18 fragments (Figure 7A), which was detected in the enriched mitochondrial fractions only but not in the whole cell lysates (Figure 5C), consistent with the observed MMD following CD37 ligation (Figure 5A). Furthermore, *BIM* down-modulation by siRNA (Figure S5A) resulted in inhibition of mitochondrial depolarization, with increased intact mitochondria (Figure 7B) and partial reduction of SMIP-016-induced cytotoxicity compared to the scrambled siRNA control (Figure 7C). SHP1 has been implicated in negative regulation of neuronal survival by inhibiting phosphorylation of MAPK/ERK and AKT and increasing *BIM* expression (Marsh et al., 2003). To determine whether proximal SHP1 activation by SMIP-016 directly contributes to *BIM* upregulation, siRNA to SHP1 was used. As shown in Figure 7D, SHP1-specific siRNA antagonized *BIM* upregulation in CLL cells. Collectively, these studies suggest a direct role for SHP1 in downregulating the activity of AKT, which, in turn, inhibits FoxO3a nuclear translocation leading to induction of *BIM* (Figure 7E).

SMIP-016, but not trastuzumab, also induced nuclear translocation of FoxO3a (Figure S5B) and upregulation of *BIM* in WT CD37⁺FLAG 697 cells (Figure S5C). AKT phosphorylation was absent in the WT cell line at 18 hr (Figure S5D), corresponding to a later time where *BIM* induction is seen. Moreover, the deletion of Tyr¹³ but not Tyr²⁷⁴ prevented SMIP-016-induced upregulation of *BIM* in CD37⁺FLAG 697 cells (Figure S5E). Together, these results support our hypothesis that CD37 directly regulates CLL cell survival.

DISCUSSION

Our study focused on elucidating the role of CD37 in the transduction of apoptotic signals in transformed B cells. Analysis of

(E) Lysates from trastuzumab+ α Fc-treated (T) or SMIP-016+ α Fc-treated (S) WT or C-t(-) cells (15 min) were immunoprecipitated with anti-FLAG, followed by 4G10 or FLAG immunoblot.

(F) A portion of the immunoprecipitated lysates from E was treated with λ -protein phosphatase (λ -PPase) and analyzed by 4G10 immunoblot. Irrelevant lanes were cropped out the gel.

(G) Lysates derived from WT or C-t(-) cells treated with trastuzumab+ α Fc (T) or SMIP-016+ α Fc (S) (15 min) were immunoprecipitated using anti-SYK, -LYN, -SHP1, or 4G10 antibody, followed by immunoblot analysis with the indicated antibodies.

(H) Lysates derived from WT, C-t(-), and Tyr¹³-Phe cells treated with trastuzumab+ α Fc (T) or SMIP-016+ α Fc (S) (15 min) were immunoprecipitated with anti-FLAG antibody, followed by immunoblot analysis using 4G10 or anti-FLAG antibodies.

(I) Lysates derived from WT, C-t(-), and Tyr¹³-Phe cells treated with trastuzumab+ α Fc (T) or SMIP-016+ α Fc (S) (15 min) were immunoprecipitated using anti-LYN, -SHP1, or 4G10 antibody, followed by immunoblot analysis with the indicated antibodies.

(J) WT or C-t(-) cells were pretreated with either DMSO or herbimycin (10 μ M) for 45 min before the addition trastuzumab+ α Fc (T) or SMIP-016+ α Fc (S) (15 min). Lysates derived from these cells were immunoprecipitated with anti-SHP1 antibody and analyzed by FLAG and SHP1 immunoblot.

(K) Lysates derived from WT and C-t(-) cells treated with trastuzumab+ α Fc (T) or SMIP-016+ α Fc (S) (15 min) were immunoprecipitated with anti-p85 or p110 δ antibodies followed by immunoblot with the indicated antibodies. Representative of two experiments is shown.

(L) Lysates derived from trastuzumab+ α Fc-treated (T) or SMIP-016+ α Fc-treated (S) WT and C-t(-) cells were analyzed by immunoblot using the indicated antibodies.

(M) WT and C-t(-) cells were pretreated with LY294002 for 45 min before the addition of α Fc, trastuzumab+ α Fc (T), or SMIP-016+ α Fc (S). Cell death was measured 24 hr after treatment by annexin-V/PI (n = 15).

(N) Lysates derived from trastuzumab+ α Fc-treated (T) or SMIP-016+ α Fc-treated (S) WT and C-t(-) cells (15 min) were immunoprecipitated using p110 γ antibody followed by FLAG immunoblot (representative of two experiments). Data are represented as mean \pm SD for all the relevant panels.

See also Figure S2.

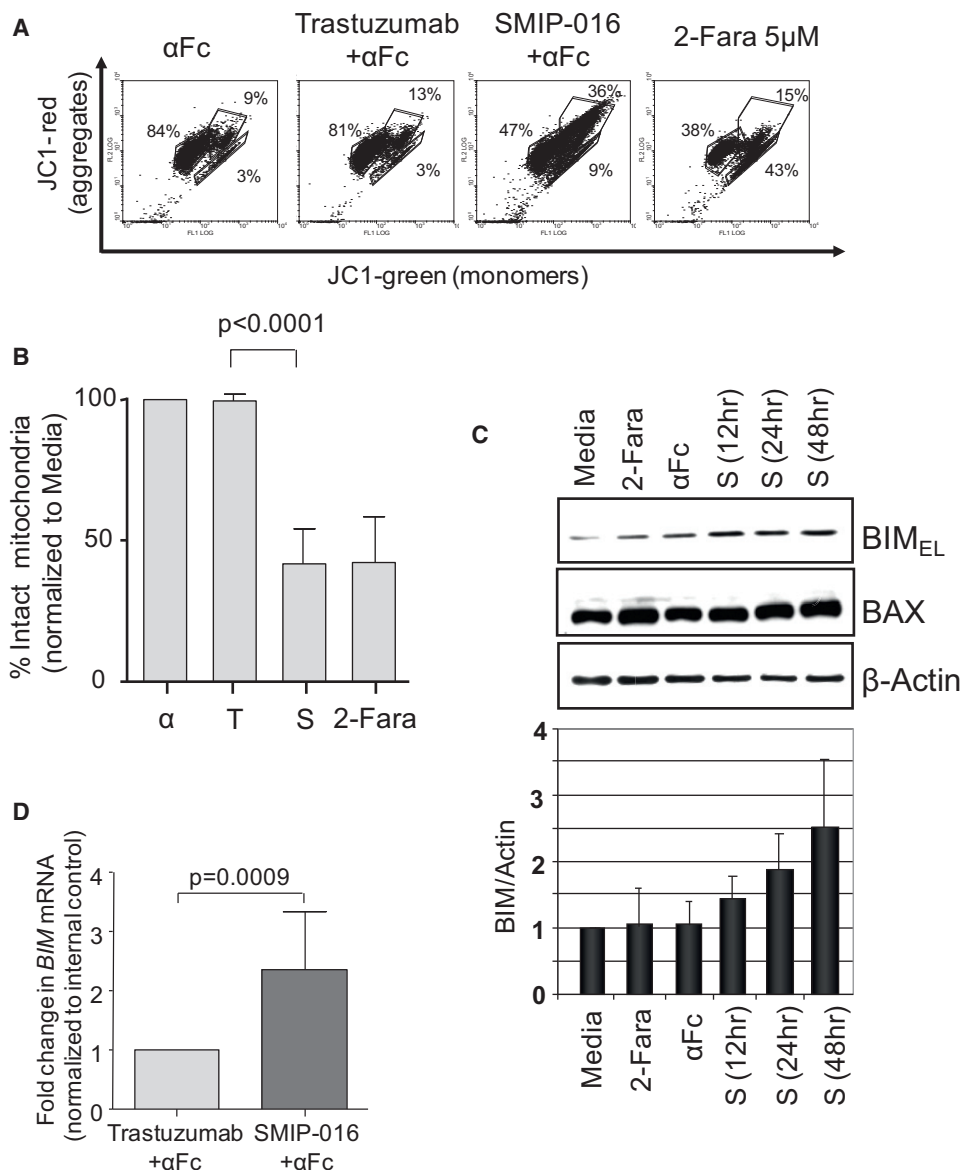


Figure 5. CD37 Ligation Mediates Mitochondrial Membrane Depolarization in Primary CLL Cells

(A and B) Representative data for JC-1 staining of CLL cells treated with αFc, trastuzumab+αFc, SMIP-016+αFc, or 2-fluoro-ara-A (2-Fara) for 12hr (A). A gate was drawn around the population with aggregated JC-1 (intact mitochondria) in untreated cells. Using this gate, the percentage of cells with intact mitochondria in treated samples was then calculated relative to the untreated sample, set at 100% (n = 12) (B).

(C) Lysates derived from CLL cells treated as indicated were analyzed by immunoblot for expression of BIM and BAX. β-Actin was used as loading control. The BIM level relative to the loading control was determined from five immunoblots using different patient samples.

(D) Real-time PCR analysis of BIM mRNA in trastuzumab+αFc- or SMIP-016+αFc-treated CLL cells (12 hr, n = 7). Data are represented as mean ± SD for all the relevant panels.

See also Figure S3.

the CD37 protein sequence revealed three tyrosine residues in its cytoplasmic domains with two opposing functions. One of these residues is localized at the N-t domain within the sequence IKYFLFV that resembles an ITIM-motif (V/L/IxYxxV/L) but with an additional residue between the tyrosine and valine. The other two tyrosine residues are located at the C-t domain of CD37, one of which is in a YxxL context within a single ITAM-like signaling motif. ITAM-like motifs were originally described in Dectin-1,

and since then, examples of ITAM-based signaling that do not conform precisely to the standard model are becoming increasingly common (Underhill et al., 2005). Moreover, it has been demonstrated that a synthetic peptide based on the phosphorylated single YxxL motif of Dectin-1 binds to SYK (Rogers et al., 2005), suggesting that a single tyrosine phosphorylation might be sufficient to recruit SYK. Through the use of independent biochemical and proteomic approaches, we demonstrate that,

upon cross-ligation, CD37 is tyrosine phosphorylated directly at two distinct tyrosine residues within the N-t (ITIM-like) and C-t (ITAM-like) cytosolic regions. Differences in baseline level of phosphorylation observed in primary CLL cells but not in the CD37⁺FLAG 697 cell line noted in our experiments could be attributed to in vivo stimulation of CLL cells by hitherto unidentified natural ligand for CD37. When a tyrosine in the ITIM is phosphorylated, it forms a docking site for the SRC homology 2 (SH2) recognition domains of the tyrosine phosphatase SHP1. Conversely, ITAM motifs are phosphorylated by SYK. Once phosphorylated the pITAM motif activates SYK, which in turn phosphorylates downstream targets that facilitate survival signaling through PI3K.

We further investigated which complex was recruited by each of these tyrosine domains and demonstrated, as expected, opposing roles for these two tyrosine residues in cell survival. We found that upon ligation of CD37, the N-t tyrosine within the ITIM-like motif becomes phosphorylated and associates with a specific complex of proteins, including LYN, SHP1, SYK, and PI3K γ , whereas p85 and PI3K δ were specifically recruited at the C-t domain. Taken together, these data indicate that at least two counteracting signaling pathways originate from ligation of CD37. One pathway acts through phosphorylation and activation of the ITIM-like motif at the N-t of CD37 by LYN kinase, leading to SHP1 recruitment and FoxO3a-dependent *BIM* upregulation and subsequent mitochondrial depolarization and cell death. These ITIM-like and ITAM-like functions also influence NK cell-mediated SMIP cytotoxicity, demonstrating the potential for tumor target antigen signaling influencing innate immune cell killing.

Our data clearly demonstrate that SHP1 is the major driving pathway of death of CD37 ligation but do not exclude the possibility that other signaling pathways, including proximal LYN and SYK, might be involved as well. The second pathway acts through tyrosine phosphorylation of the ITAM-like motif at the CD37 C-t domain, with recruitment and activation of PI3K and AKT, phosphorylation of GSK3 β , and promotion of cell survival. The binding of p85 to the phosphorylated YxxL peptide is direct, rather than through a phosphorylated adaptor protein such as SYK. However, these findings do not completely exclude the involvement of an unidentified adaptor protein in p85/PI3K recruitment. This complicated signaling network affords the potential for approaches to augment CD37-directed therapy. Combination treatment with SMIP-016 and the PI3K δ isoform-specific inhibitor CAL-101 demonstrated synergy, providing clinical rationale for combining these approaches in clinical trials. A diagram of the signaling induced by CD37 ligation is shown in Figure 8.

Although we showed that SMIP-016 efficacy is independent of traditional prognostic factors in CLL, a large variability in cell death was observed, which can be partially attributed to the heterogeneity of CD37 expression in CLL cells and to the simultaneous activation of both pro-death (N-t) and survival (C-t) signaling with SMIP-016 ligation of CD37. No mutations in the CD37 were identified among 120 patients studied (data not shown), although this cannot exclude that CD37 or SHP1 can become mutated or otherwise altered in resistant cells and warrants further study. Additionally, the mechanism by which BIM induction occurs with the CD19 antibody warrants further study.

In summary, we demonstrated herein (1) that CD37 can function as a death receptor in B cells, (2) the presence of two distinct regulatory motifs with opposing functions within the same molecule, and (3) a direct involvement of a tetraspanin in cell death signaling in CLL cells.

EXPERIMENTAL PROCEDURES

Cell Isolation

Blood was obtained from patients with CLL as defined by 2008 IWCLL criteria (Cheson et al., 1996; Hallek et al., 2008). All patients provided informed consent under an Ohio State University Institutional Review Board-approved protocol. CLL B cells were isolated and cultured as previously described (Lapalombella et al., 2010). The purity of tumor cells in the enriched populations was always greater than 95% as detected by dual CD19/CD3 staining.

Chemical Reagents and Cell Treatment

SMIP-016 (5 μ g/ml) was produced by Emergent BioSolutions (previously Trubion Pharmaceuticals, Seattle, WA) and is the chimeric parental molecule of TRU-016; 2-fluoro-ara-A (2-Fara, 5 μ M), rituximab (10 μ g/ml), and trastuzumab (10 μ g/ml) were obtained from the OSU pharmacy; goat anti-human IgG (α Fc, at 5X antibody concentration) was purchased from Jackson ImmunoResearch Laboratories; sodium stilboglucuronate and LY294002 were obtained from Sigma (St. Louis, MO); and FITC-labeled annexin V and propidium iodide (PI) were purchased from BD Pharmingen, (San Diego, CA).

Protein Fractionation and Immunoblotting

Cytosolic, nuclear, and mitochondrial fractions were prepared using reagents from Pierce (Rockford, IL) according to the manufacturer's directions. Immunoblots were performed as described elsewhere (Lapalombella et al., 2010). A detailed list of antibodies used can be found in the Supplemental Information.

Quantitative RT-PCR

cDNA was prepared as previously described (Lapalombella et al., 2008). Primers and probes were obtained from Applied Biosystems (Life Technologies, Carlsbad CA). The expression of *BIM* relative to the internal control gene was calculated by plotting the Ct (cycle number required to reach detection threshold), and the average relative expression for each group was determined using the comparative method (Livak and Schmittgen, 2001). Also see Supplemental Information for additional details.

Chromatin Immunoprecipitation

Chromatin immunoprecipitation assay was performed using the MagnaEZ ChIP Assay Kit (Millipore) according to the manufacturer's standard protocol (Das et al., 2004). DNA was quantified using real-time RT-PCR with SYBR green incorporation (Applied Biosystems). Also see Supplemental Information for additional details.

Immunoprecipitation and Coimmunoprecipitation

Cell lysates were prepared in RIPA (for immunoprecipitation) or Co-IP buffer (for coimmunoprecipitation). A detailed procedure is provided in Supplemental Information.

Electrophoretic Mobility Shift Assays

EMSA procedure and sequence of the ³²P-labeled *BIM* promoter probes are described in Supplemental Information.

Oligonucleotide Pull-Down Assay

Oligonucleotide pull-down assays were performed as previously described (Essafi et al., 2005). The detailed procedure is described in Supplemental Information.

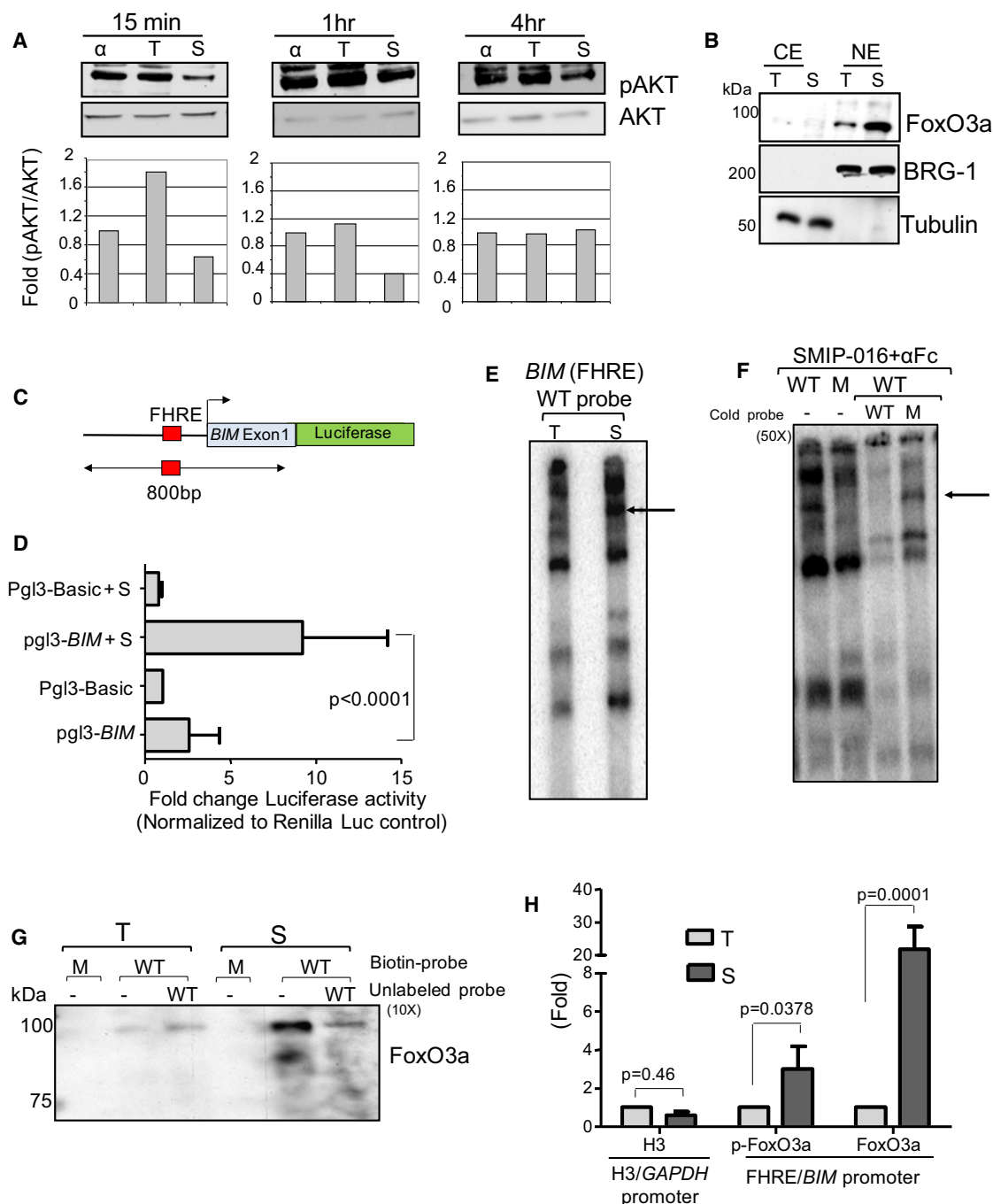


Figure 6. CD37 Cross-Ligation Increases FoxO3a-Dependent Transcription of BIM

(A) Top, immunoblot of nuclear extracts derived from α Fc, trastuzumab+ α Fc-treated (T) or SMIP-016+ α Fc-treated (S) CLL cells; bottom, quantization of the pAKT/total AKT signals in the immunoblots.

(B) Immunoblot analysis of nuclear extracts (NE) and cytoplasmic extracts (CE) from CLL cells stimulated with trastuzumab+ α Fc (T) or SMIP-016+ α Fc (S) using FoxO3a antibody. BRG-1 and Tubulin were used to confirm quality of the separations.

(C) Schema of the Pgl3-BIM reporter construct that includes the reported FoxO3a binding site (FHRE) in the BIM promoter.

(D) Luciferase activity of CLL cells transfected with Pgl3-Basic or Pgl3-BIM reporter constructs along with the Renilla luciferase vector and treated without or with SMIP-016+ α Fc (S) for 12 hr. All values were corrected for cotransfected renilla activity. Data shown are normalized to trastuzumab+ α Fc-treated cells (n = 4).

(E) Nuclear extract from trastuzumab+ α Fc-treated (T) or SMIP-016+ α Fc-treated (S) CLL cells were incubated with 32 P-labeled wild-type (WT) BIM probe containing FoxO3a binding site and analyzed by EMSA. Representative of nine patient samples is shown.

(F) Nuclear extract from SMIP-016+ α Fc-treated CLL cells were incubated with 32 P-labeled wild-type (WT) or mutant (M) BIM probes in the presence or absence of 50x unlabeled wild-type or mutant BIM probes.

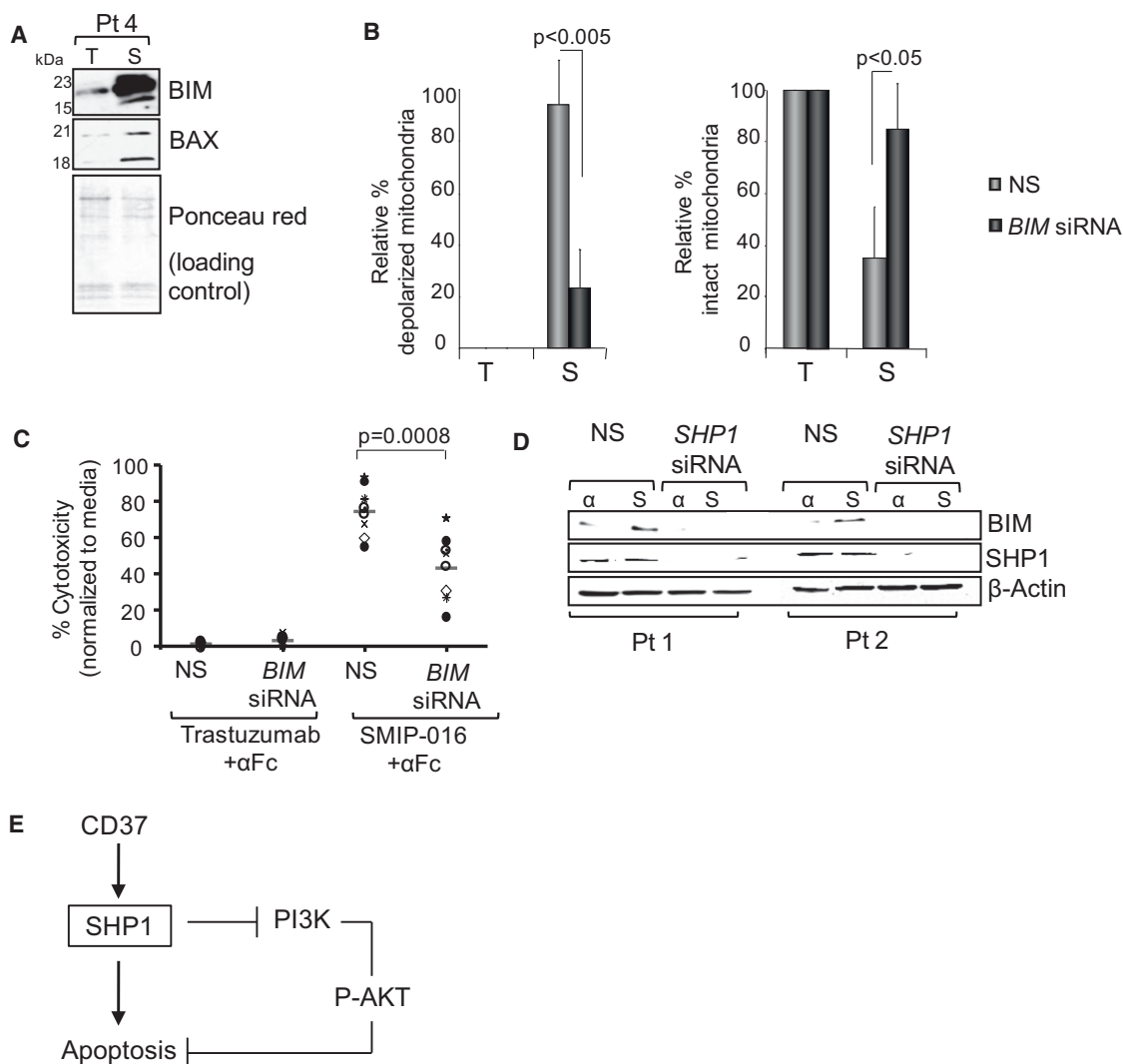


Figure 7. BIM Upregulation Contributes to CD37 Ligation-Mediated Apoptosis

(A) BIM and BAX in mitochondrial extracts from CLL cells treated with trastuzumab+ α Fc (T) or SMIP-016+ α Fc (S) for 24 hr were analyzed by immunoblot. Representative of six patient samples is shown.

(B) CLL cells were transiently transfected with *BIM* siRNA for 24 hr and then treated with trastuzumab+ α Fc (T) or SMIP-016+ α Fc (S) for an additional 24 hr. Cells were then assayed for mitochondrial membrane integrity by JC-1 staining (mean \pm SD; $n = 4$). NS, nonsense siRNA.

(C) Trastuzumab+ α Fc or SMIP-016+ α Fc induced cytotoxicity in CLL cells from (B), as measured by annexin-V/PI staining (24 hr). Each symbol represents a different CLL patient sample; red line represents the average.

(D) BIM and SHP1 immunoblot analysis of CLL cells, from two different patients, transfected with *SHP1*-specific or nonsense (NS) siRNA. Two representative samples out of a total of five are shown.

(E) Diagram depicting CD37-induced apoptosis.

See also Figures S5.

SHP1 Activity Assay

SHP1 phosphatase activity was assessed using the malachite green system (Upstate Biotechnology, Lake Placid, NY) according to the manufacturer's instruction. Detailed protocol is described in [Supplemental Information](#).

PI3K Assay

The PI3K assay was performed on whole-cell lysates from CLL cells. The enzyme-linked immunosorbent assay (Echelon Biosciences, Salt Lake City, UT) was performed according to the manufacturer's instructions as previously described ([Herman et al., 2010](#)).

(G) Biotinylated double-stranded oligonucleotides containing FHRE, coupled to streptavidin agarose beads, were incubated with nuclear extracts from trastuzumab+ α Fc-treated (T) or SMIP-016+ α Fc-treated (S) CLL cells. Bound proteins were eluted and analyzed by FoxO3a immunoblot. Representative of four patient samples is shown. M, mutant probe; WT, wild-type probe.

(H) Chromatin from trastuzumab+ α Fc-treated (T) or SMIP-016+ α Fc-treated (S) CLL cells (12 hr) was analyzed by ChIP assay for binding of FoxO3a to the *BIM* promoter ($n = 4$). The binding of H3 to the *GAPDH* promoter (H3 element) was also evaluated as a control because SMIP-016 does not affect *GAPDH* expression. Data are represented as mean \pm SD for all the relevant panels.

See also Figure S4.

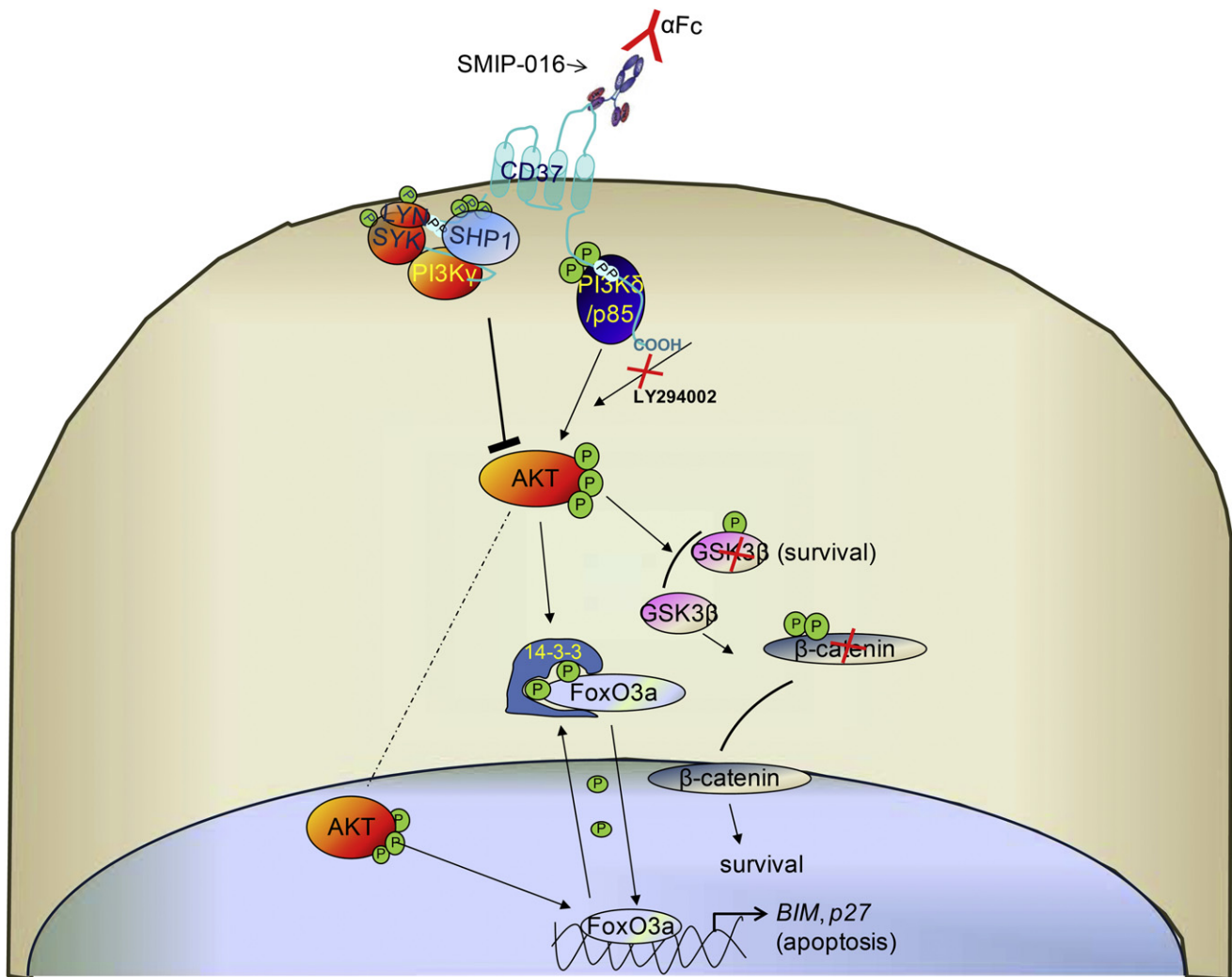


Figure 8. Schema for SMIP-016-Induced Cytotoxicity

Upon ligation of CD37, two signaling pathways are generated, one acting through phosphorylation of the N-t ITIM-like motif of CD37 by LYN kinase, leading to SHP1-dependent *BIM* upregulation and cell death. A second pathway acts through tyrosine phosphorylation of the C-t ITAM-like motif of CD37 with activation of GSK3 β and promotion of cell survival.

Apoptosis and Mitochondrial Membrane Depolarization Studies

Cell death was assessed using annexin-V and propidium iodide (PI) flow cytometry-based assays (BD Biosciences, San Diego, CA) as previously described (Lapalombella et al., 2008). Mitochondrial membrane potential changes were assessed using the voltage-sensitive lipophilic cationic dye 5,5',6,6'-tetrachloro-1,1',3,3'-tetraethylbenzimidazolyl carbocyanine iodide (JC-1; Molecular Probes, Eugene, OR) as previously described (Alinari et al., 2011).

Transient Transfection and *BIM* Luciferase Activity

Luciferase assay was performed as previously described (Lapalombella et al., 2010). The detailed protocol is described in Supplemental Information.

LC-MS/MS Studies

Briefly, after electrophoresis, gels were fixed, washed, and then stained using Coomassie Brilliant Blue. Gels were then trypsin-digested before the peptides were extracted and concentrated under vacuum to a final volume of 20 μ L. Peptides were separated by reversed-phase HPLC and analyzed by mass spectrometry. The detailed procedure is described in the Supplemental Information.

Retrovirus Vectors and Generation of CD37⁺ Cell Lines

Construction of the human CD37 FLAG in pRetro-tight-puro or pBabe-puro and retroviral infection to establish the CD37⁺FLAG 697 cell line are described in detail in Supplemental information.

Statistical Analyses

All analyses were performed by the OSU Center for Biostatistics. A detailed description of statistical tests used is included in the Supplemental Information.

SUPPLEMENTAL INFORMATION

Supplemental Information includes five figures and Supplemental Experimental Procedures and can be found with this article online at doi:10.1016/j.ccr.2012.03.040.

ACKNOWLEDGMENTS

We thank the members of the CLL Experimental Therapeutics laboratory, Freitas laboratory, and Dr. Guido Marcucci, for critical comments and review

of the final manuscript, and Dr. Shu-Huei Wang for *BIM* promoter reporter plasmids. We are grateful for research support from The Leukemia and Lymphoma Society and the National Cancer Institute (grants P50 CA140158, PO1 CA95426, PO1 CA81534, 1K12 CA133250, and RO1 CA107106). Mr. and Mrs. Michael Thomas, The Harry Mangurian Foundation, and The D. Warren Brown Foundation also supported this work.

P.A. and S.S. are employees of Emergent BioSolutions and have financial interests in TRU-016 development. B.L. is an employee of Gilead Pharmaceuticals and has financial interest in Cal-101 development. P.T. was a past employee of Trubion Pharmaceuticals with financial interest in development of TRU-016.

Received: July 31, 2011

Revised: December 13, 2011

Accepted: March 5, 2012

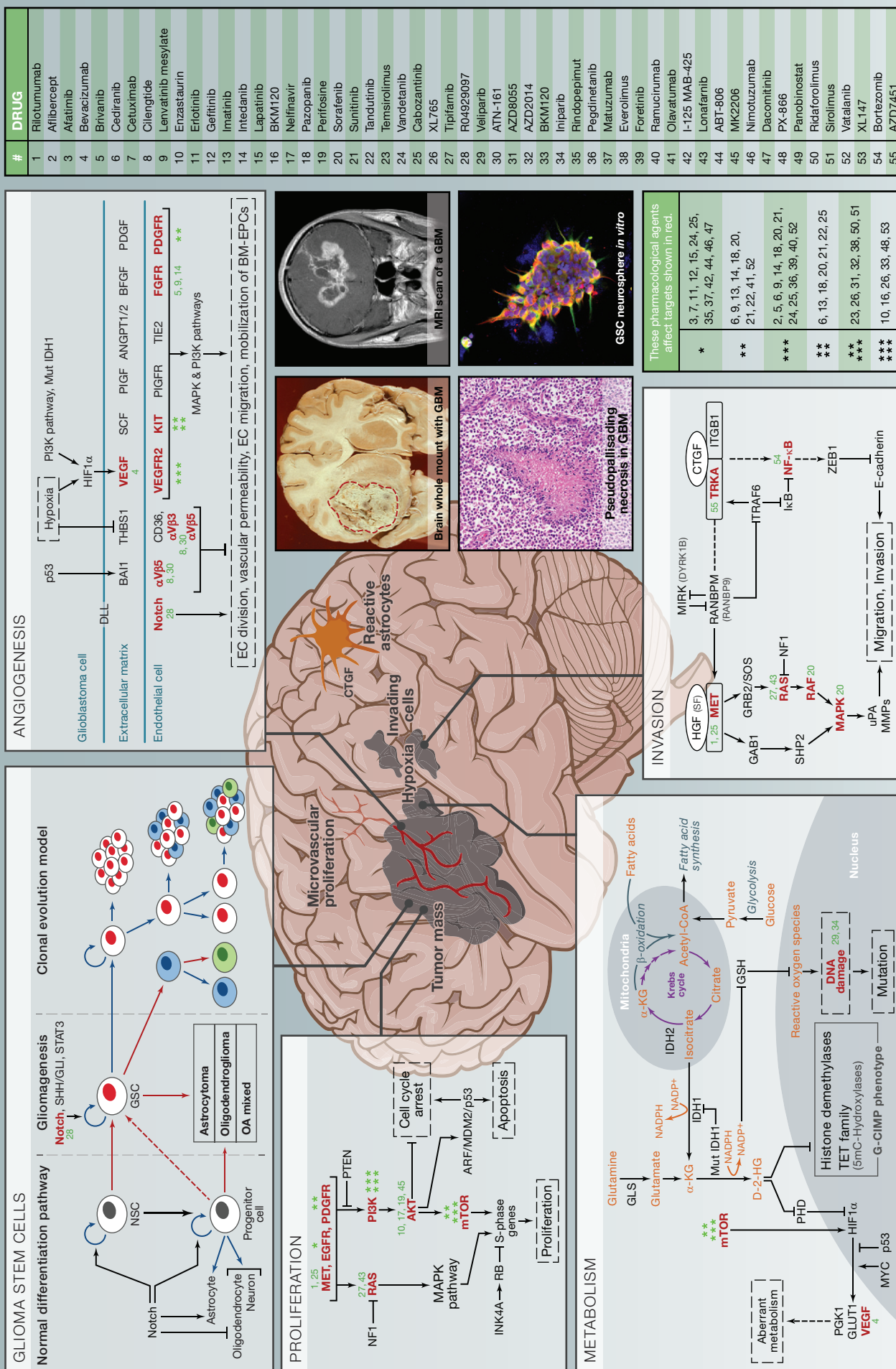
Published: May 14, 2012

REFERENCES

- Alinari, L., Yu, B., Christian, B.A., Yan, F., Shin, J., Lapalombella, R., Hertlein, E., Lustberg, M.E., Quinion, C., Zhang, X., et al. (2011). Combination anti-CD74 (milatuzumab) and anti-CD20 (rituximab) monoclonal antibody therapy has in vitro and in vivo activity in mantle cell lymphoma. *Blood* 117, 4530–4541.
- Angelisová, P., Hilgert, I., and Horejsí, V. (1994). Association of four antigens of the tetraspanin family (CD37, CD53, TAPA-1, and R2/C33) with MHC class II glycoproteins. *Immunogenetics* 39, 249–256.
- Berditchevski, F., Bazzoni, G., and Hemler, M.E. (1995). Specific association of CD63 with the VLA-3 and VLA-6 integrins. *J. Biol. Chem.* 270, 17784–17790.
- Carmo, A.M., and Wright, M.D. (1995). Association of the transmembrane 4 superfamily molecule CD53 with a tyrosine phosphatase activity. *Eur. J. Immunol.* 25, 2090–2095.
- Cheson, B.D., Bennett, J.M., Grever, M., Kay, N., Keating, M.J., O'Brien, S., and Rai, K.R. (1996). National Cancer Institute-sponsored Working Group guidelines for chronic lymphocytic leukemia: revised guidelines for diagnosis and treatment. *Blood* 87, 4990–4997.
- Cooney, D.S., Phee, H., Jacob, A., and Coggeshall, K.M. (2001). Signal transduction by human-restricted Fc gamma RIIa involves three distinct cytoplasmic kinase families leading to phagocytosis. *J. Immunol.* 167, 844–854.
- Cuevas, B., Lu, Y., Watt, S., Kumar, R., Zhang, J., Siminovitsh, K.A., and Mills, G.B. (1999). SHP-1 regulates Lck-induced phosphatidylinositol 3-kinase phosphorylation and activity. *J. Biol. Chem.* 274, 27583–27589.
- Das, P.M., Ramachandran, K., vanWert, J., and Singal, R. (2004). Chromatin immunoprecipitation assay. *Biotechniques* 37, 961–969.
- Essafi, A., Fernández de Mattos, S., Hassen, Y.A., Soeiro, I., Mufti, G.J., Thomas, N.S., Medema, R.H., and Lam, E.W. (2005). Direct transcriptional regulation of Bim by FoxO3a mediates STI571-induced apoptosis in Bcr-Abl-expressing cells. *Oncogene* 24, 2317–2329.
- Hallek, M., Cheson, B.D., Catovsky, D., Caligaris-Cappio, F., Dighiero, G., Döhner, H., Hillmen, P., Keating, M.J., Montserrat, E., Rai, K.R., and Kipps, T.J.; International Workshop on Chronic Lymphocytic Leukemia. (2008). Guidelines for the diagnosis and treatment of chronic lymphocytic leukemia: a report from the International Workshop on Chronic Lymphocytic Leukemia updating the National Cancer Institute-Working Group 1996 guidelines. *Blood* 111, 5446–5456.
- Heider, K.H., Kiefer, K., Zenz, T., Volden, M., Stilgenbauer, S., Ostermann, E., Baum, A., Lamche, H., Küpcü, Z., Jacobi, A., et al. (2011). A novel Fc-engineered monoclonal antibody to CD37 with enhanced ADCC and high proapoptotic activity for treatment of B-cell malignancies. *Blood* 118, 4159–4168.
- Herman, S.E., Gordon, A.L., Wagner, A.J., Heerema, N.A., Zhao, W., Flynn, J.M., Jones, J., Andritsos, L., Puri, K.D., Lannutti, B.J., et al. (2010). Phosphatidylinositol 3-kinase- δ inhibitor CAL-101 shows promising preclinical activity in chronic lymphocytic leukemia by antagonizing intrinsic and extrinsic cellular survival signals. *Blood* 116, 2078–2088.
- Horejsí, V., and Vlcek, C. (1991). Novel structurally distinct family of leucocyte surface glycoproteins including CD9, CD37, CD53 and CD63. *FEBS Lett.* 288, 1–4.
- Imai, T., and Yoshie, O. (1993). C33 antigen and M38 antigen recognized by monoclonal antibodies inhibitory to syncytium formation by human T cell leukemia virus type 1 are both members of the transmembrane 4 superfamily and associate with each other and with CD4 or CD8 in T cells. *J. Immunol.* 151, 6470–6481.
- Janas, E., Priest, R., Wilde, J.I., White, J.H., and Malhotra, R. (2005). Rituxan (anti-CD20 antibody)-induced translocation of CD20 into lipid rafts is crucial for calcium influx and apoptosis. *Clin. Exp. Immunol.* 139, 439–446.
- Kheirallah, S., Caron, P., Gross, E., Quillet-Mary, A., Bertrand-Michel, J., Fournié, J.J., Laurent, G., and Bezombes, C. (2010). Rituximab inhibits B-cell receptor signaling. *Blood* 115, 985–994.
- Knobeloch, K.P., Wright, M.D., Ochsenbein, A.F., Liesenfeld, O., Löhler, J., Zinkernagel, R.M., Horak, I., and Orinska, Z. (2000). Targeted inactivation of the tetraspanin CD37 impairs T-cell-dependent B-cell response under suboptimal costimulatory conditions. *Mol. Cell. Biol.* 20, 5363–5369.
- Lapalombella, R., Yu, B., Triantafyllou, G., Liu, Q., Butchar, J.P., Lozanski, G., Ramanunni, A., Smith, L.L., Blum, W., Andritsos, L., et al. (2008). Lenalidomide down-regulates the CD20 antigen and antagonizes direct and antibody-dependent cellular cytotoxicity of rituximab on primary chronic lymphocytic leukemia cells. *Blood* 112, 5180–5189.
- Lapalombella, R., Andritsos, L., Liu, Q., May, S.E., Browning, R., Pham, L.V., Blum, K.A., Blum, W., Ramanunni, A., Raymond, C.A., et al. (2010). Lenalidomide treatment promotes CD154 expression on CLL cells and enhances production of antibodies by normal B cells through a PI3-kinase-dependent pathway. *Blood* 115, 2619–2629.
- Livak, K.J., and Schmittgen, T.D. (2001). Analysis of relative gene expression data using real-time quantitative PCR and the 2(-Delta Delta C(T)) method. *Methods* 25, 402–408.
- Loeffler, M., Daugas, E., Susin, S.A., Zamzami, N., Metivier, D., Nieminen, A.L., Brothers, G., Penninger, J.M., and Kroemer, G. (2001). Dominant cell death induction by extramitochondrially targeted apoptosis-inducing factor. *FASEB J.* 15, 758–767.
- Maecker, H.T., Todd, S.C., and Levy, S. (1997). The tetraspanin superfamily: molecular facilitators. *FASEB J.* 11, 428–442.
- Marsh, H.N., Dubreuil, C.I., Quevedo, C., Lee, A., Majdan, M., Walsh, G.S., Hausdorff, S., Said, F.A., Zoueva, O., Kozlowski, M., et al. (2003). SHP-1 negatively regulates neuronal survival by functioning as a TrkA phosphatase. *J. Cell Biol.* 163, 999–1010.
- Matsumoto, A.K., Martin, D.R., Carter, R.H., Klickstein, L.B., Ahearn, J.M., and Fearon, D.T. (1993). Functional dissection of the CD21/CD19/TAPA-1/Leu-13 complex of B lymphocytes. *J. Exp. Med.* 178, 1407–1417.
- Mone, A.P., Huang, P., Pelicano, H., Cheney, C.M., Green, J.M., Tso, J.Y., Johnson, A.J., Jefferson, S., Lin, T.S., and Byrd, J.C. (2004). Hu1D10 induces apoptosis concurrent with activation of the AKT survival pathway in human chronic lymphocytic leukemia cells. *Blood* 103, 1846–1854.
- Ozaki, Y., Satoh, K., Kuroda, K., Qi, R., Yatomi, Y., Yanagi, S., Sada, K., Yamamura, H., Yanabu, M., Nomura, S., et al. (1995). Anti-CD9 monoclonal antibody activates p72syk in human platelets. *J. Biol. Chem.* 270, 15119–15124.
- Rogers, N.C., Slack, E.C., Edwards, A.D., Nolte, M.A., Schulz, O., Schweighoffer, E., Williams, D.L., Gordon, S., Tybulewicz, V.L., Brown, G.D., and Reis e Sousa, C. (2005). Syk-dependent cytokine induction by Dectin-1 reveals a novel pattern recognition pathway for C type lectins. *Immunity* 22, 507–517.
- Rubinstein, E., Le Naour, F., Billard, M., Prenant, M., and Boucheix, C. (1994). CD9 antigen is an accessory subunit of the VLA integrin complexes. *Eur. J. Immunol.* 24, 3005–3013.
- Schwartz-Albiez, R., Dörken, B., Hofmann, W., and Moldenhauer, G. (1988). The B cell-associated CD37 antigen (gp40-52): structure and subcellular expression of an extensively glycosylated glycoprotein. *J. Immunol.* 140, 905–914.

- Semac, I., Palomba, C., Kulangara, K., Klages, N., van Echten-Deckert, G., Borisch, B., and Hoessli, D.C. (2003). Anti-CD20 therapeutic antibody rituximab modifies the functional organization of rafts/microdomains of B lymphoma cells. *Cancer Res.* 63, 534–540.
- Truman, J.P., Ericson, M.L., Choqueux-Séébold, C.J., Charron, D.J., and Mooney, N.A. (1994). Lymphocyte programmed cell death is mediated via HLA class II DR. *Int. Immunol.* 6, 887–896.
- Underhill, D.M., Rossmagale, E., Lowell, C.A., and Simmons, R.M. (2005). Dectin-1 activates Syk tyrosine kinase in a dynamic subset of macrophages for reactive oxygen production. *Blood* 106, 2543–2550.
- van Spriel, A.B., Puls, K.L., Sofi, M., Pouniotis, D., Hochrein, H., Orinska, Z., Knobloch, K.P., Plebanski, M., and Wright, M.D. (2004). A regulatory role for CD37 in T cell proliferation. *J. Immunol.* 172, 2953–2961.
- Wright, M.D., and Tomlinson, M.G. (1994). The ins and outs of the transmembrane 4 superfamily. *Immunol. Today* 15, 588–594.
- Wu, C., Sun, M., Liu, L., and Zhou, G.W. (2003). The function of the protein tyrosine phosphatase SHP-1 in cancer. *Gene* 306, 1–12.
- Yi, T.L., Cleveland, J.L., and Ihle, J.N. (1992). Protein tyrosine phosphatase containing SH2 domains: characterization, preferential expression in hematopoietic cells, and localization to human chromosome 12p12-p13. *Mol. Cell. Biol.* 12, 836–846.
- Zhao, X., Lapalombella, R., Joshi, T., Cheney, C., Gowda, A., Hayden-Ledbetter, M.S., Baum, P.R., Lin, T.S., Jarjoura, D., Lehman, A., et al. (2007). Targeting CD37-positive lymphoid malignancies with a novel engineered small modular immunopharmaceutical. *Blood* 110, 2569–2577.

Svetlana Kotliarova and Howard A. Fine
Center for Cancer Research, National Cancer
Institutes of Health, Bethesda, Maryland



SnapShot: Glioblastoma Multiforme

Svetlana Kotliarova and Howard A. Fine

Center for Cancer Research, National Cancer Institute, National Institutes for Neurological Disorder and Stroke, National Institutes of Health, Bethesda, MD 20892, USA

Glioblastoma multiforme (GBM) is the most common and lethal type of primary brain tumor. Although nonmetastasizing, GBM cells can diffusely infiltrate the normal cerebral cortex, resulting in death, with a median survival of 14 months despite combined surgical resection, radiotherapy, and chemotherapy. Standard therapy has been relatively ineffective for many reasons, not the least of which is the extensive invasion of GBM cells into normal brain tissue, which limits the extent of surgical resection and high dose radiotherapy for fear of unacceptable permanent neurological damage to the patient. Traditional chemotherapy has limited value because of poor blood-brain barrier penetration, intrinsic glioma resistance, and nonselective toxicity. Thus, the development of improved therapies rests on a greater understanding of the biology of GBM.

Several molecular and genomic datasets have recently been generated that have allowed us to identify at least four subtypes of GBM: classical, mesenchymal, proneural, and neural. **Classical** subtype is characterized by chromosome 7 amplification, focal *CDKN2A* deletion, chromosome 10 loss, *EGFR* amplification/mutation, a lack of *TP53* mutations, RB pathway alterations, *NES* expression, and high Notch and Hedgehog pathway activity. **Mesenchymal** subtype has frequent mutation or loss of *NF1*, *TP53*, and *PTEN*; frequent chromosomal aberrations at *CDK6*, *MET*, *PTEN*, *CDKN2A*, and *RB1* loci; activation of NF- κ B and TNF pathways; and overexpression of *MET*, *CD44*, *MERTK*, and *CHI3L*. **Proneural** subtype frequently has *IDH1* or *IDH2* mutations; *PDGFR* amplification or *PIK3CA/PIK3R1* mutations; loss or mutation of *TP53*, *CDKN2A*, and *PTEN*; activation of HIF, PI3K, and *PDGFR* pathways; *OLIG2*, *NKX2-2*, and *PDGFRA* oligodendrocytic marker expression; and *TCF4*, *SOX*, *DCX*, *DLL3*, and *ASCL1* proneural marker expression. **G-CIMP** methylator phenotype characterizes a subgroup of proneural GBM that may represent a distinct tumor type. **Neural** subtype is related to the classical subtype but has a higher frequency of *TP53* mutation; *EGFR* amplification/overexpression; and *NEFL*, *GABRA1*, *SYT1*, and *SLC12A5* neuronal marker expression.

The traditional strategy in oncology of attempting tumor eradication has been challenged with the concept that even without killing every last cancer cell, interfering with critical aspects of tumor biology may translate to significant clinical benefit. The accompanying SnapShot diagrammatically captures several key biological properties and the responsible molecular pathways that represent the current focus of GBM clinical trials.

Proliferation

Cell cycle deregulation in GBMs is in part a result of abnormal signaling by several different receptor tyrosine kinases (RTKs) including *EGFR*, *PDGFR*, and *MET*. These RTKs act downstream to deregulate MAPK and PI3K pathways. The greatest emphasis in targeted drug development for GBM has focused on RTK inhibitors. Recent preclinical and clinical work indicates redundancy in RTK signaling, suggesting the need for simultaneous inhibition of multiple RTKs or inhibition of downstream signals; hence, there has been great interest in the clinical testing of inhibitors of PI3K, AKT and the TORC1/2 complexes. Although there was an initial interest in CDK inhibitors, early clinical data suggest nonselectivity of the agents and toxicity to normal proliferating cells.

Metabolism

GBMs, like other tumors, prefer aerobic glycolysis (a phenomenon known as the Warburg effect). Preclinical data has demonstrated a dependency on altered glucose and fatty acid metabolism, but drugs that selectively interfere with these biochemical pathways are only now coming into clinical development. This altered metabolism also results in the generation of excess reactive oxygen species (ROS), which has led to the development of several new agents that interfere with the GBM cell's ability to neutralize ROS. Moreover, about 80% of low grade gliomas and about 5%–10% of GBMs have mutations in *IDH1* or *IDH2* causing altered 2-hydroxyglutarate production and altered DNA methylation, which has led to trials with *IDH1* inhibitors and demethylating agents to address the epigenomic changes associates with this genotype.

Glioma Stem Cells

There is increasing evidence that only a subpopulation of cells within a GBM truly has tumorigenic properties. The nature of these cells remains controversial, but it is clear that at least some canonical stem cell signaling pathways are operative in glioma stem/initiating cells (GSCs). It appears that Notch signaling is vital for proliferation and survival of GSCs, leading to a series of clinical trials in GBM with γ -secretase inhibitors. There is also evidence to suggest that at least some GSC lines are dependent on the Hedgehog and Wnt pathways, paving the way for clinical trials with Smo inhibitors and inhibitors of Wnt ligands.

Angiogenesis

GBMs are highly angiogenic and vasculogenic. VEGF is a primary mediator of tumor angiogenesis and GBM-associated cerebral edema. Anti-VEGF bevacizumab can significantly decrease cerebral edema and potentially inhibit tumor growth in patients. Small molecule inhibitors of VEGFR, however, have proven less effective in the clinic to date. Ongoing clinical trials are investigating agents that target other angiogenic factors and their receptors (e.g., *PDGFR*, *c-KIT*, *FGFR*) as well as endothelial cell-associated integrins.

Invasion

Since GBMs generally kill via their invasiveness, patient morbidity and survival might be greatly improved by inhibiting invasion. PI3K and MAPK pathway deregulation has been linked with increased cellular motility via *EGFR* signaling in GBM. Amplification and/or overexpression of the *HGF/MET* pathway have also been implicated in GBM invasion, leading to clinical trials of *MET* inhibitors. Recently, *TRKA* has been implicated as an important mediator of GBM stem cell migration, leading to the testing of novel TRK inhibitors.

It is unlikely that inhibiting any one pathway will result in dramatic clinical benefit, but it is hoped that interfering with two or more key biological functions will. For example, recent preclinical and clinical data suggest that VEGF inhibition leads to increased GBM invasiveness. New clinical trials, therefore, are now being developed to combine angiogenic inhibitors such as bevacizumab with *MET* and/or TRK inhibitors. These future trials likely hold the most promise for improved therapy for this devastating disease.

REFERENCES

- Edwards, L.A., Woolard, K., Son, M.J., Li, A., Lee, J., Ene, C., Mantey, S.A., Maric, D., Song, H., Belova, G., et al. (2011). Effect of brain- and tumor-derived connective tissue growth factor on glioma invasion. *J. Natl. Cancer Inst.* 103, 1162–1178.
- Noushmehr, H., Weisenberger, D.J., Diefes, K., Phillips, H.S., Pujara, K., Berman, B.P., Pan, F., Pelloski, C.E., Sulman, E.P., Bhat, K.P., et al. (2010). Identification of a CpG island methylator phenotype that defines a distinct subgroup of glioma. *Cancer Cell* 17, 510–522.
- Phillips, H.S., Kharbanda, S., Chen, R., Forrest, W.F., Soriano, R.H., Wu, T.D., Misra, A., Nigro, J.M., Colman, H., Soroceanu, L., et al. (2006). Molecular subclasses of high-grade glioma predict prognosis, delineate a pattern of disease progression, and resemble stages in neurogenesis. *Cancer Cell* 9, 157–173.
- Singh, S.K., Hawkins, C., Clarke, I.D., Squire, J.A., Bayani, J., Hide, T., Henkelman, R.M., Cusimano, M.D., and Dirks, P.B. (2004). Identification of human brain tumour initiating cells. *Nature* 432, 396–401.
- Stupp, R., Mason, W.P., van den Bent, M.J., Weller, M., Fisher, B., Taphoorn, M.J., Belanger, K., Brandes, A.A., Marosi, C., Bogdahn, U., et al. (2005). Radiotherapy plus concomitant and adjuvant temozolomide for glioblastoma. *N. Engl. J. Med.* 352, 987–996.
- Turcan, S., Rohle, D., Goenka, A., Walsh, L.A., Fang, F., Yilmaz, E., Campos, C., Fabius, A.W., Lu, C., Ward, P.S., et al. (2012). *IDH1* mutation is sufficient to establish the glioma hypermethylator phenotype. *Nature* 483, 479–483.
- Verhaak, R.G., Hoadley, K.A., Purdom, E., Wang, V., Qi, Y., Wilkerson, M.D., Miller, C.R., Ding, L., Golub, T., Mesirov, J.P., et al. (2010). Integrated genomic analysis identifies clinically relevant subtypes of glioblastoma characterized by abnormalities in *PDGFRA*, *IDH1*, *EGFR*, and *NF1*. *Cancer Cell* 17, 98–110.
- Yan, H., Parsons, D.W., Jin, G., McLendon, R., Rasheed, B.A., Yuan, W., Kos, I., Batinic-Haberle, I., Jones, S., Riggins, G.J., et al. (2009). *IDH1* and *IDH2* mutations in gliomas. *N. Engl. J. Med.* 360, 765–773.